UNIVERSITY OF OKLAHOMA
GRADUATE COLLEGE

3-D BASIN ANALYSIS OF THE CENOZOIC WAGWATER TROUGH, JAMAICA

A THESIS
SUBMITTED TO THE GRADUATE FACULTY
in partial fulfillment of the requirements for the
Degree of
MASTER OF SCIENCE

By
THOMAS PAUL WARD
Norman, Oklahoma
2009

© Copyright by THOMAS PAUL WARD 2009
All Rights Reserved.

ACKNOWLEDGEMENTS

There are a number of people that have helped me in my endeavor to get my Masters degree. A special thanks to my thesis advisor, Dr. John D. Pigott, for supporting me with his extensive knowledge on scientific problems and endless hours of draft revisions. Great appreciation goes to Dr. R. Douglas Elmore and Dr. Michael J. Soreghan for their valuable comments and for spending time to be on my thesis committee.

I would also like to thank Victor Parra for his friendship and assistance in the field helping me with my field work and my field interpretations.

Very special thanks to my dear wife, Danette, for supporting me in my pursuit of this degree and assisting me in the field. I also was to thank her for her patience spending days and nights without me while working on my thesis and for spending late nights helping me revise thesis drafts.

Finally, I would like to thank my daughter, Vanessa, for being understanding while I was away and not spending as much time with her as we both would have liked.

TABLE OF CONTENTS

LIST OF TABLES

LIST OF FIGURES

ABSTRACT

The Wagwater trough in eastern Jamaica is a fault-bounded half graben that formed as a result of regional dextral shear at a releasing bend connecting the Septentiornal-Oriente-Swan-Motagua and Plantain Garden-Swan fault systems. There are two major stages of tectonic development: (1) Paleocene to Middle Eocene fault mechanical crustal subsidence (66-51 Ma; β=1.66), (2) Middle Eocene to Middle Miocene thermal subsidence (51-10 Ma), and (3) Middle Miocene to Holocene crustal shortening (10-0 Ma; β=0.81). Clastic sedimentation prevailed during the period of fault mechanical crustal subsidence with the deposition of the Wagwater Formation and Richmond Formation, while the period of thermal subsidence was period with carbonate deposition of the Yellow Limestone and White Limestone Groups. Early-rifting commenced with the sedimentation of Wagwater alluvium. A marine transgression allowed the deposition of Richmond shelf and slope deposits and later Yellow and White Limestone deposits. Middle Miocene marks a period of time when regional dextral shear was reversed. The Wagwater Trough experienced negative tectonic subsidence caused by regional sinistral shear at a constraining bend. This caused crustal shortening and surface exposure of the sediments of the Wagwater Trough. By constraining the present-day depth to basement using the Bouguer gravity anomaly, basin subsidence produced sediment thicknesses up to 6,000 meters.

Two end-member rifting heat flow models likely bracket and constrain the heat flow of the basin: (1) calculated from a present-day heat flow of 0.96 H.F.U. and (2) calculated from a present-day heat flow of 1.4 H.F.U. Both modeled thermal conditions allow for the shale layers of the Richmond Formation to range from mature enough to be

in the early oil and mid oil windows for the 0.96 H.F.U. model to middle and late oil windows and gas window for the 1.4 H.F.U. model. The first in situ oil for the rifting 1.4 H.F.U. model commenced at 52 Ma, while that for the rifting 0.96 H.F.U. model is 49 Ma. First expulsion time was 50 Ma for rifting 1.4 H.F.U. model and was 41 Ma for the rifting 0.96 H.F.U. case. Hydrocarbons could potentially accumulate in traps based on two cases: the impermeable fault model and the permeable fault model.

1. INTRODUCTION

1.1 Statement of Problem

On the east side of the island of Jamaica there is a rift basin with a complex geologic history called the Wagwater trough. Mann and Burke (1990) stated that the Wagwater Trough is an exceptionally well exposed example of a transverse intra-arc rift that formed during an abrupt transition from convergent to strike-slip tectonics. It began rifting during the Paleocene and continued into the Eocene (Mann and Burk, 1990). Wescott and Ethridge (1983) stated that during the Early Paleocene Period, Jamaica was part of an emergent landmass that rifted from north to south, and the Wagwater Trough developed as a graben separating lands to the east and west. It is comprised mainly of clastic rocks with some limestone deposits and igneous lava and ash flows.

By performing a basin analysis of the Wagwater Trough, models can be developed to determine basin subsidence history, thermal properties, and hydrocarbon potential. This will help in determining the basin evolution history and the probability to prospect the region for oil and gas production.

1.2 Location and Physiography

The island of Jamaica measures approximately 225 km east to west and 100 km north to south and lies on the northern boundary of the Caribbean Plate. It originally formed as an emergent landmass on the Nicaraguan Rise (Figure 1.2.1) (Mann et al., 1985 and Arden, 1975).

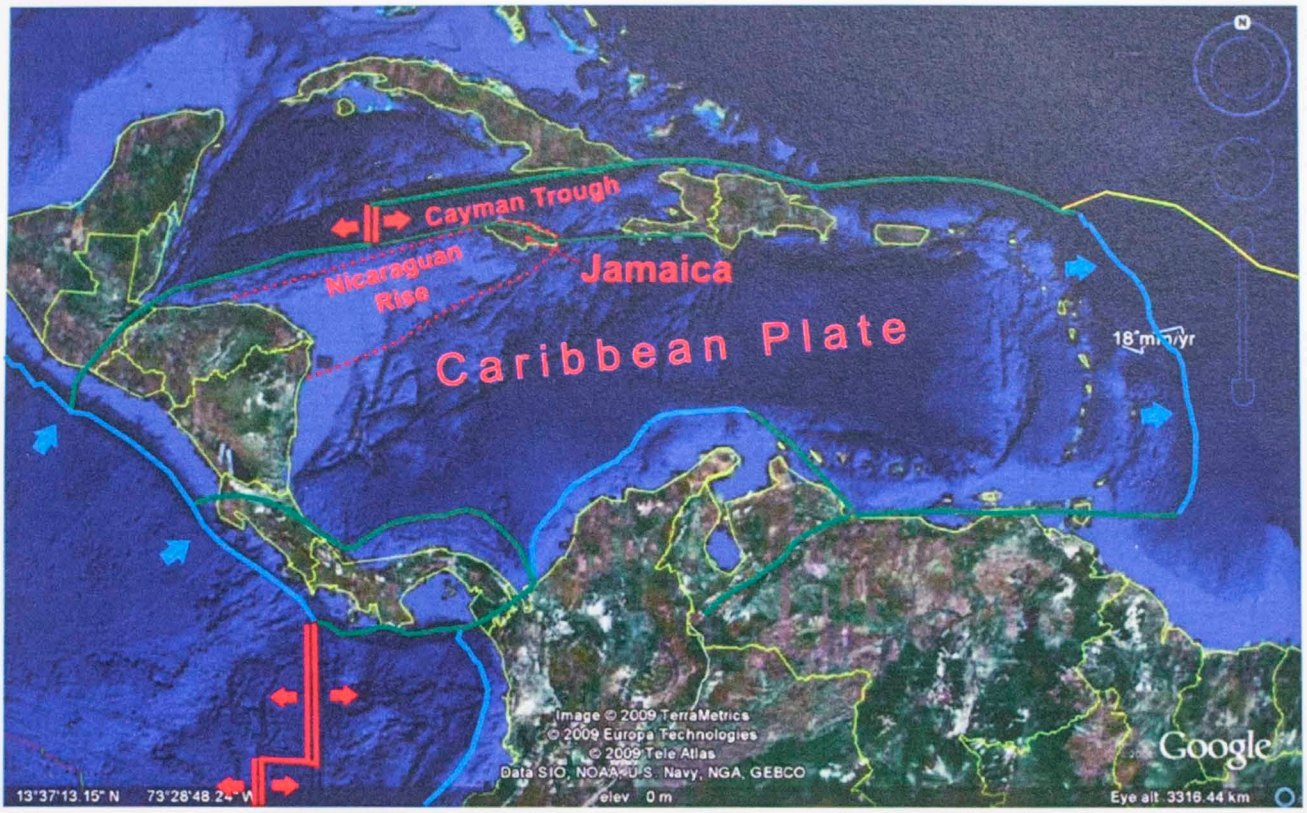

Figure 1.2.1: Map showing the orientation of the Caribbean Plate, Nicaraguan Rise, and Jamaica. Presently, the Caribbean Plate is moving in an eastward direction relative to the surrounding plates. Jamaica lies on the northern boundary of the Caribbean Plate and is just south of the Cayman Trough. It is part of the Nicaraguan Rise. Spreading zones are traced in red, collision zones are traced in blue, and transform zones are traced in green.

The Nicaraguan rise is a broad submarine swell of intermediate crustal thickness (~22 km). It extends from Honduras, Central America to southern Haiti, Hispañola (Figure 1.2.1). During the Jurassic and into the Cretaceous, the Nicaraguan Rise was a mobile belt of vast submarine lava flows and mafic intrusions. As this active volcanism subsided, Paleogene clastic and chemical sedimentation became the dominate mechanism for island growth on Jamaica. (Arden, 1969).

The Wagwater trough is a northwest to southeast trending fault bounded basin located between the Benbow inlier and the Blue Mountain inlier (Figure 1.2.2) (Wescott and Ethridge, 1983; Mann and Burke, 1990).

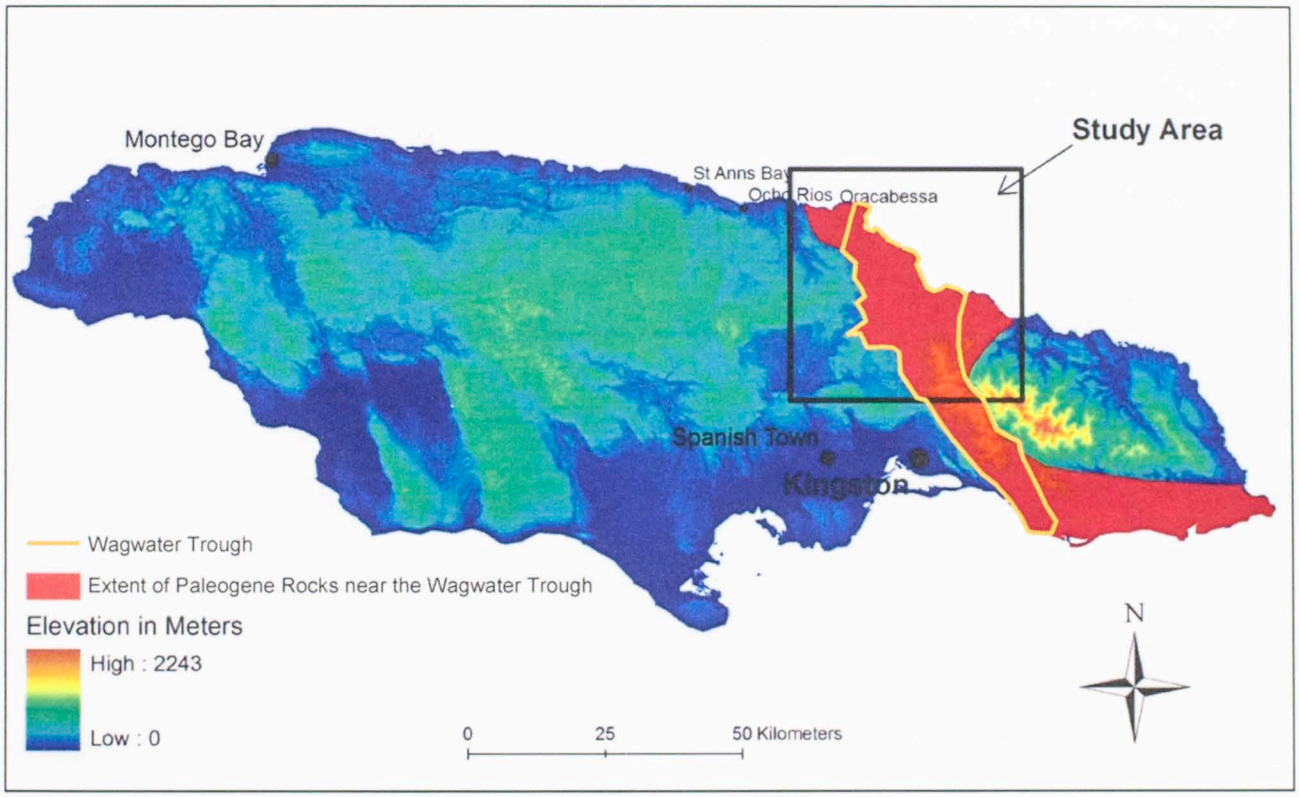

Figure 1.2.2: Relief Map of Jamaica. The Wagwater Trough trends northwest to southeast in the northern and central regions, and it trends west to east in the southern region. The extent of the Wagwater Trough is colored in red. The area selected for this study is the northernmost region. It has experienced the least amount of post-basinal deformation (After Perry, 1984).

2. STRATIGRAPHIC SETTING

2.1 Introduction

The Wagwater Trough has a minimum of 6,800 meters of Early Paleogene clastic sediment unconformably overlaying Albian to Maastrichtian volcanic, volcaniclastic, and plutonic rocks. These basement rocks are typical of those found in arcs built entirely of oceanic crust, and they have been interpreted as an intra-oceanic arc complex, active throughout most of the Cretaceous (Mann et al., 1985; Mann and Burke 1990; Roobol, 1972; Horsfield and Roobol, 1974; Draper, 1979; Grippi and Burke, 1980).

Mesozoic rocks in Jamaica are exposed in a number of elongate inliers that have been uplifted along northwest-striking, reverse faults (Mann et al., 1985). There are three Mesozoic inliers near the Wagwater Trough: The Blue Mountain inlier to the east and the Central and Benbow inliers to the west. The rocks of these three inliers in Eastern Jamaica make up a significant amount of the clastic source material for sediments found within the Wagwater Trough. The unconformity between the Late Cretaceous and Early Eocene divides the pre-rifting Jurassic and Cretaceous rocks from the Early Paleogene clastic deposits which make up the majority the sedimentation in the Wagwater Trough.

2.2 Early Paleogene Formations

There are three distinct periods of Paleogene sedimentation in the Wagwater trough: early-rifting coarse alluvium deposits in alluvial fans and alluvial fan-deltas (Wagwater Formation), late-rifting coarse sandy and shaley deposits in deltas and submarine slope fans (Richmond Formation), and post-rifting deep marine limestone

deposits and slides (Yellow and White Limestone Formations) (Figure 2.2.2) (Mann and Burke, 1990).

Perry (1984) suggested that these three periods of sedimentation in the Wagwater Trough were related to deposition due to subsidence from rifting. During initial rifting stages, Middle to Late Paleocene terrestrial deposition in the trough of alluvium in fans was further transported north out of the trough through alluvial fan-deltas (Figure 2.2.1a). This depositional event is marked by the Wagwater Formation. During the Late Paleocene and into the early to Middle Eocene, a marine transgression into the trough was reflected by deposition of coarse delta facies in the trough and delta-front turbidites in the more northern region of the trough beyond the shelf (Figure 2.2.1b). This period is marked by the deposition of the Richmond Formation. As rifting ceased and sediment supply began to diminish, Middle to Late Eocene, deep sea limestone deposits began to accumulate (Figure 2.2.1c). These deposits are the Yellow Limestone Formation during the Late Eocene and Early Oligocene and the White Limestone Formation during the Middle Oligocene and Miocene.

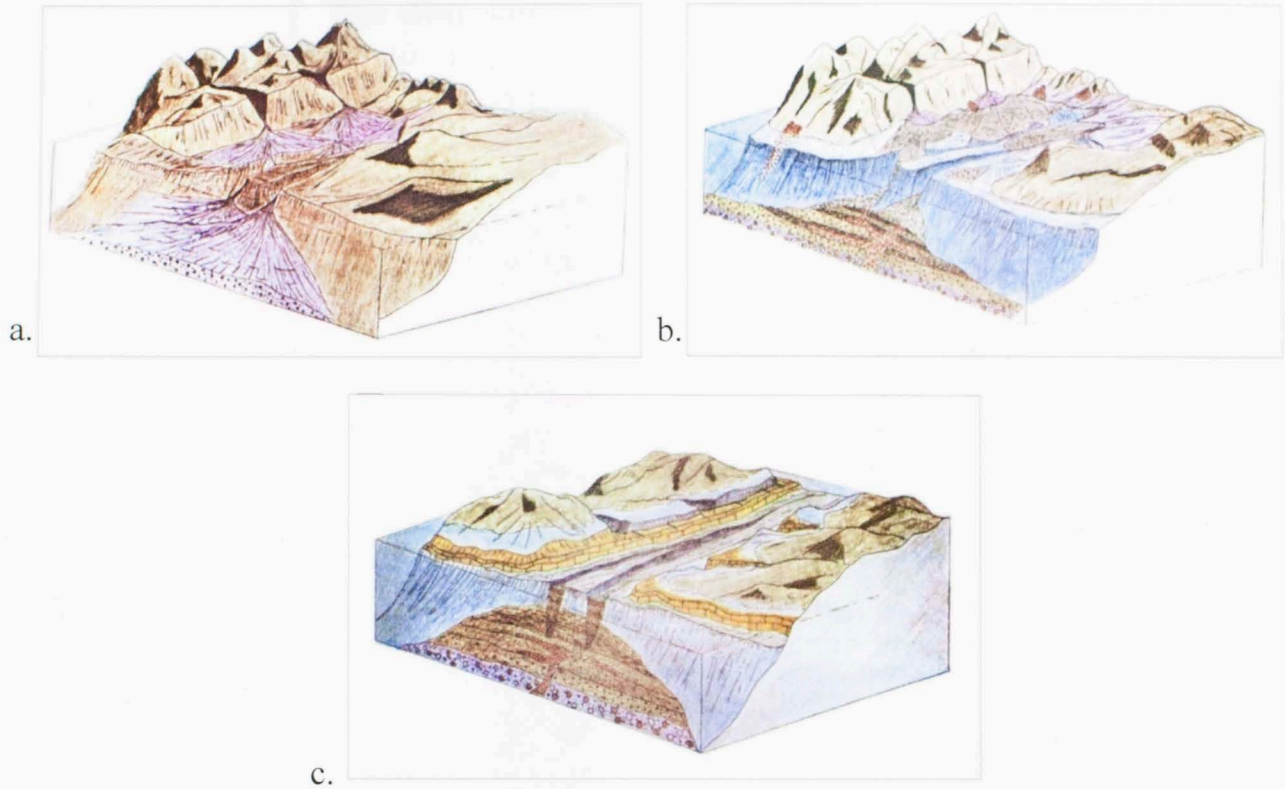

Figure 2.2.1: Models showing inferred depositional environments during three different stages of deposition by Perry (1984): a. early-rifting deposition in alluvial fans and fan-deltas (Wagwater Formation), b. late-rifting deposition in deltas, submarine slope and basin floor (Richmond Formation), and c. post-rifting deep-water carbonate banks (Font Hill Formation of the Yellow Limestone Group).

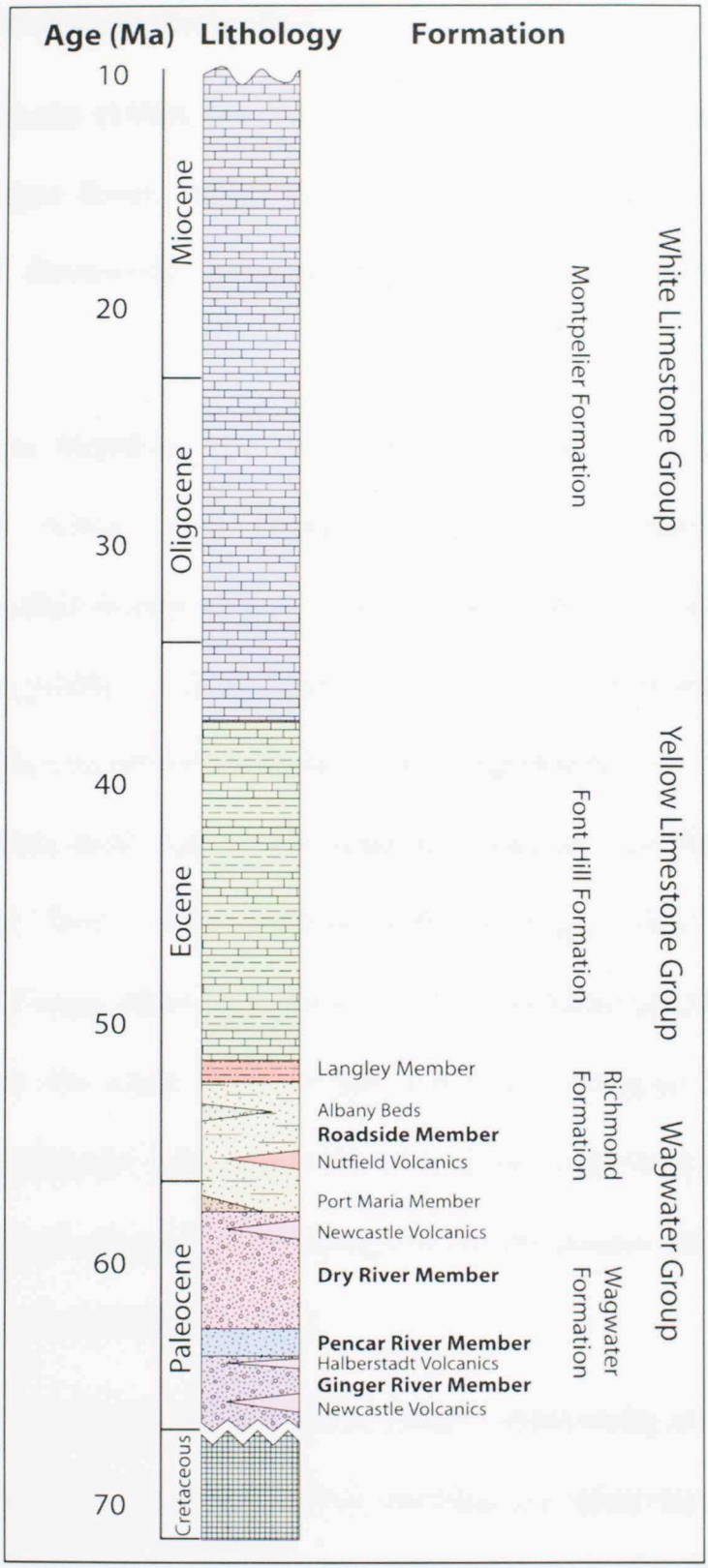

Figure 2.2.2: Generalized stratigraphic column of the Wagwater Trough. The Wagwater Formation is comprised of three members: Ginger River, Pencar River, and Dry River. The Richmond Formation has four members: Roadside, Port Maria, Albany, and Langley. Post-rifting carbonate deposition dominated from the Middle Eocene until the region was uplifted in the Miocene (after Mann and Burke, 1990).

2.3 Early-Rifting Wagwater Formation

Mann and Burke (1990) divided the lithology of the Wagwater Formation into three members: Ginger River, Pencar River, and Dry River Members. These members mark a period of dominantly subaerial deposition with a brief period of marine deposition.

Ginger River Member. The Ginger River Member has a maximum measured thickness of 3800 meters. It is mostly a very poorly sorted, purple, polymict conglomerate. The conglomerate clasts contain metamorphic and volcanic rock fragments ranging in size from pebbles to boulders up to three meters in diameter. No plutonic rock clasts are found in the Ginger River Member. The conglomerates are clast-supported with a poorly-sorted muddy-sand matrix. The beds are massive with thicknesses up to ten meters (Mann and Burk, 1990; Wescott and Ethridge, 1983). The depositional environment of the Ginger River Member is that of a proximal alluvial fan deposit. The large grain sizes of the clasts indicate that deposition occurred in periods of high discharge in fluvial channels from adjacent highlands on to the head of the fan. The fans appear to be deposited adjacent to the scarps of the Wagwater fault zone (Mann and Burke, 1990; Wescott and Ethridge, 1983).

The Ginger River Member was unsuccessfully dated using microfossils by Ming-Jung and Robinson (1987). The Ginger River Member was relatively dated by Mann and Burke (1990) to be Paleocene in age, because it conformably underlies the Pencar River Member which has been dated by Ming-Jung and Robinson (1987) to be Latest Paleocene to Earliest Eocene (Jung and Robinson, 1987; Mann and Burke, 1990).

Pencar River Member. Conformably overlying the Ginger River Member is a 300 meter section of sandstones and conglomerates. This unit is confined mainly to the southern and central region of the Wagwater trough and pinches out in the northern region. In the north-central region of the trough, it consists of a dark grey to green, coarse sandstone and conglomerate. Ripple marks are present on some bedding surfaces. Below the conformable contact with the overlying Dry River Member there are thin lenses of grey, limestone. This unit represents a brief landward transgression of sea water into the Wagwater Trough, and, near the top of the Pencar River Member, a seaward regression (Mann and Burke, 1990).

The age of the Pencar River Member was determined by Ming-Jung and Robinson (1987) using the fossils *Coccolithus pelagicus*, *Toweius*, *Discoaster multiradiatus*, and *Fasciculithus*. They determined that the Pencar River Member had an age of Late Paleocene to Early Eocene or zones NP9 and NP10 by Martini (1971).

Dry River Member. The Dry River Member conformably overlies the Pencar River Member and has a measured thickness up to 1000 meters. The Dry River Member consists mainly of inter-bedded poorly sorted, purple and polymict conglomerates, sandstones, and shales. Lithologically, they are similar to the Ginger River Member, but distinguished by its dark red to purple color and its granodioritic clast content. They are massive, clast-supported conglomerates that have a mud-sand matrix with crude horizontal laminae. The Clasts include granodiorite rocks, porphyritic volcanic rocks, metamorphic rocks, and a few limestone and gypsum fragments. Bedding is rarely seen except where lenses of coarse sandstone weakly define bedding (Mann and Burke, 1990; Wescott and Ethridge, 1983).

Because there are no fossil dates, the age of the Dry River was determined relatively by Mann and Burke (1990) to be Late Paleocene because it is overlain by the Early Eocene Richmond Formation.

Petroleum Potential of the Wagwater Formation. The Wagwater formation is considered to have a low petroleum potential. It generally has a Type III kerogen, because it contains an abundance of terrigenous, woody materials. In general the sandstones and conglomerates of the Wagwater Formations are very immature and poorly sorted with low porosity and permeability. The Wagwater Formation probably has both low reservoir potential and low source rock potential. However, some coarse, better-sorted sandstones and conglomerates of the formation, probably representing channel infillings, may provide small stratigraphic traps of reasonable porosity and permeability (Eva, 1980).

Newcastle and Halberstadt Volcanics. Green (1977) identified five massive andesite and dacite lava flows which individually range up to 600 m in thickness. The Newcastle Volcanic Formation is most abundant in the Dry River Member of the Wagwater Formation but can also be found in the Ginger River and Pencar River Members of the Wagwater Formation and even some in the Roadside Member of the Richmond Formation. They are composed of porphyritic andesite, dacite, and quartz keratophyre lava flows and their sedimentary derivatives (Roobol, 1972; Mann and Burke, 1990). The Newcastle dacites only outcrop in the central and southern regions of the Wagwater Trough. In the southern portions of the Wagwater Trough, a 200-300 meter thick basalt pillow lava pile outcrops near the town of Halberstadt known as the

Halberstadt Volcanics. It is contained within the Paleocene Pencar River Member (Mann and Burke, 1990).

2.4 Late-Rifting Richmond Formation

Mann and Burke (1990) divided the Richmond Formation into four sedimentary members: Port Maria, Roadside, Albany, and Langley Members. The Richmond Formation is thicker in the northern section of the Wagwater Trough (1200 meters) relative to the southern section of the Wagwater Trough (1000 meters). Depositional paleo-currents of the Richmond formation indicate two main directions of flow from the sides of the basin (about N45E) and parallel to the Wagwater and Yallahs-Silver Hill fault zones (N30W) Mann and Burke (1990) suggested that the deposition of the Richmond Formation continued to be affected by the underlying boundary faults of the graben. (Mann and Burke, 1990; Cambray and Jung, 1970; Mann 1983).

Port Maria Member. The Port Maria Member makes up part of the base of the Richmond Formation with thicknesses measured up to 250 meters. It consists of calcite cemented brown-weathering conglomerate beds that are generally clast-supported and massive inter-bedded sandstone and silt layers (Mann and Burke, 1990; Wescott and Ethridge, 1983). It is distinguished from the Dry River Member of the Wagwater Formation by its un-weathered grey color, weathered brown color, and calcite cement presence. The calcite cemented clasts are generally smaller in size and better rounded than the Dry River Member. The clasts are made up of limestone, sandstone, granodiorite, and metamorphic rock fragments. Rudist, mollusk, and other limestone fragments are fairly common and indicate deposition in a marine environment as a submarine slump deposit. This unit is only exposed in sea cliffs between just north of

Port Maria and Anotto Bay (Mann and Burke, 1990; Wescott and Ethridge, 1983; Trechmann, 1924).

Trechmann (1924) used the mollusks from the cliffs near the city of Port Maria to assign an age of Early to Middle Eocene to the Port Maria Member.

Roadside Member. The Roadside member is the thickest and best exposed member of the Richmond Formation. It consists of 800 meters of thin horizontal inter-beds of sandstone, siltstone, and mudstone, each a few centimeters to a few tens of centimeters thick. The sandstone beds are graded and fine upward into the overlying mudstone. The sandstone units commonly have parallel laminations and are amalgamated. They appear as sheet sands; however, when seen in more extensive exposures they have definite lenticular shapes (Mann and Burke, 1990; Wescott and Ethridge, 1983).

Flutes, grooves, and load casts are seen on the bottom surfaces of the sandstone layers. Paleocurrent studies from sole marks indicate that current directions were both parallel and perpendicular to the bounding faults of the Wagwater Trough. Horizontally laminated sandstone layers are overlain by ripple cross-laminated sandstones and siltstones and then parallel laminated shales. Each sandstone-shale couplet is interpreted as Bouma B-C-E sequences by Wescott and Ethridge (1983). The inter-bedded sandstone and shale sequences are extensively bioturbated by vertical and horizontal feeding and dwelling burrows, including Thalassinoides (Figure 2.4.1). According to Ekdale et al. (1984), it is part of the Cruziana ichnofacies, and deposition occurred in the sub-littoral zone at about 200 meters water depth. Mann and Burke (1990) measured the proportion of sandstone to siltstone/shale in the Roadside Member to range from about 1:1 to 1:4

(Mann and Burke, 1990; Wescott and Ethridge, 1983; Cambray and Jung, 1970; Ekdale et al., 1984).

Figure 2.4.1: Thalassinoides fossil burrows found in and below the base of the sandstone layer identified in figure 2.4.2. According to Ekdale et al. (1984), these trace fossils indicate a depositional depth of about 200 meters. It appears that bioturbated layers were disturbed and ripped up as turbidity currents brought new sediments. The surface viewed in this particular sample is the bottom side of the hand sample.

The Roadside Member contains an abundance of Early Eocene planktonic foraminifera that include *Tremastegina lopeztrigoi* and *Helicostegina sp.* Nannofossils are indicative of NP12 zone or Early Eocene, because it contains an abundance of *Marthasterites tribrachiatus* and *Disoaster lodoensis* (Ming-Jung and Robinson, 1987).

Figure 2.4.2: Roadside Member of the Richmond Formation along highway A3 between Whitehall and Albany. It consists of horizontal and thin-bedded sandstone, siltstone, and mudstone. The sandstone beds are graded and some of their basal surfaces are marked by flute, groove, and load casts. The sandstone units commonly have parallel laminations, are commonly amalgamated, and in more extensive exposures, definite lenticular shapes. Bioturbation is common throughout the unit. The location of the bioturbated sample in figure 2.4.1 is identified by the red arrow (Mann and Burke, 1990; Wescott and Ethridge, 1983).

Albany Member. Contained within the Roadside Member are two mapable units: the Albany Beds and the Nutfield Volcanics (mentioned later in this paper). The Albany Beds consist of clast-supported conglomerate beds that have very poor-sorting. The clast composition is similar to the Port Maria Member; however the clast sizes are smaller than the Port Maria Member (pebble to cobble sized). Mollusks and coral heads are common in this layer, indicating marine deposition. Individual conglomerate beds are lenticular

and bounded by scour surfaces. This member indicates a period of shelf slumping and contains blocks of thinly bedded sandstone and shale typical of the overlying and underlying Roadside Member (Mann and Burke, 1990; Wescott and Ethridge, 1983).

Figure 2.4.3: Albany Member of the Richmond Formation along highway A3 between Whitehall and Albany. It is composed of massive, very poorly sorted conglomerates with a sandy mudstone matrix. The beds are clast-supported, but appear matrix-supported. The painted red dots can be used for scale. Each represents one foot in measurement (Wescott and Ethridge, 1983).

Langley Member. The Langley Member conformably overlies the Roadside Member. It measures about 200 meters in thickness, and consists of evenly bedded alternating dark grey and greenish-grey organic-rich laminated mudstone and siltstone. The laminae average two to three mm in thickness. There are coarser, graded layers of silt to coarse sandstone, of similar thickness to the mudstones and containing shell fragments. The Langley member has similar properties to the Roadside Member, and, in order to help simplify the models in this study, the two are combined and called the Roadside Member (Mann and Burke, 1990).

The age of the Langley Member was determined in part by Robinson (1969) using the species *Globorotalia palmerae* which indicated the *Acarinia pentacamerata* zone as well as benthonic species, shell fragments, and algal detritus. Ming-Jung and Robinson (1987) determined that nannofossils from the lower part of the member yield an age of Early to Middle Eocene or the NP14 zone Mann and Burke, 1990).

Petroleum Potential of the Richmond Formation. The petroleum potential of the Richmond formation is better than the Wagwater Formation; however, much of the published literature states that it still has a low petroleum potential. The Richmond formation contains a reasonably large proportion of marine mudstones and shales, often containing thin horizons of lignite (Eva, 1980 and Robinson, 1976). These could locally act as source beds and/or seals for hydrocarbons. Reservoir potential is not very high in the sand lenses. Pre-cement porosity in the sandstone layers range from 55% to 10% with an average value of 25%. However, calcite cement has filled in the porosity in the samples that were collected and retained post-cement porosity in thin section is less than 5% effective porosity (Perry, 1984).

Figure 2.4.4: A buckle fold in the Roadside Member along highway A3 between Whitehall and Albany. These types of folds are likely common throughout the Wagwater Trough, because there is substantial deformation that has occurred since the Middle Miocene. Owing to the weak nature of the rock, caused by the abundance of weak shale layers, ductile deformation (flexural slip) is common. Pictured in this photo for scale are members of Dr. John Pigott's 2007 Basin Analysis class on a field trip in Jamaica.

Nutfield Volcanics. In the center of the northernmost region of the Wagwater Trough, near the town of Nutfield, the Nutfield volcanic flows conformably outcrop in the Roadside Member of the Richmond Formation over an area of several square kilometers. They are the youngest volcanic unit in the Wagwater trough and consists of a sheet of basaltic pillow lava conformably overlain by a dacite flow (Roobol, 1972; Mann and Burke, 1990). The maximum thickness of the basalt-dacite unit is about 100 meters (Mann, 1983). Eruption occurred in a marine environment during the deposition of the Richmond Formation as result of extensive rifting.

Figure 2.4.5: Interpreted pillow lava structures in the basalt member of the Nutfield Volcanics along Nutfield Road, north of the town of Nutfield. Pillows are interpreted by red outlines. This basalt unit accompanied early rifting. It was erupted in a marine environment.

2.5 Deep Marine Late Paleogene Limestone Deposits

There are three limestone groups that were deposited post-rifting in the Wagwater Trough: Yellow Limestone, White Limestone, and Coastal Limestone Groups. Most of the deposited limestone has been eroded away since the region has been uplifted (~10 Ma). About a minimum thickness of 1500 meters of limestone was deposited within the Wagwater Trough before erosion (Green, 1977).

Yellow Limestone Group. The Eocene Yellow Limestone Group is the first of the two groups of widespread limestone throughout Jamaica. The top of Langley Member of the Richmond Formation grades into the oldest formation in the Yellow Limestone

Group, the Font Hill Limestone Formation. It was deposited post-Wagwater rifting during a period of gradual subsidence. It is described as deep-marine biomicrites that are bioclastic at the base (Mann and Burke, 1990; Robinson, 1974).

White Limestone Group. The Eocene-Miocene White Limestone Group is the second of the two groups of limestone that are exposed throughout Jamaica. The White Limestone Group formations and facies are controlled by fault blocks. It comprises the most commonly exposed rocks throughout Jamaica; however, the only formation in the White Limestone Group found in the Wagwater region is the Montpelier Formation. The Montpelier Formation is a series of submarine slope chalk deposits. It is possible that other White Limestone formations could have been deposited; however, only the Montpelier Formation was preserved (Mann and Burke, 1990).

Coastal Limestone Group. The Pleistocene coastal limestone group consists of small outcrops found along the coast northwest of Anotto Bay. It is rich in coral heads and other modern reef fossils, and it is likely a stratigraphic equivalent to the Falmouth and Hope Gate Formations found in the Discovery Bay region.

3. TECTONIC SETTING

3.1 Introduction

Tectonics in Jamaica played a major in the development of the Wagwater Trough. Today, Jamaica lies entirely within a 200 km wide seismic zone of left-lateral transform motion between the North American and Caribbean plates. Just north of Jamaica, extending from Belize to Haiti, is the narrow rift basin called the Cayman trough. Two major through-going transform faults, related to the boundary between the Caribbean Plate and the Cayman Trough, pass through the island of Jamaica. The first is the Septentrional-Oriente-Swan-Motagua fault system. It passes to the north of Jamaica and bounds the Cayman Trough pull-apart structure (Mann et al., 1985; Holcombe et al., 1973). The second fault is the Plantain Garden-Swan fault system. It extends from the Dominican Republic in central Hispañola, through Jamaica. The faults merge on the island of Jamaica as the Duanvale Fault Zone (Mann et al., 1985; Burke et. al, 1980; Mann, 1983).

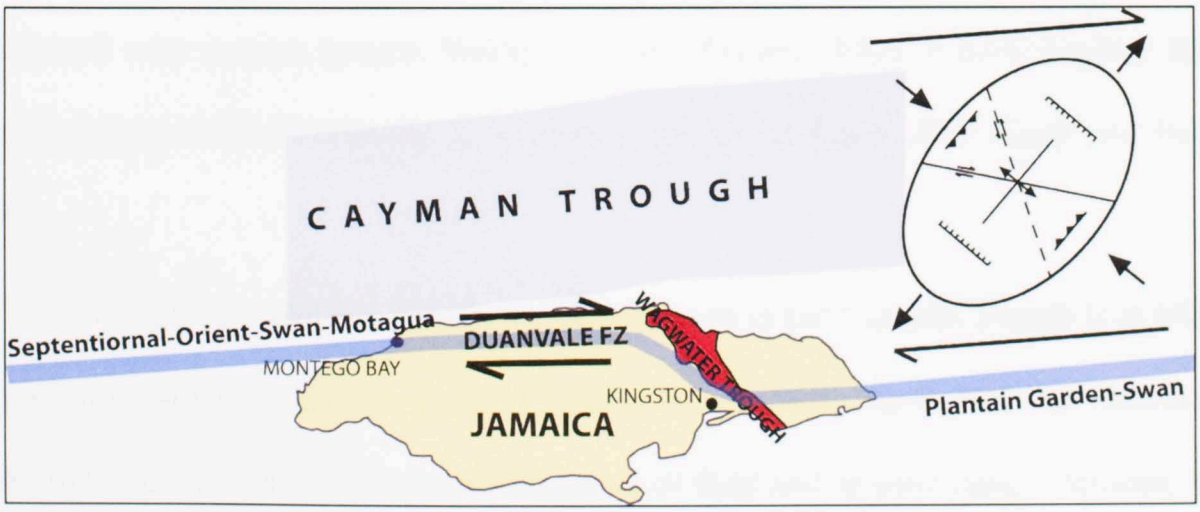

Figure 3.1.1: Map showing a possible Paleocene position of Jamaica. The Wagwater Trough (Red) formed along a releasing bend in the present-day Septentiornal-Orient-Swan-Motagua and the Plantain Garden-Swan fault systems (Blue).

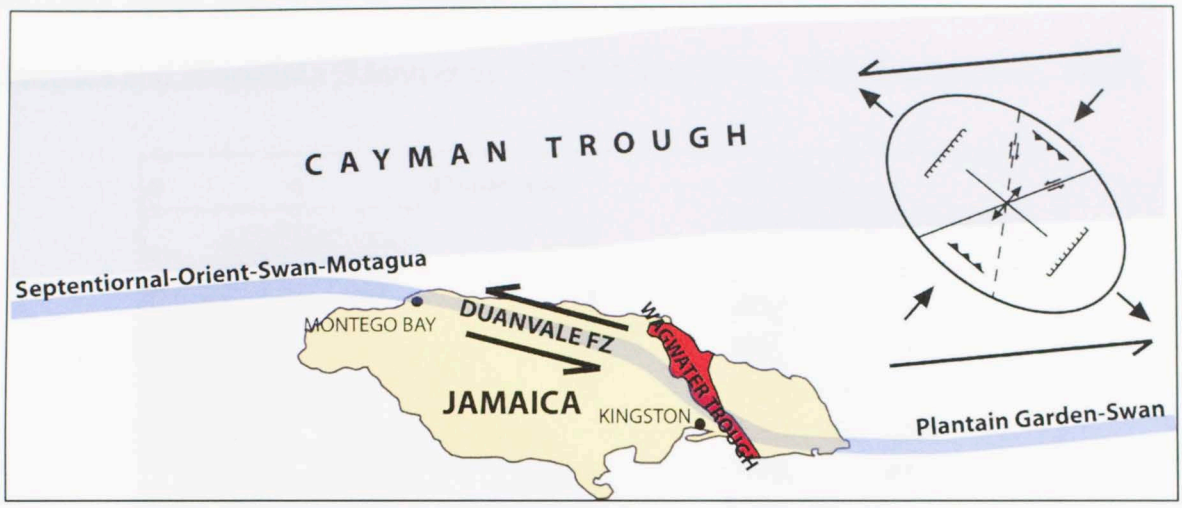

Figure 3.1.2: Map showing the present-day Septentiornal-Orient-Swan-Motagua and the Plantain Garden-Swan fault systems connecting at a restraining bend (Blue). These fault systems separate the Cayman Trough (Light Grey) from the Caribbean Plate. The restraining bend is directly over the Wagwater Trough (Red), and as a result significant uplift and faulting has occurred (after Mann and Burke, 1990).

The Wagwater Trough is highly faulted and deformed. There are a number of major faults that affect the Wagwater Trough (Figure 3.1.3). The major basin bounding faults are the Wagwater Fault on the West and the Yallahs-Silver Hill Fault on the East Figure 3.1.4). These faults trend northwest to southeast. These basin bounding faults were reactivated with reverse motion during the Late Miocene. West to East trending faults formed during the Late Miocene as left-lateral strike-slip faults (after Mann and Burke, 1990).

Currently the total rate of relative plate motion in the Cayman Trough is at least 2 cm yr^{-1} and perhaps as fast as 4 cm yr^{-1}(Mann et al., 1985; Macdonald and Holcombe, 1978; Sykes et al., 1982). Using a combination of field and seismic data, it appears, as a general rule, that strike-slip faults in this part of the Caribbean parallel predicted east-trending intra-plate slip lines (Mann et al., 1985; Jordan, 1975). Reverse faults, however,

commonly strike northwest to southeast and are associated with uplifted land areas such as Jamaica and Hispañola (Mann et al., 1985; Mann et al., 1984; Burke et al., 1980).

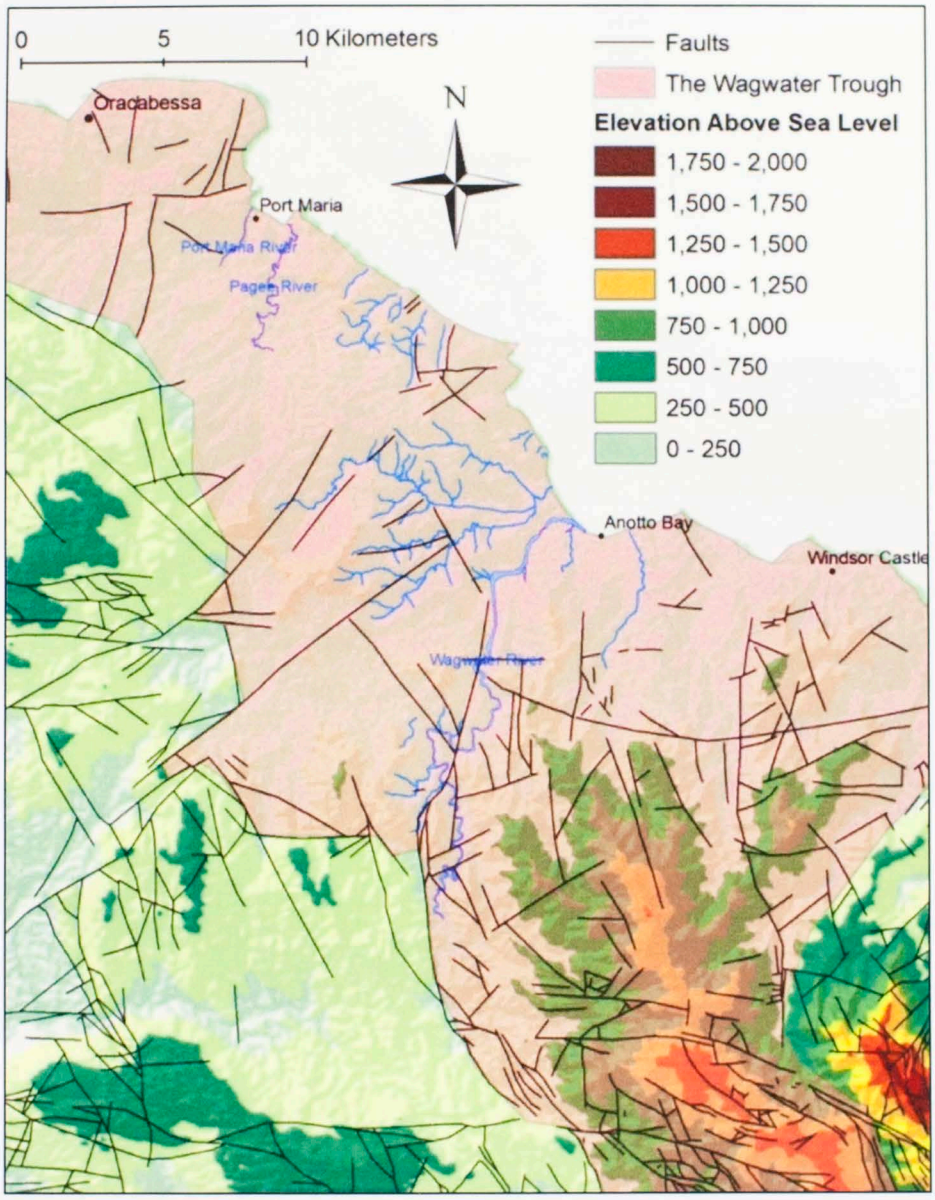

Figure 3.1.3: Map showing all the mapped faults in the Northern Wagwater Trough region. This area has seen an immense amount of faulting and deformation (after Mines and Geology Division, 1978, multiple sheets).

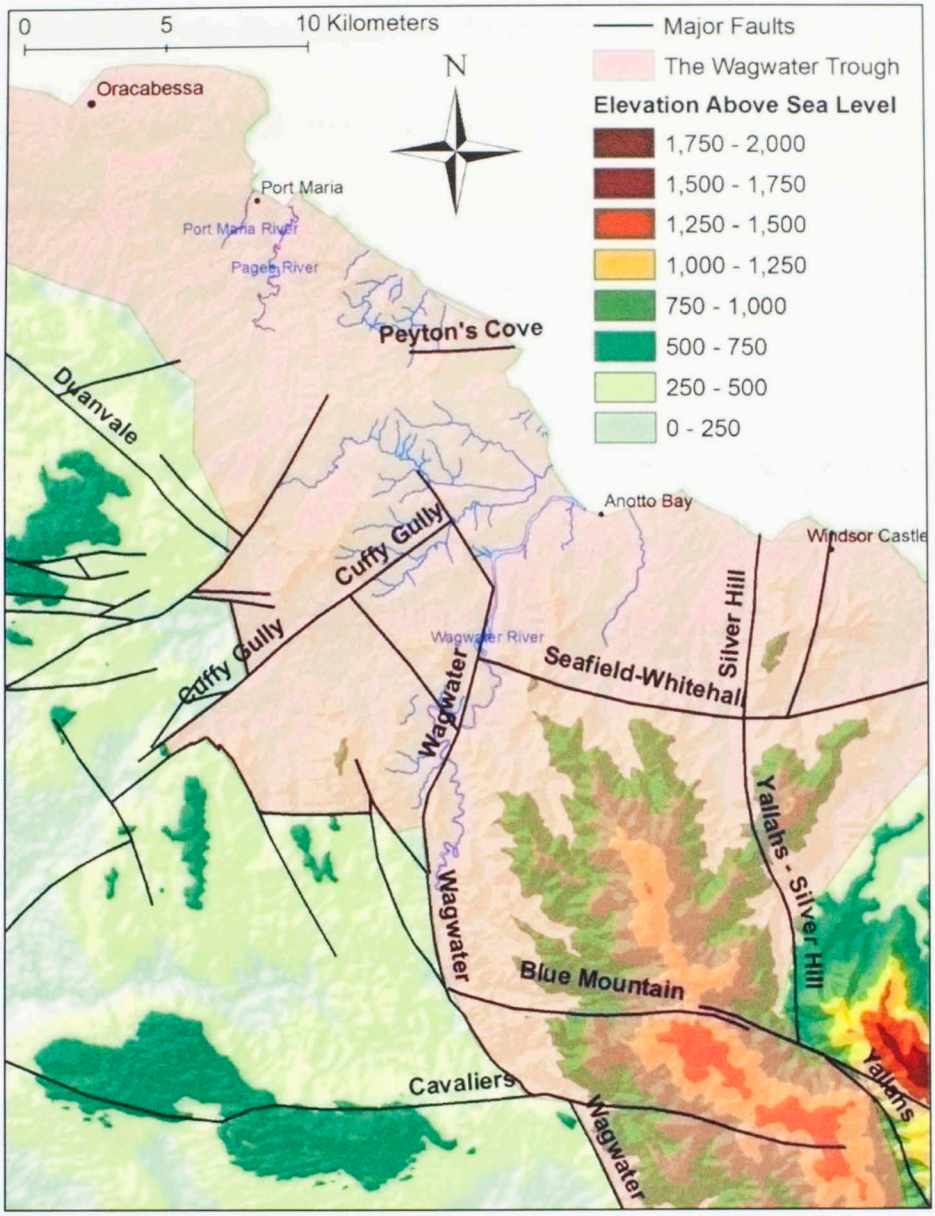

Figure 3.1.4: Map showing the major faults in the northern Wagwater Trough region. In order to simplify the model, only the major faults will be included in the modeling process (see figure 3.1.3 for all the mapped faults). Faults trending northwest to southeast were original basin-forming faults that were reactivated as reverse faults during the Late Miocene. West to East trending faults formed during the Late Miocene as left-lateral strike-slip faults (after Mann and Burke, 1990).

3.2 Tectonic Model for the Development of the Wagwater Trough

Perry (1984) suggested that Paleogene rifting in eastern Jamaica (Wagwater Trough) is a result of a failed rift associated with the spreading in the Cayman Trough. The Wagwater trough initially rifted in the Paleocene and continued into the Eocene (Mann and Burke, 1990).

Early Paleocene Rifting. The Ginger River Member of the Wagwater Formation was interpreted by Mann and Burke (1990) as occupying a half-graben formed along the Wagwater fault zone (See figure 3.2.1). This rifting was part of a much larger regional extensional event at the distal end of the Cayman Trough pull-apart basin and on the Nicaraguan rise. No preserved deposition occurred in the eroding highlands on the footwall (western) block of the Wagwater fault zone. During this period of rifting deposition was dominantly subaerial in alluvial fans and fan-deltas, because no incursion of seawater had occurred within the trough (Wescott and Etheridge, 1983).

Late Paleocene Rifting. Continued rifting in the Late Paleocene was accompanied by deposition of the Pencar River Member during a brief incursion of seawater into the trough. In the southern region of the trough evaporite and terrestrial red bed sedimentation occurred. As sea level went down, continued down-throw of the block allowed for deposition of the Dry River Member of the Wagwater Formation (Mann and Burke, 1990).

Early Eocene Rifting. Rifting and volcanism continued in the Early Eocene but in a submarine setting. The Wagwater fault zone remained active, but the Yallahs-Silver Hill fault zone reactivated for the first time since the Mesozoic. Submarine slides and

turbidites of the Richmond Formation were deposited during this period. This marks the end of the main rifting phase in the Wagwater Trough, although some faults may have remained active throughout the Eocene (Mann and Burke, 1990).

Middle Eocene-Miocene Carbonate Growth. Localized submarine slides of the Middle to Late Eocene age in basinal carbonate rocks over the Wagwater Trough indicate the persistence of steep slopes, perhaps related to the rejuvenated faults (Robinson, 1967). During this period of time deep-water carbonates developed as the basin slowly subsided.

Late Miocene-Present Basin Inversion. East-west, left-lateral strike-slip motion on the Enriquillo-Plantain Garden fault zone reactivated the half-graben at a restraining bend (Mann et al., 1985). Reverse motion on or close to the Wagwater fault zone caused the rift sequence to be moved back up along the old extensional fault surface. The Yallahs-Silver Hill fault zone may have been reactivated as a back-thrust during basin inversion. This uplifting of the facies in the basin has exposed the rocks at the surface, allowing for field analysis.

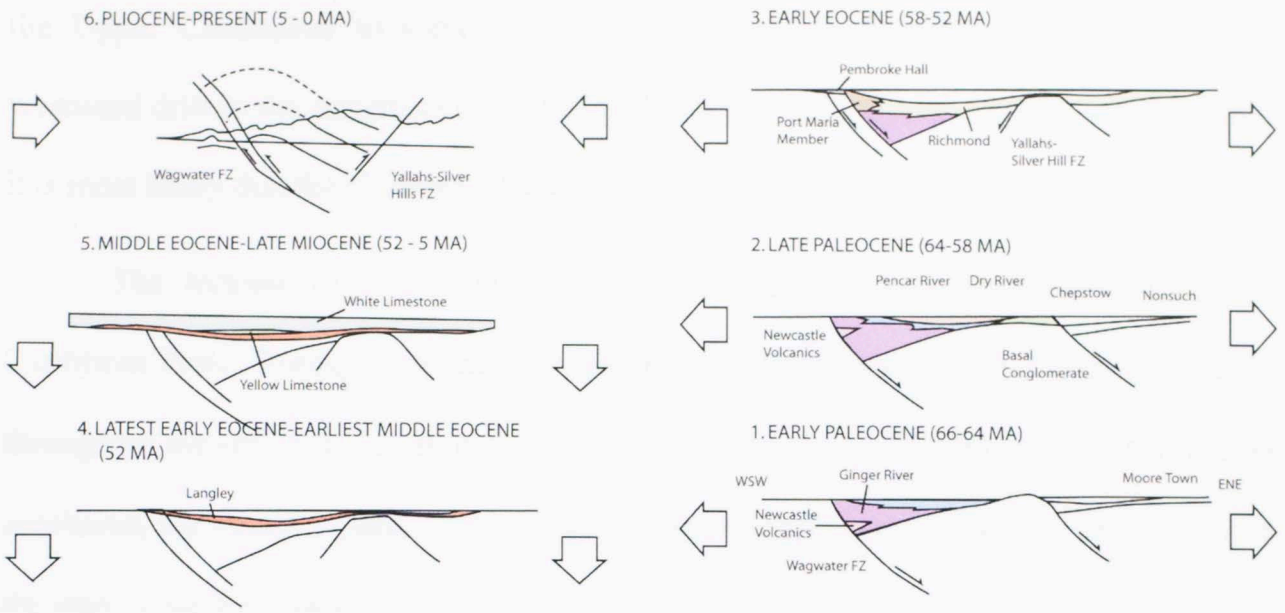

Figure 3.2.1: Schematic cross-section models developed by Mann and Burke (1990) showing the stages of tectonic development of the Wagwater Trough. (1) The Ginger River Member of the Wagwater Formation occupies a half-graben formed along the Wagwater fault zone. (2) Continued rifting in the Late Paleocene was accompanied by deposition of the Pencar River Member during a brief incursion of seawater into the trough. As sea level receded, continued down-throw of the block allowed for deposition of the Dry River Member. (3) Rifting and volcanism continued in the Early Eocene in a submarine setting. The Wagwater fault zone remained active, and the Yallahs-Silver Hill fault zone reactivated. Submarine slides and turbidites of the Richmond Formation were deposited during this period. This marks the end of the main rifting phase in the Wagwater Trough. (4) Localized submarine slides of the Middle to Late Eocene age in basinal carbonate rocks over the Wagwater Trough indicate the persistence of steep slopes, perhaps related to the rejuvenated faults. (5) Deep water carbonates developed as the basin slowly subsided. (6) Reverse motion caused the rift sequence to be moved back up along the old extensional fault surface (after Mann and Burke, 1990; Wescott and Etheridge, 1983; Robinson, 1967; Mann et al., 1985).

3.3 Tectonic Development of the Caribbean Region

Geologic development in the Caribbean region is complex. The origin of the Caribbean plate has two possibilities: generated by seafloor spreading between Yucatan and South America and, therefore, represents lithosphere of the arm of the Atlantic; or generated in the Pacific (Farallon Plate lithosphere) such that Proto-Caribbean crust which was already formed by the separation of the Americas was then subducted beneath

the Upper Cretaceous to Cenozoic arc systems of the Caribbean Plate during the westward drift to the Americas from Africa (Pindell, 1994). Pindell (1994) suggested that it is most likely that the Caribbean Plate is from Pacific origin.

The tectonic events in Jamaica are directly related to the movement of the Caribbean Plate. During the Mesozoic, the breakup of Pangaea created immense rifting throughout the region as North America separated from South America. While this rifting continued, the Farallon plate continued to subduct beneath the Antilles Amaime, which is the start of the formation of the Caribbean Plate.

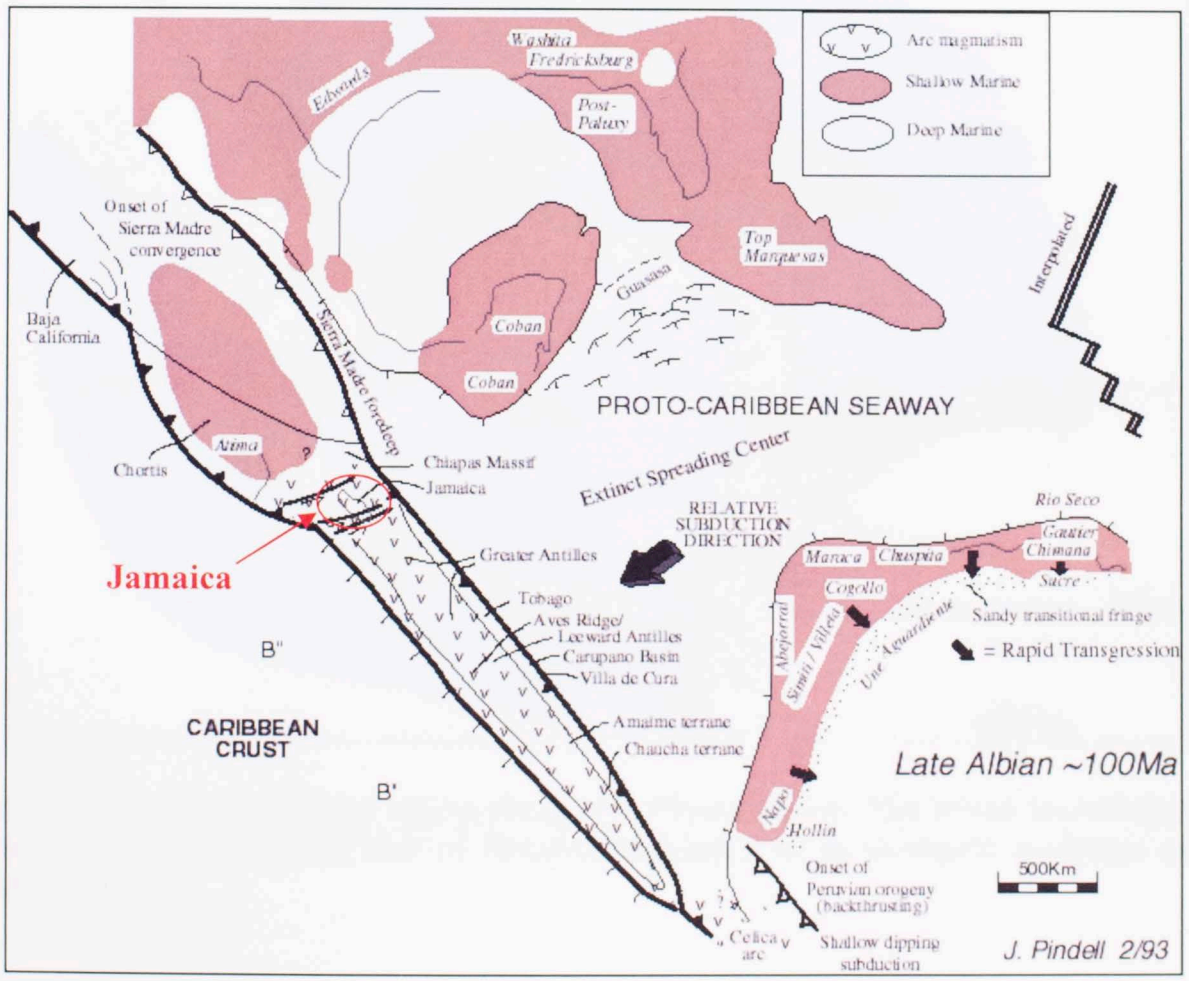

Figure 3.3.1: The Caribbean region during the Late Albian. Subduction began on the eastern side of the Antilles, and the Caribbean Plate began to grow in size and convex eastward. The east side of Jamaica was also part of the island arc above the subduction zone. (from Pindell, 1993).

By the Late Albian, subduction had begun on the eastern side of the Antilles, and starting from this period, the Caribbean Plate began to grow in size and convex eastward into the Atlantic (Figure 3.3.1). It should also be noted that during this time the east side of Jamaica was also part of the island arc above the subduction zone. However, by Maastrichtian time, the island arc/subduction zone system had advanced east of Jamaica, leaving it as an emergent landmass (Pindell, 1994; Wescott and Ethridge, 1983; Mann et al., 1985).

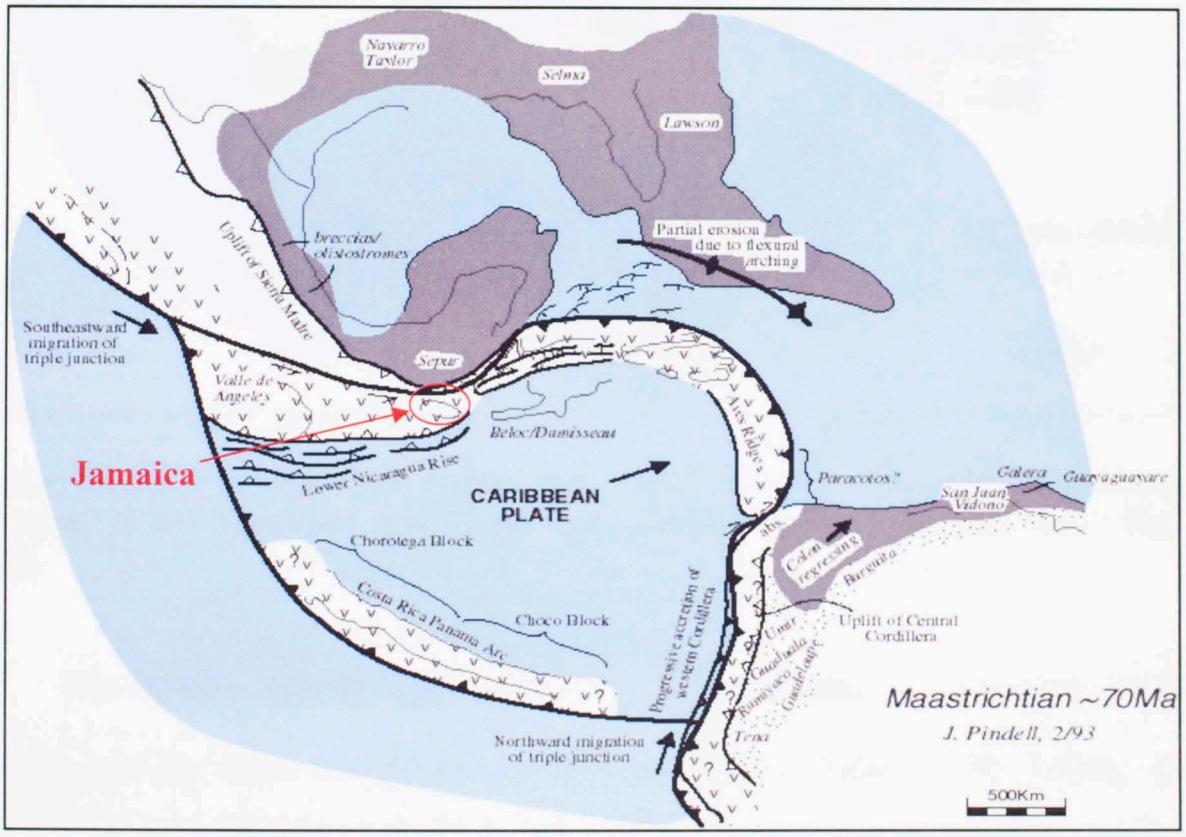

Figure 3.3.2: The Caribbean region during the Maastrichtian. The island arc/subduction zone system had advanced east of Jamaica, leaving it as an emergent landmass (after Pindell, 1993).

During the Cenozoic, the Caribbean Plate continued migration relatively eastward. The Yucatan block prevented simple eastward motion of the Nicaraguan Rise and Jamaica with the rest of the Caribbean Plate. Consequently, Jamaica was internally

deformed as the Wagwater and Montpelier Troughs formed in Jamaica, and other rifts formed in the Nicaraguan Rise (Figure 3.3.3) (Pindell 1994).

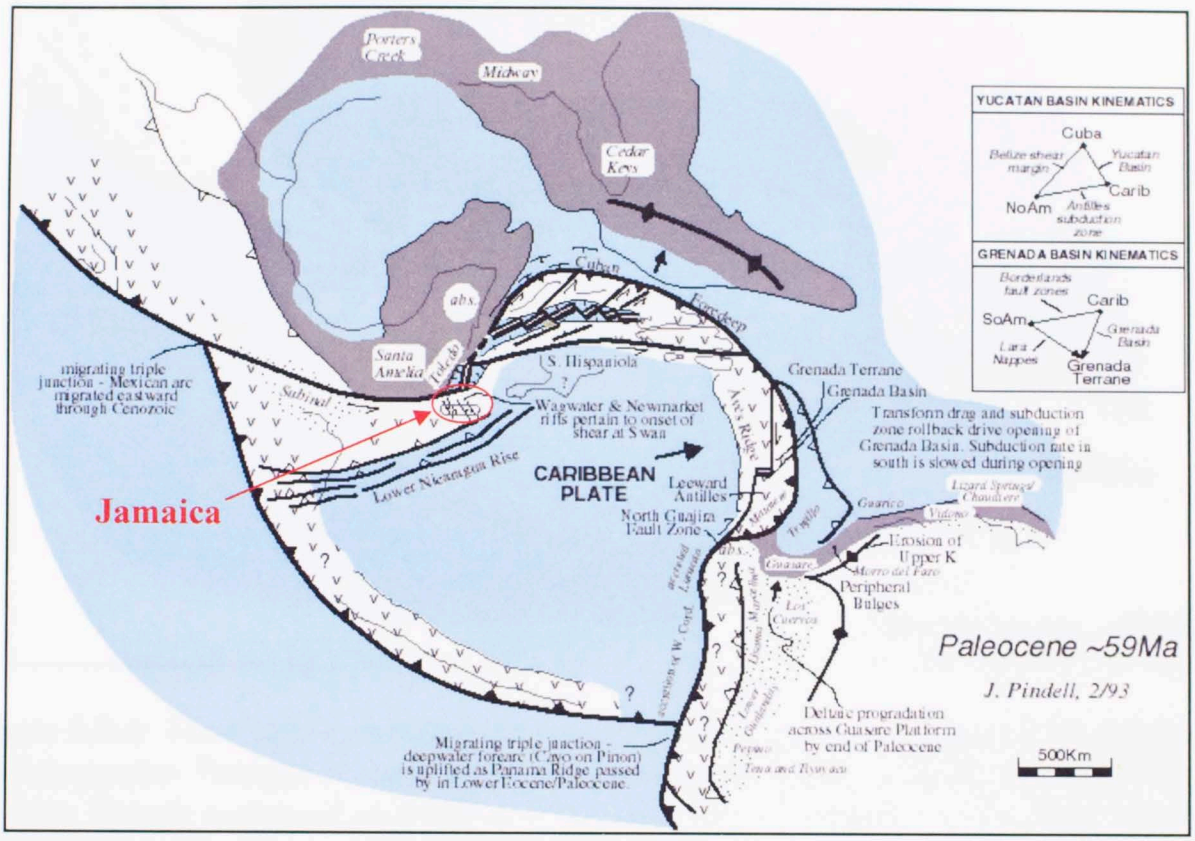

Figure 3.3.3: The Caribbean region during the Paleocene. Jamaica was internally deformed as the Wagwater and Montpelier Troughs rifted in Jamaica (after Pindell, 1993).

The Middle Eocene was marked by the termination of Bahamian-Antillean collision and the onset of platform deposition in Cuba (Figure 3.3.4). Rifting of the Wagwater and Montpelier Troughs in Jamaica slowed and ceased by the end of this period as the Cayman Trough nucleated as a pull-apart basin between Yucatan and Jamaica spreading in an east-west direction. This would become the northern Caribbean boundary (Pindell, 1994).

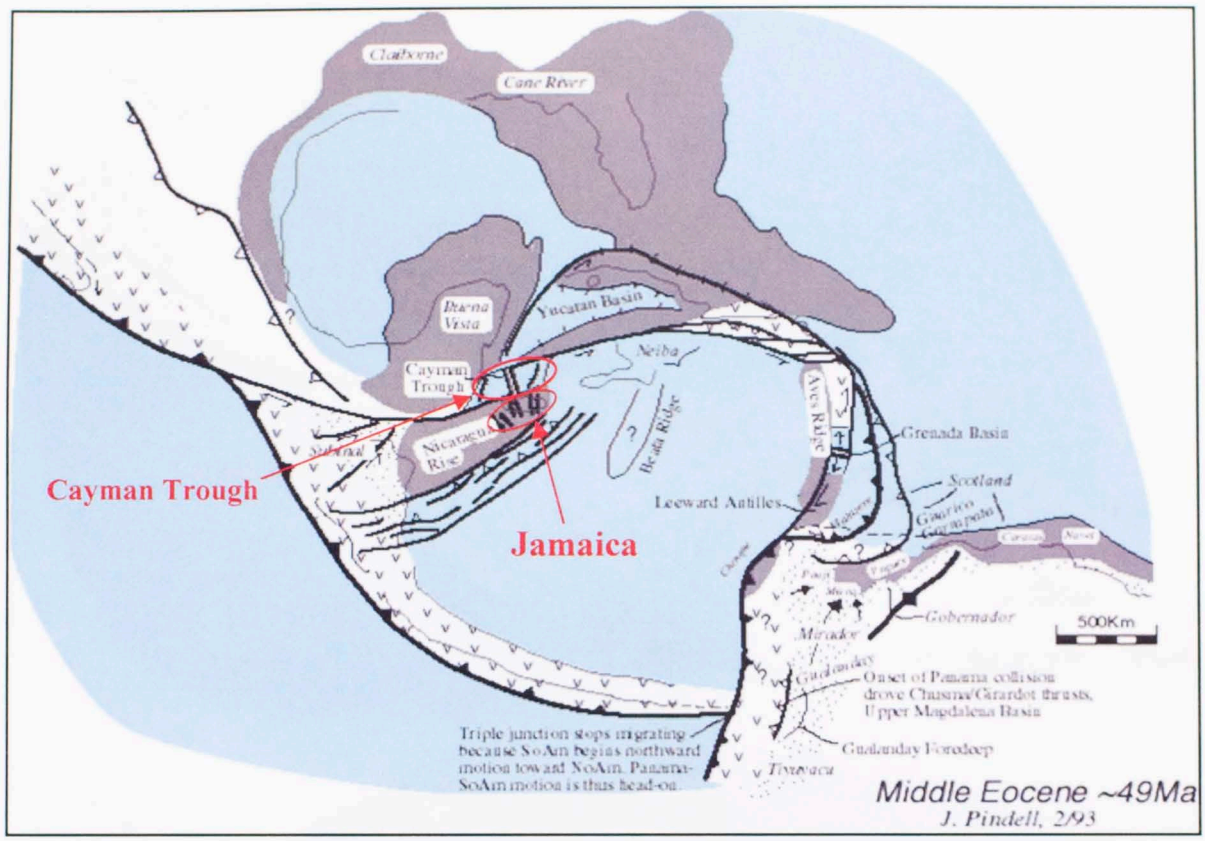

Figure 3.3.4: The Caribbean region during the Middle Eocene. Rifting of the Wagwater and Montpelier Troughs in Jamaica slowed and ceased by the end of this period as the Cayman Trough nucleated as a pull-apart basin between Yucatan and Jamaica spreading in an east-west direction. (after Pindell, 1993).

Oligocene and Early Miocene time was marked by a passive period in Jamaica. The Caribbean Plate with Jamaica continued to move eastward, and the Cayman Trough continued to spread apart, while the Wagwater and Montpelier Troughs had little to no spreading at all. During this period, carbonate banks and immense limestone deposition occurred on in Jamaica as the Yellow Limestone and White Limestone Groups.

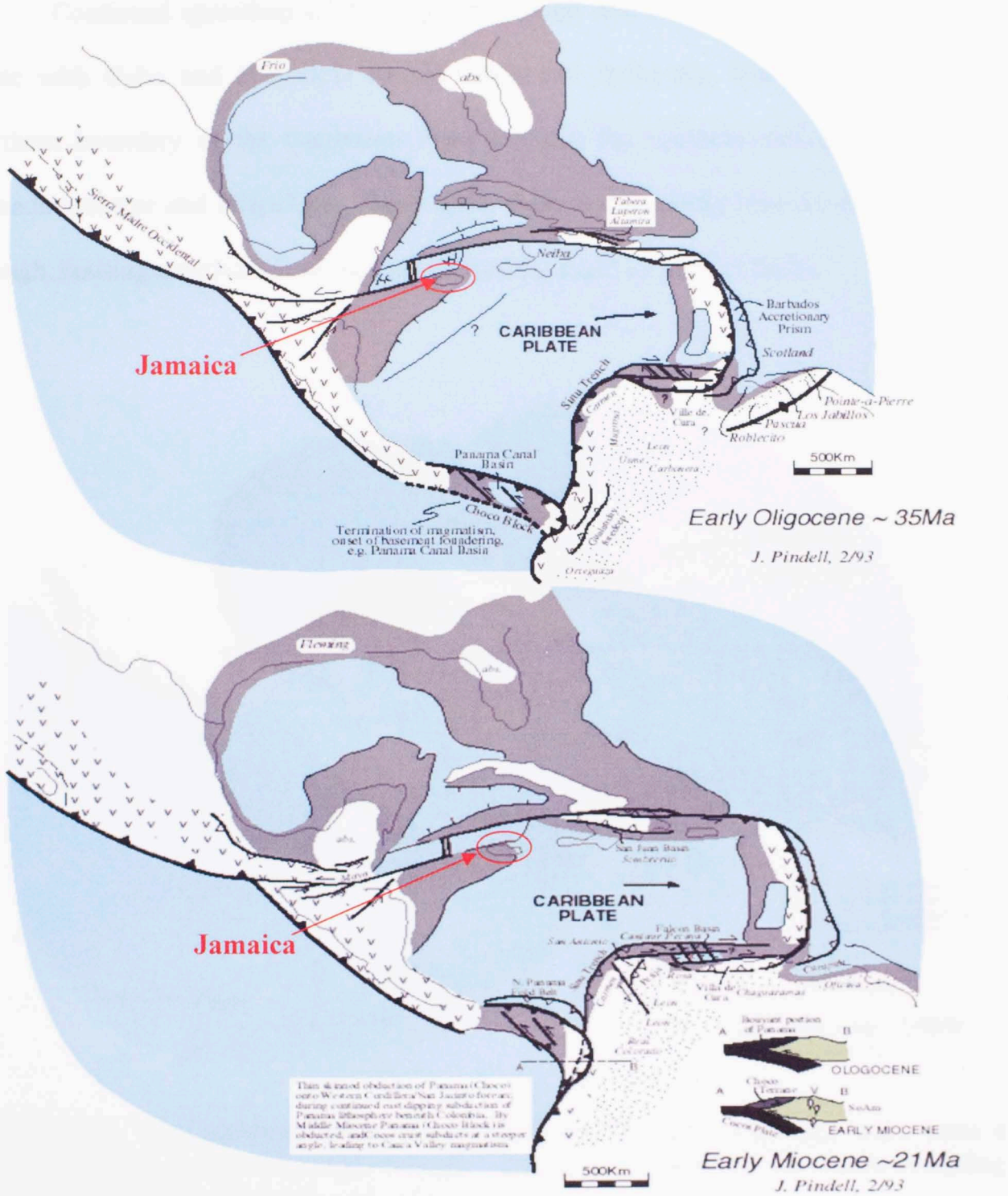

Figure 3.3.5: The Caribbean region during the Oligocene and Early Miocene. Rifting of the Wagwater and Montpelier Troughs in Jamaica had ceased altogether. Carbonate banks and immense limestone deposition occurred on Jamaica as the Yellow Limestone and White Limestone Groups. (after Pindell, 1993).

Continued spreading of the Cayman Trough and interactions of the Caribbean Plate with Cuba and Hispañola caused left-lateral strike-slip faults to form on the northern boundary of the Caribbean Plate between the southern end of the Cayman spreading center and Hispañola. These faults make a restraining bend in the Wagwater Trough, causing reactivation of the basin bounding faults as reverse faults.

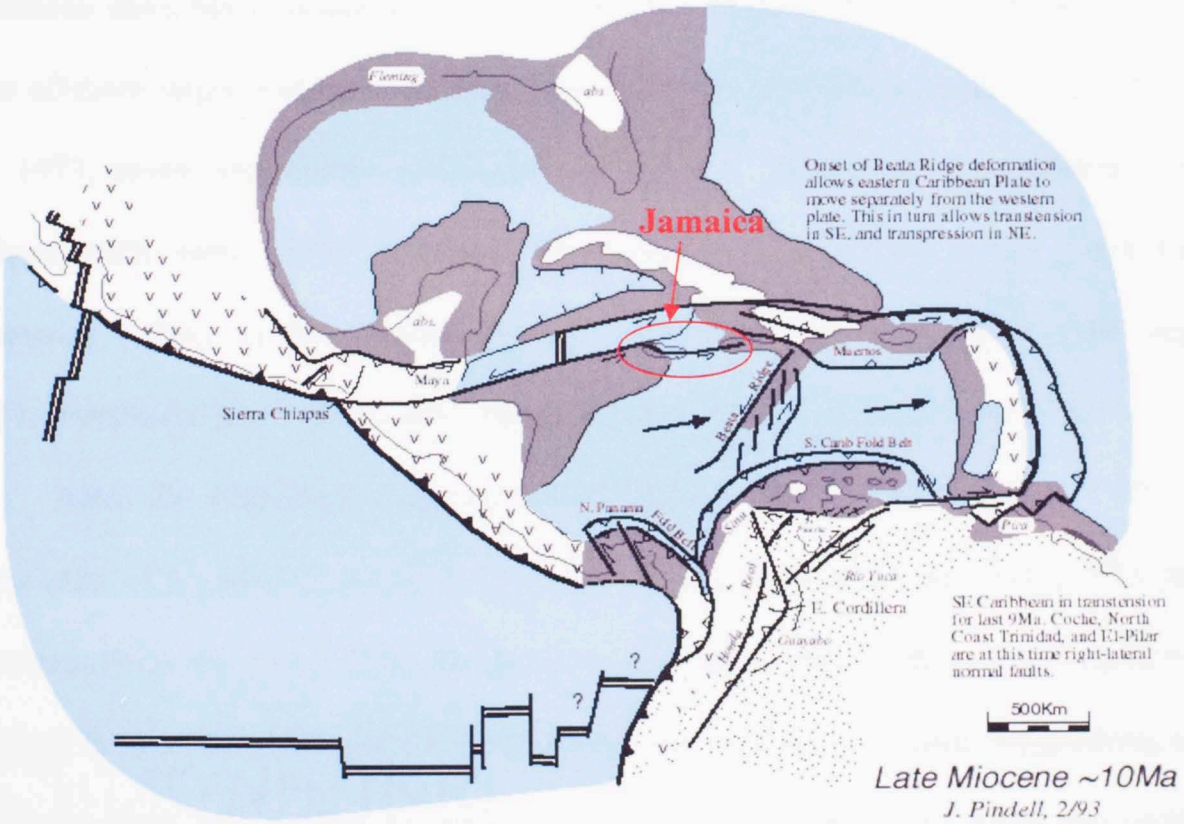

Figure 3.3.6: The Caribbean region during the Late Miocene. Strike-slip faults make a restraining bend in the Wagwater Trough, causing reactivation of the basin bounding faults as reverse faults (after Pindell, 1993).

4. PETROLEUM EXPLORATION HISTORY IN JAMAICA

4.1 Introduction

The search for oil in Jamaica can be divided into two phases, the first involving private industry entirely, and the second involving, primarily, the state-owned company, Petroleum Corporation of Jamaica (PCJ). The first phase spanned the period from 1955 to 1973, and the second phase covers the period from 1974 to the present. The exploratory operations have been conducted both onshore and offshore, the Pedro Bank being the main offshore target. Eleven wells have been drilled in Jamaican territory. Between 1955 and 1973, seven exploratory wells were drilled, six onshore and one offshore. The onshore wells were drilled at Negril Spots (1955), near Munro in the Santa Cruz Mountains (1956), in the southern part of the Cockpit Country (1957), West Negril (1957), Portland Ridge (1971), and Content, Westmoreland (1972) (Wright, 1996).

After the Petroleum Corporation of Jamaica was formed in June 1979, the momentum of exploration activity increased. During the period 1981-1982, PCJ, with assistance from the Inter-American Development Bank, drilled three wells onshore at Hertford in Westmoreland, Retrieve, St. James, and Windsor, St Ann. An offshore well on Pedro Bank was drilled by Union Texas/AGIP in 1981. The most encouraging development involved oil and gas shows in two of the wells, (Windsor and Retrieve) drilled by Petroleum Corporation of Jamaica. Further development has been stagnant, and at this time, all of Jamaica is open to exploration activity from private industry (Wright 1996).

Year	Operator	Well	Total Depth
1955	Canadian Base Metals	Negril Spots	1925 m
1956	Pan Jamaican	Santa Cruz	2662 m
1957	Pan Jamaican	West Negril	2818 m
1957	Pan Jamaican	Cockpit	1684 m
1970	Oxy-Signal	Pedro Bank	1979 m
1971	Oxy-Signal	Portland Ridge	2262 m
1972	Kirby-Weaver	Content	2319 m
1981	Petroleum Corporation of Jamaica (PCJ)	Hertford	3035 m
1982	PCJ	Windsor	3907 m
1982	PCJ	Retrieve	3447 m
1982	Union Texas/AGIP/PCJ	Arawak	4588 m

Table 4.1.1: Table of eleven exploration wells drilled in Jamaica.

Figure 4.1.1: Map showing the location of the exploration wells (except for Pedro Bank which was drilled on the offshore Pedro Bank southwest of Jamaica (from Petroleum Corporation of Jamaica).

4.2 Petroleum Corporation of Jamaica Windsor #1

Windsor #1 is located on the north coast of Jamaica near the town of St Ann. It has a total drilling depth of 3907 meters, and it was drilled because of its proximity to a gas seep and anticline structure mapped at the surface and confirmed by seismic. The well was eventually abandoned as a dry hole; however it did have minor oil and gas shows. One core was recovered from the well and it was bleeding brown oil and minor gas bubbles from hairline fractures.

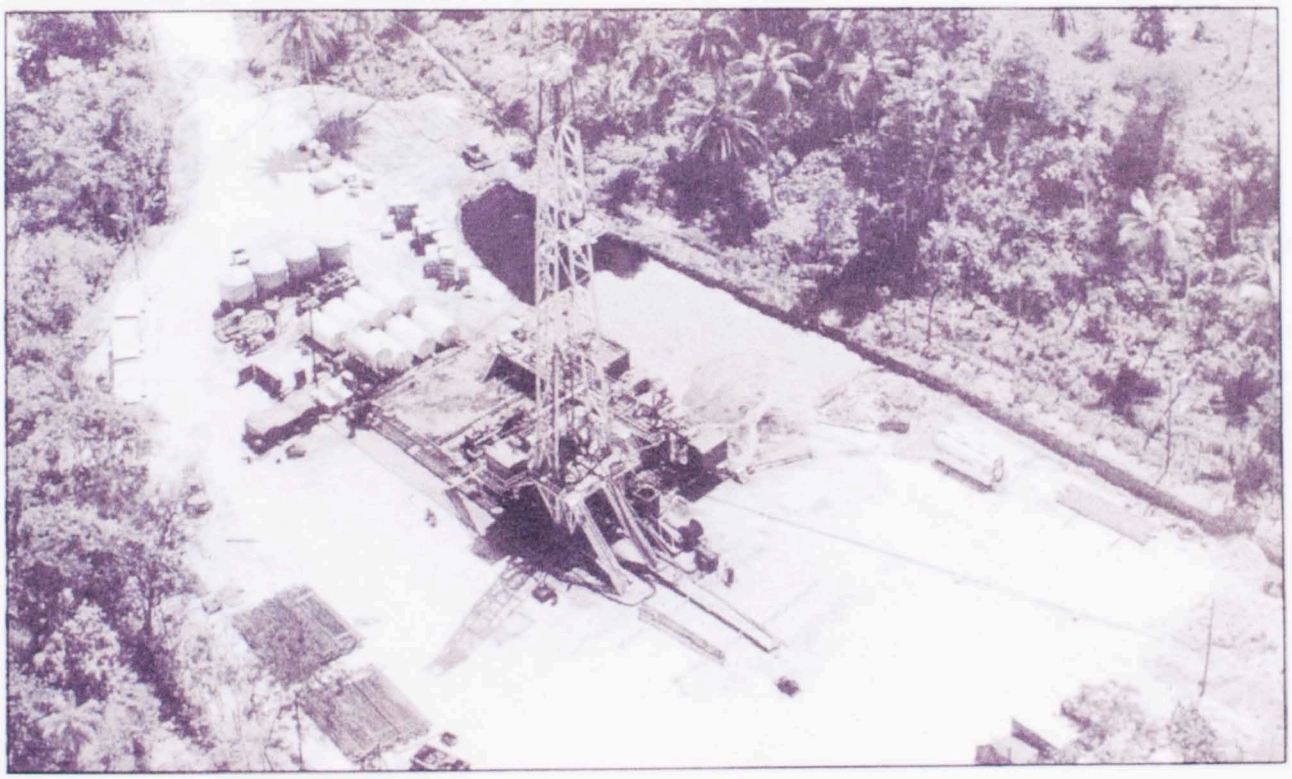

Figure 4.2.1: Photograph of drilling operations onshore at Windsor #1, St Ann in 1982. This well had small oil shows and minor gas shows. It had one core recovered and was tight limestone bleeding brown oil and minor gas bubbles from hairline fractures. Windsor #1 proved that sediments in the Jamaican region are capable of generating hydrocarbons (from Wright, 1996).

4.3 Petroleum Potential of the Wagwater Trough

There has been no petroleum exploration in the Wagwater Trough to date. The closest well to the Wagwater Trough is Windsor #1. However, it is not in the Wagwater Trough and is located more than 25 km from the western edge of the Wagwater Trough. Eva (1980) stated that many of the sediments in the Wagwater Belt are likely to have been heated to considerable temperatures, and that heat flow is relatively high in active marginal basins. Perry (1984) stated that the heat flow is significant enough to be favorable for the early maturation of hydrocarbons within the Wagwater Trough, and this is due to the close association of thermo-tectonic events in the Cayman and Wagwater Troughs, plus a thick overburden of sediments in the trough. Thus hydrocarbons have probably been generated at depth in the Wagwater Belt. He further explained that abandoned-rift basins and aulacogens have commonly proven to be ideal exploration targets.

5. GRAVITY MODELING PRINCIPLES

5.1 Introduction

In order to perform any basin analysis at all, the depth to the basement must be known. Usually this is determined from seismic and well-data. However, in the Wagwater Trough no such data exists. So by using a regional Bouguer anomaly map (Figure 5.1.1) published by the Jamaican Geologic Survey, the Bouguer anomaly data can be used to determine the depth to basement. For this study a combination of field data, published data, and published maps were used to extrapolate lithologic formations and facies into the subsurface. Five cross-sections were created using a combination of collected field, published geologic map, and published data (Figure 5.1.1). The Bouguer anomaly data were used to constrain the cross-sections. The basic theory behind the methods used is described in the following section.

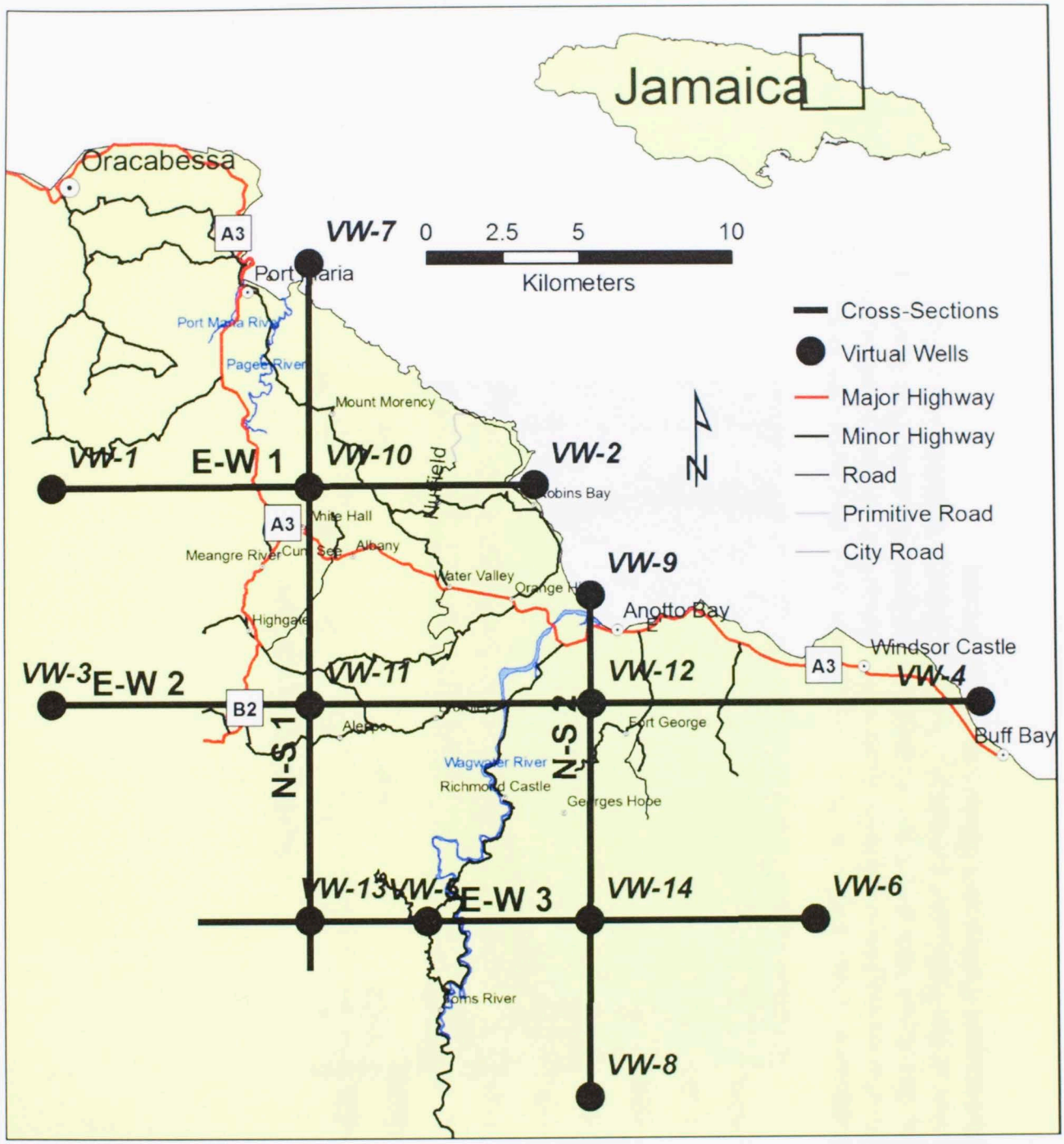

Figure 5.1.1: Base map of the Northern Wagwater Trough. The locations of fourteen virtual wells and five cross-sections and subsequently 2-D models are labeled on the map. Cross-sections E-W 1, E-W 2, and E-W 3 run west-to-east and cross-sections N-S 1 and N-S 2 run north-to south.

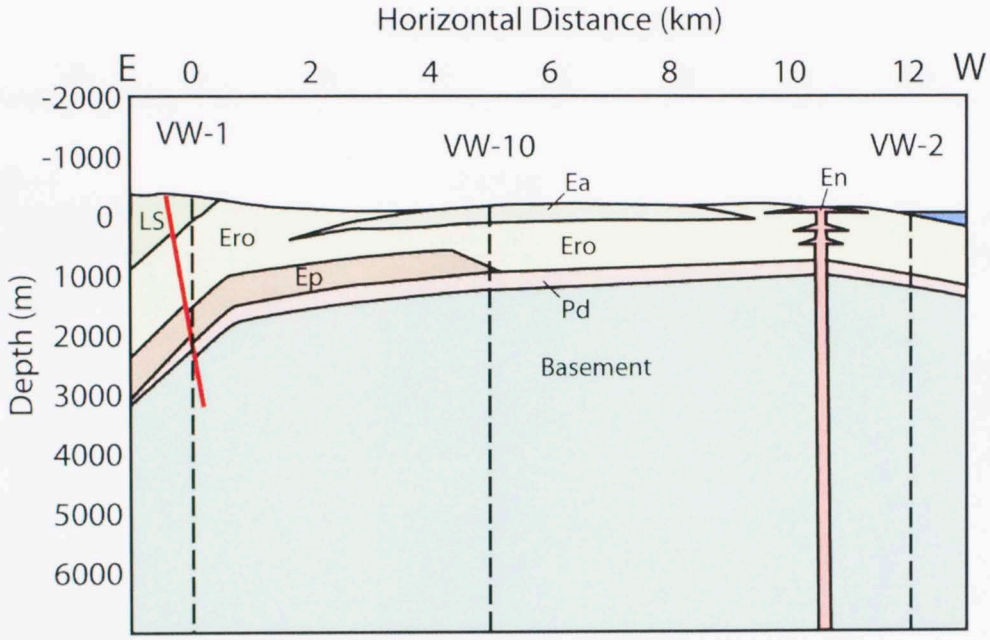

Figure 5.1.2: East-west basement-constrained cross-section E-W 1. This cross-section runs across the most northern region between Port Maria and Anotto Bay. Location of cross-section is show in figure 4.1.1. Formation labels: Basement is the undifferentiated pre-rifting Mesozoic formations, Pd is the Dry River Member of the Wagwater Formation, Ep is the Port Maria Member of the Richmond Formation, Ero is the Roadside Member of the Richmond Formation, Ea is the Albany Member of the Richmond Formation, En is the Nutfield Formation, and LS is undifferentiated Yellow and White Limestone Groups.

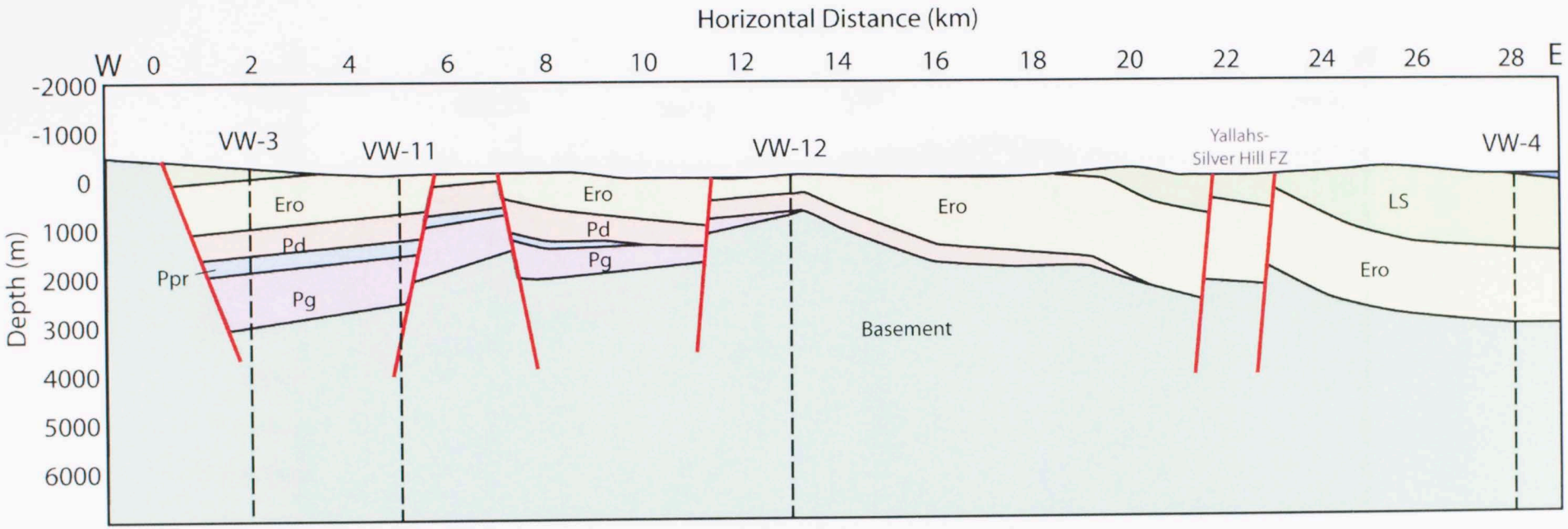

Figure 5.1.3: East-west basement-constrained cross-section E-W 2. This cross-section runs across the central region, from west of Richmond to Windsor Castle. Location of cross-section is show in figure 4.1.1. Formation labels: Basement is the undifferentiated pre-rifting Mesozoic formations, Pg is the Ginger River Member of the Wagwater Formation, Ppr is the Pencar River Member of the Wagwater Formation, Pd is the Dry River Member of the Wagwater Formation, Ero is the Roadside Member of the Richmond Formation, and LS is undifferentiated Yellow and White Limestone Groups.

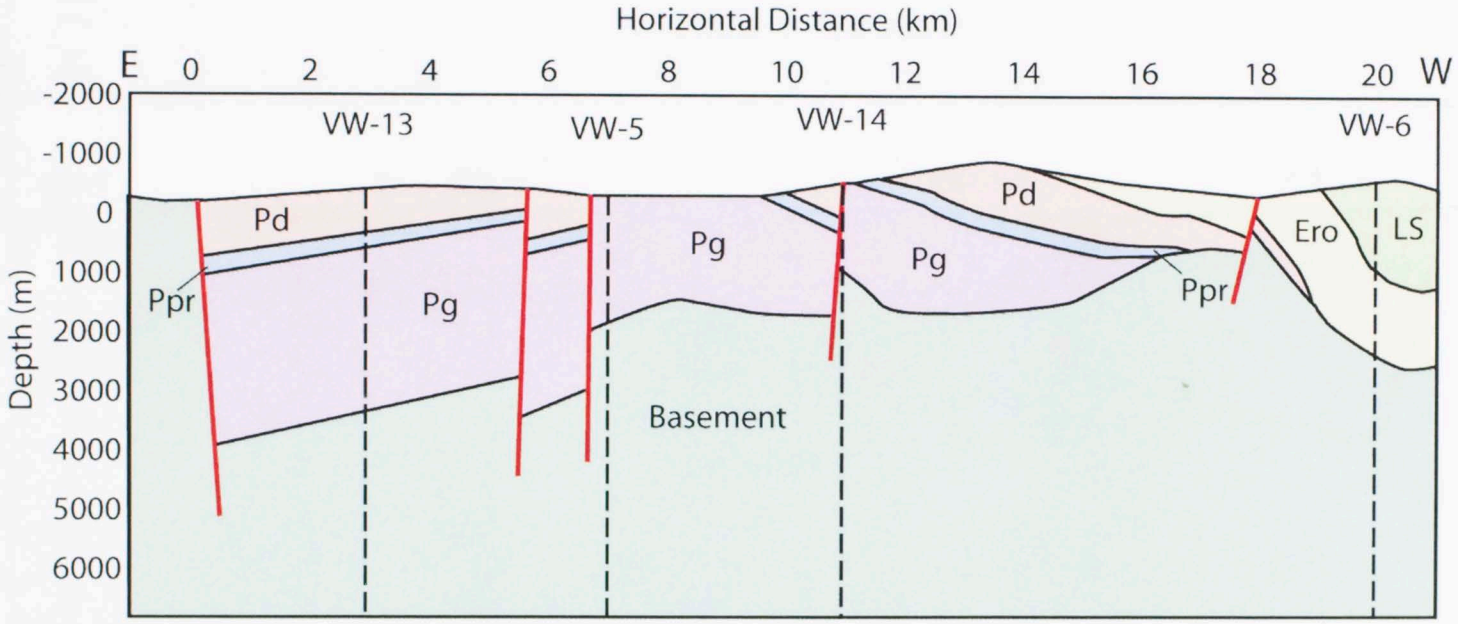

Figure 5.1.4: East-west basement-constrained cross-section E-W 3. This cross-section runs across the most southernmost region of the study area. Location of cross-section is show in figure 4.1.1. Formation labels: Basement is the undifferentiated pre-rifting Mesozoic formations, Pg is the Ginger River Member of the Wagwater Formation, Ppr is the Pencar River Member of the Wagwater Formation, Pd is the Dry River Member of the Wagwater Formation, Ero is the Roadside Member of the Richmond Formation, and LS is undifferentiated Yellow and White Limestone Groups.

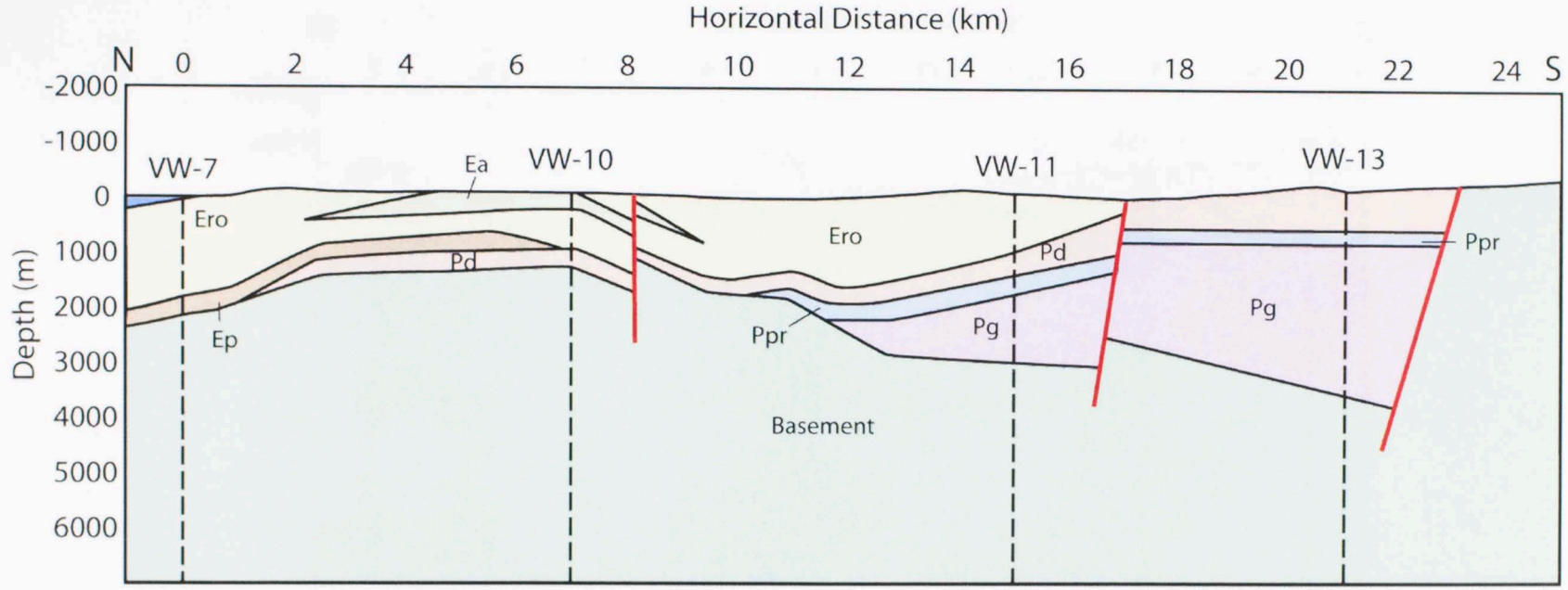

Figure 5.1.5: North-south basement-constrained cross-section N-S 1. This cross-section runs west of along the western side of the trough, west of Tom's River to just East of Port Maria. Location of cross-section is show in figure 4.1.1. Formation labels: Basement is the undifferentiated pre-rifting Mesozoic formations, Pg is the Ginger River Member of the Wagwater Formation, Ppr is the Pencar River Member of the Wagwater Formation, Pd is the Dry River Member of the Wagwater Formation, Ep is the Port Maria Member of the Richmond Formation, Ero is the Roadside Member of the Richmond Formation, Ea is the Albany Member of the Richmond Formation, and LS is undifferentiated Yellow and White Limestone Groups.

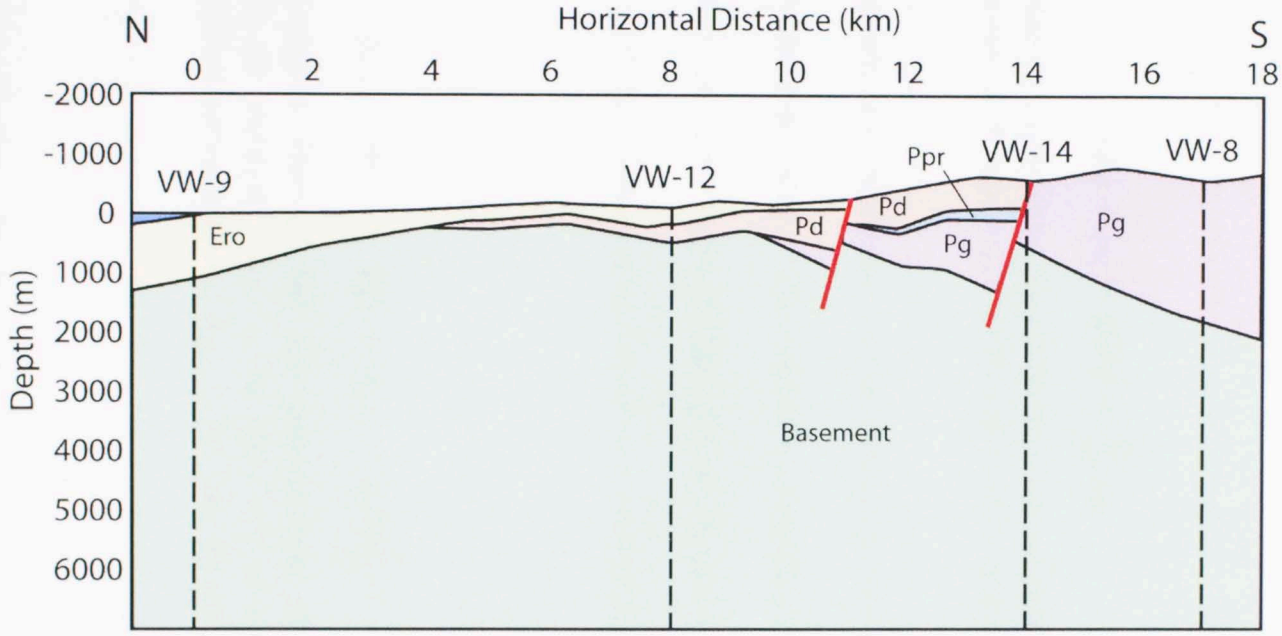

Figure 5.1.6: North-south basement-constrained cross-section N-S 2. This cross-section runs through the eastern region of this Wagwater Trough study area, south of Anotto Bay. Location of cross-section is show in figure 4.1.1. Formation labels: Basement is the undifferentiated pre-rifting Mesozoic formations, Pg is the Ginger River Member of the Wagwater Formation, Ppr is the Pencar River Member of the Wagwater Formation, Pd is the Dry River Member of the Wagwater Formation, Ero is the Roadside Member of the Richmond Formation, and LS is undifferentiated Yellow and White Limestone Groups.

5.2 The Bouguer Anomaly

Free-Air Correction. The free-air correction which is added to the measured gravity value to correct it to a sea-level value is calculated in equation 5.2.1 (Fowler, 1990).

$$\delta g_F = g_0 - g(h) = \frac{2h}{R} g_0$$

Equation 5.2.1: The free-air correction. δg_F is the free-air correction, g_0 is the measured gravity, $g(h)$ is the gravity at elevation h, and R is the radius of the Earth.

As gravity decreases with height above the surface, points above sea level are corrected to sea level by adding $2hg_0/R$. This correction amounts to 3.1 x 10^{-6} m s^{-2} per meter of elevation. A more accurate value of this correction can be made by using McCullagh's formula for the gravitational attraction of a rotating spheroid (Equation 5.2.2).

$$g_F = g_{obs} - g(\lambda) + \delta g_F = g_{obs} - g(\lambda)\left(1 - \frac{2h}{R}\right)$$

Equation 5.2.2: McCullah's formula for the gravitational attraction of a rotating spheroid. g_F is the free-air anomaly, g_{obs} is the observed or measured gravity value, $g(\lambda)$ is the latitude variation correction, and δg_F is the free-air correction (Fowler, 1990).

Bouguer Plate Correction. The Bouguer plate correction compensates for the effect of a layer of rock whose thickness corresponds to the elevation difference between the measurement and the reference levels, and it compensates for the gravitational attraction of the rocks between the measurement point and sea level. This is assuming

that these rocks are of infinite horizontal extent. The Bouguer plate correction is given by equation 5.2.3 (Fowler, 1990; Lowrie, 2007).

$$\Delta g_{BP} = 2\pi G\rho h$$

Equation 5.2.3: The Bouguer plate correction. Δg_{BP} is the Bouguer plate correction, G is Gravitational or Newtonian Constant (6.67×10^{-11} m^3 kg^{-1} s^{-2}), ρ is Density in kg m^{-3}, h is height above sea level in meters (Fowler, 1990; Lowrie, 2007).

The datum for the Bouguer plate and terrain corrections is sea level and a standard density of 2.7 kg m^{-3} (Fowler, 1990).

Bouguer Anomaly. Combining the free-air, Bouguer plate, and terrain corrections together allows the Bouguer anomaly to be calculated (equation 5.2.4).

$$g_B = g_F - \delta g_{BP} + \delta g_T = g_{obs} - g(\lambda) + \delta g_F - \delta g_B + \delta g_T$$

Equation 5.2.4: The Bouguer anomaly. g_B is the Bouguer anomaly, g_F is the free-air anomaly, δg_B is the Bouguer correction, δg_T is the terrain correction, g_{obs} is the observed or measured gravity value, $g(\lambda)$ is the latitude variation correction, and δg_F is the free-air correction (Fowler, 1990).

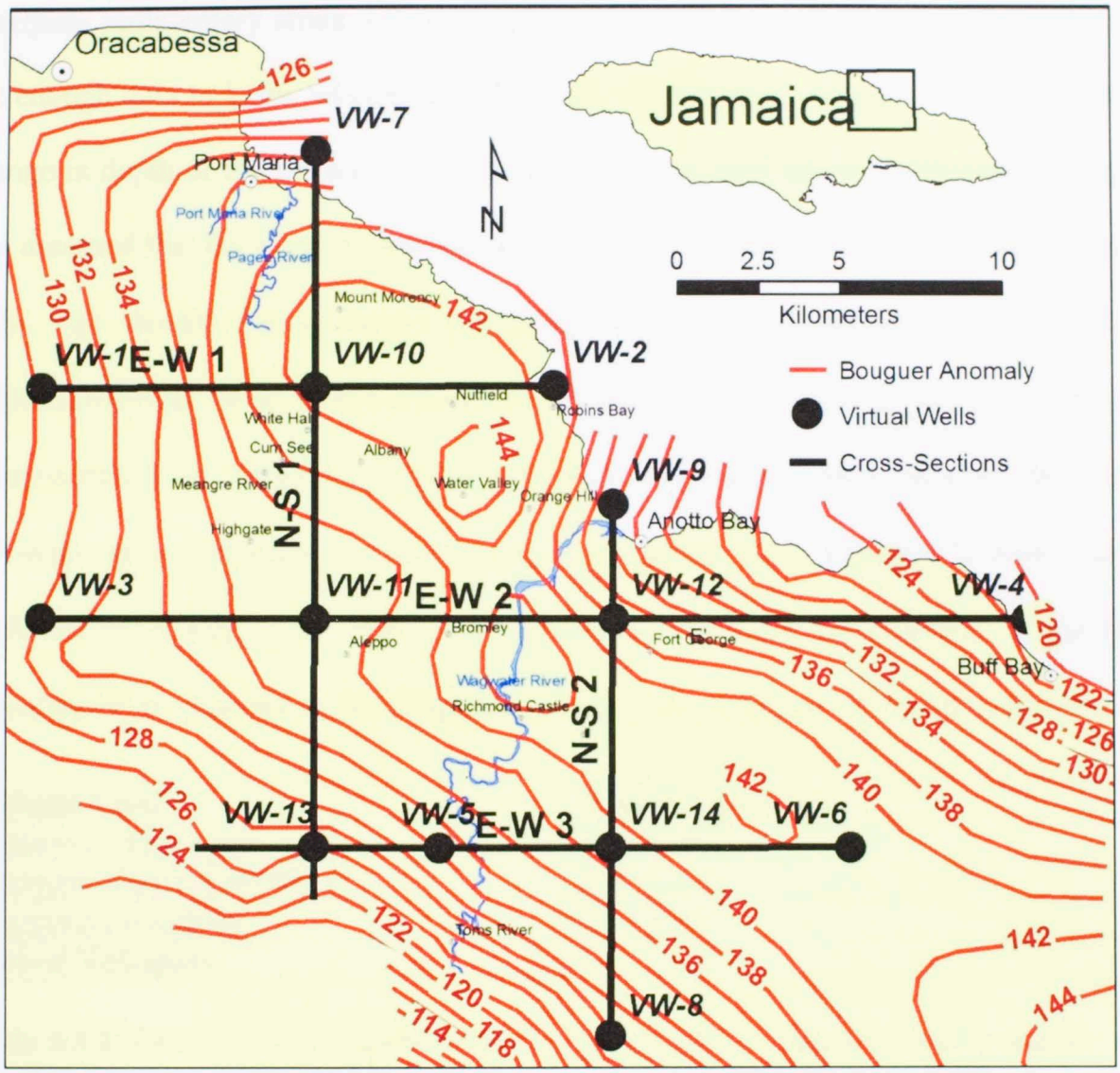

Figure 5.2.1: Map showing the Bouguer anomaly values in the northern Wagwater Trough. The higher values trend from the Blue Mountains in the southeast toward Oracabessa and Port Maria in the northwest (after Andrew et al., 1992).

5.3 Determining Basement Depth Using the Bouguer Anomaly

The Bouguer anomaly can be used to determine the depth to a crystalline basement in a sedimentary basin, because the Bouguer anomaly corrects for elevation change and is, therefore, unaffected by changes in surface elevation. Bouguer gravity maps essentially show three things with respect to the basin: (1) a change in depth of the crystalline basement rocks, (2) a change in density of either the basement rocks or

overlying sedimentary strata, (3) or the presence of an igneous intrusion. Since there is not enough data to know whether the change in the Bouguer anomaly is controlled by a change in depth of the basement or density of the basement and/or sedimentary rocks, it was assumed that the simplest method would be used: a change in depth of the basement rocks with density for all layers remaining constant. It is known that the Nutfield Volcanics formed flows, pillows, and dikes in the northern region of the study area (see cross-section A-A', figure 4.1.2). However, no other intrusions have been documented in the study area. Densities for the various rock layers were determined using values published by Wadge et al. (1983), who determined the depth-to-basement for the Blue Mountain Inlier, just east of the Wagwater Trough. These values are found in table 5.3.1

Geologic Units	**Average Densities**
Cretaceous Basement	2.84 g cm^{-3}
Paleogene Clastic Sediments	2.59 g cm^{-3}
Paleogene Limestone	2.61 g cm^{-3}
Nutfield Volcanics	2.82 g cm^{-3}

Table 5.3.1: Density values inserted into GYM-SYS(PRO). This software is used to calculate the basement depth using the Bouguer anomaly (Wadge et al., 1983)

To simplify the process, each cross-section is created separately in a program called GM-SYS(PRO), developed by Northwest Geophysics Assoc. By creating a cross-section and adding in density values for each lithologic unit, including the basement, the depth of the basement can be constrained as the data is fit to the Bouguer anomaly data points (figure 5.3.1).

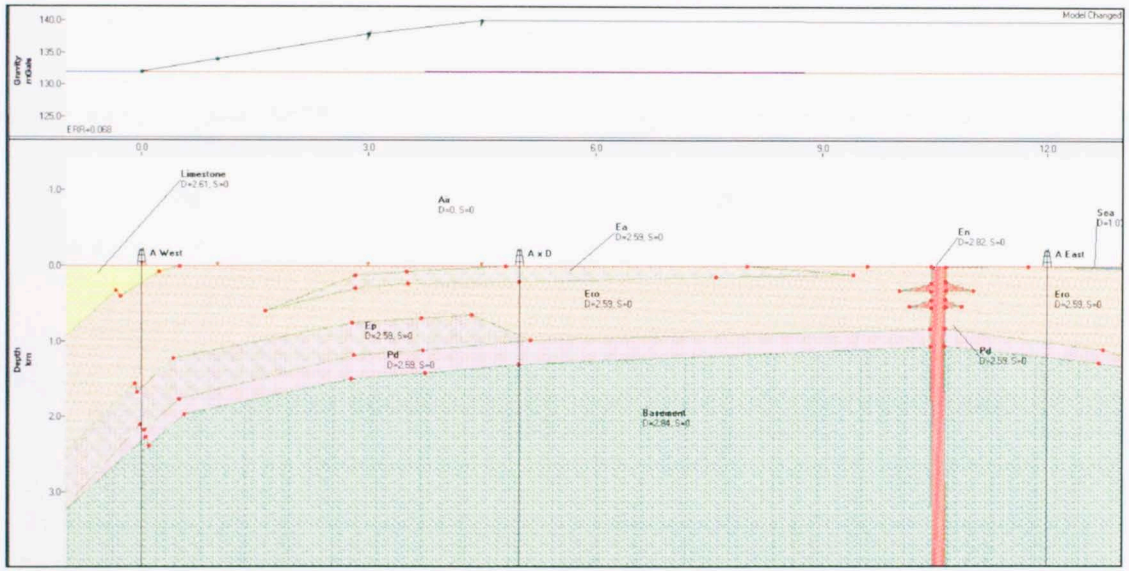

Figure 5.3.1: Cross-section E-W 1 copied from Gym-Sys showing how the subsurface data is constrained to fit a Bouguer anomaly curve. Using density values for each unit, the measured Bouguer anomaly points can be fit with a curve representing the modeled Bouguer Anomaly.

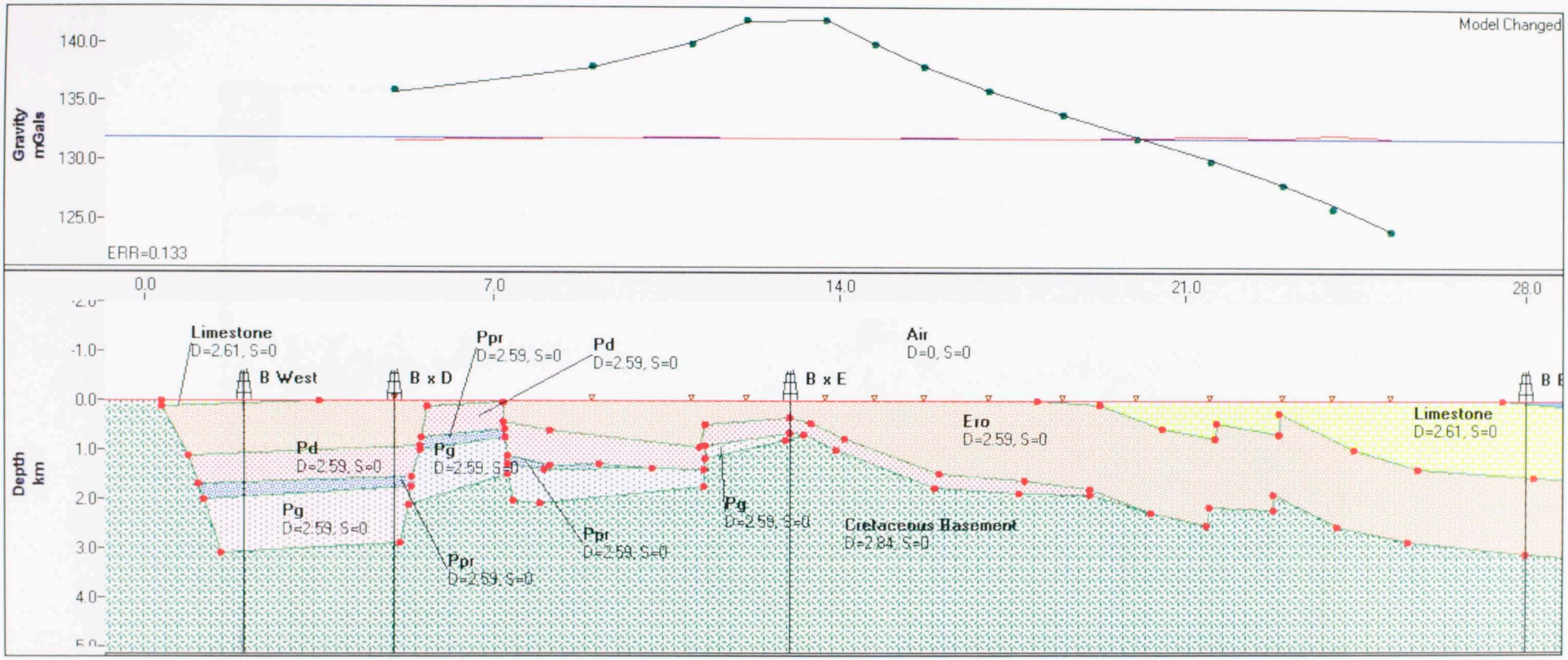

Figure 5.3.2: Cross-section E-W 2 copied from Gym-Sys showing how the subsurface data is constrained to fit a Bouguer anomaly curve. Using density values for each unit, the measured Bouguer anomaly points can be fit with a curve representing the modeled Bouguer Anomaly.

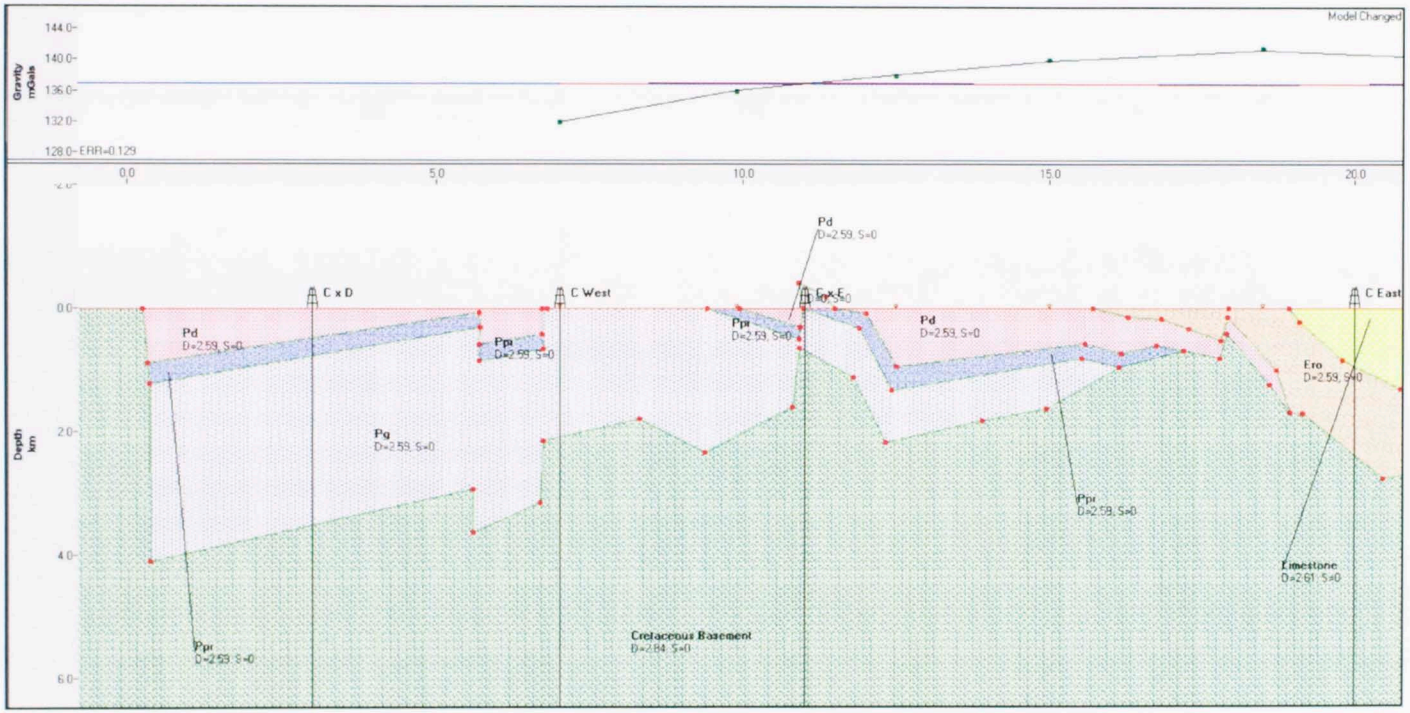

Figure 5.3.3: Cross-section E-W 3 copied from Gym-Sys showing how the subsurface data is constrained to fit a Bouguer anomaly curve. Using density values for each unit, the measured Bouguer anomaly points can be fit with a curve representing the modeled Bouguer Anomaly.

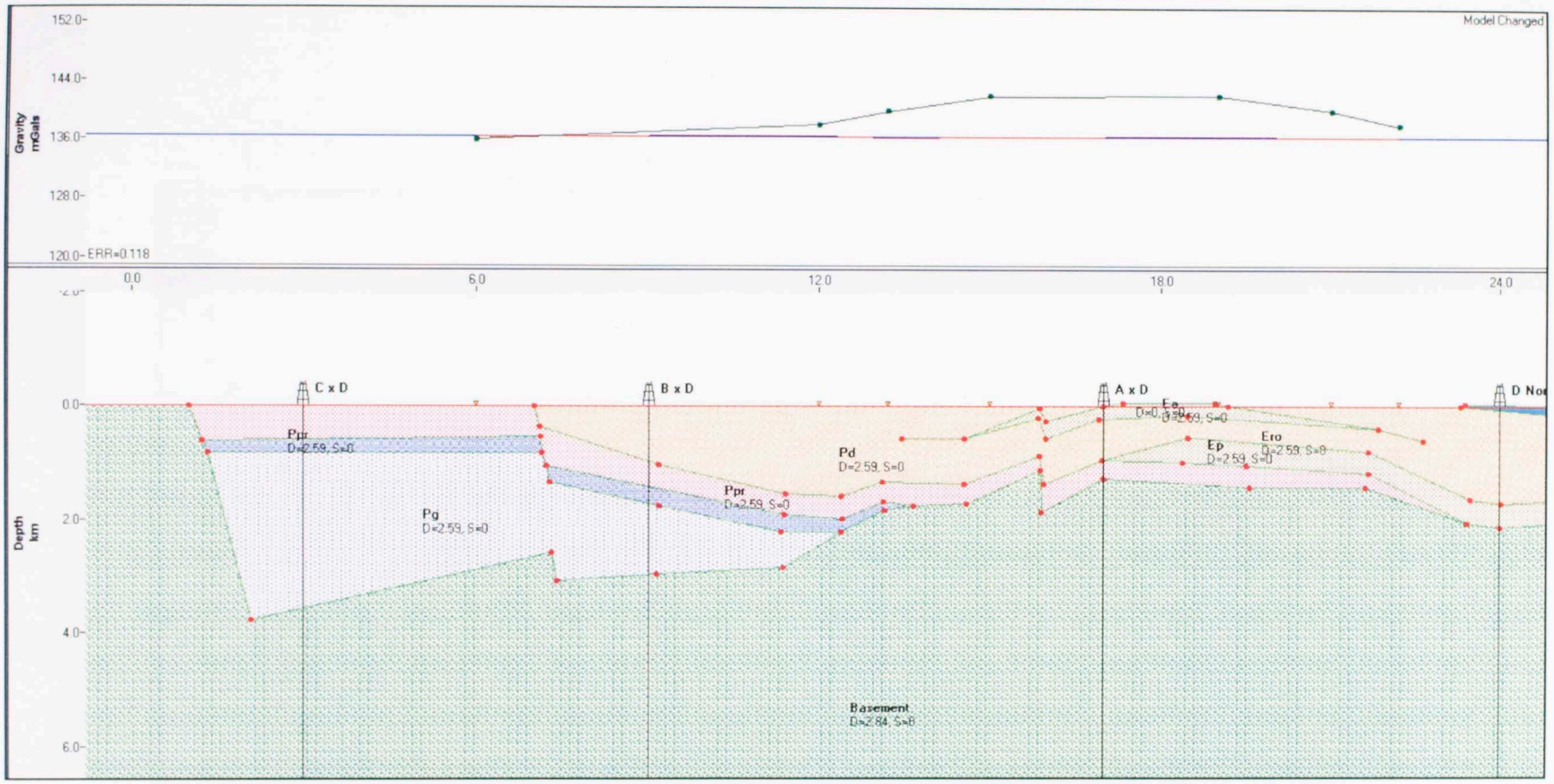

Figure 5.3.4: Cross-section N-S 1 copied from Gym-Sys showing how the subsurface data is constrained to fit a Bouguer anomaly curve. Using density values for each unit, the measured Bouguer anomaly points can be fit with a curve representing the modeled Bouguer Anomaly.

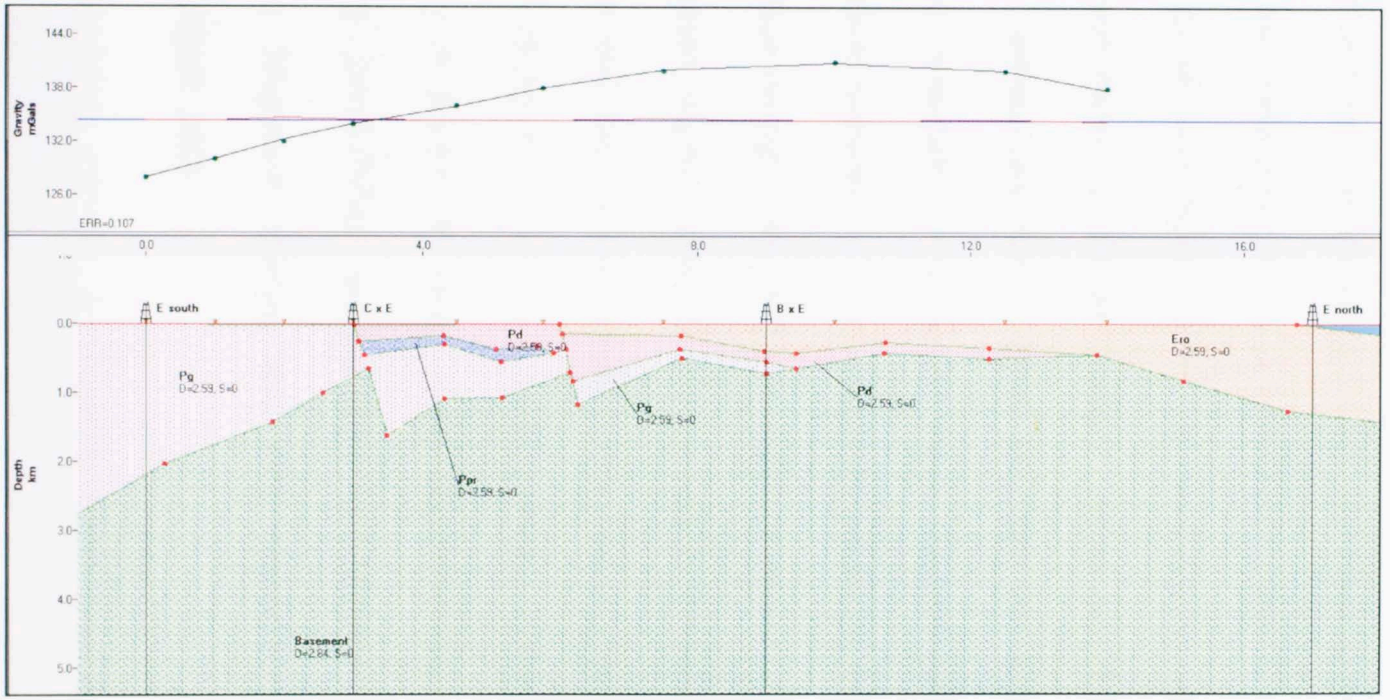

Figure 5.3.5: Cross-section N-S 2 copied from Gym-Sys showing how the subsurface data is constrained to fit a Bouguer anomaly curve. Using density values for each unit, the measured Bouguer anomaly points can be fit with a curve representing the modeled Bouguer Anomaly.

6. BASIN MODELING METHODS

6.1 Introduction

The evolution of sedimentary basins is controlled by a combination of geomechanical factors such as basin subsidence (growing) and basin uplift (destruction caused by erosion) (Pigott and Sattayarak, 1993). A petroleum system in a sedimentary basin was defined by Metwalli and Pigott (2005) as "a dynamic, inter-dependent assemblage of materials and processes linked together within non-discrete spatial-temporal boundaries in a sedimentary basin, which provides the accumulation of hydrocarbon". Some of these materials include source rocks, reservoir rocks, and seals, and essential processes include formation of traps, migration pathways, accumulation of hydrocarbons, and preservation through time. Different stages in basin evolution, marked by local changes in the tectonic regime, allow the source rock to be buried, generating hydrocarbons, transportation, and reservoir-trap accumulation. Source generation criticals include source generation volume or total organic carbon (TOC), quantity, quality or kerogen type, and maturity or designated source rocks. Reservoir-trap accumulation criticals refer to the quality (permeability and porosity), hydrocarbon type, seal and closure of reservoir rocks. Migration criticals deal with migration pathways and mechanisms (Metwalli and Pigott, 2005).

In this study, basin modeling software, developed by Platte River Associates, will be used in both one and two dimensions (1-D and 2-D) to calculate maturity of hydrocarbons in source rocks, migration of hydrocarbons from out of the source rocks, and migration of hydrocarbons into the reservoir rocks.

6.2 One Dimensional (1-D) Basin Modeling Principles

The primary function of BasinMod 1-D is to construct a geologic model of stratigraphy versus time and depth in which a number of parameters can be inputted so that as much data as available can be exploited (BasinMod 1-D Manual, 2005).

Data gathered for BasinMod 1-D include formation top depths, ages, thicknesses, lithologies, initial TOC values, kerogen types, and measured porosities. This can be used to model tectonic subsidence, thermal maturation, and burial history of the basin. Due to the absence of true well data, 14 virtual wells were placed in strategic locations in the basin. Therefore much of the data used in BasinMod 1-D needed to be estimated using as much surface data as possible. These assumptions will be discussed later in this thesis.

Formation or Event Name	Type	Begin Age (my)	Top Depth (m)	Present Thick (m)	Eroded Thick (m)	Lithology	Organofacies / Kerogen	Initial TOC
Surface Erosion	E	10			-2450			
LS-dep	D	51			1500	Limestone	Type II (BMOD-1D LLNL)	3
Ero-dep	D	54			950	Sandstone	Type II (BMOD-1D LLNL)	6
Ero	F	57	0	950		Sandstone	Type II (BMOD-1D LLNL)	6
Pd	F	63	950	610		Sandstone	Type III (BMOD-1D LLNL)	5
Ppr	F	63.6	1560	220		Sandstone	Type II (BMOD-1D LLNL)	7
Pg	F	65.6	1780	1110		Sandstone	Type III (BMOD-1D LLNL)	10

Figure 6.2.1: Data input to BasinMod 1-D. Formations are entered with both a top depth and present thickness, eroded deposits are entered with only an eroded thickness, and erosion events are entered with thickness of erosion.

6.3 Subsidence Principles.

There are four models that cause subsidence in a basin: (1) water loading, (2) sediment loading, (3) flexure, and (4) tectonics. Subsidence from water loading (S_{wl}) causes subsidence using the relationship in equation 6.3.1 (Metwalli and Pigott, 2005).

$$S_{wl} = \Delta SL * \frac{\rho_w}{\rho_m - \rho_w}$$

Equation 6.3.1: Subsidence due to water-loading. S_{wl} is the amount of subsidence caused by water loading, ΔSL is the change in sea level, ρ_w is the density of sea water (1.028 kg m^{-3}), ρ_m is the density of the mantle (3.3 kg m^{-3}) (Metwalli and Pigott, 2005).

Inserting density values into the equation gives the relationship between water loading and sea level change (Equation 6.3.2).

$$S_{wl} = 0.452 * \Delta SL$$

Equation 6.3.2: Relationship between sea level changes and subsidence due to water loading.

This means that for every one kilometer of sea level rise, the basin subsides 452 meters.

Subsidence from sediment loading (S_{sedl}) is directly related to the amount of sedimentation in a basin by equation 6.3.3 (Metwalli and Pigott, 2005).

$$S_{sedl} = S * \frac{\rho_s - \rho_w}{\rho_m - \rho_w}$$

Equation 6.3.3: Subsidence due to sediment loading. Where S_{sedl} is subsidence due to sediment loading, S is sediment thickness, and ρ_s is the sediment density (2.65 kg m^{-3}) (Metwalli and Pigott, 2005).

This equation can be simplified to show the relationship that one kilometer of sediment has on sediment loading subsidence (Equation 6.3.4).

$$S_{sedl} = 0.71\ km$$

Equation 6.3.4: Relationship showing that for every 1 km of sediment loaded onto a basin, 0.71 km of basin subsidence occurs.

For every one kilometer of sediment deposited in a basin, 710 meters of subsidence occurs. Subsidence due to flecture (S_{flex}) contrubutes less than one percent of basin subsidence, and it is not significant enought to be used in this study. Tectonic subsidence (S_{tec}) has the most profound effect in basin subsicence. It can be quantitatively described in equation 6.3.5 (Metwalli and Pigott, 2005).

$$S_{tec} = \frac{t_l\left(1 - \frac{1}{\beta}\right) * \left[(\rho_m - \rho_c) * \left(\frac{t_c}{t_l}\right) * \left(1 - \frac{\alpha * T_m * t_c}{2 * t_l}\right) - \left(\frac{\alpha * T_m * \rho_m}{2}\right)\right]}{\rho_m * (1 - \alpha * T_m) - \rho_w}$$

Equation 6.3.5: Tectonic subsidence equation. S_{tec} is the amount of tectonic subsidence, t_c is the thickness of the crust, t_l is the thicknes of the lithosphere, ρ_m is the density of the mantle (3.33 kg m^{-3}), ρ_c is the density of the crust (2.8 kg m^{-3}), ρ_w is the density of seawater (1.03 kg m^{-3}), α is the thermal expansion coefficient ($3.3*10^{-5}$ C^{-1}), β is the stretching factor, and T_m is the temperature of the mantle (1350 C) (Metwalli and Pigott, 2005).

The total subsidence in a basin is a sum of the subsidences caused by tectonics, sediment loading, and water loading. The process used to determine the amount of load-induced subsidence is isostatic back stripping. This method removes sediment layers, correcting for deompation, fluctuation of sea level, and sea depth. The tectonic subsidence is expressed by equation 6.3.6 (Metawalli and Pigott, 2005 after Pigott and Sattayarak, 1993).

$$S_{tec} = S_{total} - S_{sedl} - S_{wl} \pm \Delta SL$$

Equation 6.3.6: Total subsidence equation. S_{tec} is corrected subsidece, S_{total} is total subsidence, S_{sedl} is sediment loading, S_{wl} is water loading, and ΔSL is sea level change.

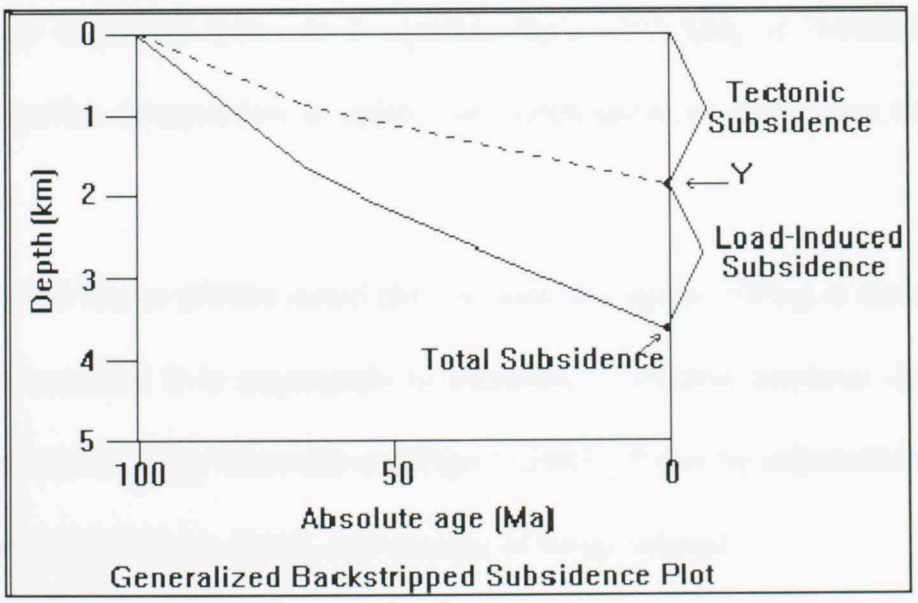

Figure 6.3.1: Generalized backstripped subsidence plot. As explained in equation 6.3.6, the total subsidence is the sum of tectonic subsidence and the load-induced subsidence (water-loading and sediment-loading) (from BasinMod 1-D Manual, 2005).

6.4 Stretching Factor β (Beta)

When basins are stretched the crust and lithosphere is thinned. More streching causes more thinning just as less stretching causes less thinning. As mentioned in the Tectonic Subsidence Equation (Equation 6.3.5), beta (β) is the stretching factor. β is calculated from the ratio of lithosphere thickness before stretching/rifting to lithosphere thickness immediately after stretching/rifting (Equation 6.4.1).

$$\beta = \frac{T_{lith0}}{T_{lith}}$$

Equation 6.4.1: Stretching Factor (β). T_{lith} is the lithosphere thickness immediately after stretcing and T_{lith0} is the thickness of the lithosphere before stretching.

When β is greater than one it signifies basin stretching or extension, when less than one it signifies compaction or uplift, and when equal to one means that no change has occurred.

Mann and Burke (1990) stated that because the age of rifting is too old and basin inversion has occurred it is impossible to calculate β without borehole data. However, using a method devised by Metwalli and Pigott (2005), β can be calculated from tectonic subsidence, stretching along faults, and change in basin volume.

Determining β From Tectonic Subsidence (1-D). β can be calculated in each of the virtual wells using a method devised by Pigott, Metwalli and Pigott (2005). 1-D tectonic subsidence can be modelled using BasinMod 1-D (Figure 6.4.1). Using the amount of fault mechanical tectonic subsidence (rifting) determined from the BasinMod 1-D models, β can be calculated using equation 6.3.5 assuming that the thicknesses of the

crust and lithosphere before subsidence are 40 km and 120 km respectively, and assuming uniform extension as a first approximation that the beta of the crust is equivalent to the beta of the lithosphere (Allen and Allen, 2005). Uplift can be calculated in the same manner using a negative value for tectonic subsidence, and it must be calculated separately from fault mechanical subsidence. However, because uplift often follows rifting the thickness of the crust and lithosphere are not always 40 km and 120 km respectively at the beginning of uplift, and the values must be calculated.

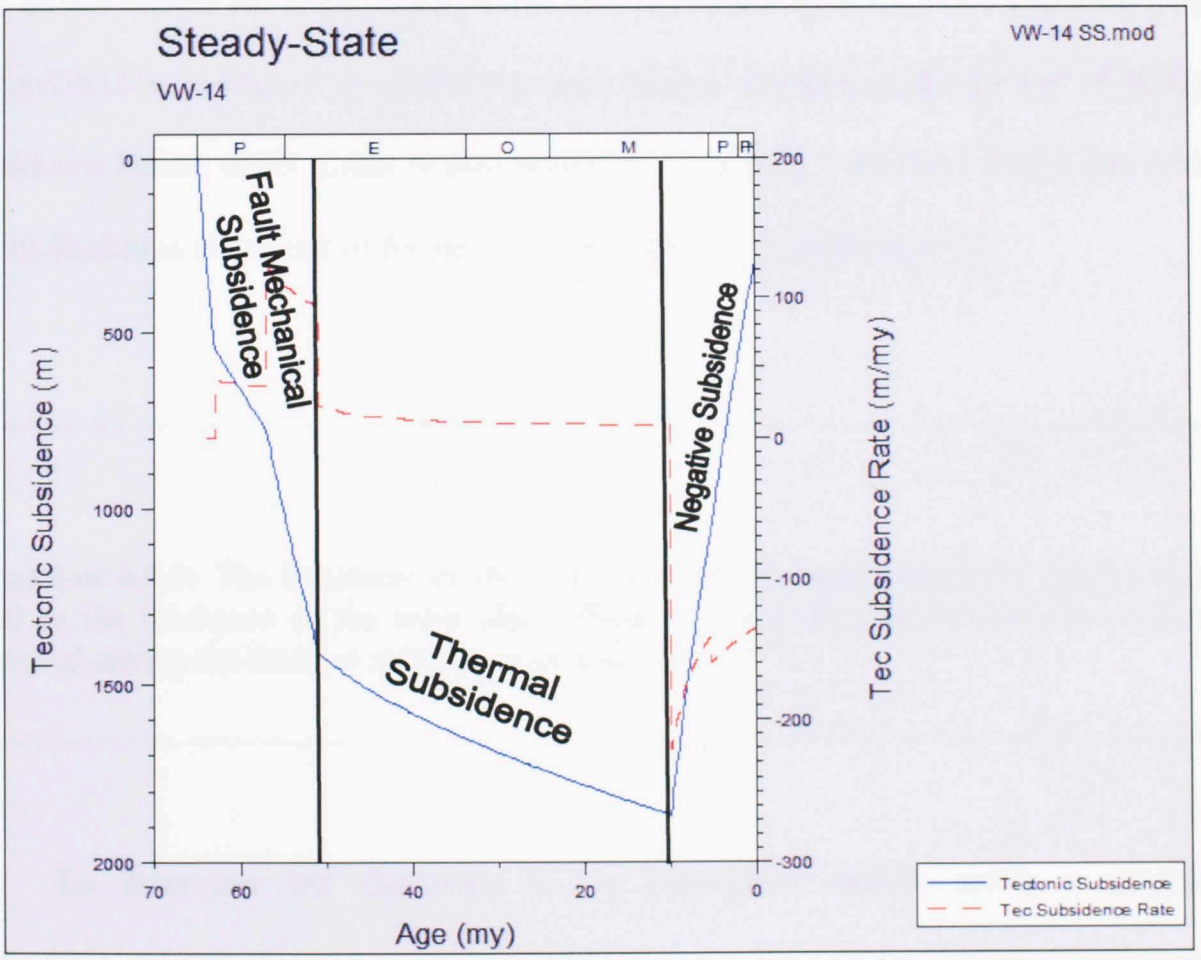

Figure 6.4.1: Graph of tectonic subsidence versus time for VW-14. Tectonic subsidence can be divided into three stages: fault mechanical subsidence (extension), thermal subsidence (drifting), and negative subsidence (shortening). Beta is only calculated for rifting and uplift. Clastic sedimentation (Wagwater and Richmond Formations) occurred during the period of fault mechanical subsidence, and carbonate sedimentation (Yellow and White Limestone Groups) occurred during the period of thermal subsidence.

$$t_c = t_{c0}/\beta$$

$$t_{lith} = t_{lith0}/\beta$$

Equation 6.4.2: Thickness of crust and lithosphere after rifting (t_c and t_{lith}) is equal to the thickness of the crust and lithosphere before rifting (t_{c0} and t_{lith0}) divided by β. The values of t_{c0} and t_{lith0} are assumed to be km and 120 km respectively.

After the new thicknesses of the crust and lithosphere after rifting is determined they do not remain the same. Because this lithosphere has been thinnned and is no longer in equilibrium, it begins to equilabrate and thicken throughout the period of thermal subsidence before uplift. Crust is also thickened by adding sediments during this period and its thickness at the end of the period is determined in equation 6.4.3.

$$t_{cf} = t_c + t_s$$

Equation 6.4.3: The thickness of the crust after the thermal subsidence period (t_{cf}) is equal to the thickness of the crust after rifting (t_c) plus the thickness of the sediment deposited during the thermal subsidence period (t_s).

To determine the thickness of the lithosphere before uplift, a graphical relationship calculated, using equation 6.4.4, between lithosphere thickness and time is used (Figure 6.4.2), assuming post-rift oceanic lithosphere behaves empirically as continental lithosphere. Lithosphere thickness after rifting is plotted on the line in the graph, and the corresponding time is determined. The period of time for thermal subsdience is added to that line and the corresponding lithosphere thickness is the

thickness of the lithosphere just before uplift. The example in red illustrates this method: a lithosphere thickness after rifting of 72 km during a period of 41 million years of thermal subsidence will thicken to 111 km just before uplift. The maximum thickness that the lithosphere can reach during thermal subsidence is 120 km.

$$T_{lith} = 0.00232\sqrt{(3.154 * 10^7)(t)}$$

Equation 6.4.4: Thickness of the lithosphere (T_{lith}) as a function of post rift time (t) (derived from Turcotte and Schubert, 2003)

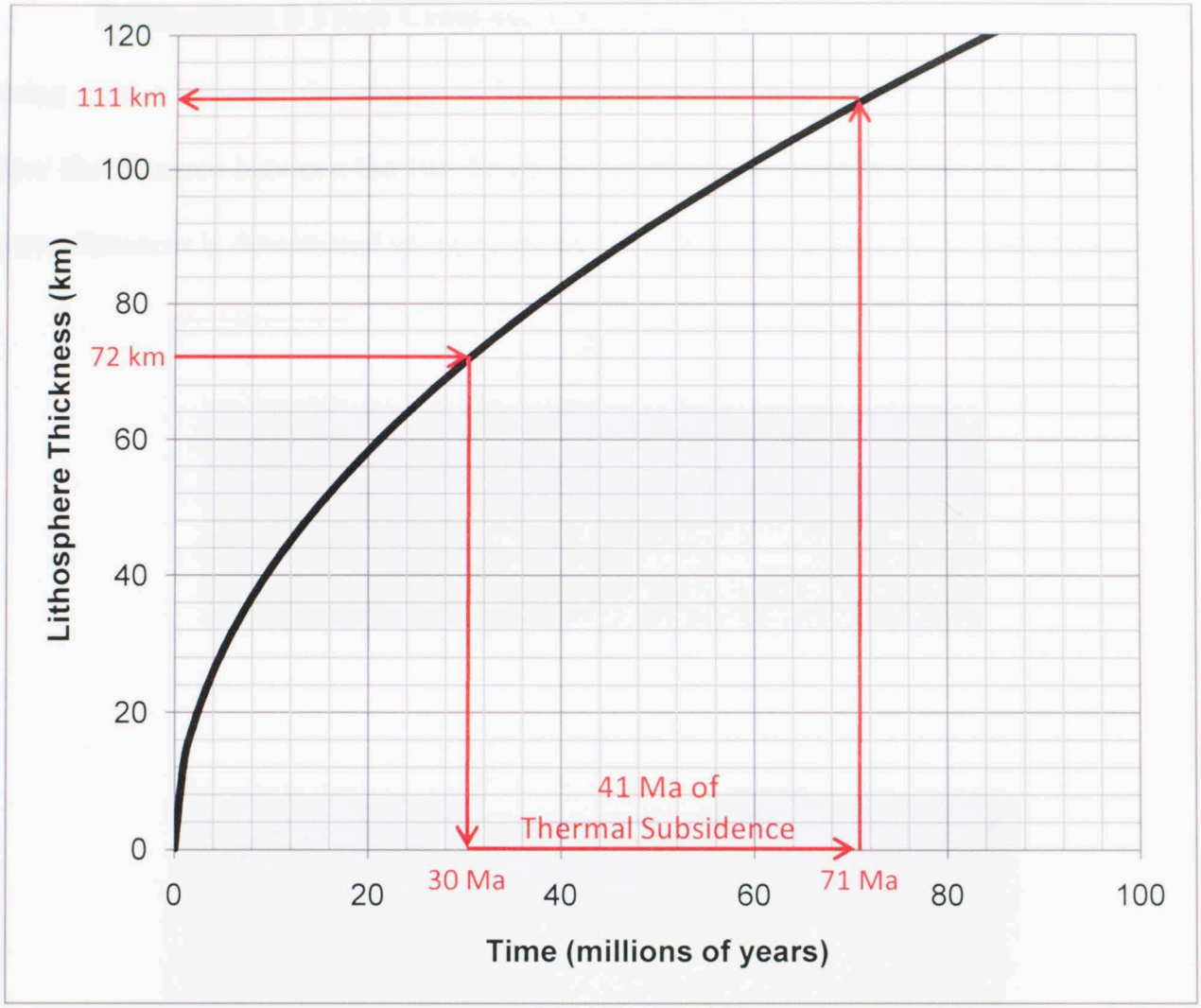

Figure 6.4.2: Graph showing the rate at which post-rifting thinned lithosphere thickens with respect to time (black line). This can be used to determine how much the lithosphere has thickened during the thermal subsidence period making it possible to calculate β for the period of uplift. Lithosphere thickness after rifting is plotted on the line in the graph, and the corresponding time is determined. The period of time for thermal subsdience is added to that line and the corresponding lithosphere thickness is the thickness of the lithosphere just before uplift. The example in red illustrates this method: a lithosphere thickness after rifting of 72 km during a period of 41 million years of thermal subsidence will thicken to 111 km just before uplift (from equation 6.4.4, derived from Turcotte and Schubert, 2003).

Determining β From Cross-section (2-D). β can be calculated from 2-D models using a ratio between the change in length prior to and post rifting. Figure 6.4.3 shows how the distance between the two faults increases as the basin is stretched. The ratio of these distances is determined using equation 6.4.5 (Pigott, unpublished lecture notes).

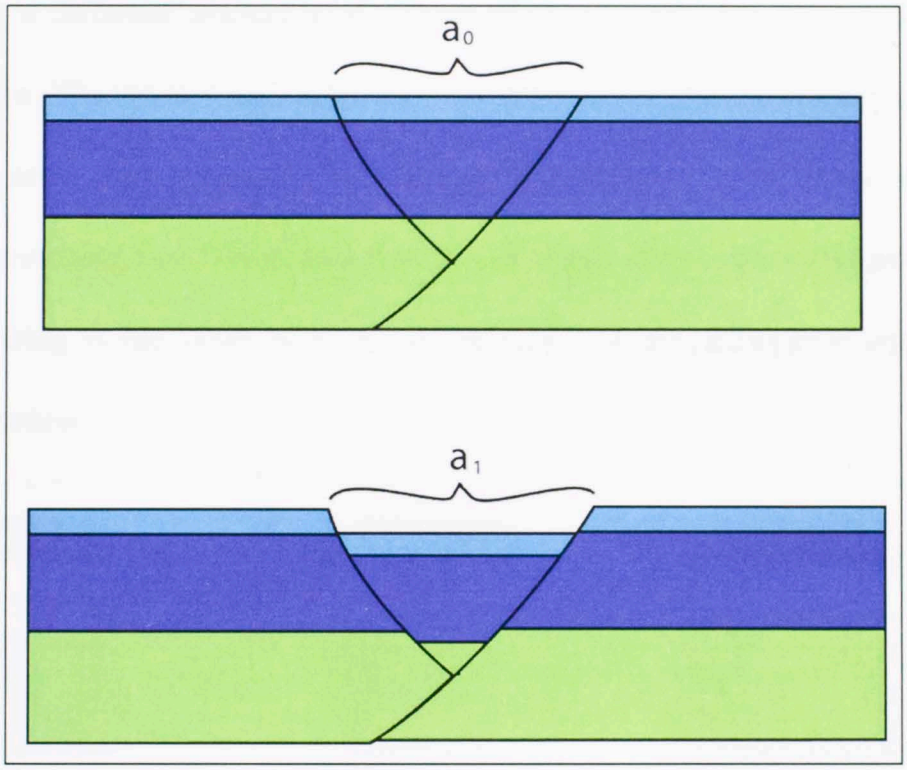

Figure 6.4.3: Schmatic showing an increase in distance as a result in rifting. The units with length a_0 are stretched and faulted to have a length a_1 (after Pigott, unpublished lecture notes).

$$\beta = \frac{a_1}{a_0}$$

Equation 6.4.5: Beta (β) is calculated as the ratio of the distance after rifting (a_1) to the distance before rifting (a_0)

Derminining β From Basin Volume (3-D). There are three models for stretching from Allen and Allen (2005): Uniform, discontinuous, and continuous depth-dependent stretching (Figure 6.4.4). Uniform extension models the crust and lithosphere extending by identical amounts. Discontinuous depth dependent extension models the crust extending by a different amount to the lithosphere, necessitating a decoupling between the two layers. The crustal and subcrustal extensions are independent but are uniform through the crust and subcrustal lithosphere. Continuous depth dependent extension models the stretching as a continuous function of depth in the subcrustal lithosphere, and crustal stretching is the same as in the continuous and discontinuous depth dependent exstension models.

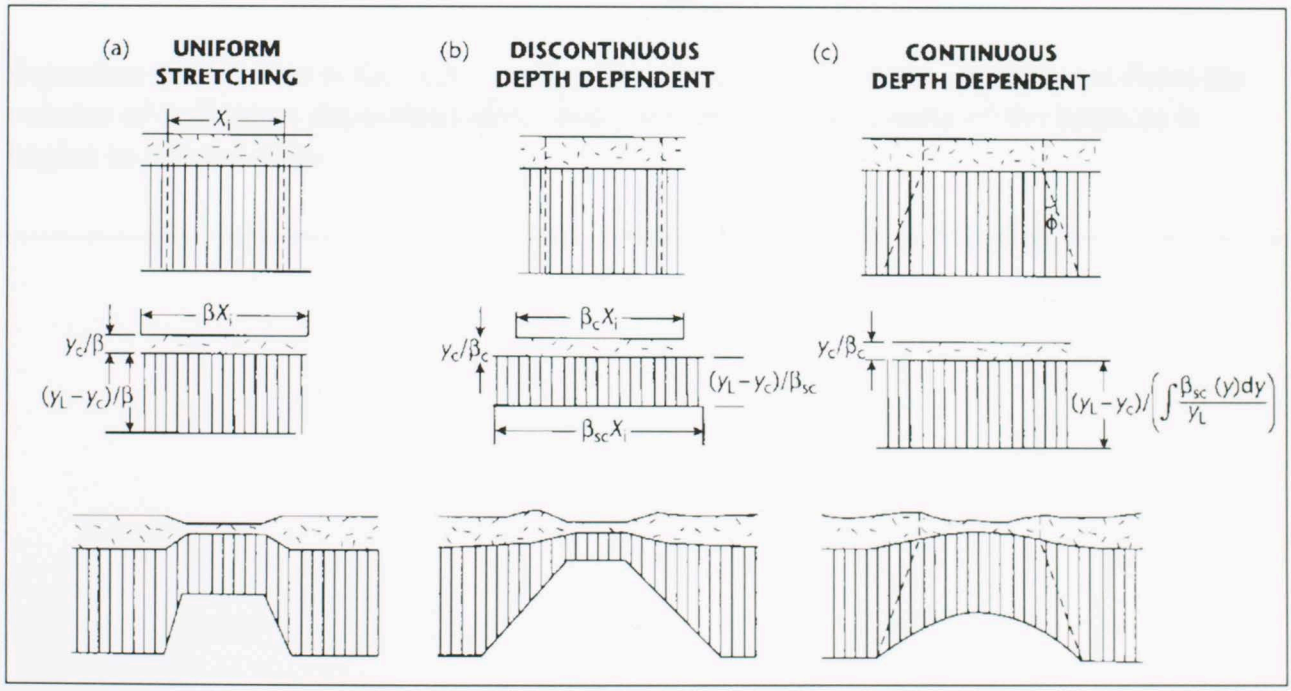

Figure 6.4.4: Schematic diagrams to illustrate differences between (a) uniform, (b) discontinuous, and (c) depth-dependent stretching. It is assumed that uniform stretching is the case in the Wagwater Trough (From Allen and Allen, 2005).

It is posible that β can be determined using the crustal volume of the stretched basin assuming rifting conforms to the uniform stretching model. This means that extension is uniform and the crust and subcrustal lithosphere extend by identical amounts.. The amount of stretching in a basin can simply be determined by taking the ratio of the basin volume at the end of rifting to the basin volume during the initial rifting stages. This is illustrated in equation 6.4.6 (Pigott, unpublished lecture notes; Allen and Allen, 2005).

$$\beta = \sqrt[3]{\frac{V_1}{V_0}}$$

Equation 6.4.6: Beta is the cubed root of the volume of the basin (determined from the volume of sediments deposited) after rifting divided by the volume of the basin as it begins to rift and form.

6.5 Heat Flow Principles

Thermal history is important in modelling maturity and kinetics. The second law of thermodynamics states that, in a closed system, no processes will tend to occur that increase the net organization (or decrease the net entropy) of the system (Encyclopædia Britannica, 2009). When referring to the transfer of energy or heat in a system it can mathematically be solved by the Thermal Boundary Value Solution which means the Temporal Heat Storage in system is equal to the the sum of the heat flux entering and the internal heat generated in a system minus the heat flux out of the system (Equation 6.5.1)(Metwalli and Pigott, 2005).

$$\frac{\rho c \partial T}{\partial t} = \frac{\partial}{\partial x, y, z}[Kx, y, z]\frac{\partial T}{\partial x, y, z} - F + G$$

Equation 6.5.1: The thermal boundary value solution. ρc is composit heat flux, T is temperature, t is time, K is thermal conductivity, F is heat flux out, and G is internal heat generation (Metwalli and Pigott, 2005).

Equation 6.5.1 can be interpreted in crustal terms as the lithospheric thermal state is equal to the sum of the spatial rate of heat flow change and radioactive heat generation minus the heat loss due to refraction and fluid flow. If cooling plutions, mountain front hydrological flow, and radioactivity is negligible, then a time invariant steady-state condition is present, and the sum of the equation is zero (Equation 6.5.2) (Metwalli and Pigott, 2005).

$$\frac{\rho c \partial T}{\partial t} = \frac{\partial}{\partial x, y, z}[Kx, y, z]\frac{\partial T}{\partial x, y, z} - F + G = 0$$

Equation 6.5.2: The thermal boundary value solution set equal to zero. This can be done when cooling plutons, mountain front hydrological flow, and radioactivity is negligible, creating a time invariant steady-state condition.

If constant temperature endpoints are specified, the integration of equation 6.4.2 yields the classic Fourier Heat Flow Equation (Equation 6.5.3).

$$Qx, y, z = -Kx, y, z\frac{\partial T}{\partial z, y, z}$$

and simplified:

$$Q = \frac{-k}{10}\left(\frac{\Delta T}{\Delta z}\right)$$

Equation 6.5.3: The Fourier Heat Flow Equation. Q is Heat flow, k is thermal conductivity, and $\frac{\Delta T}{\Delta z}$ is the geothermal gradient (Metwalli and Pigott, 2005).

Since the thermal conductivity is constant in a system the only factor that controls the amount of heat flow in a system is the geothermal gradient. Changes in maturation and kinetics change exponentially with respect to temperature and linearly with respect to time. Therefore, presentday heat flow can be used in order to construct paleoheat flow throughout the basin. However, rifting causes dramatic variations in heat that affects temperature for millions of years after the rifting event (Basinmod 1-D Manual, 2005).

To help model this more accurately BasinMod offers several approaches to construct paleoheat flow.

Steady State Heat Flow. One of the models for heat flow is in the steady state. This is calculated using a heat flow/thermal conductivity model. Each time interval of the model is calculated independently of the prior time interval, using equation 5.5.4 which has a basic relationship: Heat Flow = Thermal Conductivity * Temperature Gradient.

$$T = T_0 + Q_s \int_0^z \frac{z}{k(z)} dz$$

$$T = T_0 + Q_s \sum_{i=1}^{u} \frac{z_i - z_{i-1}}{k_i}$$

Equation 6.5.4: Steady-state heat flow equation. T_0 is surface temperature, Q_s is surface heat flow, and k_i is thermal conductivity for bed i (Basinmod 1-D Manual, 2005).

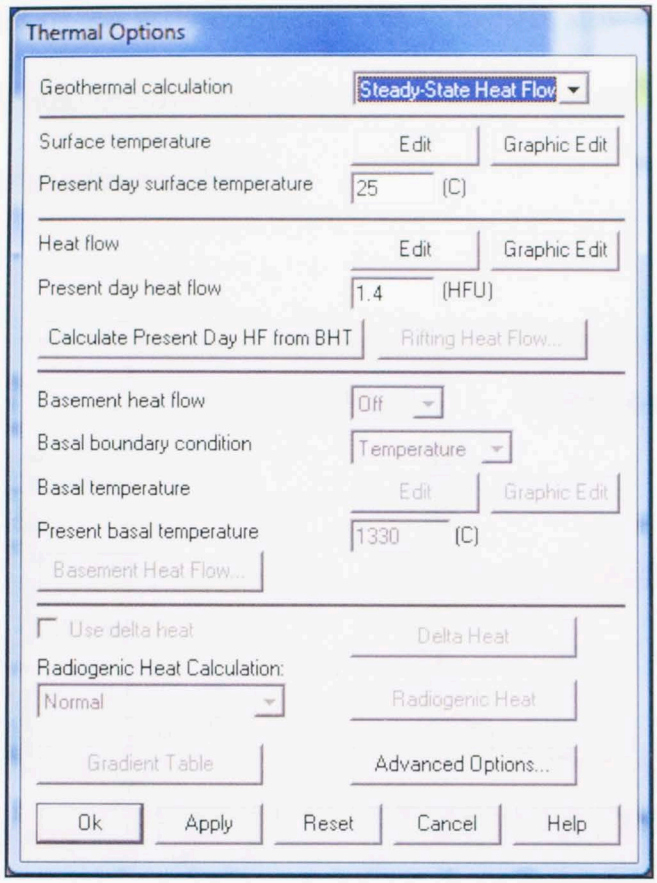

Figure 6.5.1: Thermal steady-state parameters used in BasinMod 1-D.

Rifting Heat Flow. Rifting causes pulses in thermal history that make it very difficult to model. This can cause damatic heat variations that affect temperature for millions of years after the rifting event. There have been serveral different approaches put forth to model rifiting, but there is still no universally accepted heat flow model in the literature. BasinMod offers a rifting heat flow option that is a simplification of the Jarvis and McKenzie finite rifiting model (1980) which is probably the most widely accepted theory (Allen and Allen, 2005). All prevelent rifting heat flow models seem to agree that rifting involves two phases (Basinmod 1-D Manual, 2005), a rifting phase and a subsidence or drifting phase (Figure 6.5.2). The rifting phase involves stretching, thinning, and faulting of the crust accompanied by increased heat flow due to crustal

thinning and upwelling of the asthenosphere. The subsidence or drifting phase is a post-rift period with exponential thermal decay due to re-establishment of thermal equilibrium in mantle lithosphere and asthenosphere.

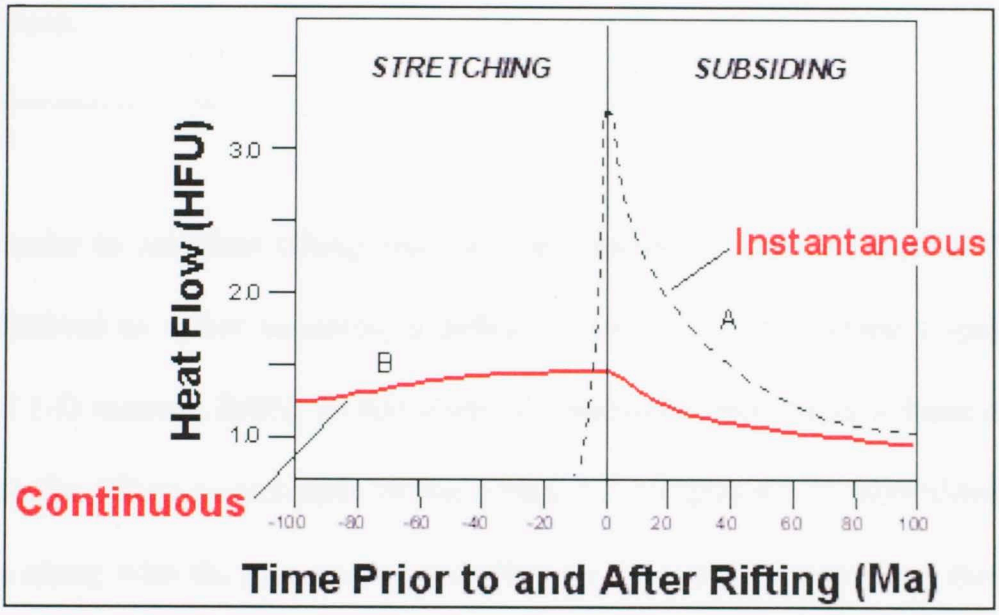

Figure 6.5.2: Heat flow changes due to rifting events. Rifting involves a rifting phase and a subsidence or drifting phase (from BasinMod 1-D Manual, 2005).

Rifting scenarios seem to range from instantaneous rifting followed by a sudden increase in heat flux to a maximum followed by exponential decay to continuous rifting where stretching occurs over a long period of time during which heat is dissipated. Basinmod uses a thermal decay equation to model rifting heat flow (Equation 6.5.5).

$$F(t) = \frac{kT_1}{z} \cdot \left\{1 + \pi \sum_{n=1}^{\infty} nb_n(-1)^{n+1} \times \exp[-n^2\pi^2(t - \Delta t)\, k/a^2]\right\}$$

Equation 6.5.5: The thermal decay equation. *F(t)* is the heat flux at the suface at time *t*, *t* is the time of rifting, *k* is the thermal conductivity, $\frac{kT_1}{z}$ is the heat flow prior to rifting, based on present day heat flow, b_n is the Eigenvalue coefficient, and *a* is the thickness of the lithosphere.

In order to calculate rifting heat flow in BasinMod, beta is required. Values for beta are obtained by either accepting a default value of two or entering a specific value (BasinMod 1-D manual, 2005). In this study, β, calculated from basin volume changes, is inputed into the rifting events table in BasinMod 1-D (Figure 6.5.3). BasinMod 1-D uses these betas along with the present-day heat flow to calculate the paleoheat flow (Figures 6.5.4 and 6.5.5).

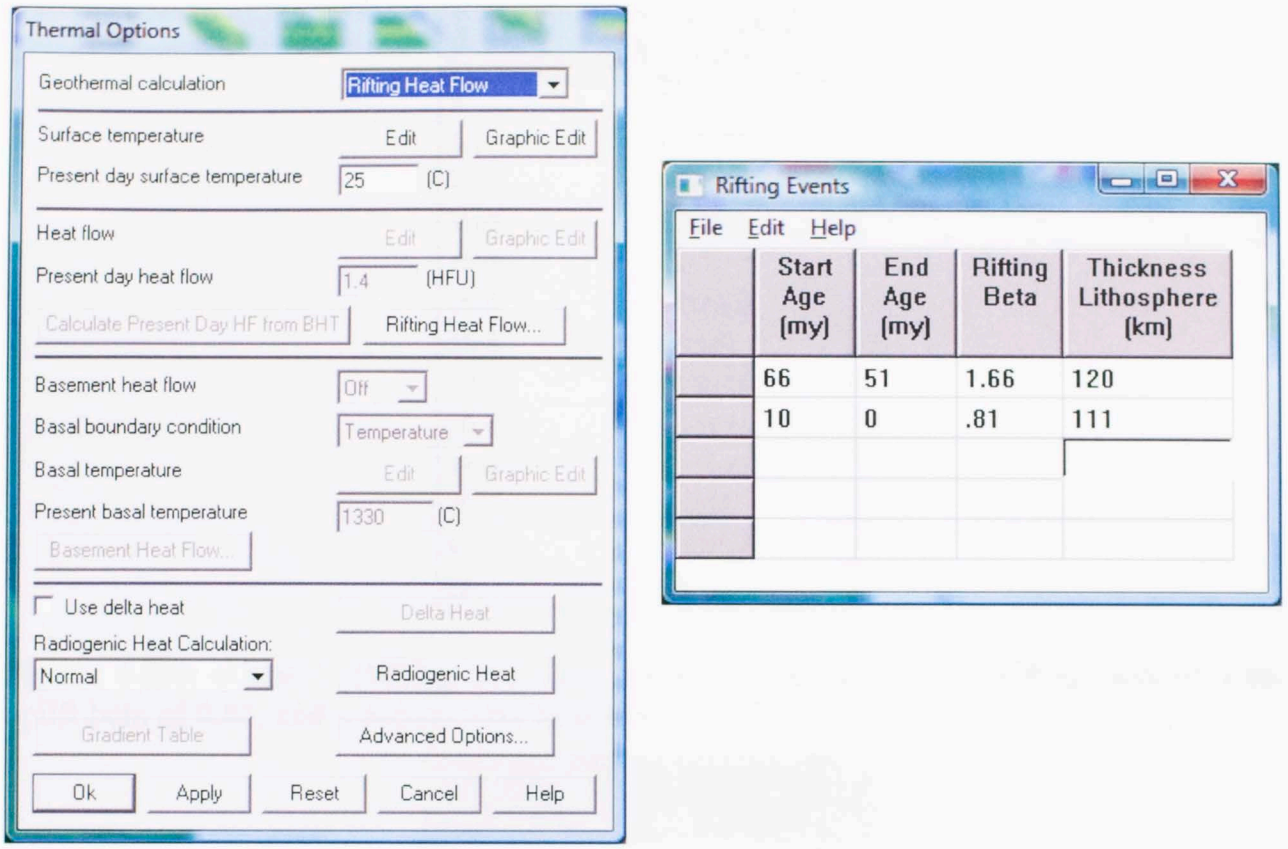

Figure 6.5.3: Thermal rifting parameters and rifting events used in BasinMod 1-D. Betas are used in the rifting events to calculate the various heat flow values during rifting.

The north coast of Jamaica has two modern published heat flow values that, in this study, will be used as end members for the present-day heat flow in the Wagwater Trough: 0.96 H.F.U., calculated by O'Neal (1984) in PetroJamaica's operated Windsor 1 by St. Ann's (Case 1) and 1.4 H.F.U. published as a more regional value by Perry (1984). Inputting these two cases of heat flow into BasinMod 1-D gives the paleoheat flow values in figures 6.5.4 and 6.5.5. For both cases, however, the initial heat flow is set to 1.5 H.F.U. which is the worldwide average (Pigott, lecture notes).

Age (my)	Heat Flow (HFU)
0	0.96
5.1	1.07099
10	1.23551
10.2	1.23672
15.3	1.26812
20.4	1.29985
25.5	1.3306
30.6	1.35819
35.7	1.37932
40.8	1.39045
45.9	1.3925
51	1.38153
66	1.5

Figure 6.5.4: (Case 1) Rifting heat flow values calculated from a rifting beta of 1.66, uplift beta of 0.81, and a present-day heat flow of 0.96 H.F.U.

Age (my)	Heat Flow (HFU)
0	1.4
5.1	1.56185
10	1.80178
10.2	1.80355
15.3	1.84934
20.4	1.89561
25.5	1.94046
30.6	1.9807
35.7	2.01151
40.8	2.02773
45.9	2.03074
51	2.01473
66	1.5

Figure 6.5.5: (Case 2) Rifting heat flow values calculated from a rifting beta of 1.66, uplift beta of 0.81, and a present-day heat flow of 1.4 H.F.U.

6.6 Two-Dimensional (2-D) Basin Modeling Principles

BasinMod 2-D allows users to take data from wells in BasinMod 1-D and connect the horizons creating two-dimensional cross-sections. These cross-sections model various values such as porosity, permeability, temperature, maturity, and expelled hydrocarbons for various formations for various model ages (Figure 5.1.2 through 5.1.6). BasinMod 2-D requires depth and age horizons for data imput. This data is obtained from the basement corrected cross-sections obtained using a Bouguer correction map. It is essential to have lithologic, surface temperature, heat flow, kerogen type, and TOC data in 2-D modeling (Figure 6.6.1).

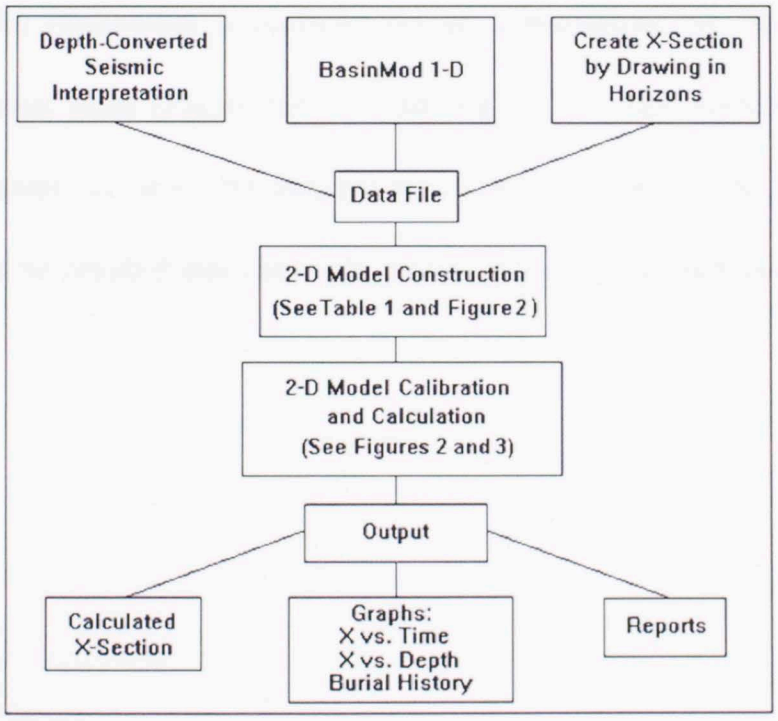

Figure 6.6.1: BasinMod 2-D working flow chart. Overview of 2-D BasinMod procedures (from BasinMod 2-D Manual, 2005).

In order for BasinMod 2-D to perform a proper basin analysis, a framework of horizons, unconformities, and faults must first be created (Figure 6.6.2). First, wells are inserted from BasinMod 1-D. Then horizons, unconformities, and faults are drawn

between the wells. Horizons generally represent the contacts between formations. Finally, horizons are attached to faults, unconformities, and other horizons when pinch-outs occur. A single period of time can be assigned to the whole line, or the time can be adjusted. In the models created in this study, most of the horizons represented the same period of time with the exception of when formations would pinch out. In order for a formation to pinch out in BasinMod 2-D, two horizons must connect in both space and time. When two horizons connect a green circle appears in BasinMod to signify the connection. The same circle appears when horizons attach to faults (purple) and unconformities (red).

After all the framework is properly set up, calculations can be run to determine the different geologic units (Figure 6.6.3). Lithologies, kerogen types, and TOCs can be added to all the units. In order for BasinMod to calculate the model for the basin, the cross-section must be divided into data cells based on horizontal distance and time.

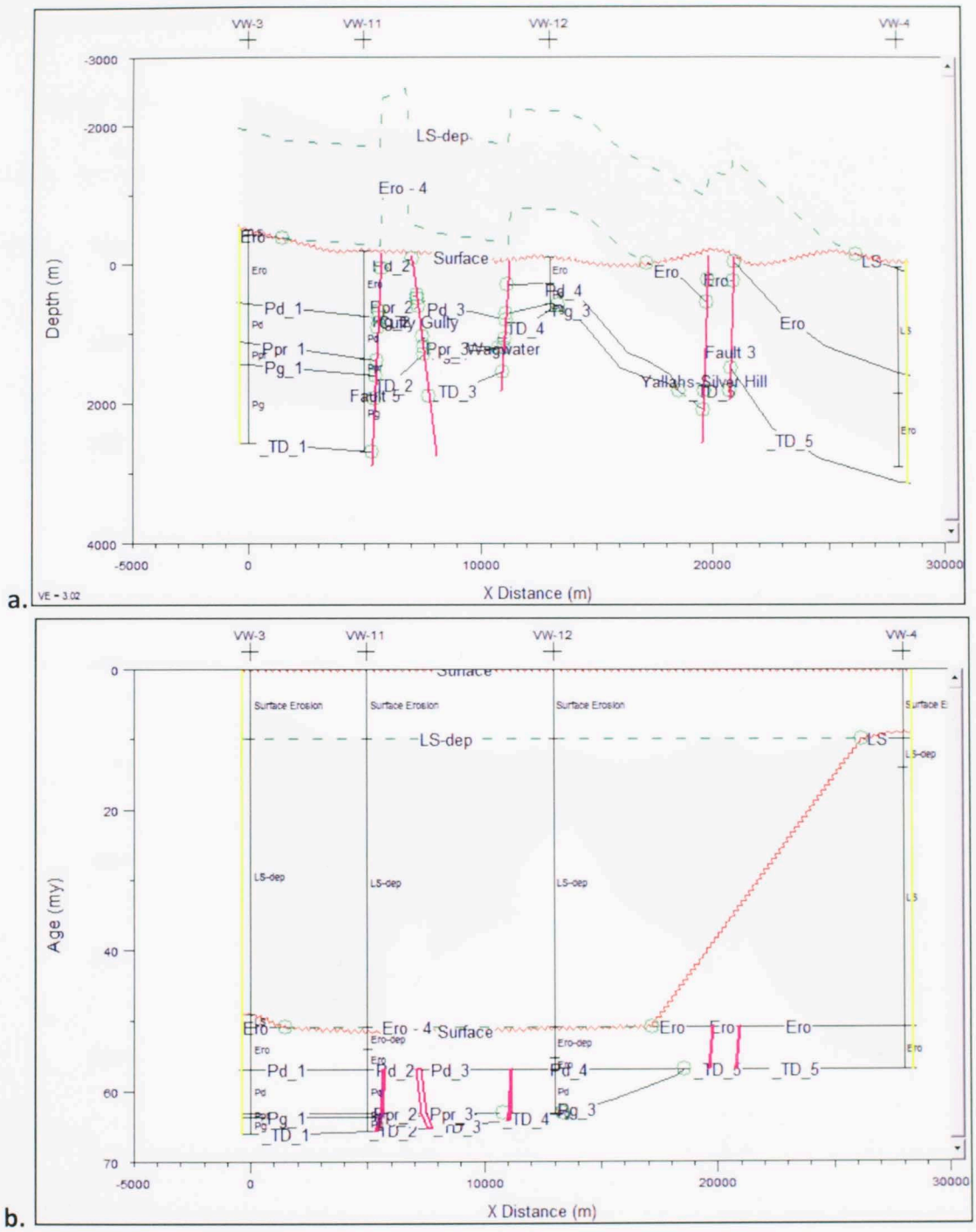

Figure 6.6.2: Preparation of 2-D model in BasinMod shown for E-W 2. First, wells are inserted from BasinMod 1-D. Then horizons, unconformities, and faults are drawn between the wells. Finally, horizons are attached to faults, unconformities, and other horizons when pinch-outs occur. These attachments are represented by a green circle. Dashed lines represent deposits that have been eroded. Figure 6.6.2a represents the cross-section with respect to depth while figure 6.6.2b with respect to time.

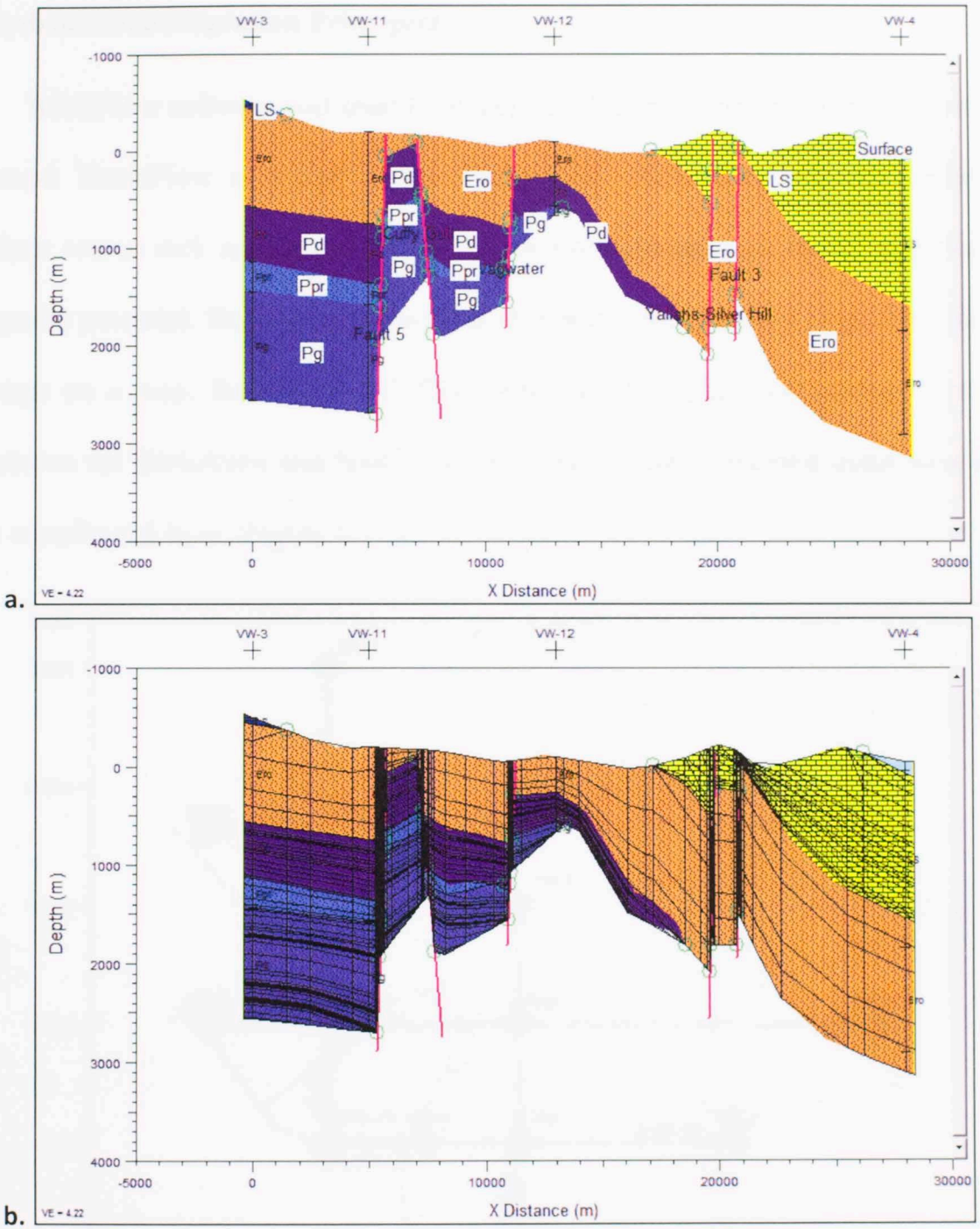

Figure 6.6.3: Preparation of 2-D model in BasinMod shown for E-W 2 continued from figure 6.6.2. After all the horizons, unconformities, and faults are attached to each other, and the appropriate ages are assigned to each, events can be calculated (Figure 6.6.3a). These events are assigned lithology types, TOC values, and kerogen types. After this is complete, data cells used in calculating the model in BasinMod 2-D are assigned to the model (Figure 6.6.3b).

6.7 Hydrocarbon Migration Principles

BasinFlow software was used to model possible hydrocarbon migration pathways and traps. BasinFlow is a part of the Platte River Associates software package. It combines source rock and carrier bed data with hydrodynamics to model migration and entrapment potential. BasinView software is used to see the modeled migration pathways and traps on a map. BasinMod 1-D files were used to build flow models, first wells uploaded to the BasinView and fault locations gathered from structural maps were drawn to the coordinated layer (Figure 6.7.1).

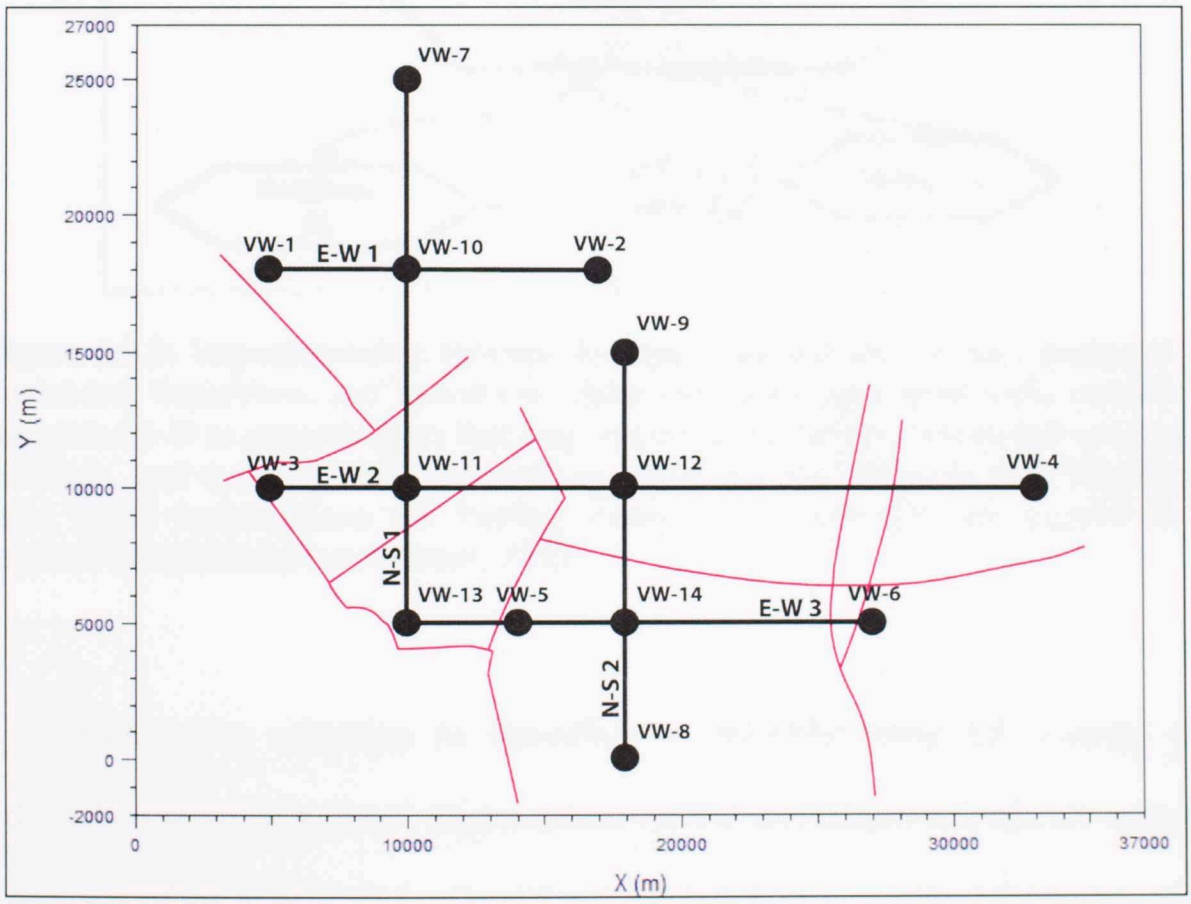

Figure 6.7.1: Map view of faults, well locations, and 2-D lines in BasinView software. Faults are drawn in light purple, wells are marked by red crosses, and 2-D lines are drawn as black lines.

A BasinFlow file is generated in BasinView software and uploaded to the BasinFlow for hydrodynamic calculations then displayed in BasinView. Interrelationship between the input data and Platte River's software package is shown in figure 6.7.2.

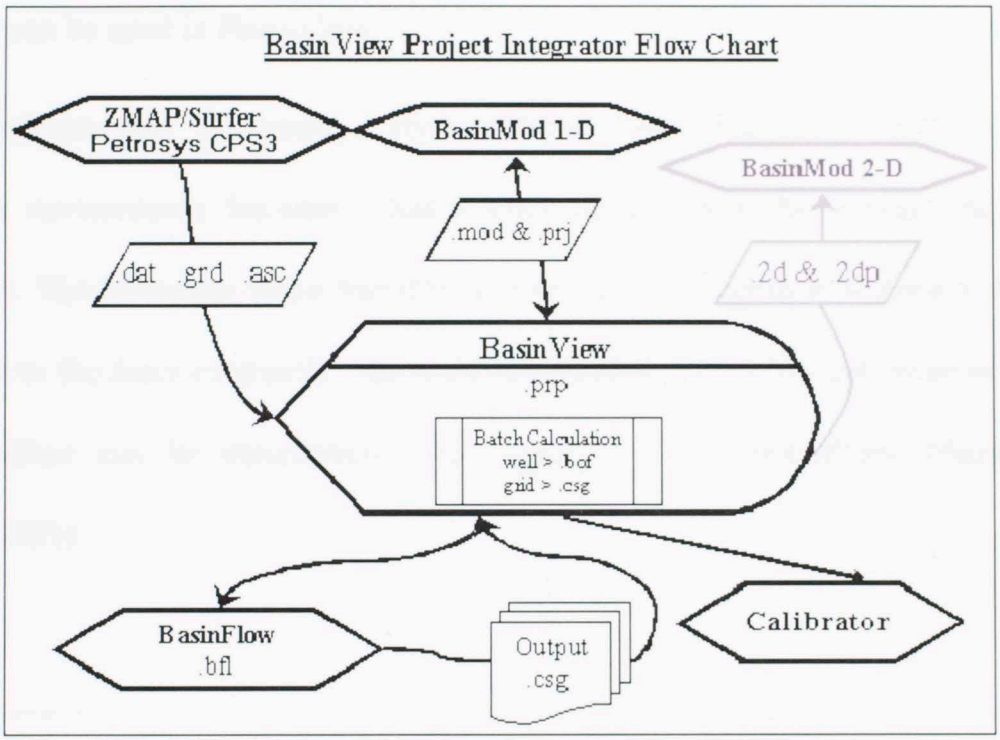

Figure 6.7.2: Interrelationship between the input data and the software packages in BasinMod, BasinView, and BasinFlow. BasinView uses input from wells created in BasinMod 1-D to generate grids that map various basin values such as unit structure, thickness, and maturity. It is also used as a base for BasinFlow to flow directions from where hydrocarbons are forming (source) to where they are trapped in a reservoir (from BasinFlow Manual, 2005).

Hydrocarbon migration in BasinFlow is modeled using the concept of a "hydrocarbon potential surface". Hydrocarbon (oil and gas) migration paths are normal to the contours of the hydrocarbon potential surface and there is potential for hydrocarbons to accumulate (trap) within closed contours around lows on the potential surface. The hydrocarbon potential in BasinFlow is calculated based on the net effect of three physical parameters that affect the migration of hydrocarbon in the subsurface: (1) the buoyancy

of hydrocarbons, (2) the flow of subsurface water or hydrodynamic drive, and (3) the effect of capillary tension at the interface between hydrocarbon and water between grains of sediment or capillary threshold pressure. Any or all of these forces for secondary migration can be used in BasinFlow.

Hydrocarbon Buoyancy. Hydrocarbons have buoyancy relative to their subsurface environment, because it has a lower density than the surrounding rock and pore water. The buoyancy force that drives hydrocarbon migration is always directed in opposition to the force of gravity. Mechanical potential energy per unit mass of a fluid in the subsurface can be determined using equation 6.7.1 (BasinFlow Manual, 2005; Hubbert, 1953).

$$\varphi = Gz + \frac{P}{\rho}$$

Equation 6.7.1: Mechanical potential energy. φ is the mechanical potential energy, G is the gravitation constant (6.67300×10^{-11} m^3 kg^{-1} s^{-2}), z is elevation (depth), P is pressure, and ρ is the fluid density.

The mechanical potential energy equation is described as "the work required to transport a unit mass of water from sea-level and atmospheric pressure to the elevation and pressure of the point considered" (Hubbert, 1953). The upward buoyancy force for oil and gas under hydrostatic conditions was given by Verweij (1993) in equation 6.7.2.

$$-G[\rho_w - \rho_o/\rho_o]$$
$$-G[\rho_w - \rho_g/\rho_g]$$

Equation 6.7.2: The upward buoyancy force for oil and gas under hydrostatic conditions. ρ_w is the density of water in the formation, ρ_o is the density of oil in the subsurface, and ρ_g is the density of gas in the subsurface (Verweij, 1993).

The method used to calculate hydrocarbon buoyancy in BasinFlow is similar to that given by Verweij (1993). The hydrocarbon buoyancy head is calculated in BasinFlow at each grid point using equation 6.7.3.

$$H_{buoy} = \left[\frac{\rho_w - \rho_{hc}}{\rho_{hc}}\right] z_{carrier}$$

Equation 6.7.3: Hydrocarbon buoyancy head. H_{buoy} is the hydrocarbon buoyancy, ρ_w is the density of water, ρ_{hc} is the density of hydrocarbons, and $z_{carrier}$ is the depth of the carrier bed.

Hydrodynamic Drive. The flow of ground water through a carrier bed will affect hydrocarbon migration and accumulation in traps. The potential energy of the groundwater flow is proportional to the hydraulic head. A potentiometric surface was defined by Dahlberg (1995) as "a calculated imaginary surface, the topography of which reflects geographic variation in the fluid potential of the formation water within a particular aquifer or subsurface reservoir" (BasinFlow Manual, 2005). Dalberg's (1995) equation is written in BasinFlow as equation 6.7.5.

$$H_w = Z_{carrier} + P_{pore}/(\rho_w G)$$

Equation 6.7.4: The hydraulic head equation. H_w is hydraulic head of water and P_{pore} is the pore pressure.

The hydrodynamic head (H_{hydro}) is calculated in BasinFlow using equation 6.7.5.

$$H_{hydro} = H_w(\frac{\rho_w}{\rho_{hc}})$$

Equation 6.7.5: The hydrodynamic head equation. H_{hydro} is hydrodynamic head, H_w is the hydraulic head, ρ_w is the density of water, and ρ_w is the density of hydrocarbons.

Capillary Threshold Pressure. Capillary threshold pressure results from hydrocarbon-water interfacial surface tension. It is expressed as a pressure difference across the interface. Variations in capillary threshold pressure result in a driving force for oil and gas. Capillary pressure is calculated in BasinFlow according to the Willis (1983) equation 6.7.6. Capillary pressure is represented in this equation as a function of the pore-throat radius.

$$P_{cap} = 2\gamma_{hc-w}/r_t$$

Equation 6.7.6. The capillary threshold pressure equation. P_{cap} is the the capillary pressure, γ_{hc-w} is the interfacial surface tension between hydrocarbon and subsurface pore water, and r_t is the pore-throat radius.

7. BASIN ANALYSIS AND MODEL

7.1 Introduction

As mentioned previously, for the petroleum system analysis, source rocks, carrier beds, reservoir rocks, and seals are essential elements, while trap formation, migration pathways, hydrocarbon accumulation, and hydrocarbon preservation are essential processes.

The Richmond Roadside Member is chosen as the main potential for both source rock and reservoir. It formed in an anoxic depositional environment with restricted water circulation. The shale layers have the best source rock potential with type II kerogen, and a TOC average of 6 %. While its reservoir potential is not excellent, the sand layers in the Roadside Member do provide adequate potential for migration and storage of hydrocarbons.

Five cross-sections (E-W 1, E-W 2, E-W 3, N-S 1, and N-S 2) previously mentioned were used in BasinMod 2-D to perform multiple 2-D basin analyses (Figures 5.1.2 through 5.1.6). However, before data was loaded into BasinMod 2-D, 1-D basin analyses were performed on fourteen virtual wells in BasinMod 1-D (Table 7.1.1).

Virtual Well Name	Approx. Latitude	Approx. Longitude	Location in Cross-sections	Approx. Elevation (m above SL)
VW-1	18.312	-76.950	West End of E-W 1	425
VW-2	18.312	-76.802	East End of E-W 1	-25
VW-3	18.250	-76.950	West End of E-W 2	500
VW-4	18.250	-76.664	East End of E-W 2	-50
VW-5	18.185	-76.839	West End of E-W 3	300
VW-6	18.185	-76.715	East End of E-W 3	600
VW-7	18.378	-76.872	North End of N-S 1	-50
VW-8	18.134	-76.784	South End of N-S 2	500
VW-9	18.281	-76.784	North End of N-S 2	-50
VW-10	18.312	-76.872	Intersection of E-W 1 and N-S 1	100
VW-11	18.225	-76.872	Intersection of E-W 2 and N-S 1	200
VW-12	18.250	-76.784	Intersection of E-W 2 and N-S 2	100
VW-13	18.185	-76.872	Intersection of E-W 3 and N-S 1	300
VW-14	18.185	-76.784	Intersection of E-W 3 and N-S 2	500

Table 7.1.1: The names and locations of 14 virtual wells in the Wagwater Trough. Refer to figure 7.1.1 for locations of the virtual wells.

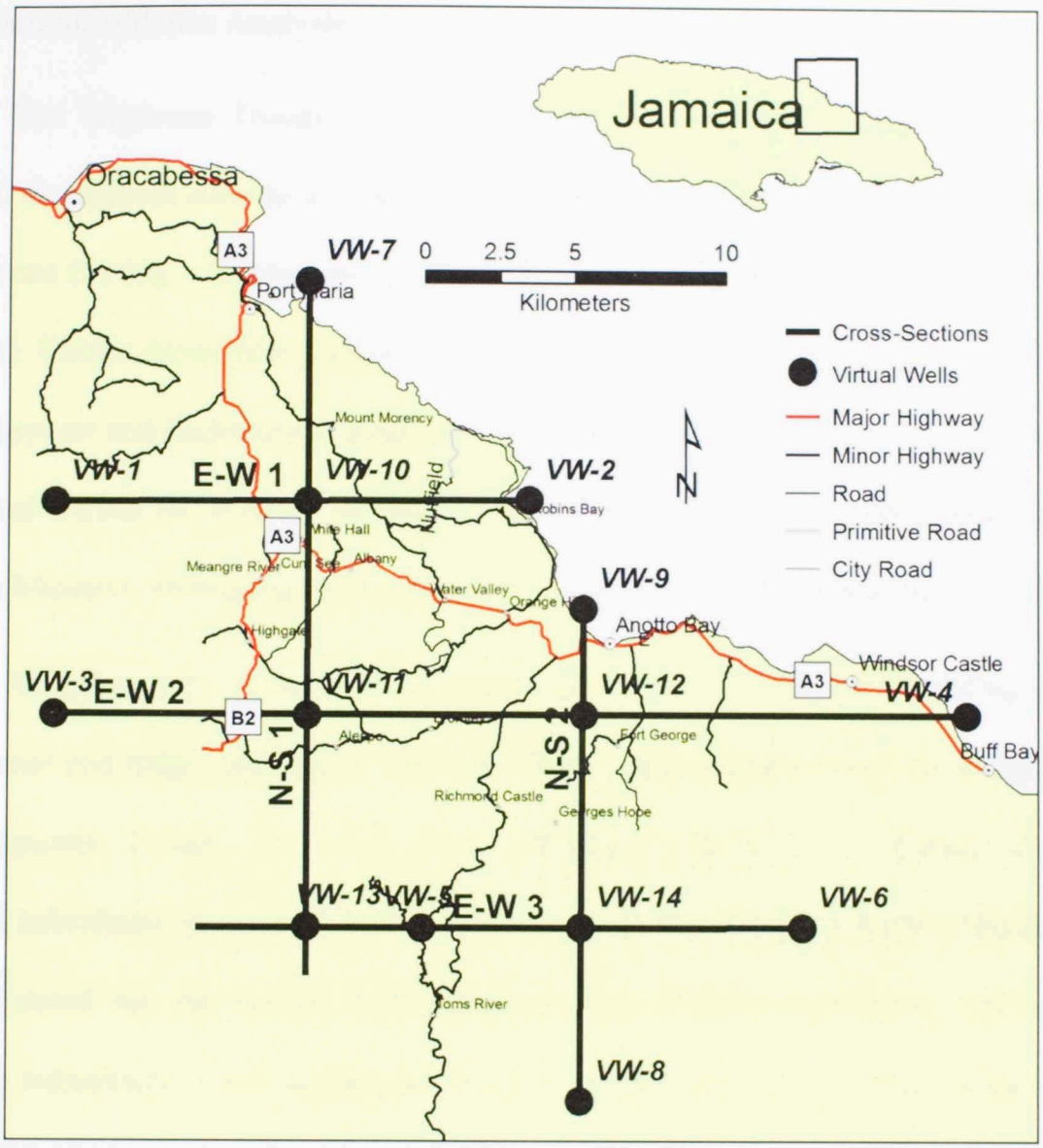

Figure 7.1.1: Base map showing the location of the fourteen virtual wells and five cross-sections.

7.2 Basin Subsidence Analysis

The Wagwater Trough exhibits a three-phase subsidence history: an early phase of fault mechanical subsidence (66 Ma – 51 Ma), a second phase of widespread thermal subsidence (51 Ma – 10 Ma), and a period of negative subsidence or shortening (10 Ma – Present). Clastic deposition is associated with the fault mechanical period which includes the Wagwater and Richmond Formations. The Yellow and White Limestone Groups were deposited during the thermal subsidence period. Due to negative subsidence since the Middle Miocene, shortening and uplift has exposed much of the sediments to erosion.

Modeling tectonic subsidence in BasinMod 1-D yields an understanding of basin subsidence and helps calculate β. There are three major stages of tectonic subsidence in the Wagwater Trough: 66-51 Ma fault mechanical subsidence or rifting, 51-10 Ma thermal subsidence or drifting, and 10-0 Ma negative subsidence or uplift. Beta can only be calculated for the periods of fault mechanical tectonic subsidence and negative tectonic subsidence. Because thermal tectonic subsidence covers a long period of time with relatively low rates of tectonic subsidence, a calculated β would be inaccurate. β was calculated using the three methods previously mentioned (1-D, 2-D, and 3-D) for the periods of fault mechanical tectonic subsidence from 66-51 Ma and negative subsidence from 10-0 Ma.

Table 7.2.1 shows calculated betas from modeled tectonic subsidence (1-D) for each virtual well. β is generally greater in wells closer to the southwest along the basin bounding faults where subsidence is greater. Betas calculated using the 1-D method average 1.53 for the period of fault mechanical tectonic subsidence and 0.66 for the period of negative subsidence.

Well #	Beta 66-51 Ma (Fault Mechanical Tectonic Subsidence)	Beta 10-0 Ma (Negative Subsidence)
VW-1	1.31	0.80
VW-2	1.24	0.77
VW-3	1.55	0.70
VW-4	1.19	0.96
VW-5	2.34	0.24
VW-6	1.14	0.91
VW-7	1.37	0.74
VW-8	1.93	0.41
VW-9	1.21	0.81
VW-10	1.30	0.74
VW-11	1.77	0.54
VW-12	1.29	0.69
VW-13	2.32	0.29
VW-14	1.46	0.58
Average:	**1.53**	**0.66**

Table 7.2.1: Betas calculated using tectonic subsidence in each virtual well (1-D). The average β for the period of fault-mechanical subsidence (66-57 Ma) is 1.53. This means that the basin deformed to be one and one half times longer than initially. The average β for uplift (10-0 Ma) is 0.66, meaning that the basin shortened by one third.

Table 7.2.2 shows betas calculated from the change in modeled tectonic extension along faults (2-D) for each cross-section. Betas calculated using the 2-D method average 1.42 for the period of fault mechanical tectonic subsidence and 0.86 for the period of negative subsidence.

Cross-section	Beta 66-51 Ma	Beta 10-0 Ma
E-W 1	1.30	0.85
E-W 2	1.28	0.91
E-W 3	1.50	0.71
N-S 1	1.55	0.85
N-S 2	1.47	0.98
Average:	**1.42**	**0.86**

Table 7.2.2: Betas calculated using the change in cross-sectional length (2-D).

Table 7.2.3 shows betas calculated from the change in modeled basin volume (3-D) for the basin. Betas calculated using the 3-D method are 1.66 for the period of fault mechanical tectonic subsidence and 0.81 for the period of negative subsidence.

	Beta 66-51 Ma	Beta 10-0 Ma
Basinwide (3-D)	1.66	0.81

Table 7.2.3: Betas calculated using the change in basin volume (3-D).

The average betas calculated using the 1-D and 3-D methods agree well with each other; however the betas calculated using the 2-D methods are slightly lower. This is likely due to the fact that the cross-sections are not perpendicular to the rifting axis in the basin (Figure 7.2.16). It should also be assumed that the beta calculations have implicit uncertainty owing to lack of knowledge concerning the bounding fault trajectories and to the complications of simple versus pure regional shear.

Figures 7.2.1 to 7.2.14 show the tectonic subsidence history modeled in each virtual well. All of the virtual wells exhibit three stages in their tectonic subsidence history: fault mechanical tectonic subsidence (66-51 Ma), thermal tectonic subsidence (51-10 Ma), and negative tectonic subsidence (10-0 Ma). Wells located closer to the major basin bounding faults in the southwest exhibit greater fault mechanical tectonic subsidences and negative subsidences.

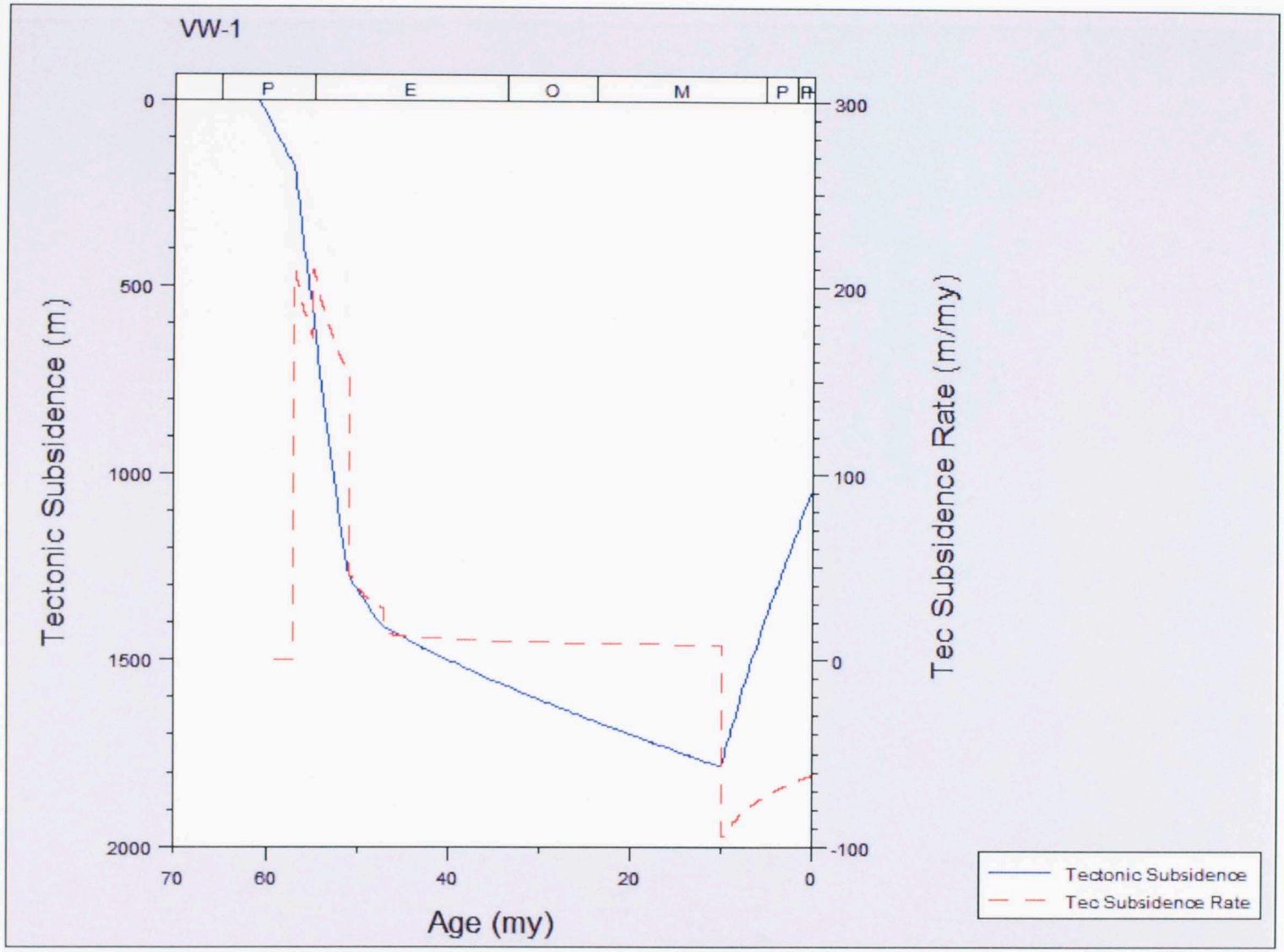

Figure 7.2.1: Tectonic subsidence of VW-1. Fault mechanical tectonic subsidence along with clastic deposition continued into the Middle Eocene before the rate of tectonic subsidence slowed and carbonate deposition dominated. By the Middle Miocene, uplift in the basin exposed much of the sediments to erosion.

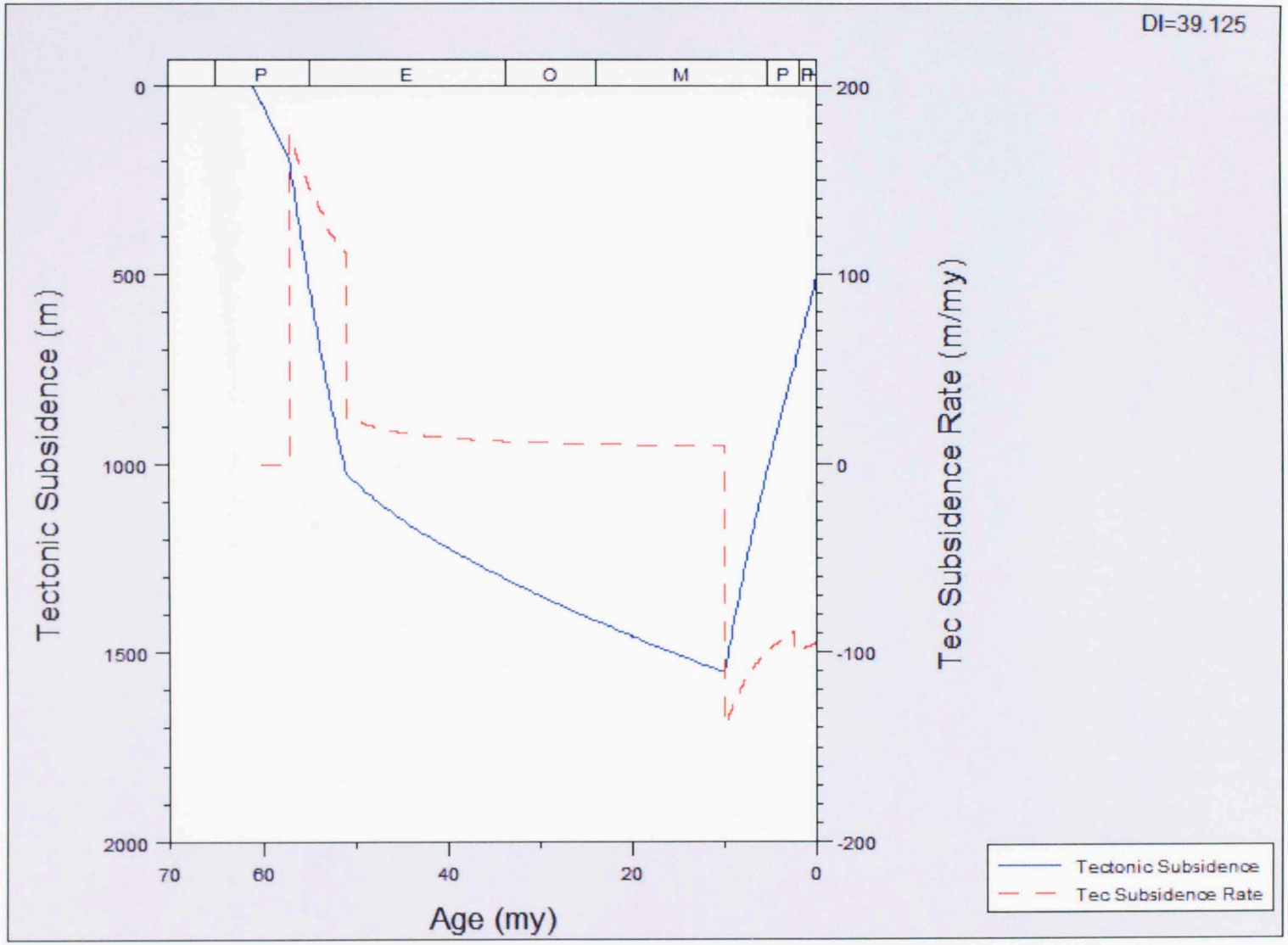

Figure 7.2.2: Tectonic subsidence of VW-2.

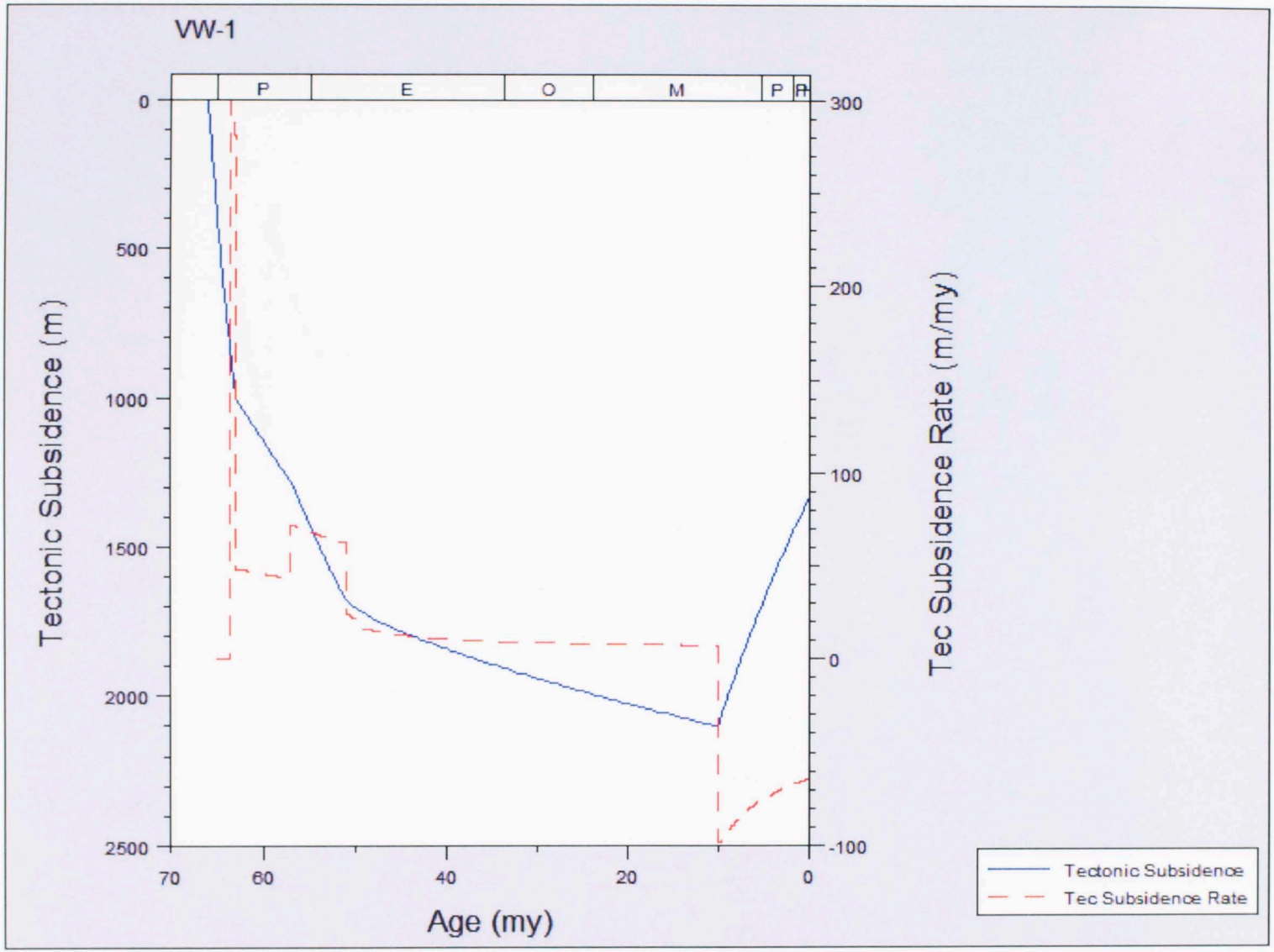

Figure 7.2.3: Tectonic subsidence of VW-3.

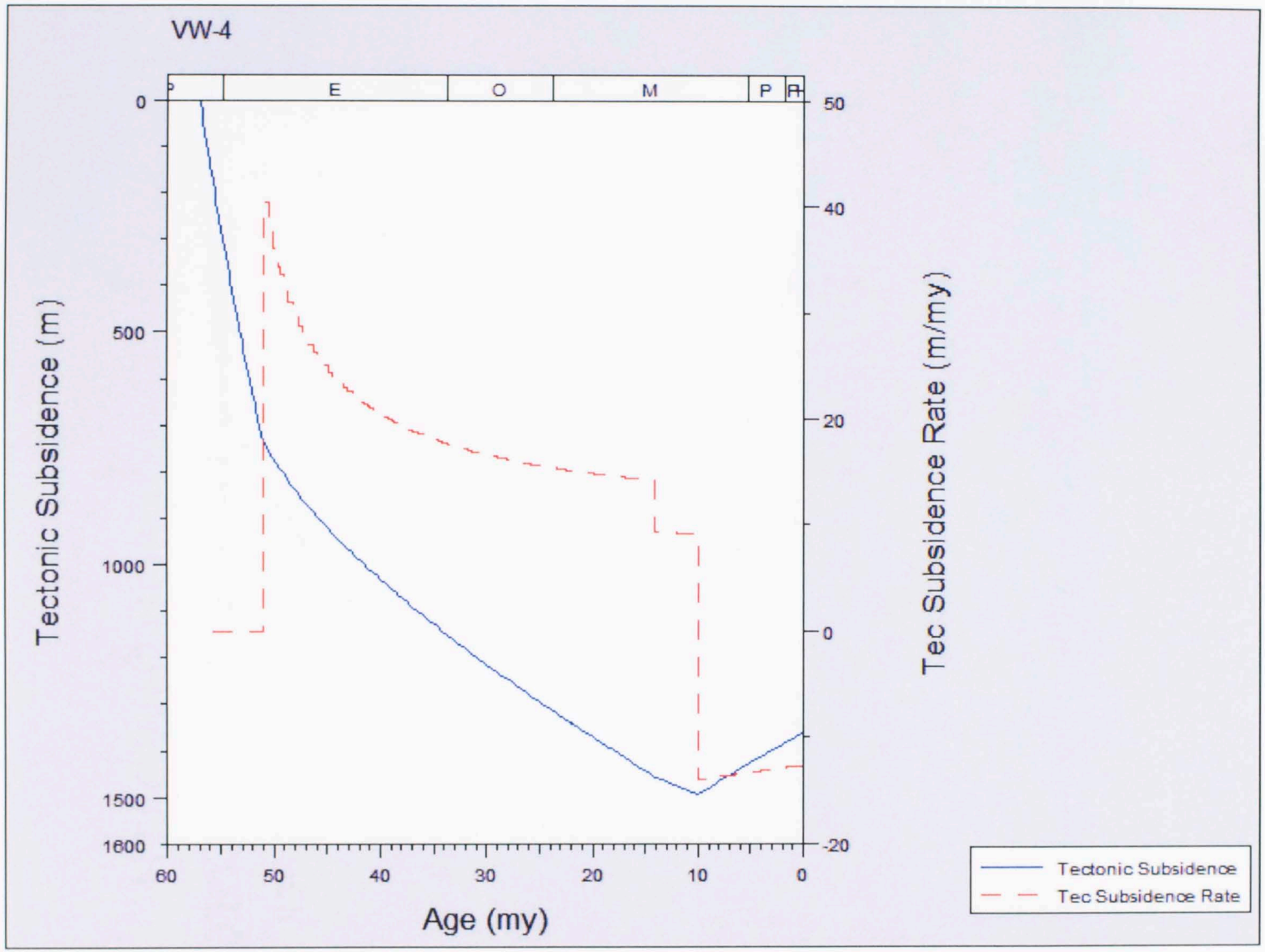

Figure 7.2.4: Tectonic subsidence of VW-4.

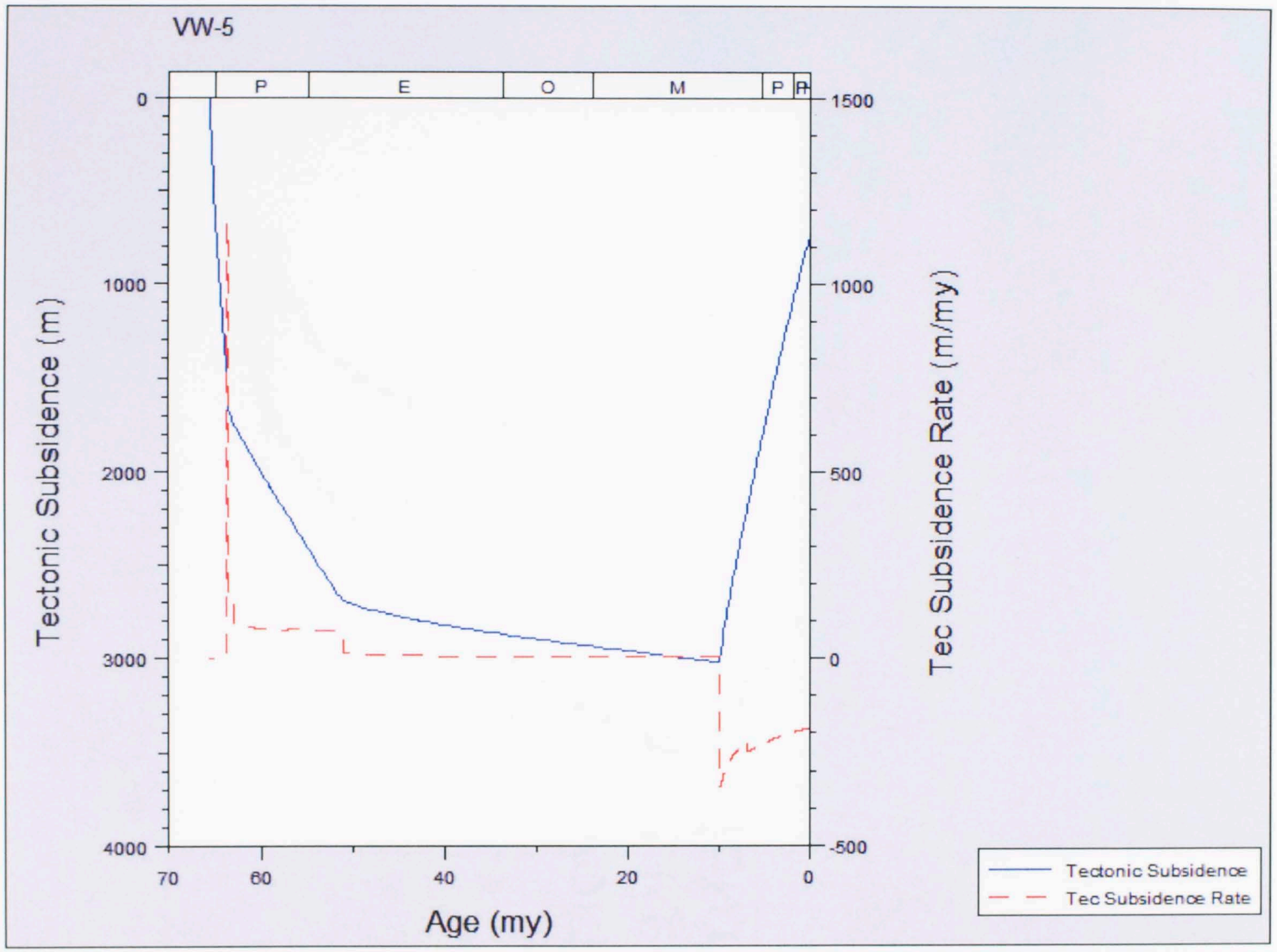

Figure 7.2.5: Tectonic subsidence of VW-5.

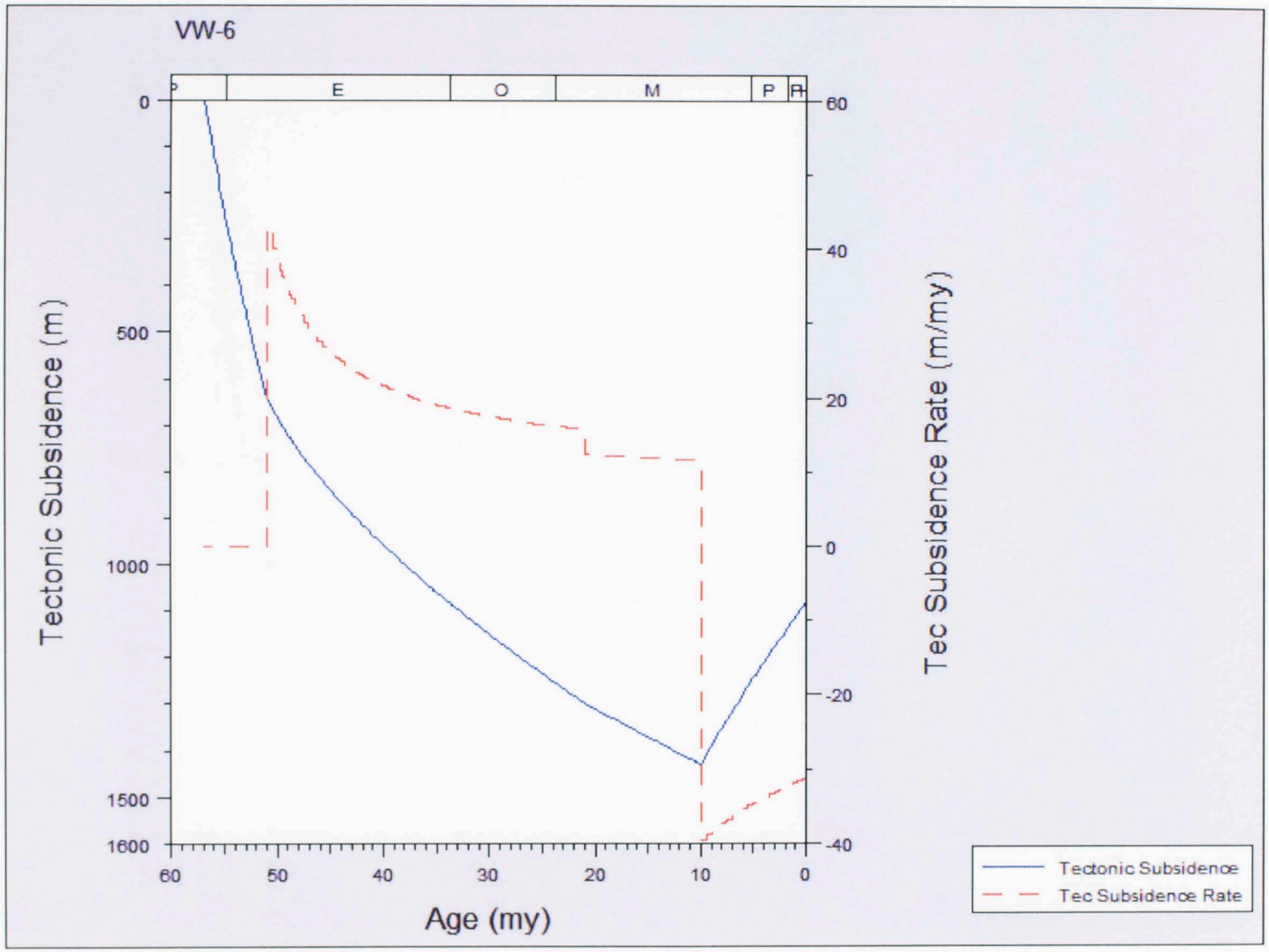

Figure 7.2.6: Tectonic subsidence of VW-6.

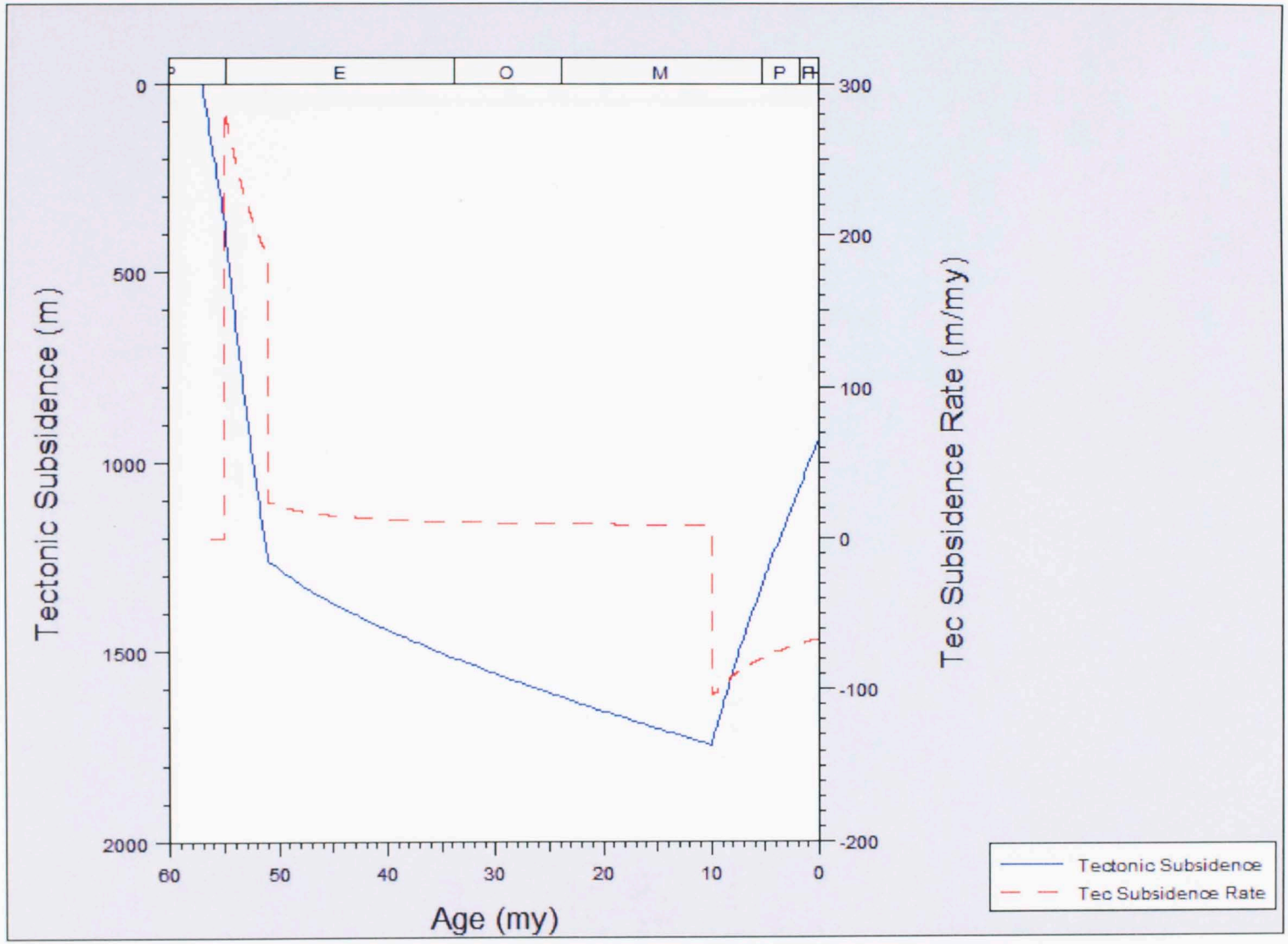

Figure 7.2.7: Tectonic subsidence of VW-7.

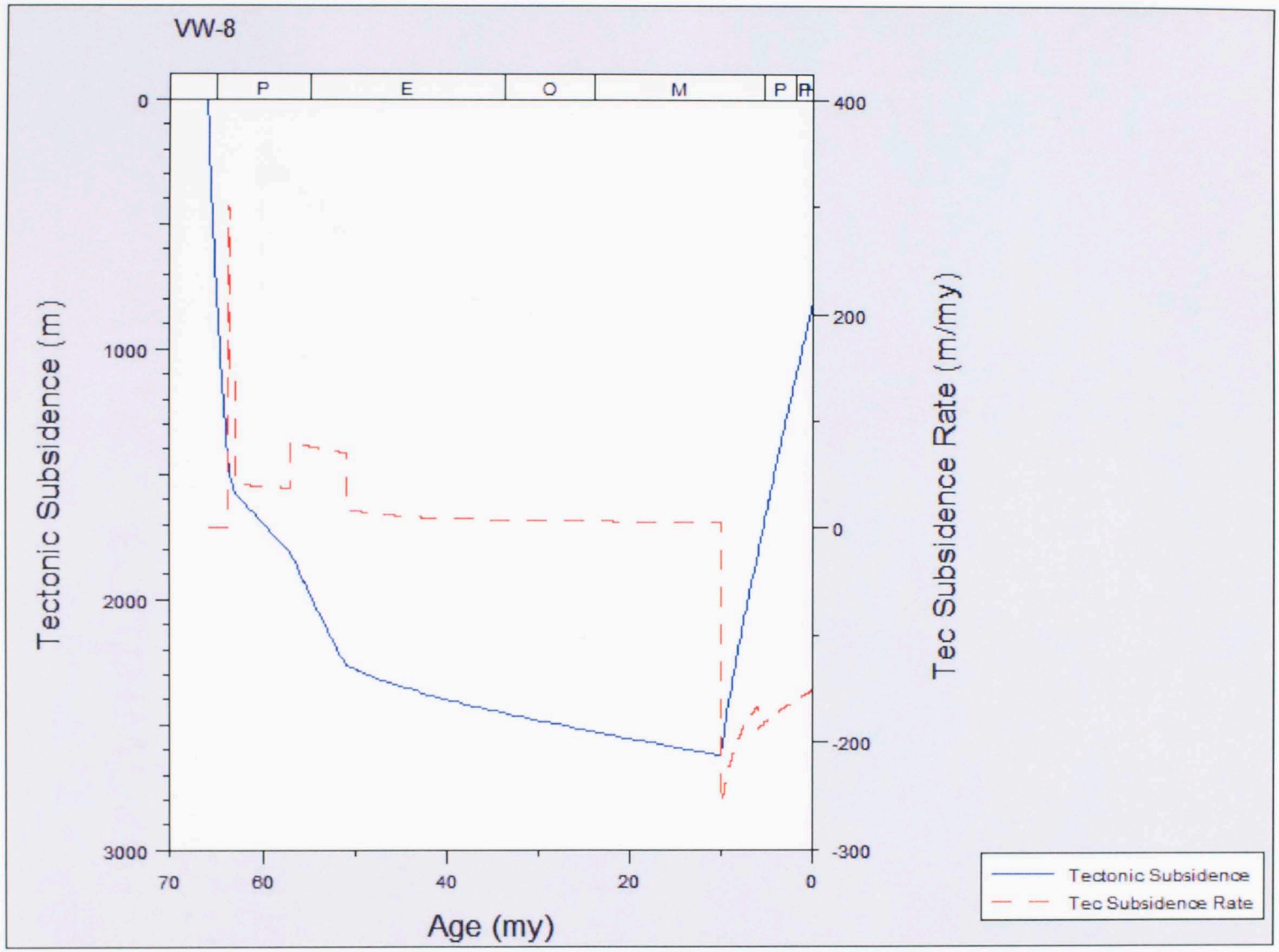

Figure 7.2.8: Tectonic subsidence of VW-8.

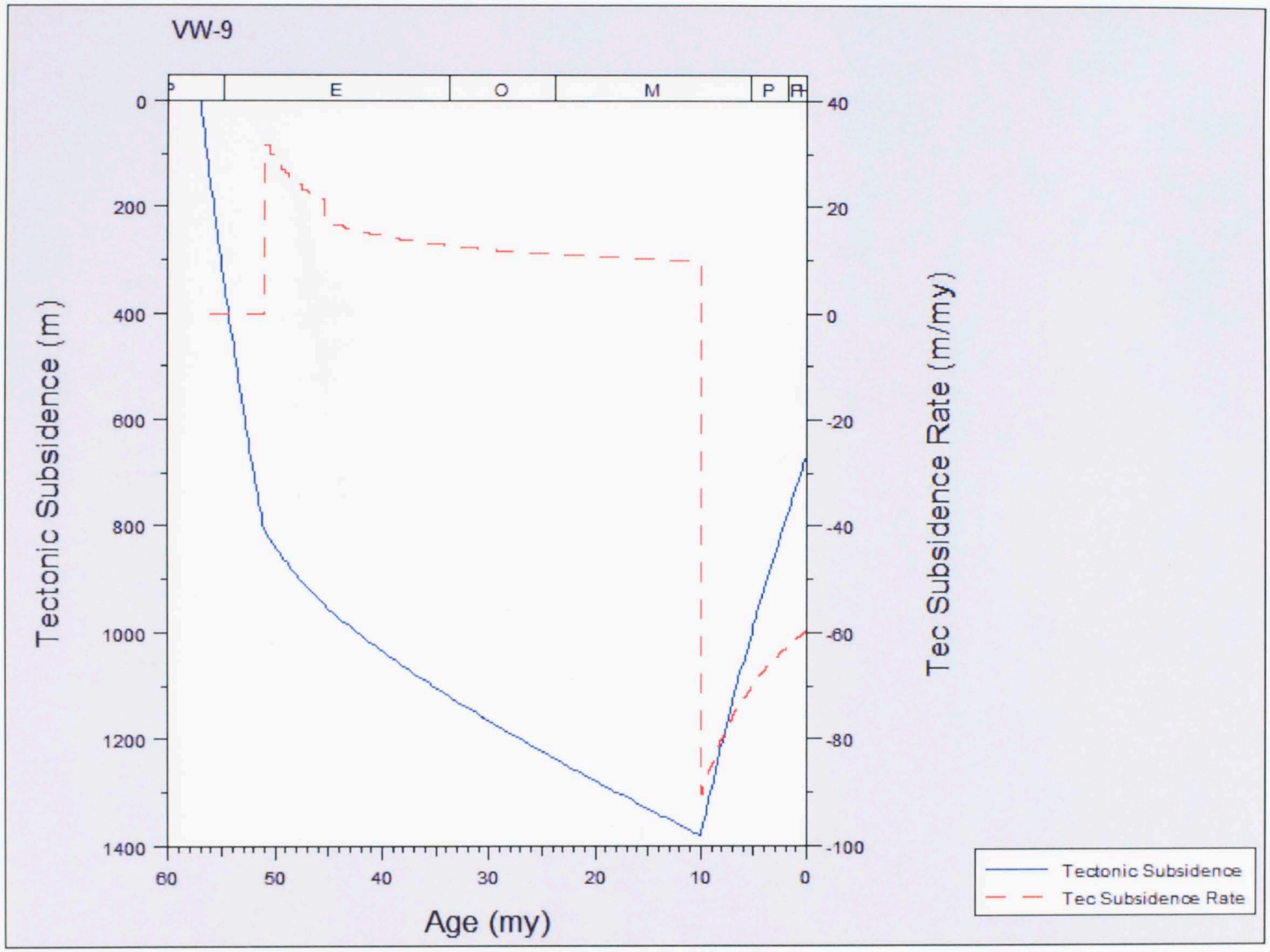

Figure 7.2.9: Tectonic subsidence of VW-9.

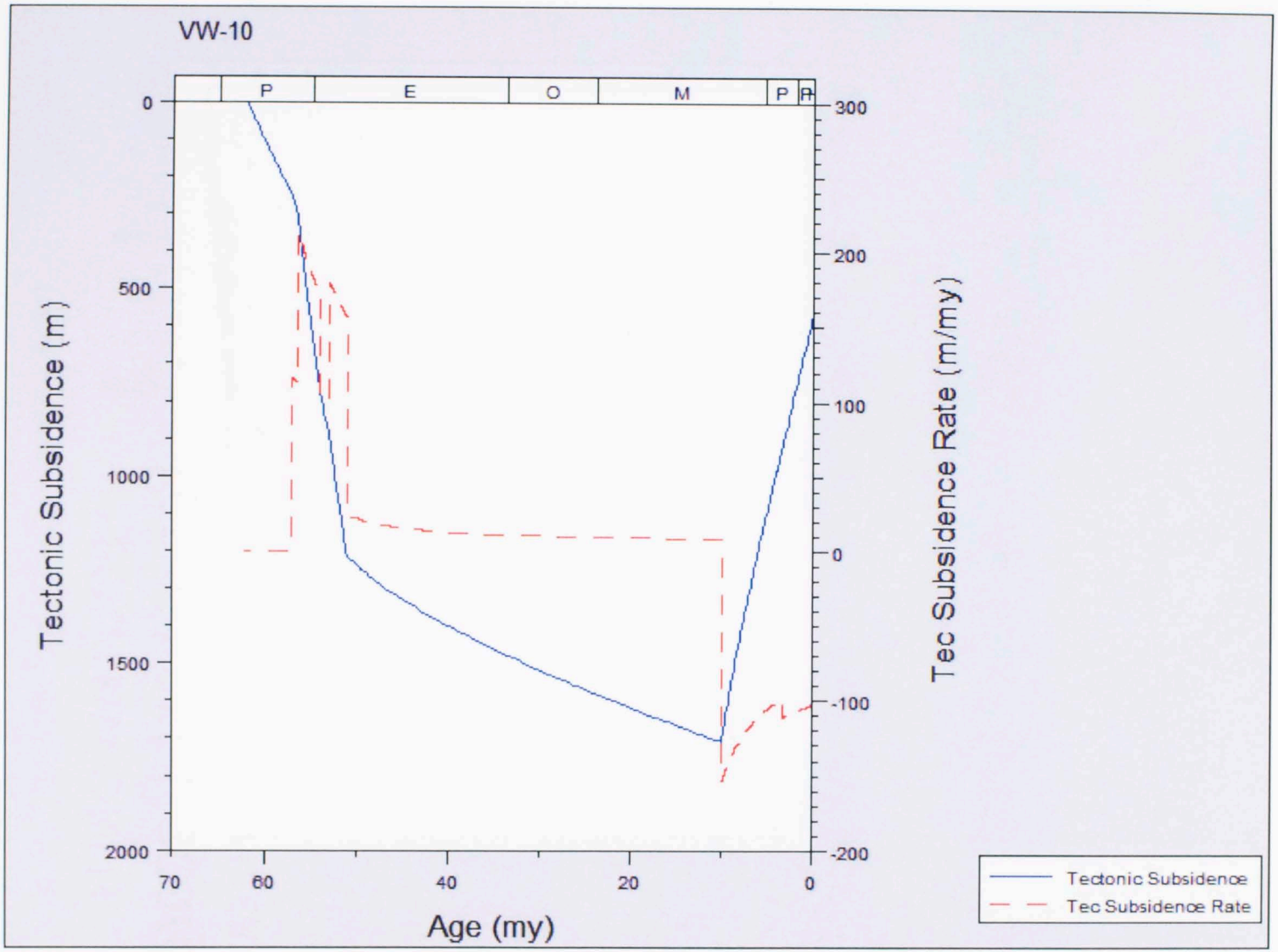

Figure 7.2.10: Tectonic subsidence of VW-10.

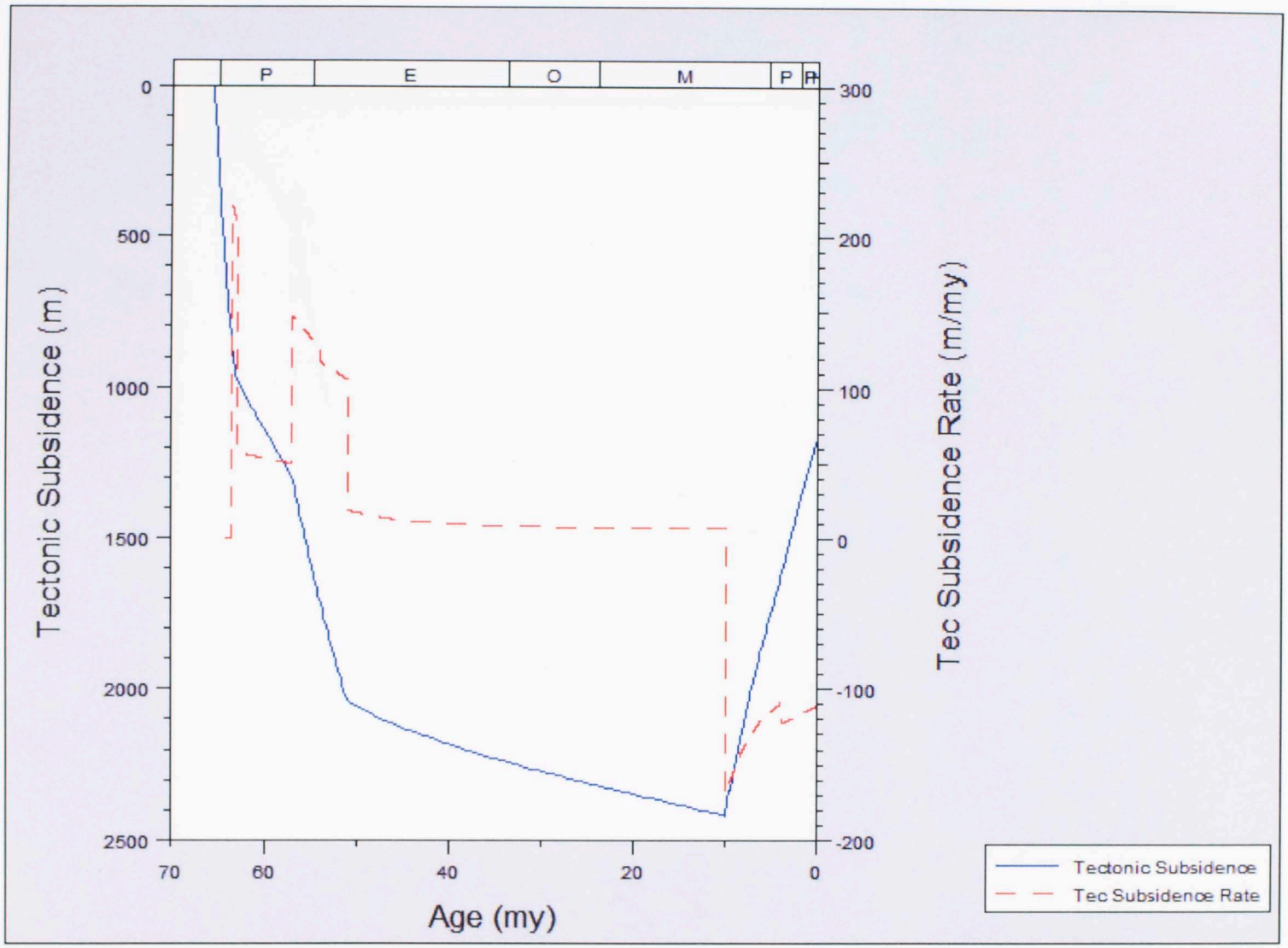

Figure 7.2.11: Tectonic subsidence of VW-11.

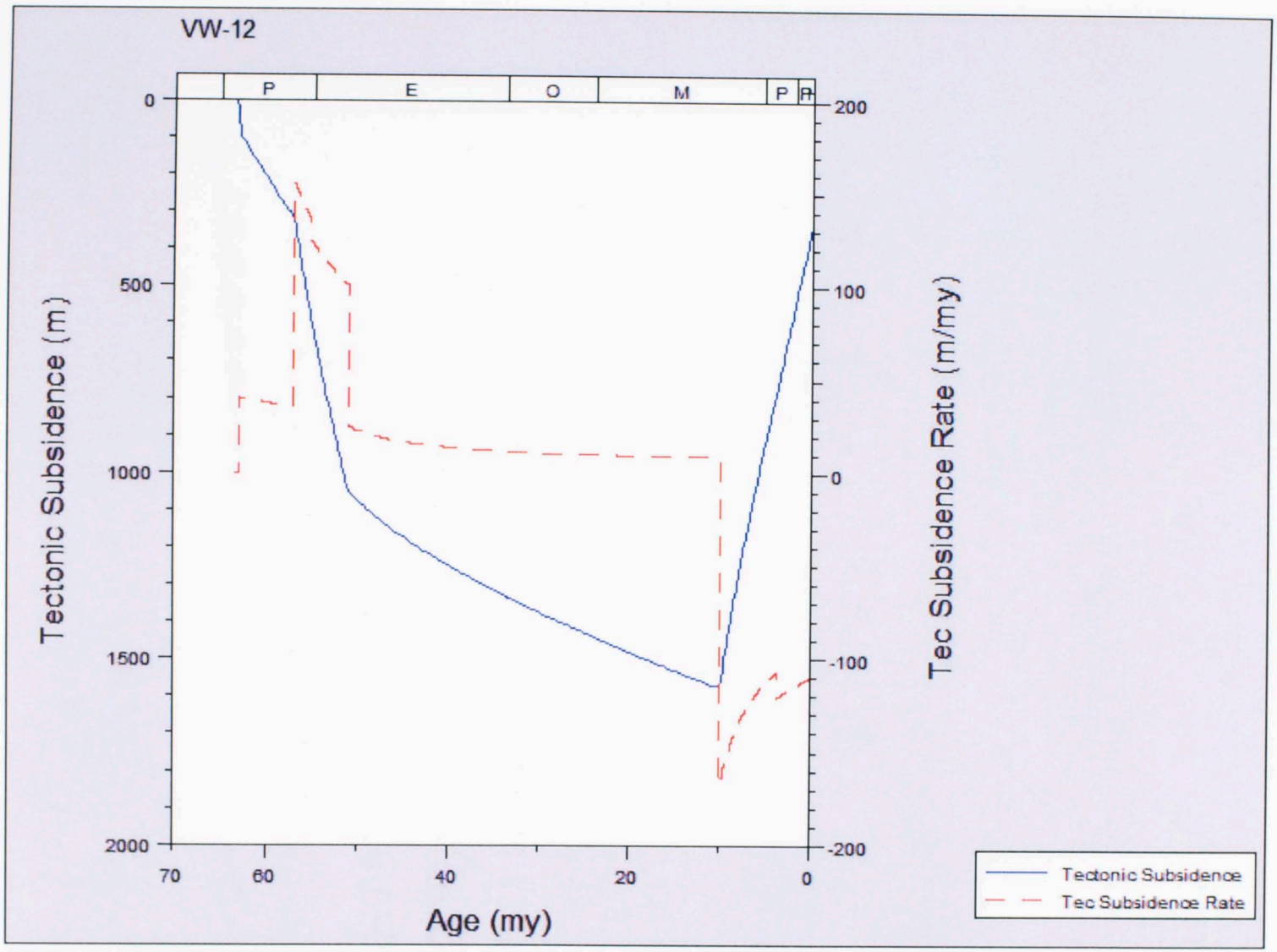

Figure 7.2.12: Tectonic subsidence of VW-12.

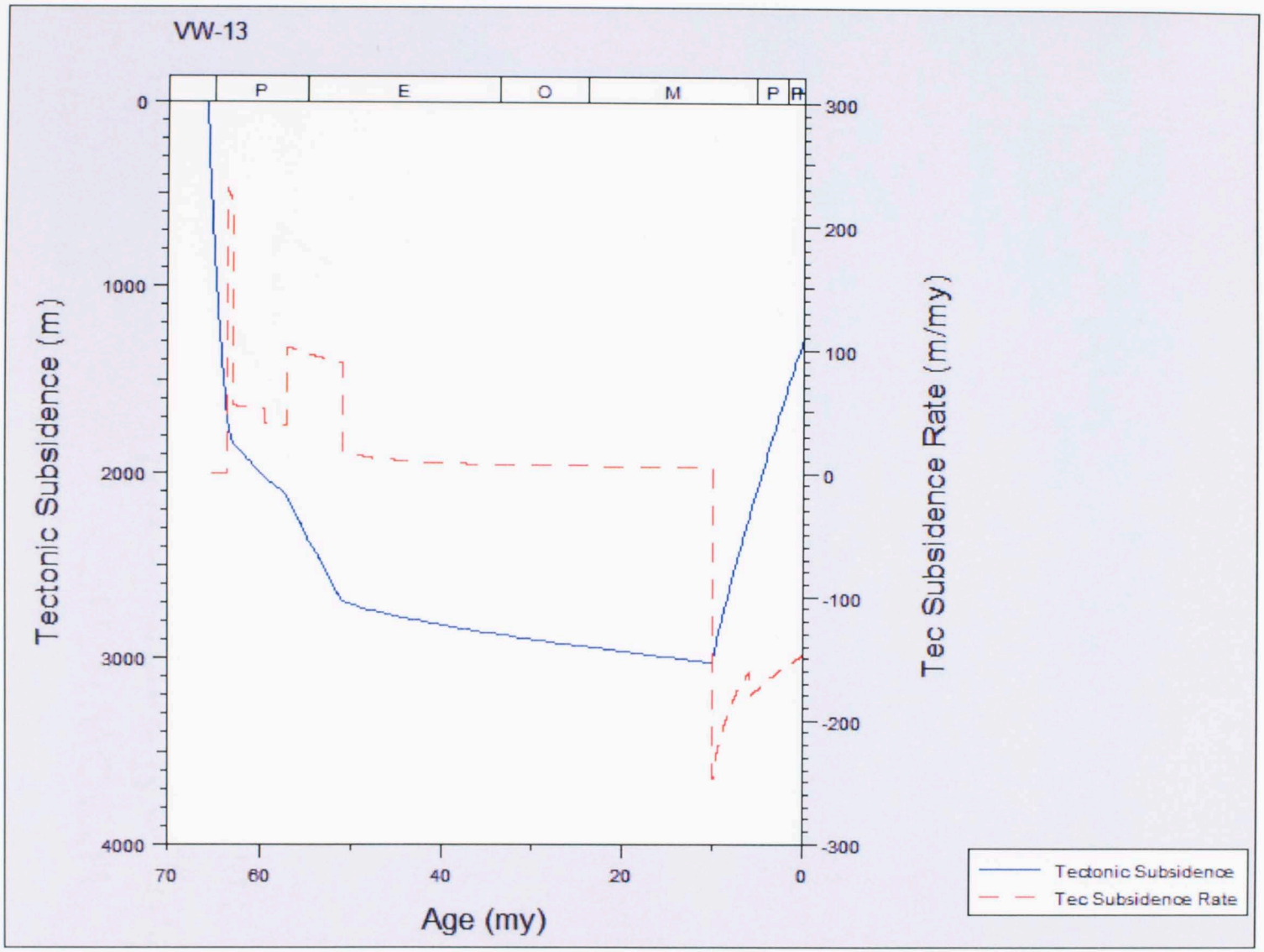

Figure 7.2.13: Tectonic subsidence of VW-13.

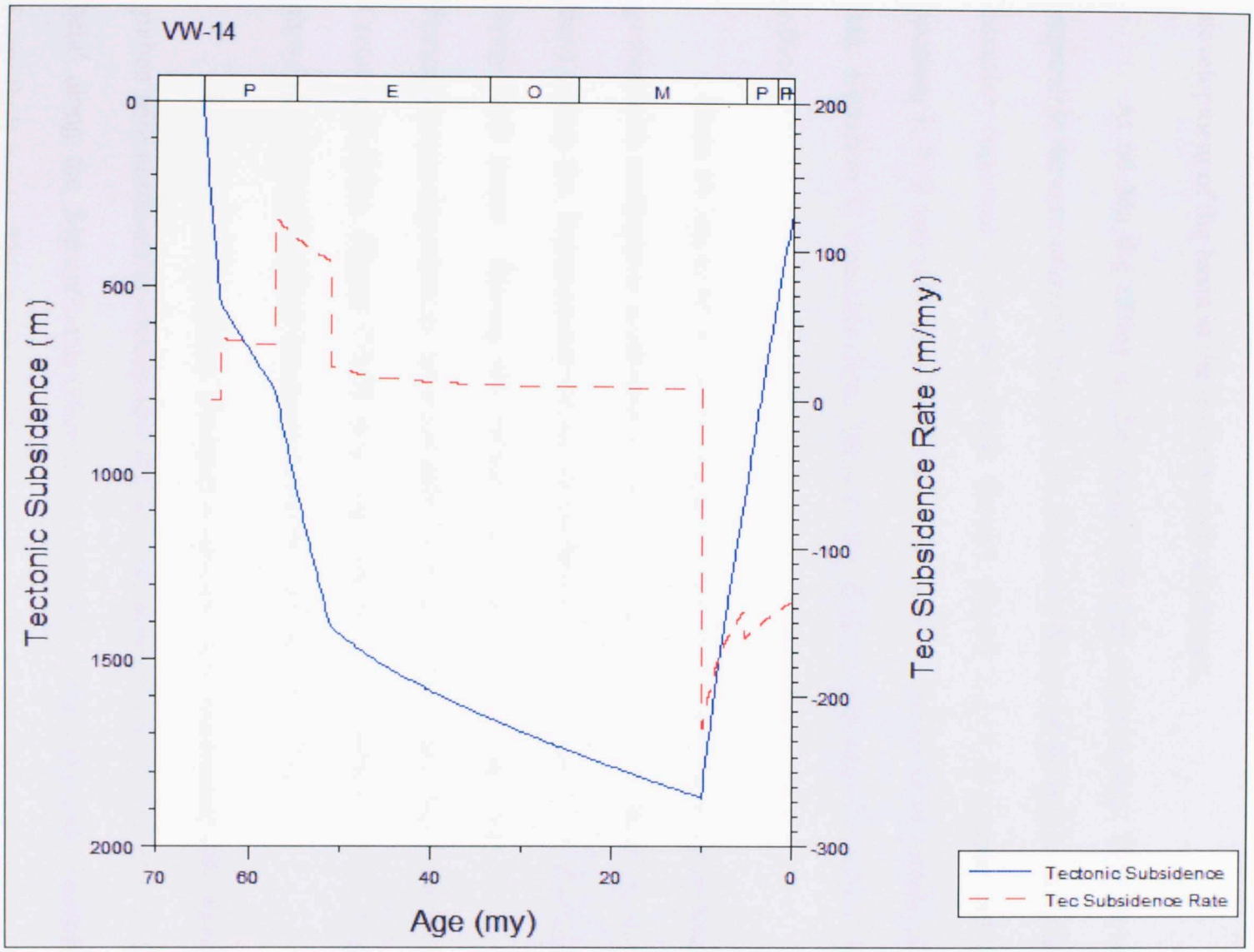

Figure 7.2.14: Tectonic subsidence of VW-14.

Figures 7.2.15 to 7.2.21 are a series of structural contour maps of elevation of the contact between the Mesozoic basement and Paleogene sediments in meters subsea with cross-sections E-W 2 and N-S 1. These maps and cross-sections demonstrate the development of the basin at the major periods of change.

At 66 Ma the rifting in the trough was just commencing. This period of time represents the unconformity between the Mesozoic Rocks of the region and Ginger River Member deposited in the Wagwater Trough. Figure 7.2.15 is a map and two cross-sections E-W 2 and N-S 1 showing structural depth to basement in meters subsea at 66 Ma. Elevation is currently zero, because the figure represents the period just before rifting.

From 66 Ma to 63.6 Ma the basin initiated fault mechanical subsidence as a half graben with northeast to southwest extension owing to simple dextral shear in a releasing bend along the Septentiornal-Orient-Swan-Motagua, Duanvale, and Plantain Garden-Sway fault zones. During this period, the Ginger River Member of the Wagwater Formation was deposited as subaerial alluvial fan conglomerates shed from the southwest Cretaceous inlier. Figure 7.2.16 is a map and two cross-sections E-W 2 and N-S 1 showing structural depth to basement in meters subsea at 63.6 Ma.

From 63.6 Ma to 63 Ma, the basin continued fault mechanical subsidence as a half graben with northeast to southwest extension owing to simple dextral shear in a releasing bend along the Septentiornal-Orient-Swan-Motagua, Duanvale, and Plantain Garden-Sway fault zones. This period marks a transgression of seawater into the basin, and the Pencar River Member of the Wagwater Formation was deposited as deltaic sandstones and conglomerates shed from the southwest Cretaceous inlier. Figure 7.2.17 is a map and

two cross-sections E-W 2 and N-S 1 showing structural depth to basement in meters subsea at 63 Ma.

From 63 Ma to 57 Ma, the basin continued fault mechanical subsidence as a half graben. However, toward the end of this period, subsidence began in the north as well. There was a brief marine transgression during the Pencar River time (63.6 – 63 Ma). This was then followed by a marine regression near the end of Pencar River time, and the Dry River Member of the Wagwater Formation was deposited as subaerial alluvial fan and fan-delta conglomerates shed from the southwest Cretaceous inlier. Figure 7.2.18 is a map and two cross-sections E-W 2 and N-S 1 showing structural depth to basement in meters subsea at 57 Ma.

From 57 Ma to 51 Ma, the basin continued fault mechanical subsidence. During this period, subsidence continued throughout the region and the Yallahs-Silver Hill Fault Zone activated as westward-dipping normal faults. A transgression of seawater during this period produced sediments in the Richmond formation as deltas, fan-deltas, marine shelf, and marine slope sandstone, shale, and conglomerate deposits. Figure 7.2.19 is a map and two cross-sections E-W 2 and N-S 1 showing structural depth to basement in meters subsea at 51 Ma.

From 51 Ma to 10 Ma, the basin ceased fault mechanical subsidence and thermal tectonic subsidence became the main drive for basin subsidence. During this period, the Yellow and White Limestone Groups were deposited as deep water shelf bank and slope deposits. Figure 7.2.20 is a map and two cross-sections E-W 2 and N-S 1 showing structural depth to basement in meters subsea at 10 Ma.

From 10 Ma to 0 Ma, the basin ceased subsidence and uplift and shortening, with a beta of 0.81, occurred along the basin faults. Erosion removed the majority of the Yellow and White Limestone Groups and exposed the members of the Richmond and Wagwater Formations at the surface. Figure 7.2.21 is a map and two cross-sections E-W 2 and N-S 1 showing structural depth to basement in meters subsea at present.

Mann and Burke (1990) presented a qualitative model of basin development and rifting history (Figure 3.2.2). They predicted that the basin developed originally as a half-graben that rifted along the Wagwater Fault Zone on the west side of the basin. Comparison between the their two dimensional qualitative model and the three dimensional quantitative model in this study shows that as initial basin subsidence occurred, a half-graben developed along faults to the southwest and filled with alluvial deposits. As rifting continued into the Early Eocene, basin-wide subsidence and marine transgressions allowed deposition of sediments over a larger area and transportation farther away from the original Mesozoic source.

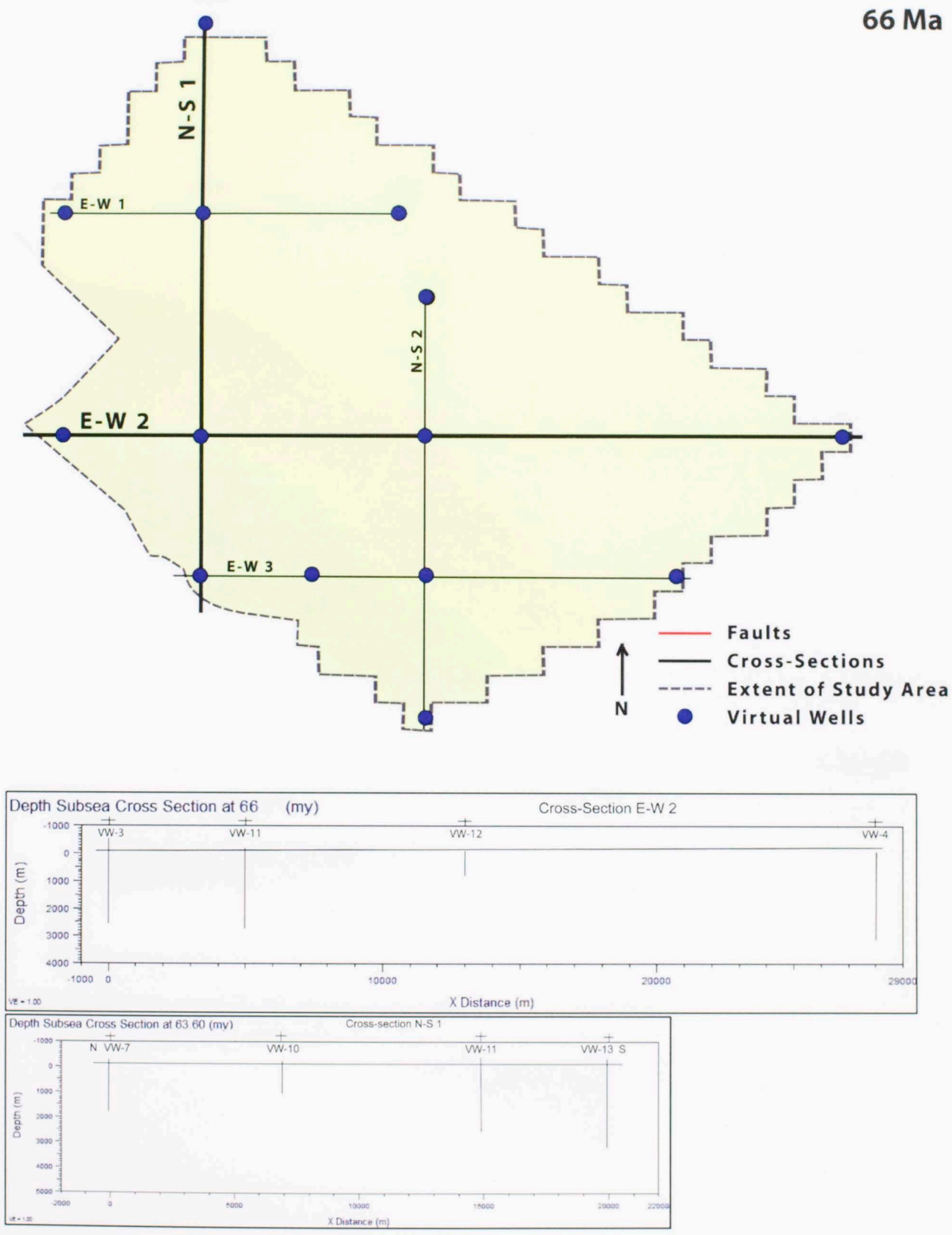

Figure 7.2.15: Map and cross-sections E-W 2 and N-S 1 showing structural depth to basement in meters subsea at 66 Ma. Elevation is currently zero, because rifting has not initiated yet. All of the rocks in the region are Mesozoic volcanic and metamorphic rocks.

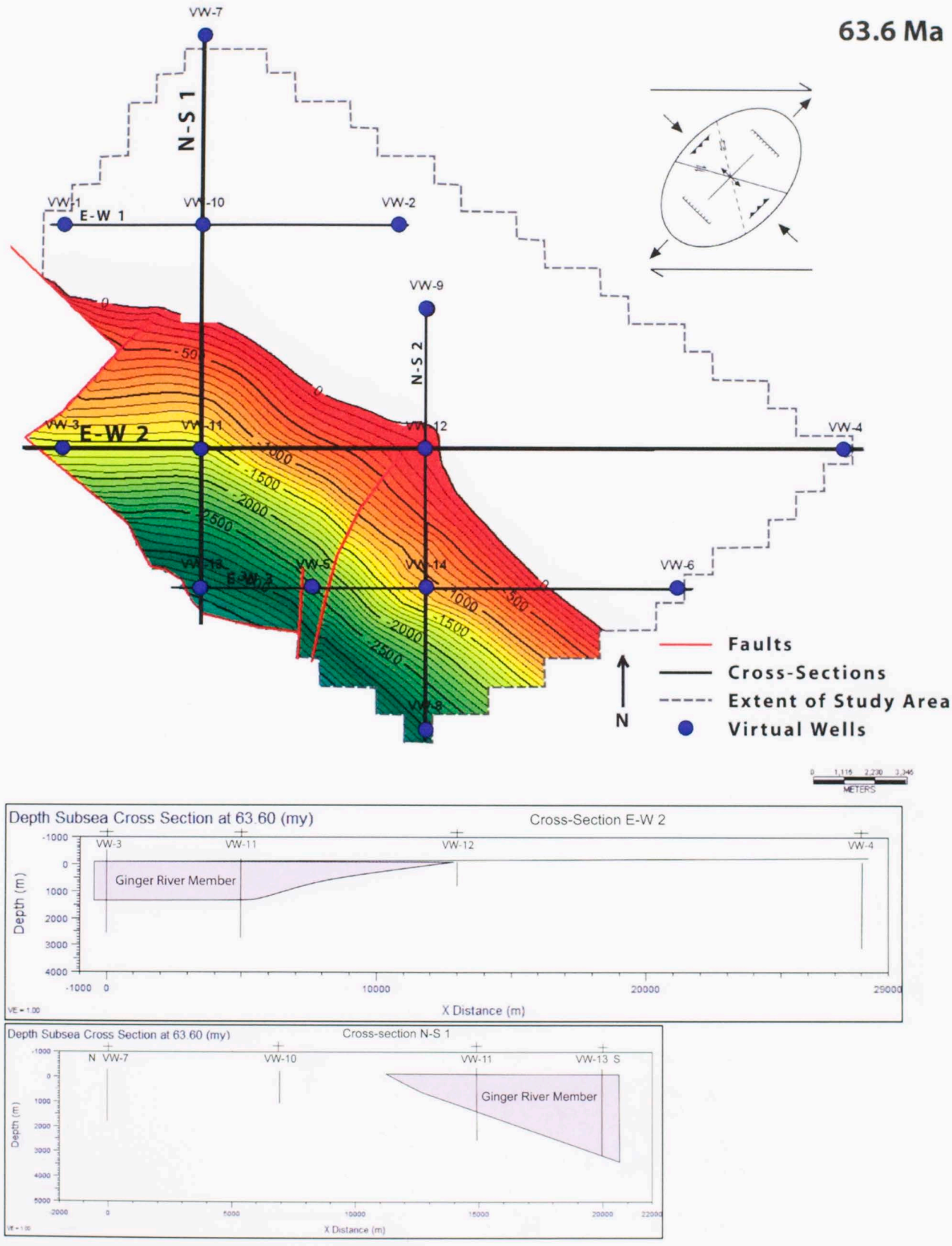

Figure 7.2.16: Map and cross-sections E-W 2 and N-S 1 showing structural depth to basement in meters subsea at 63.6 Ma. From 66 Ma to 63.6 Ma the basin initiated fault mechanical subsidence as a half graben with northeast to southwest extension owing to simple dextral(?) shear along a releasing bend in the Septentiornal-Orient-Swan-Motagua-Duanvale-Plantain Garden-Sway fault zones.

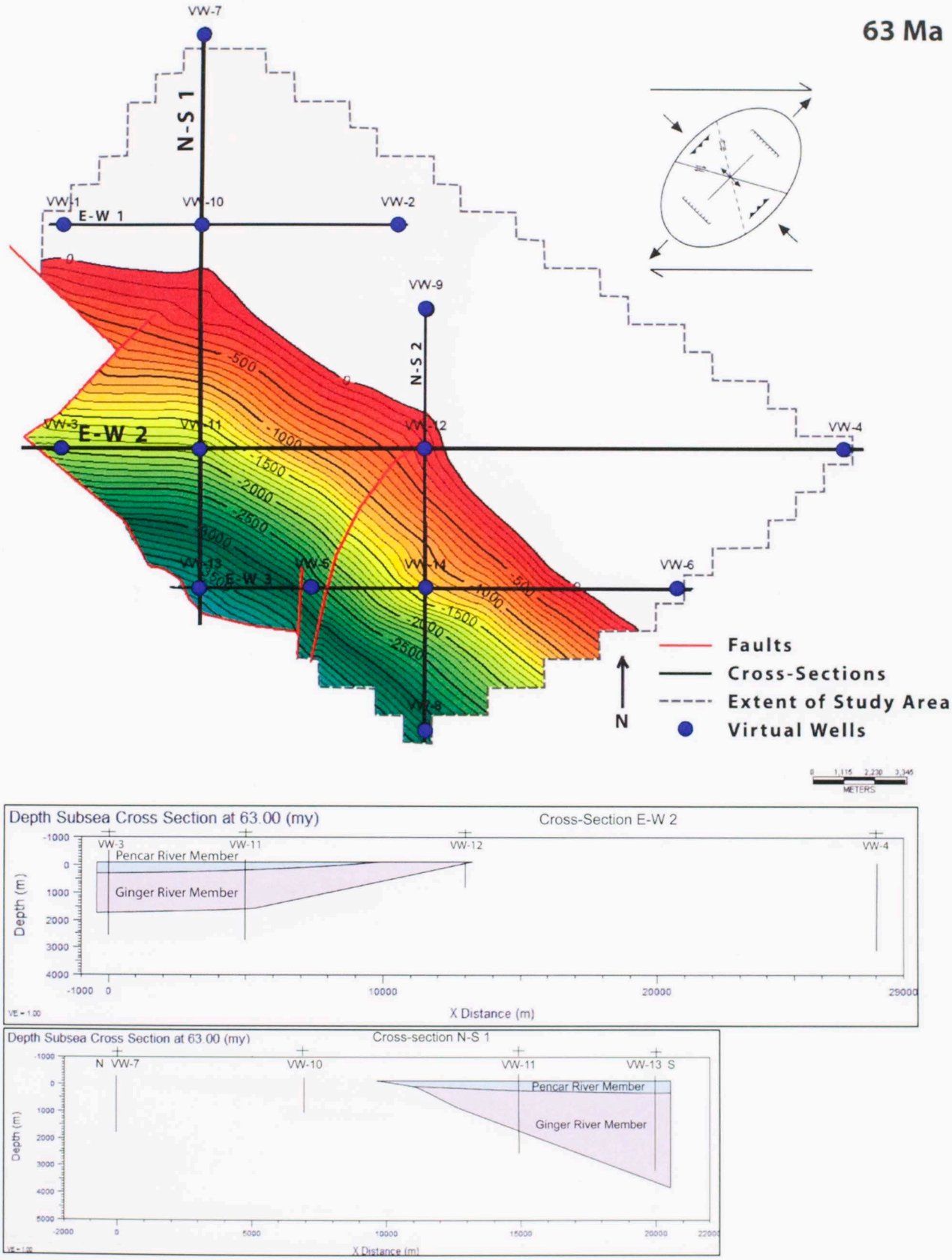

Figure 7.2.17: Map and cross-sections E-W 2 and N-S 1 showing structural depth to basement in meters subsea at 63 Ma. From 63.6 Ma to 63 Ma, the basin continued fault mechanical subsidence as a half graben with northeast to southwest extension.

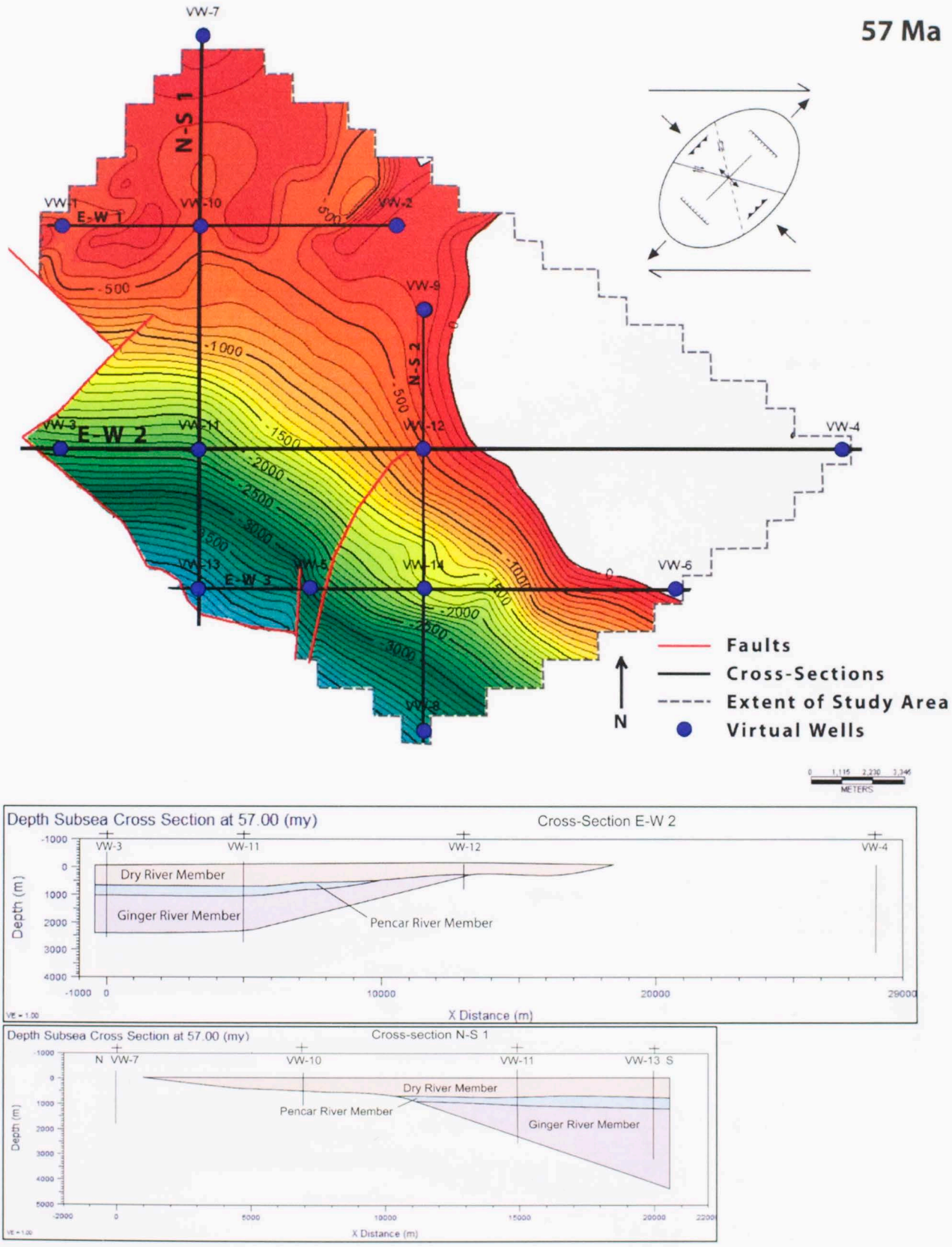

Figure 7.2.18: Map and cross-sections E-W 2 and N-S 1 showing structural depth to basement in meters subsea at 57 Ma. From 63 Ma to 57 Ma, the basin continued fault mechanical subsidence as a half graben. However, toward the end of this period, subsidence began in the north as well.

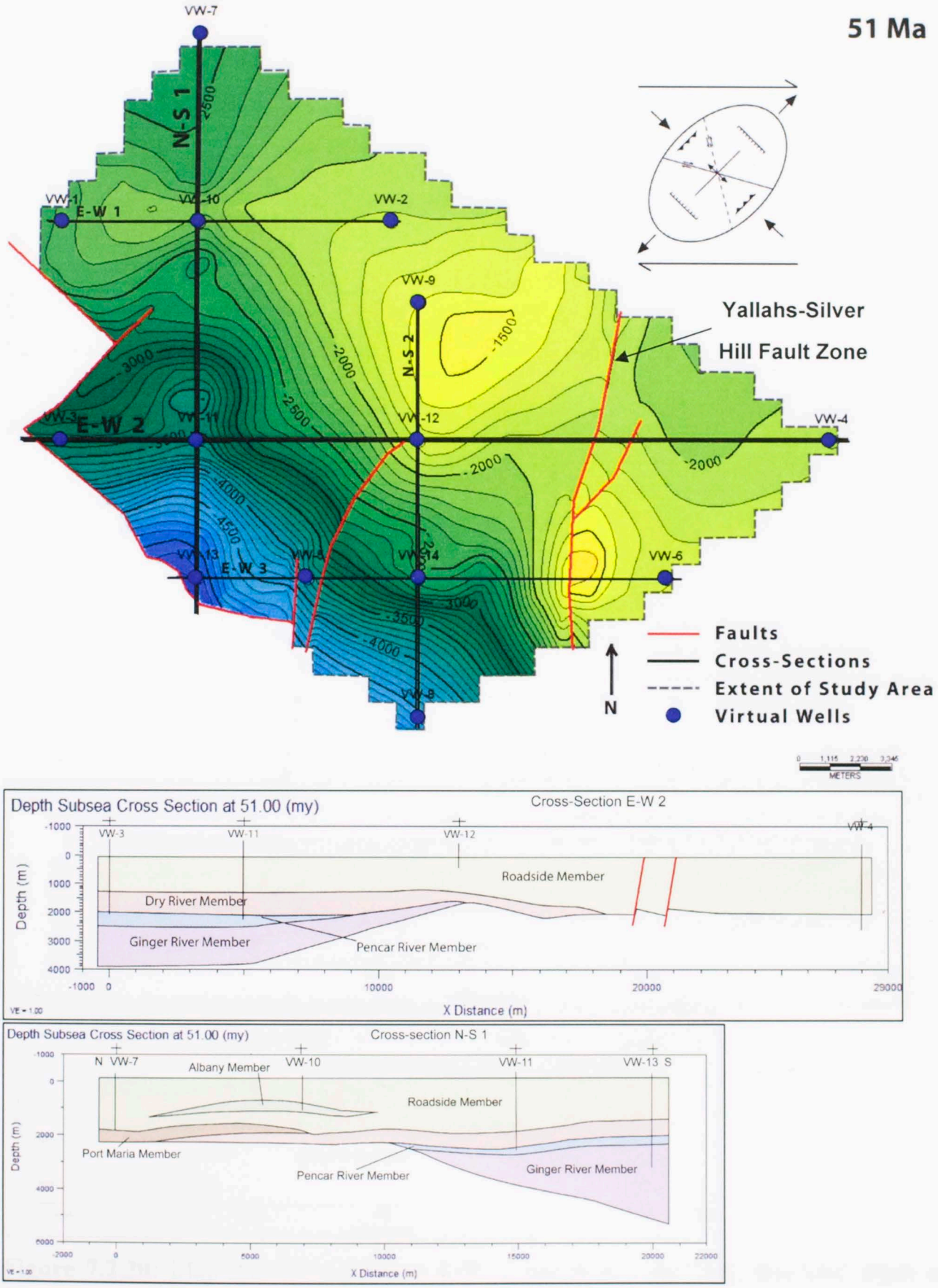

Figure 7.2.19: Map and cross-sections E-W 2 and N-S 1 showing structural depth to basement in meters subsea at 51 Ma. From 57 Ma to 51 Ma, the basin continued fault mechanical subsidence.

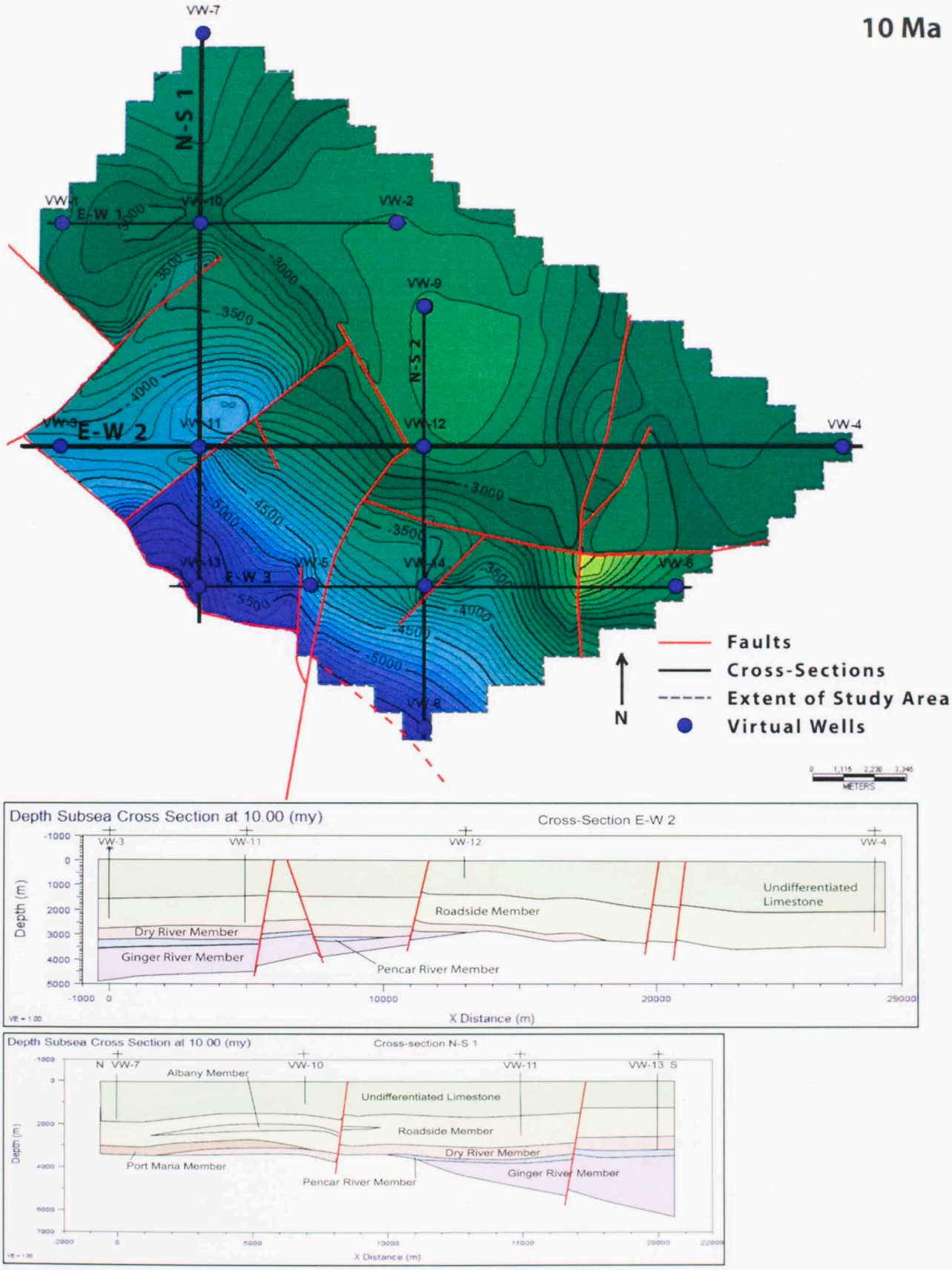

Figure 7.2.20: Map and cross-sections E-W 2 and N-S 1 showing structural depth to basement in meters subsea at 10 Ma. From 51 Ma to 10 Ma, the basin ceased fault mechanical subsidence and thermal tectonic subsidence became the main drive for basin subsidence.

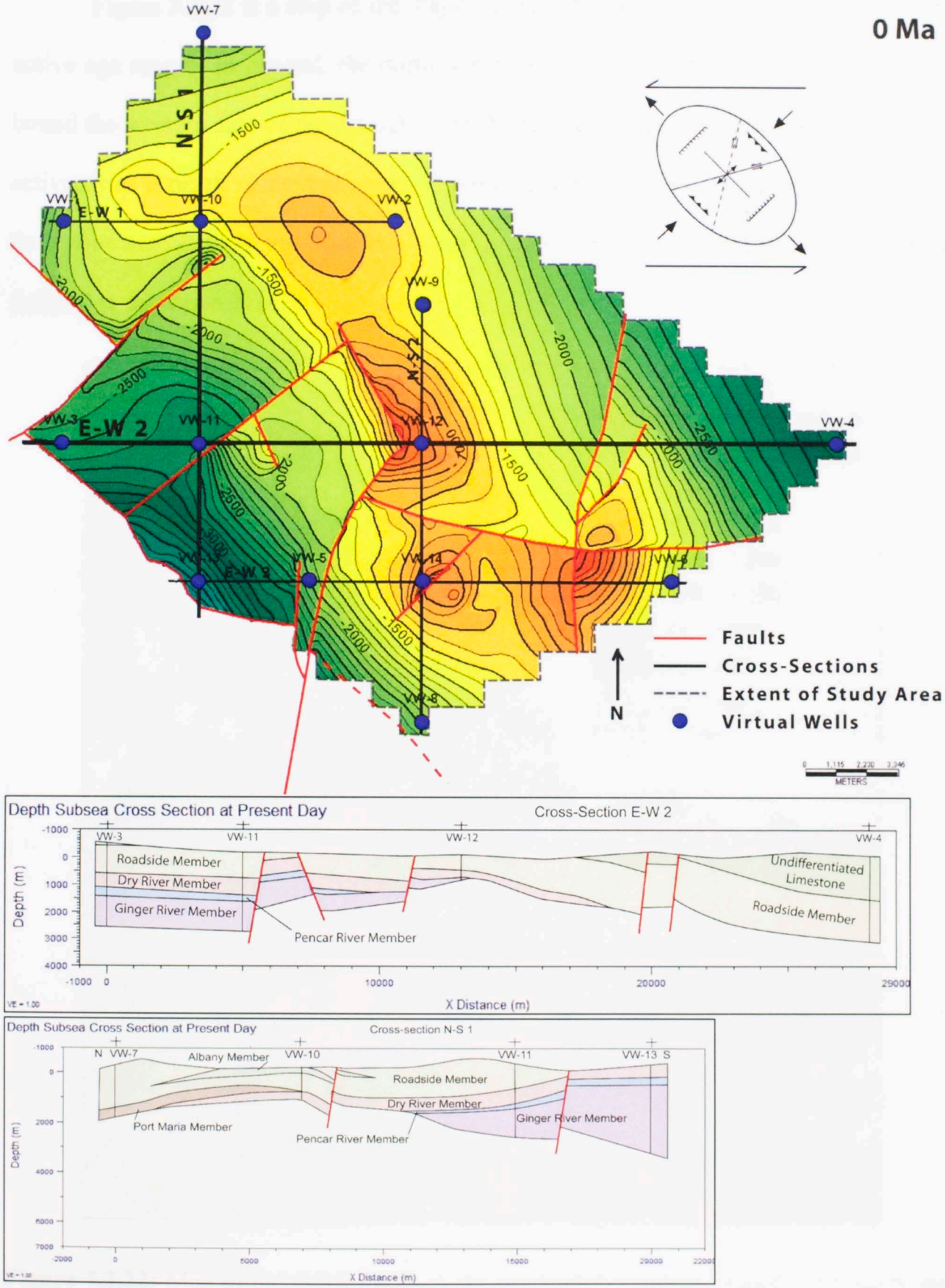

Figure 7.2.21: Map and cross-sections E-W 2 and N-S 1 showing structural depth to basement in meters subsea at present. From 10 Ma to 0 Ma, the basin ceased subsidence and uplift and shortening, with a beta of 0.81, occurred along the basin faults.

Figure 7.2.22 is a map of the major faults in the northern Wagwater Trough with active age ranges. In general, the north northwest to south southeast striking faults that bound the western side of the Trough formed first during the Paleocene as normal faults activated as a result of dextral shear. During the Early Eocene, the Yallahs-Silver Hill fault zone activated. In the Middle Miocene, the east-west striking faults activated with sinistral strike-slip motion.

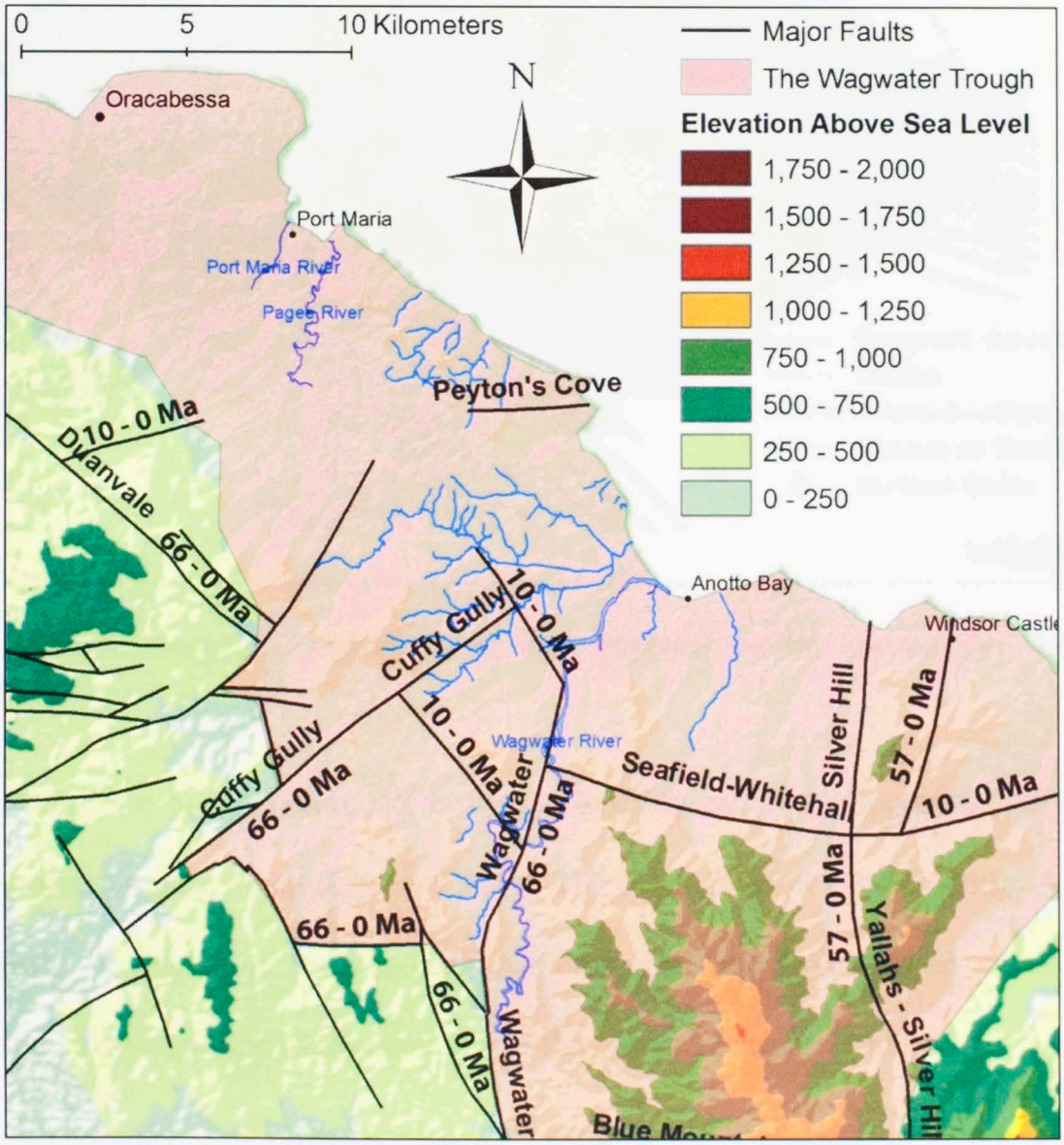

Figure 7.2.22: Map of the major faults in the northern Wagwater Trough with active age ranges.

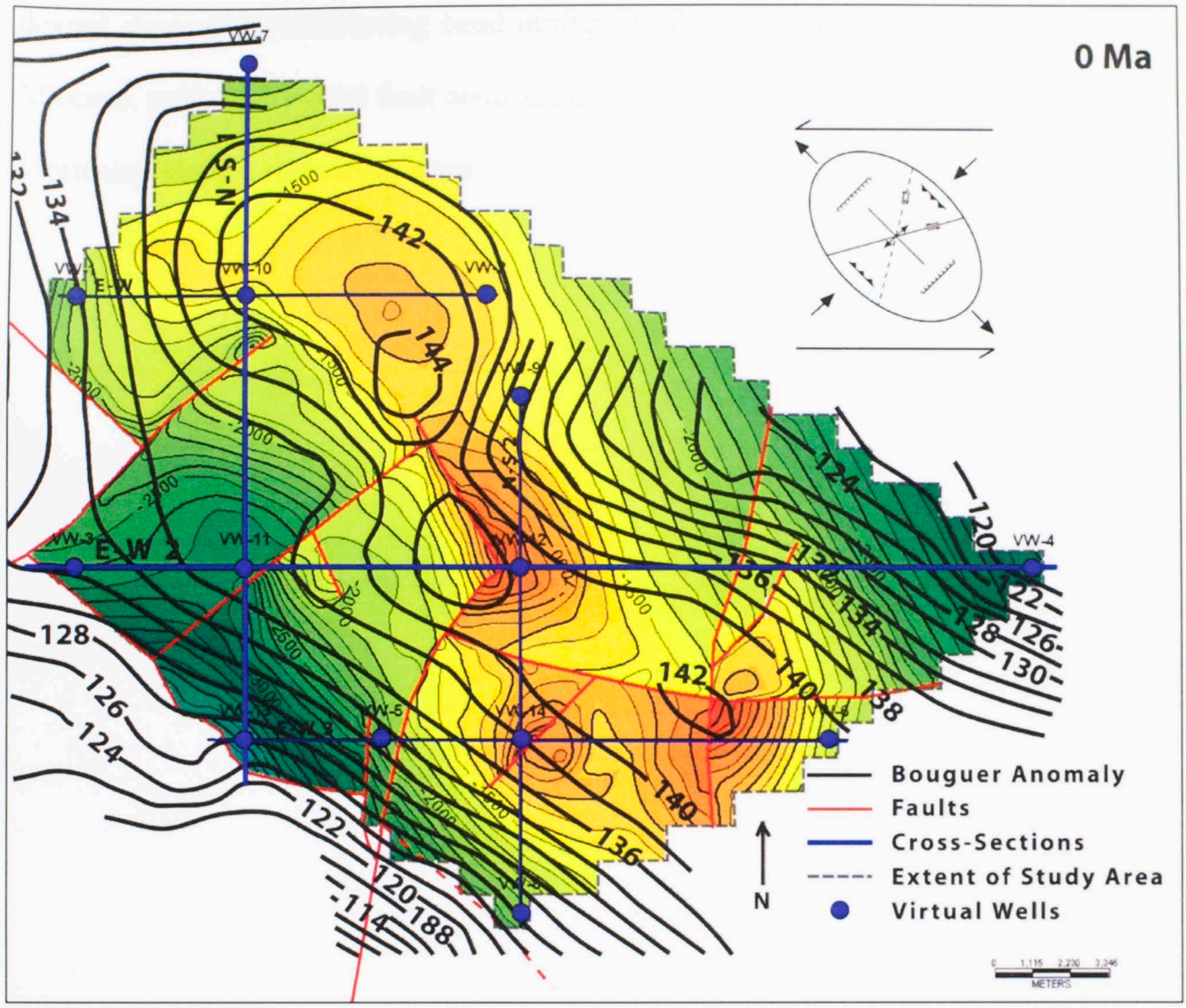

Figure 7.2.23: Bouguer Anomaly Map superimposed on the present-day basement structure map.

As a form of validation, the Bouguer Anomaly can be compared to the present-day basement structure map (Figure 7.2.23). The high values for the Bouguer Anomaly trend with the highs in the basement structure. Higher values trend northwest to southeast. This helps support the accuracy of the basement structure map.

In summary, it is proposed that the evolution and development of the Wagwater Trough is caused by regional simple shear along the Septentiornal-Orient-Swan-Motagua, Duanvale, and Plantain Garden-Sway fault zones. Extension of the basin was caused by

dextral shear along a releasing bend during the Paleocene and Eocene. By the Middle Miocene, motion along the fault zone had changed to sinistral simple shear which caused shortening along a restraining bend.

7.3 Total Organic Carbon Content

Initial total organic carbon content (TOC) has not been measured for the formations in the Wagwater Trough. To estimate these values a correlation between sedimentation rate and TOC developed by Johnson-Ibach (1982) was used. His method shows a direct relationship between measured TOC values and sedimentation rate in clastic sediments (Figure 7.3.1). This relationship exists because increasing sedimentation rate increases burial rate and increases preservation of organic materials (Metwalli and Pigott, 2005) Using Johnson-Ibach's method and assuming that clastic deposition in the Wagwater Trough was continuous, sedimentation rates were calculated and converted to initial TOC values using the graph in figure 7.3.1. Using the graph in figure 7.3.1, average sedimentation rate is converted to TOC. The Richmond Roadside Member would have a TOC of 6.0 %.

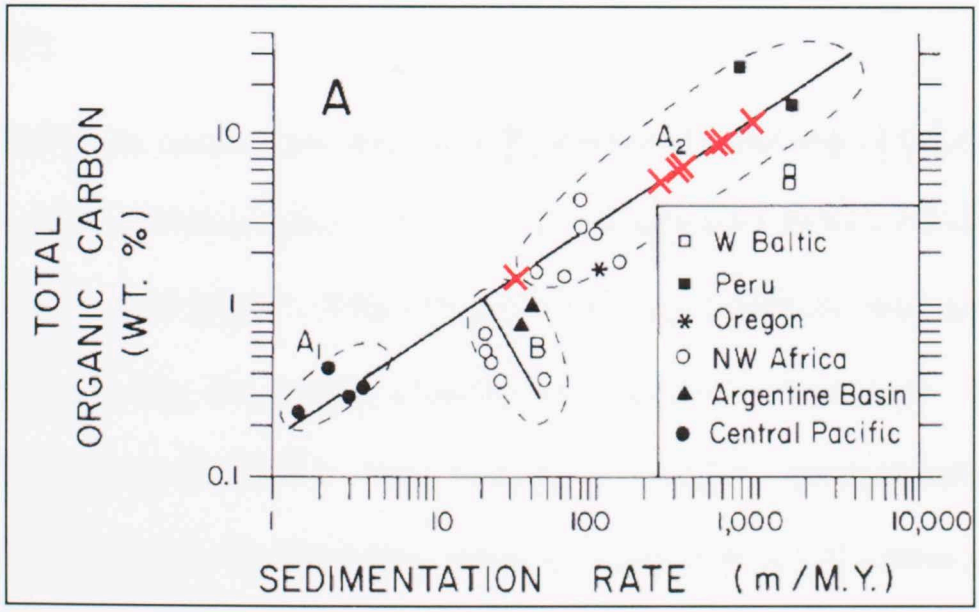

Figure 7.3.1: Graph showing the correlation between sedimentation rate to total organic carbon content (TOC). TOC content increases directly with sedimentation rate (from Johnson-Ibach, 1982). Calculated geologic units in this study are marked by red crosses.

Formation	Member	Average Sedimentation Rate (m/M.Y.)	Total Organic Carbon (%)
Wagwater	Ginger River	1051	10
	Pencar River	621	7
	Dry River	276	5
Richmond	Port Maria	389	6
	Roadside/Langley	325	6
	Albany Beds	589	7
Yellow Limestone	Font Hill	37	1.5

Table 7.3.1: Estimated TOC content values for the different sedimentary units. They were determined using the correlation of sedimentation rate to TOC (Figure 6.3.1).

7.4 Heat Flow

Currently the highest heat flow in the Northern Caribbean region is 2.25 H.F.U. at the Mid-Cayman spreading center. The heat flow declines to about 1.4 H.F.U. off the north coast of Jamaica (Perry, 1984). O'Neal (1984) calculated the heat flow from the thermal gradient using the Fourier equation in Petroleum Corporation of Jamaica's Windsor #1 well to be 0.96 H.F.U. Since there are no heat flow measurements within the Wagwater Trough, these two heat flow values (1.4 and 0.96 H.F.U.) were used as end members to bracket and constrain the heat flow models for the Wagwater Trough. Using the methods described earlier, paleo-heat flow data were calculated using betas calculated using the 3-D method and the present-day heat flow (1.4 and 0.96 H.F.U.). Three heat flow conditions were used:, rifting heat flow conditions with present-day heat flow at

0.96 H.F.U (Rifting 0.96 Models), rifting heat flow conditions with present-day heat flow at 1.4 H.F.U (Rifting 1.4 Models), and steady-state heat flow conditions. It is not likely that heat flow remained constant throughout basin development; however, steady-state conditions were used to create models for comparison.

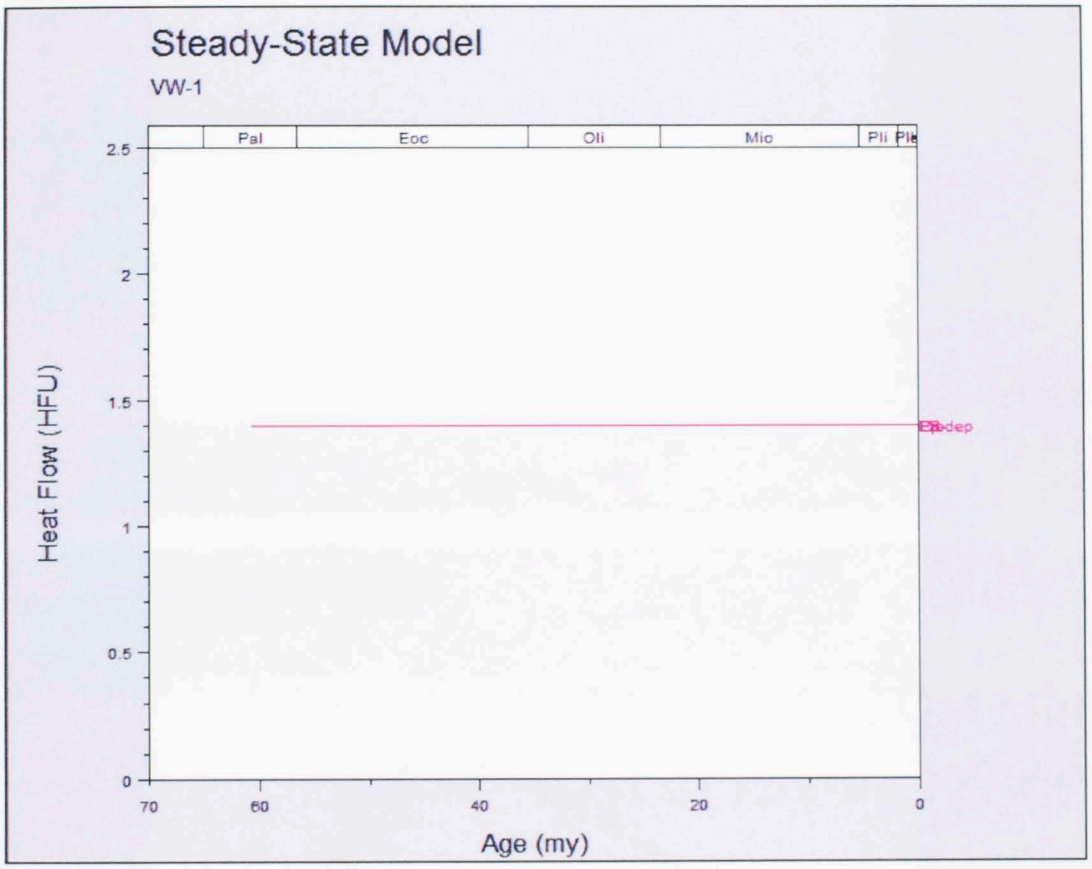

Figure 7.4.1: Modeled steady-state (constant) heat flow for VW-1. All other virtual wells in this study exhibit the same heat flow in steady-state conditions.

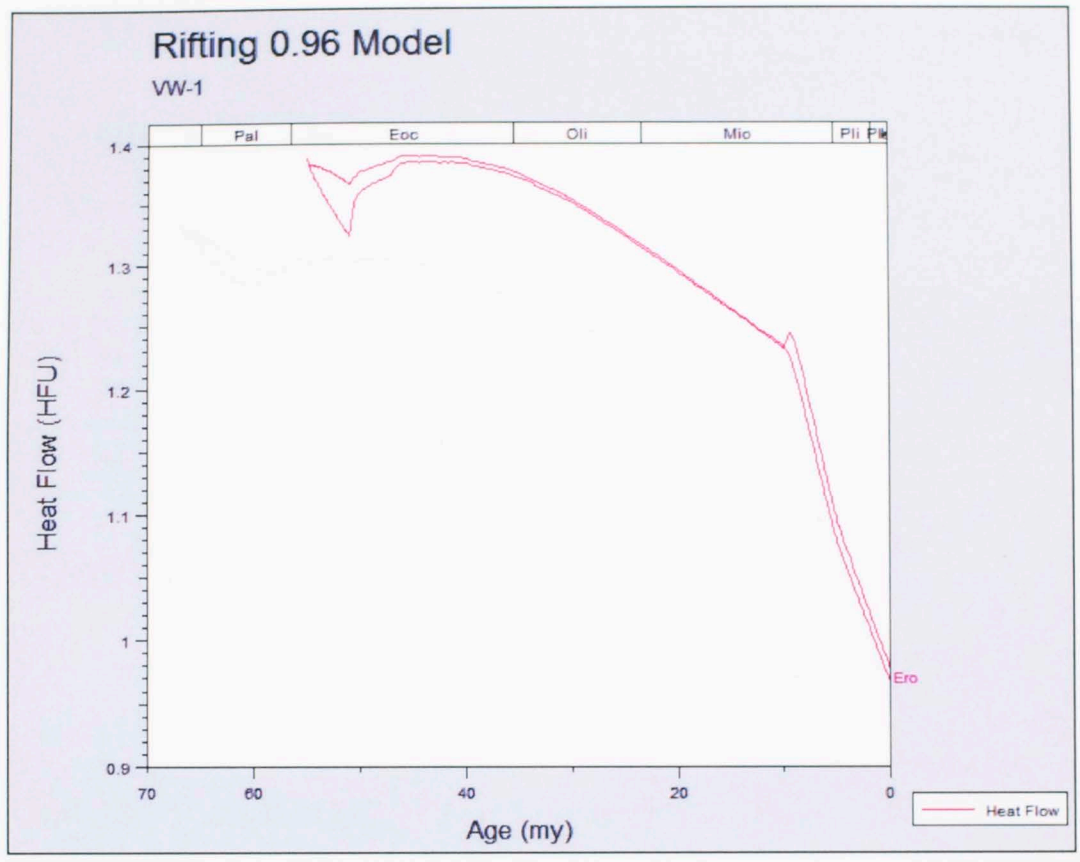

Figure 7.4.2: Modeled Heat flow for rifting 0.96 and 1.4 conditions for VW-1. Heat flow is greater in the rifting 1.4 model than the 0.96 model.

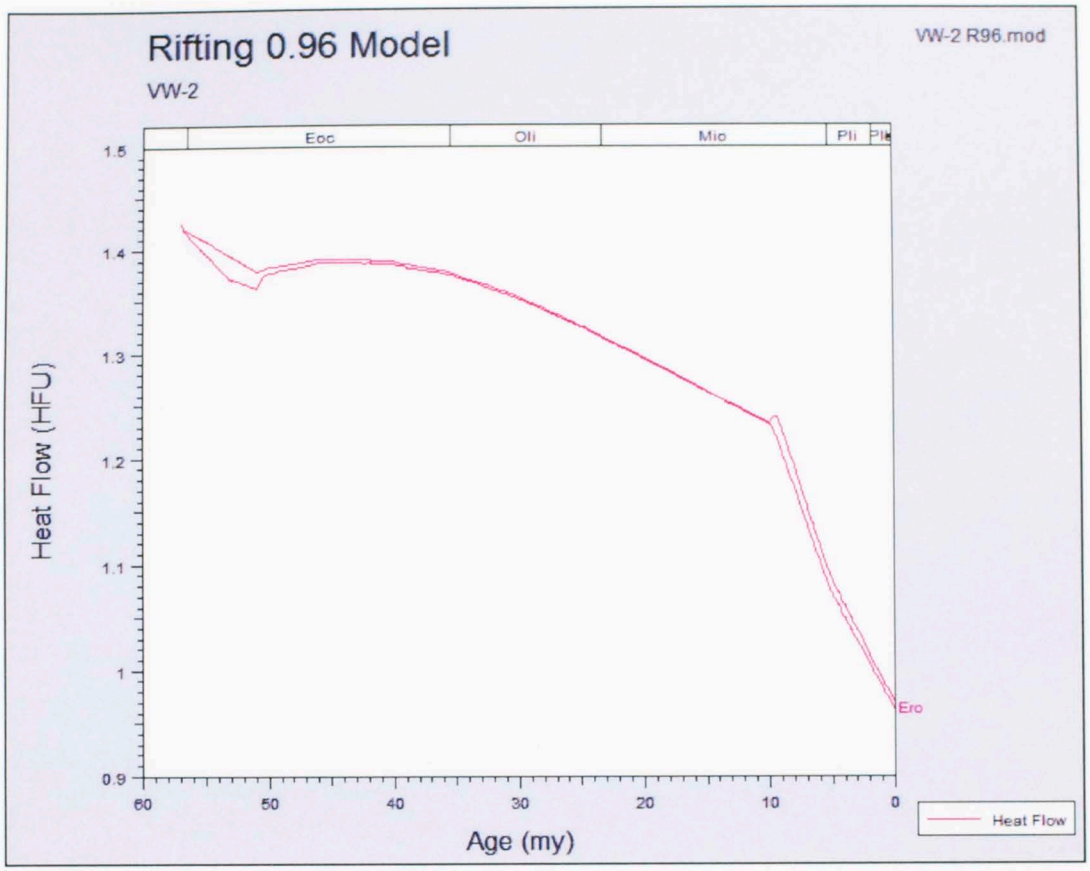

Figure 7.4.3: Modeled Heat flow for rifting 0.96 and 1.4 conditions for VW-2.

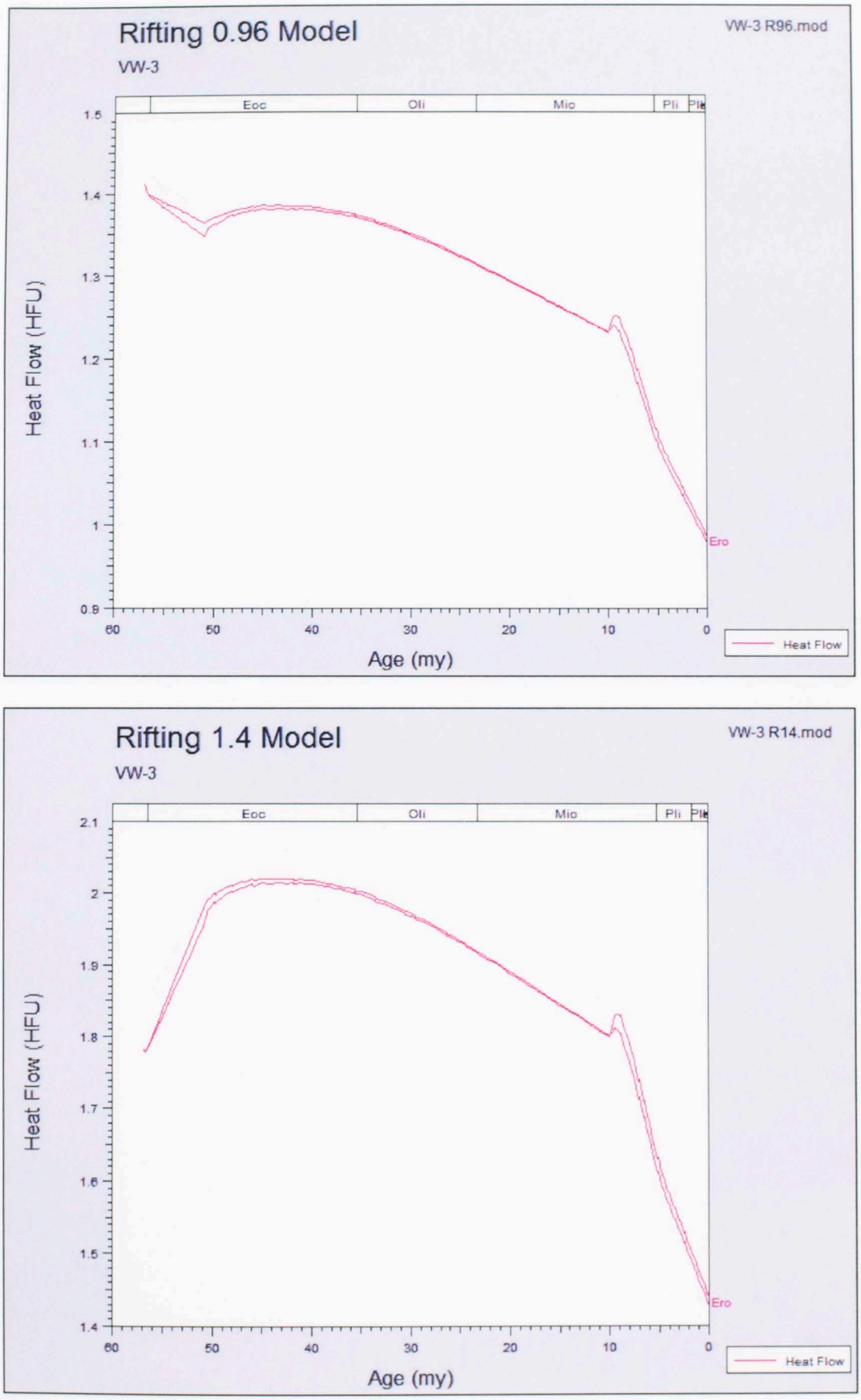

Figure 7.4.4: Modeled Heat flow for rifting 0.96 and 1.4 conditions for VW-3.

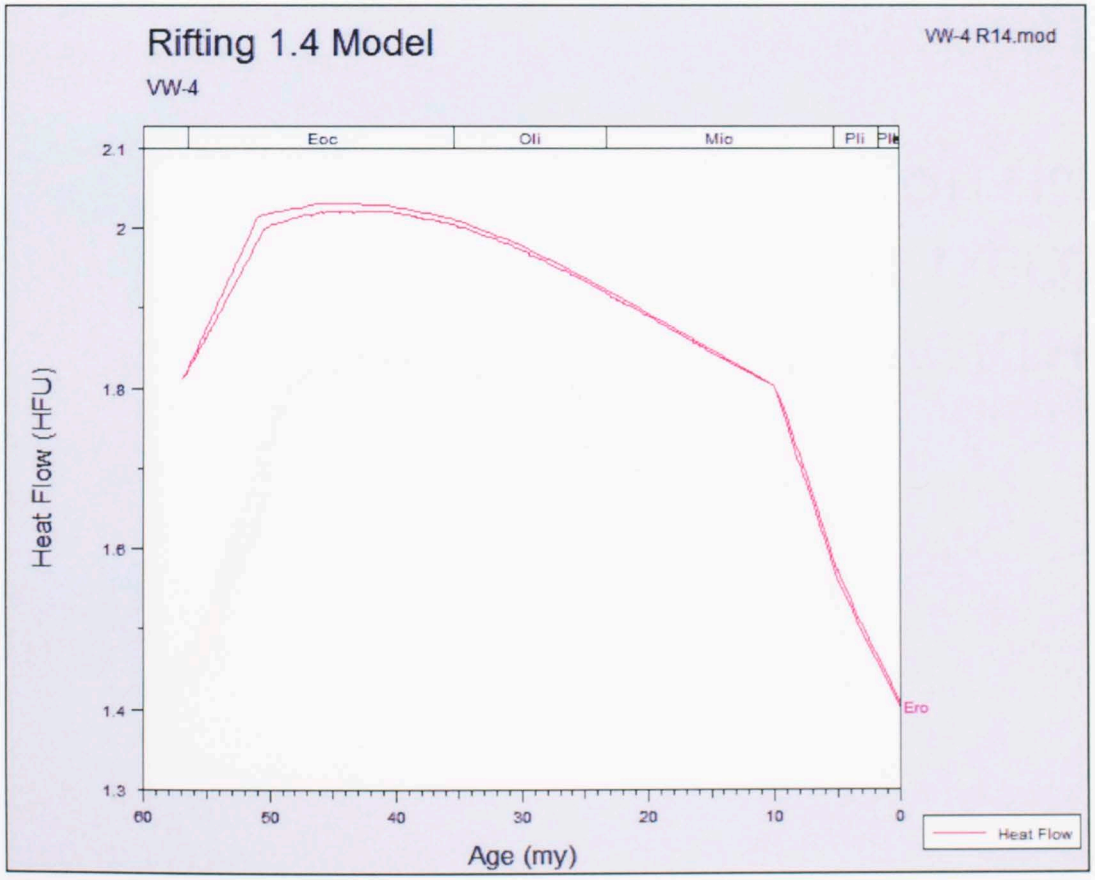

Figure 7.4.5: Modeled Heat flow for rifting 0.96 and 1.4 conditions for VW-4.

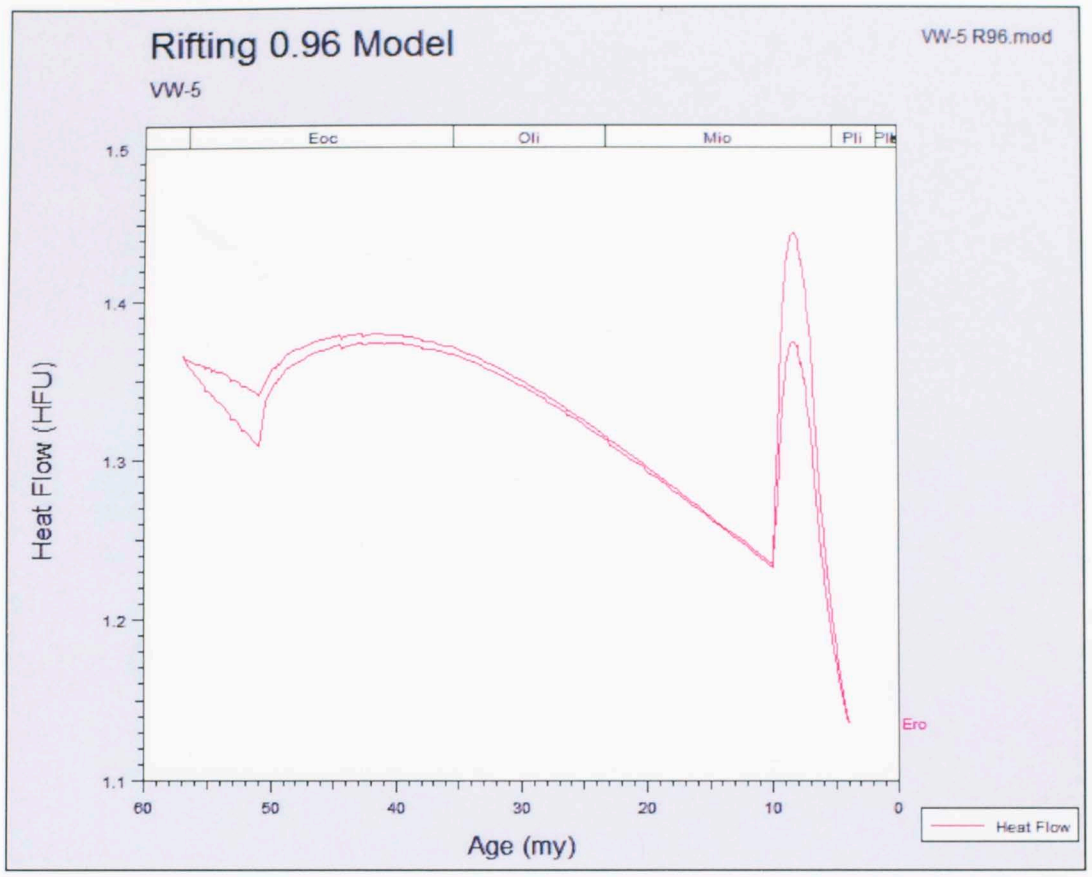

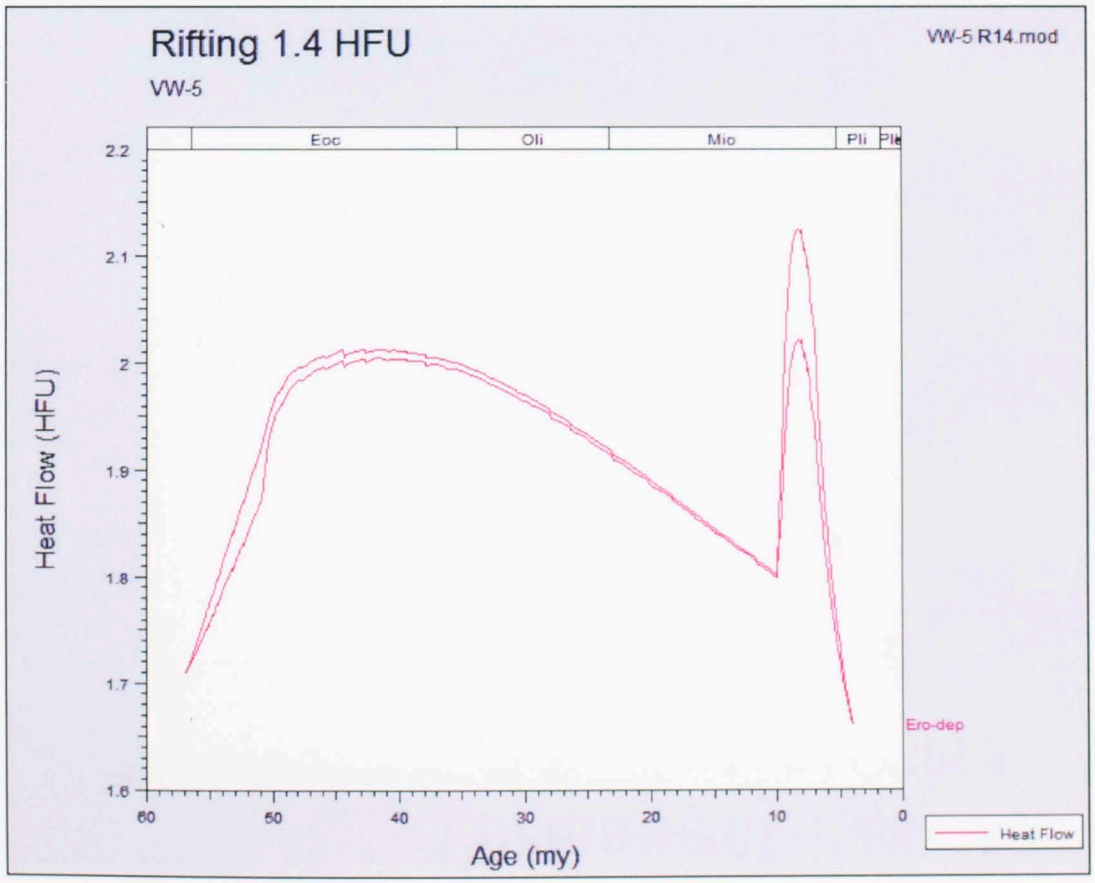

Figure 7.4.6: Modeled Heat flow for rifting 0.96 and 1.4 conditions for VW-5.

Figure 7.4.7: Modeled Heat flow for rifting 0.96 and 1.4 conditions for VW-6.

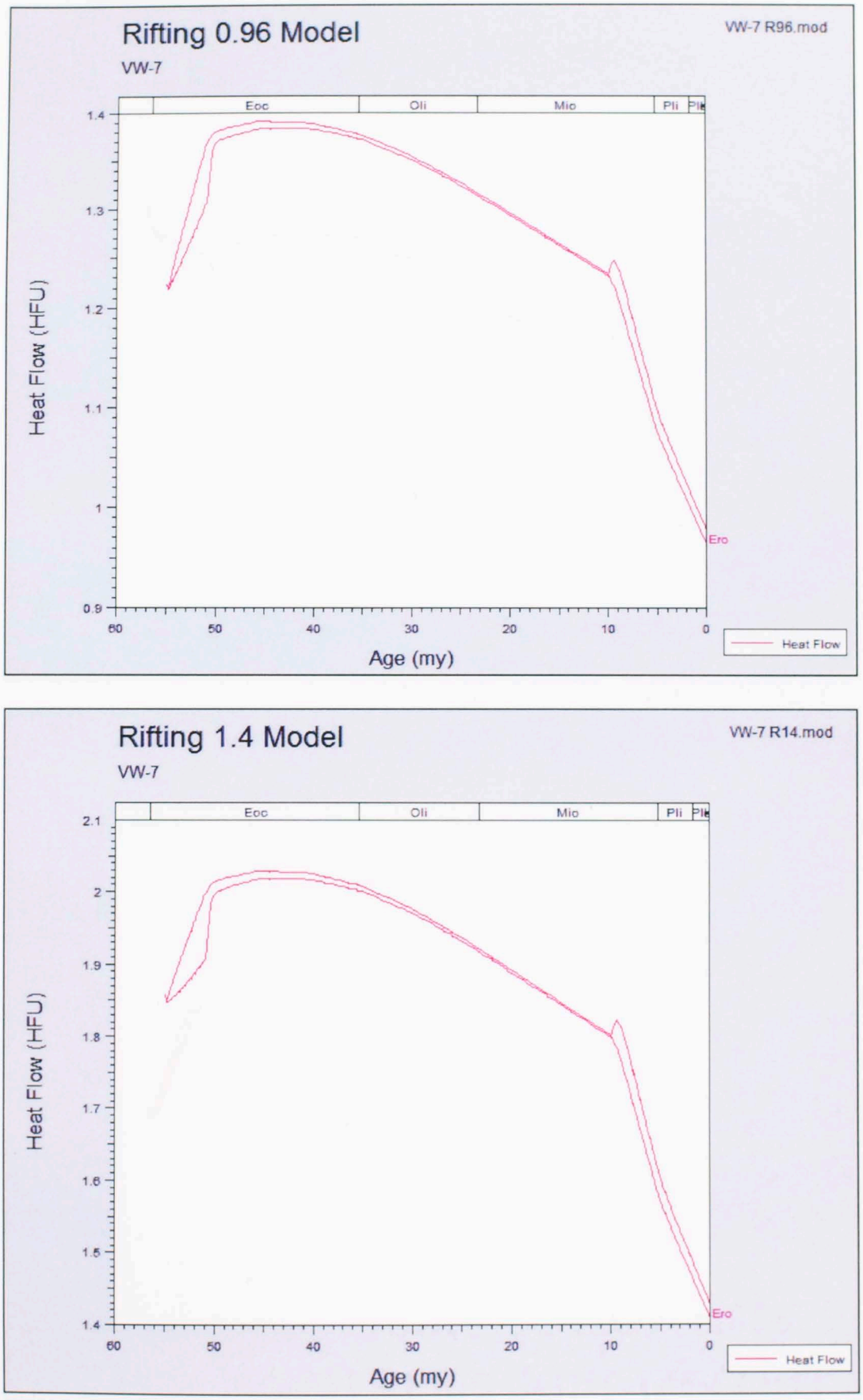

Figure 7.4.8: Modeled Heat flow for rifting 0.96 and 1.4 conditions for VW-7.

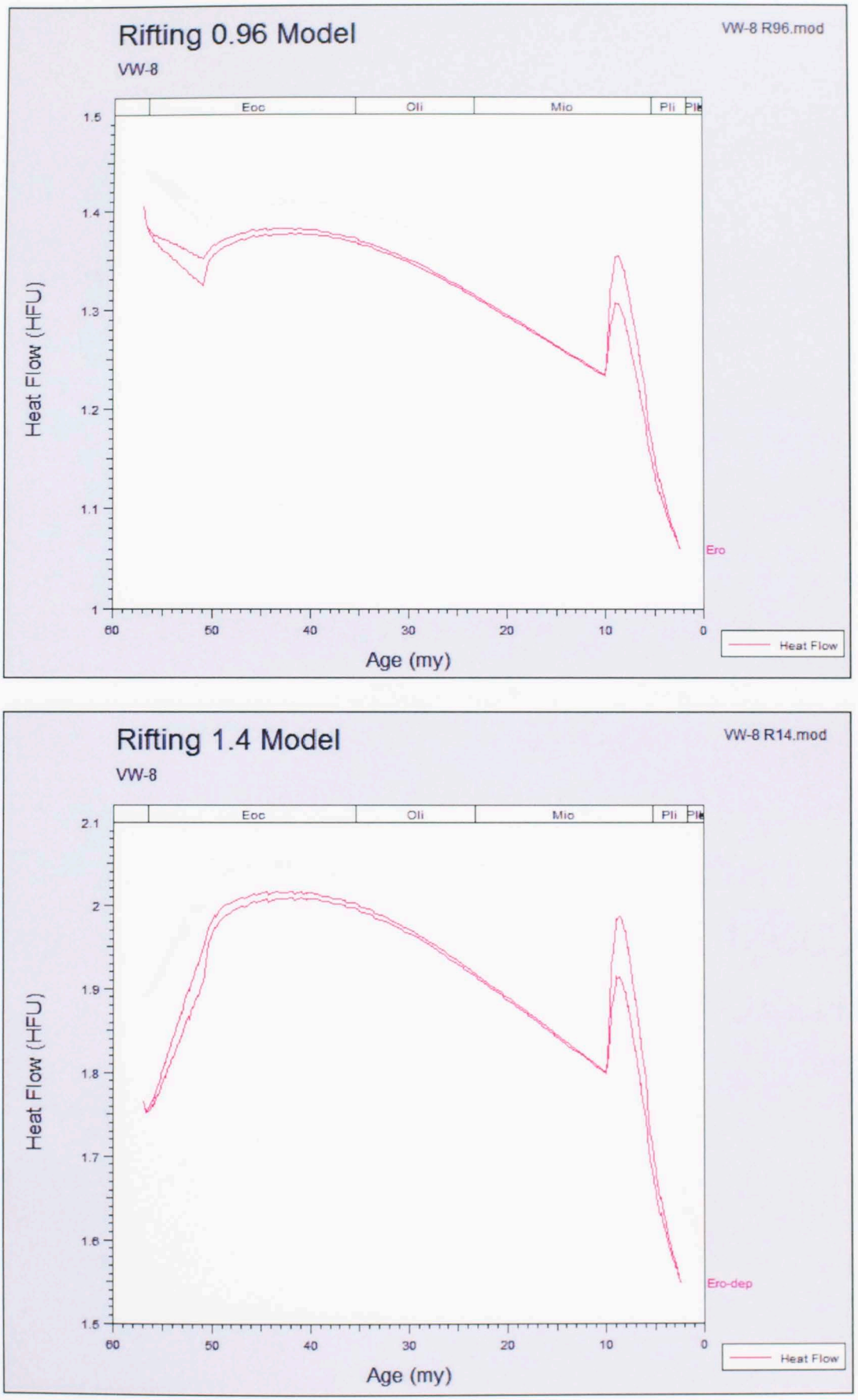

Figure 7.4.9: Modeled Heat flow for rifting 0.96 and 1.4 conditions for VW-8.

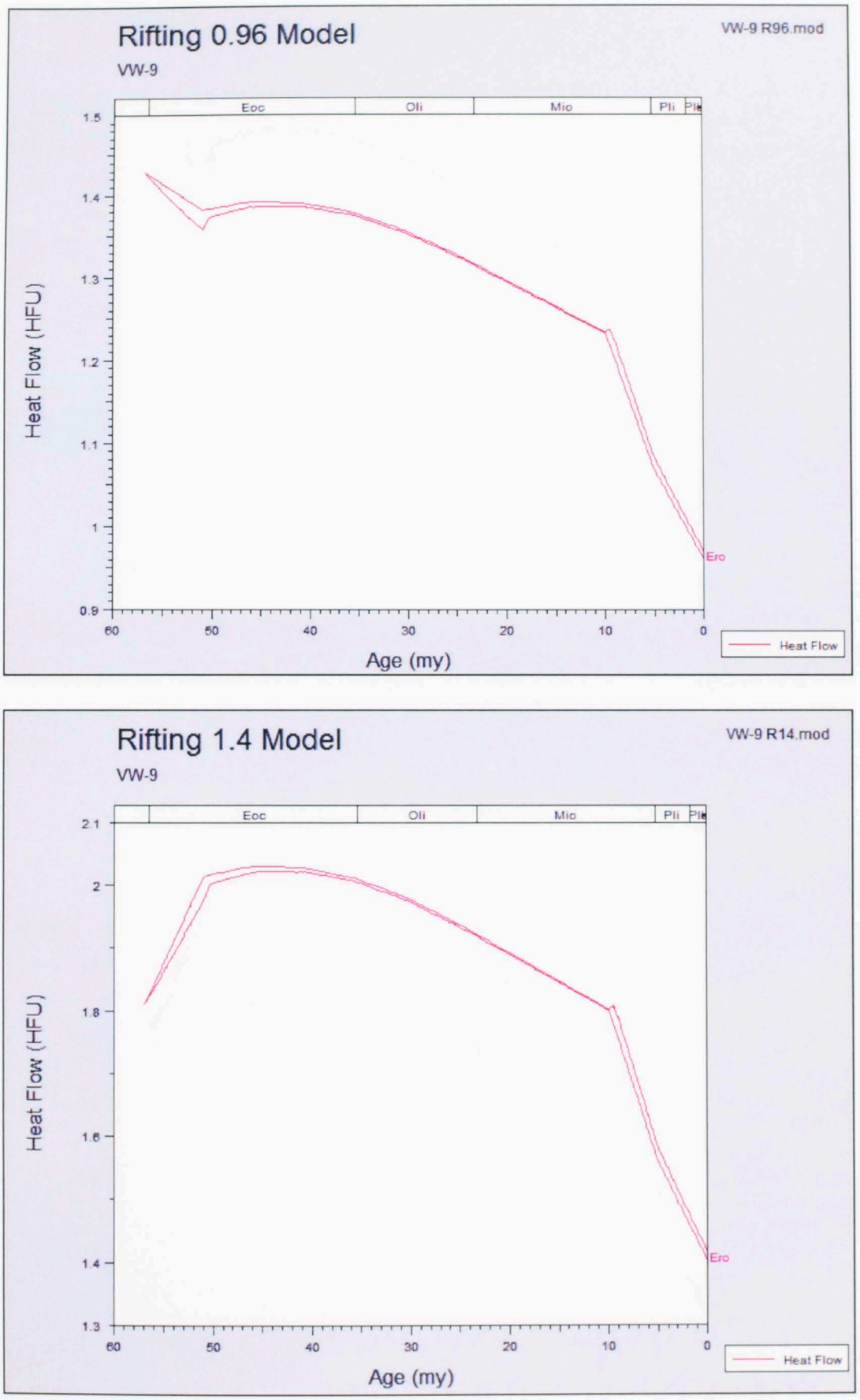

Figure 7.4.10: Modeled Heat flow for rifting 0.96 and 1.4 conditions for VW-9.

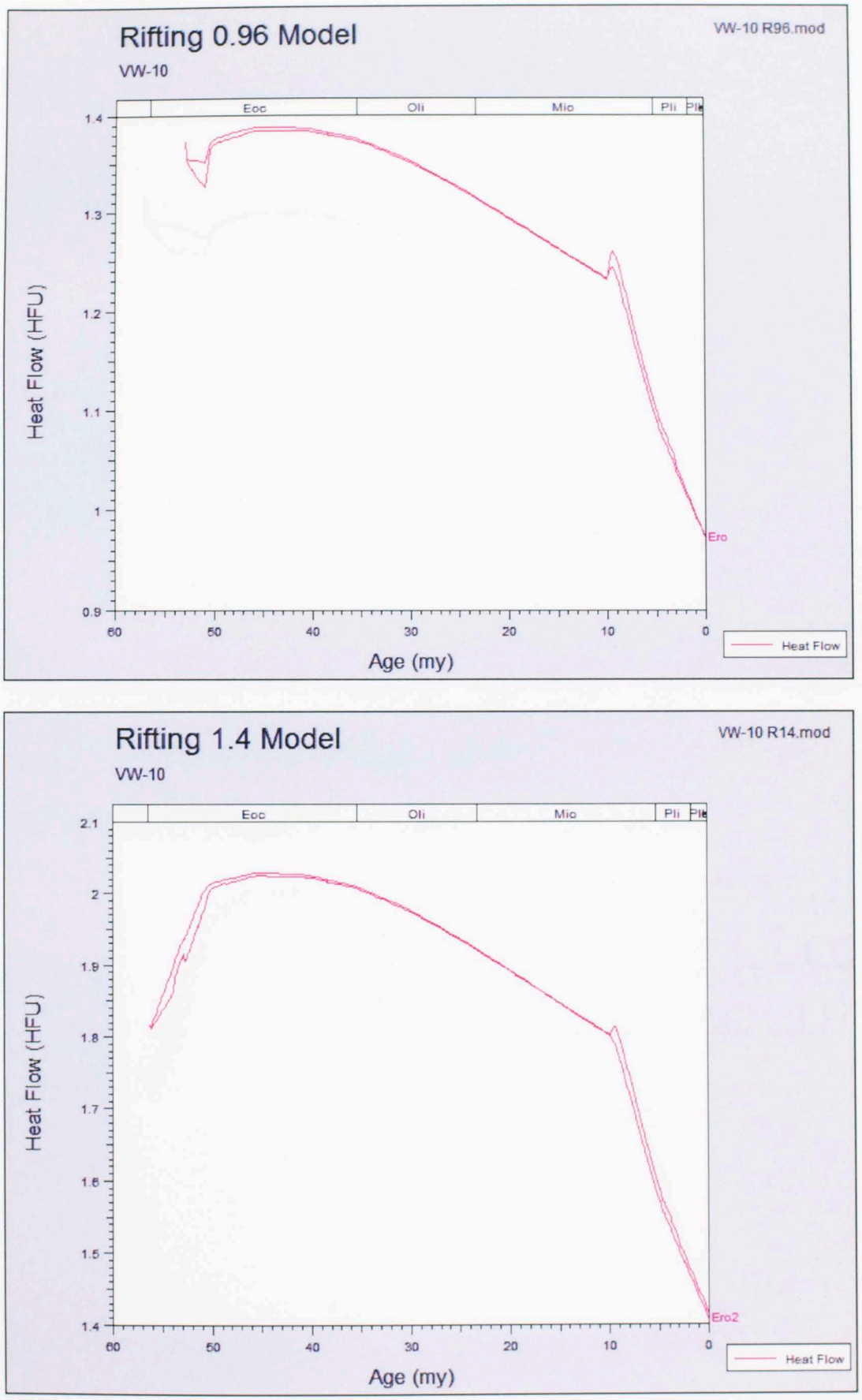

Figure 7.4.11: Modeled Heat flow for rifting 0.96 and 1.4 conditions for VW-10.

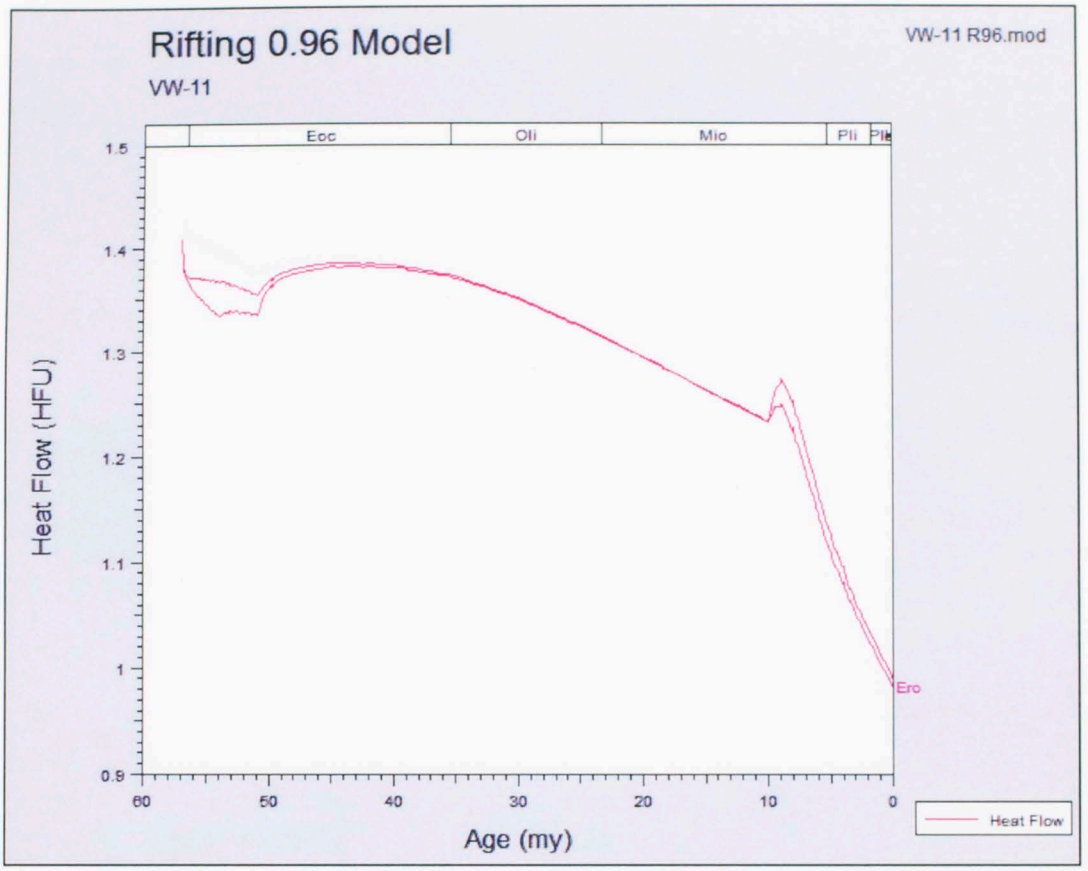

Figure 7.4.12: Modeled Heat flow for rifting 0.96 and 1.4 conditions for VW-11.

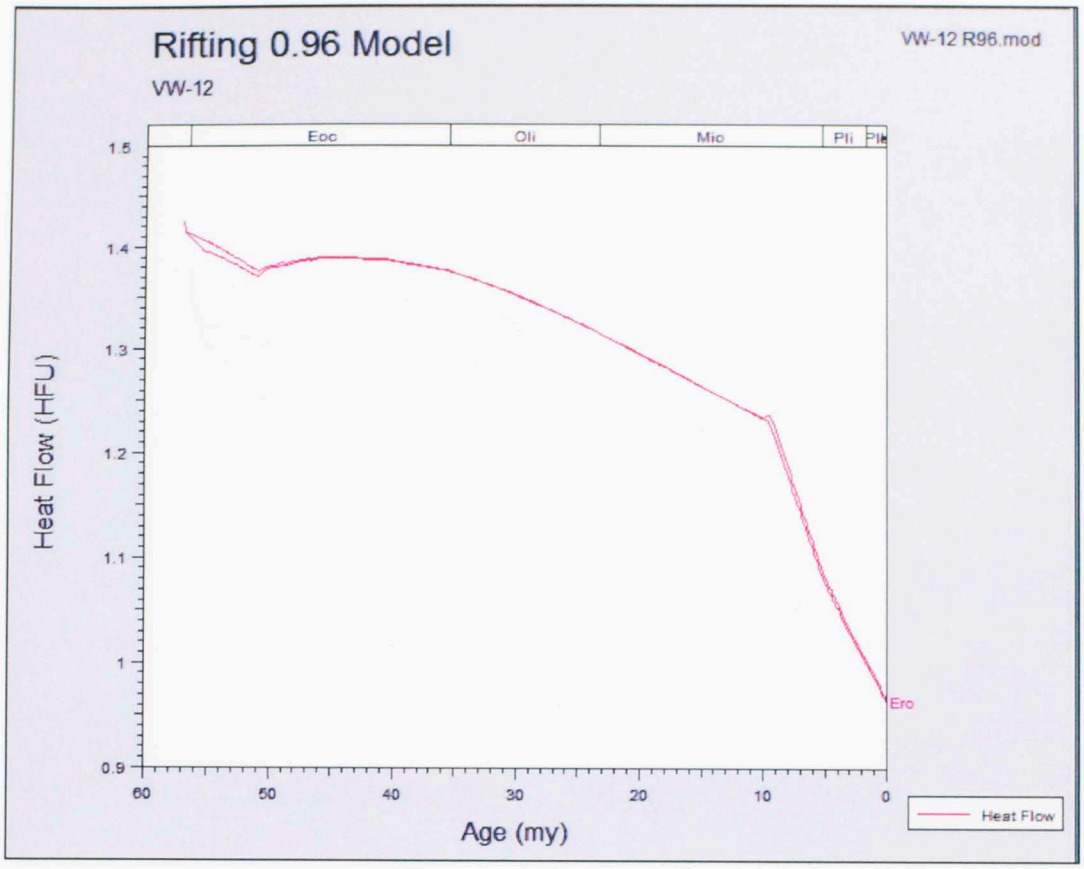

Figure 7.4.13: Modeled Heat flow for rifting 0.96 and 1.4 conditions for VW-12.

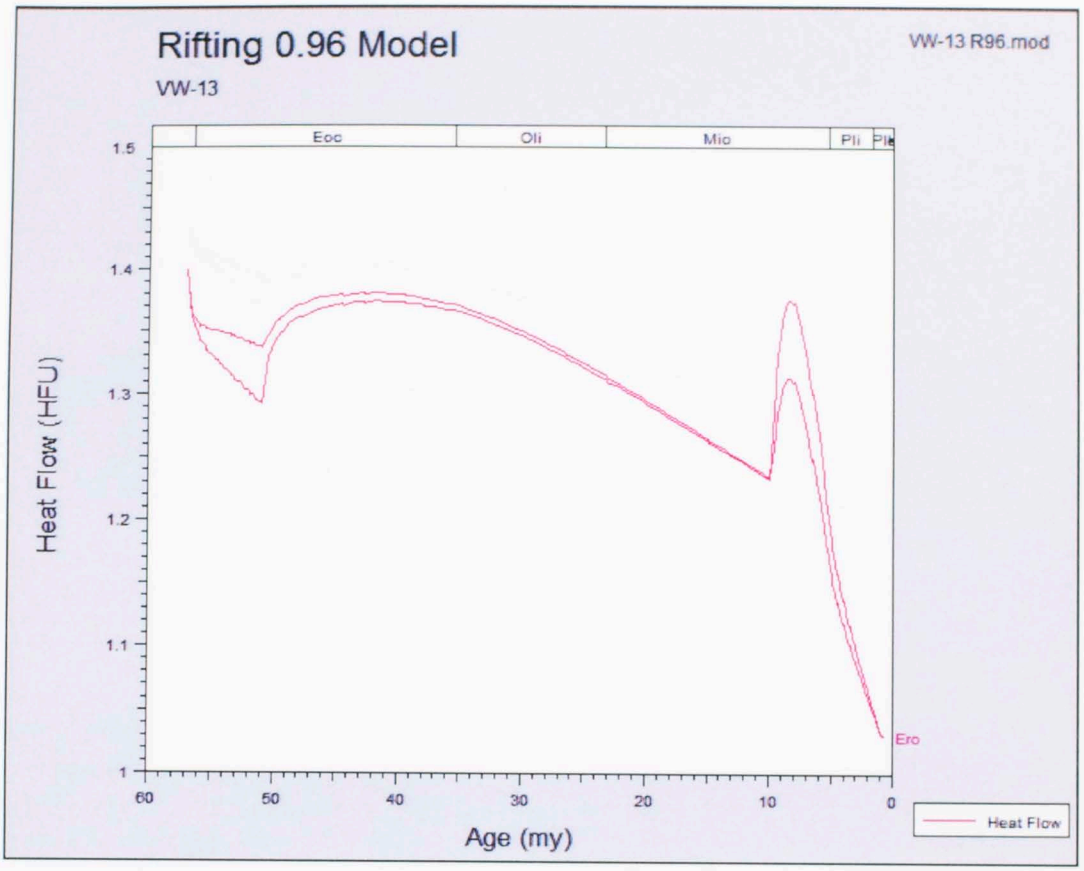

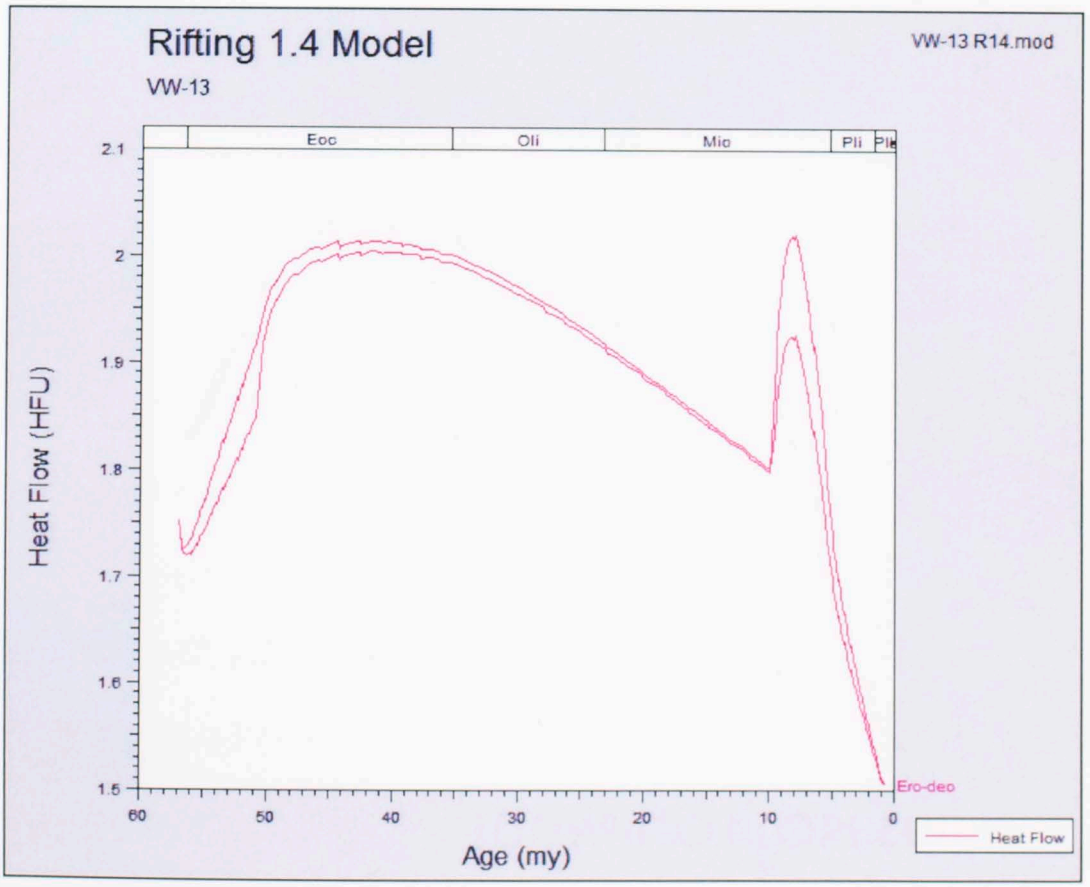

Figure 7.4.14: Modeled Heat flow for rifting 0.96 and 1.4 conditions for VW-13.

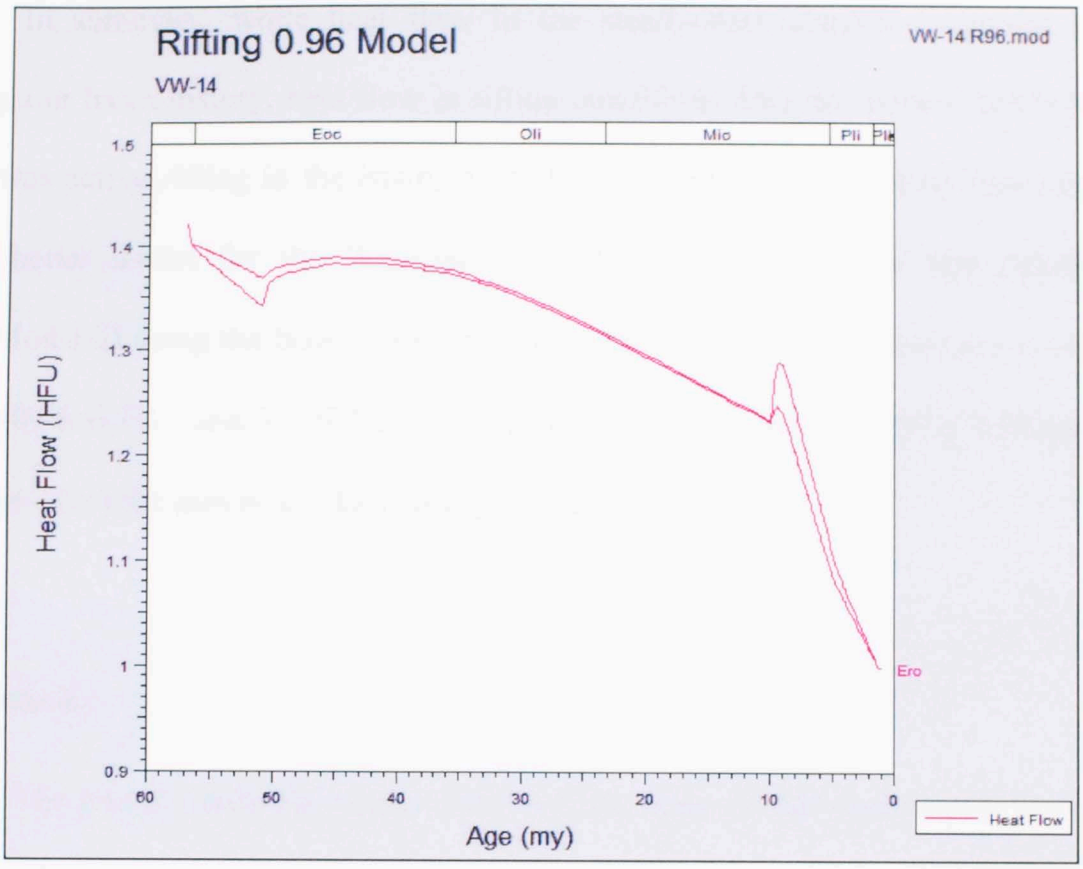

Figure 7.4.15: Modeled Heat flow for rifting 0.96 and 1.4 conditions for VW-14.

In summary, while heat flow in the steady-state condition remains constant throughout basin history, heat flow in rifting conditions does not remain constant. Since there was active rifting in the basin, it can be assumed that rifting heat flow conditions are a better model for the Wagwater Trough. Rifting heat flow was calculated in BasinMod 1-D using the betas calculated using the 3-D method and two present-day heat flows (0.96 H.F.U. and 1.4 H.F.U.). The heat flow curves for the rifting 0.96 conditions are lower than the curves for the rifting 1.4 model.

7.5 Maturity

The primary potential source rocks for this study are the shale layers inter-bedded with sandstone layers in the Richmond Roadside Formation. Source rock volume and quality (e.g. TOC, $\%R_0$, and kerogen type) of these formations were analyzed using both 1-D and 2-D basin modeling software. In each well, a maturity analysis was conducted separately for three cases: stead state heat flow, rifting heat flow with present-day heat flow at 0.96 H.F.U., and rifting heat flow with present-day heat flow at 1.4 H.F.U. Among various methods offered by basin modeling software, maturity VR LLNL was chosen for this analysis. VR LLNL is a technique proposed by Lawrence Livermore National Laboratories (LLNL), using vitrinite reflectance (VR) to evaluate the maturation of source rocks, with the primary assumptions that VR is related to the composition of kerogen, and that maturation reactions are the function of time, temperature, and pressure, in which pressure is assumed to be great enough so that only temperature and time could have direct effects on such reactions. The outputs of these calculations are displayed in the graphs of stratigraphy versus time or depth.

Comparison of steady-state heat flow conditions in figure 7.5.1 to rifting heat flow 0.96 conditions in figure 7.5.2 shows that there is very little difference in the maturity of the rock units, and therefore, steady-state heat flow conditions will be assumed similar to rifting heat flow 0.96 conditions. Results indicate that the timing and level of maturation in the cases of rifting heat flow model (present-day: 0.96 H.F.U.) to be lower than the rifting heat flow model (present-day: 1.4 H.F.U.). This is directly related to the higher heat flow curves for the rifting 1.4 cases than the 0.96 cases.

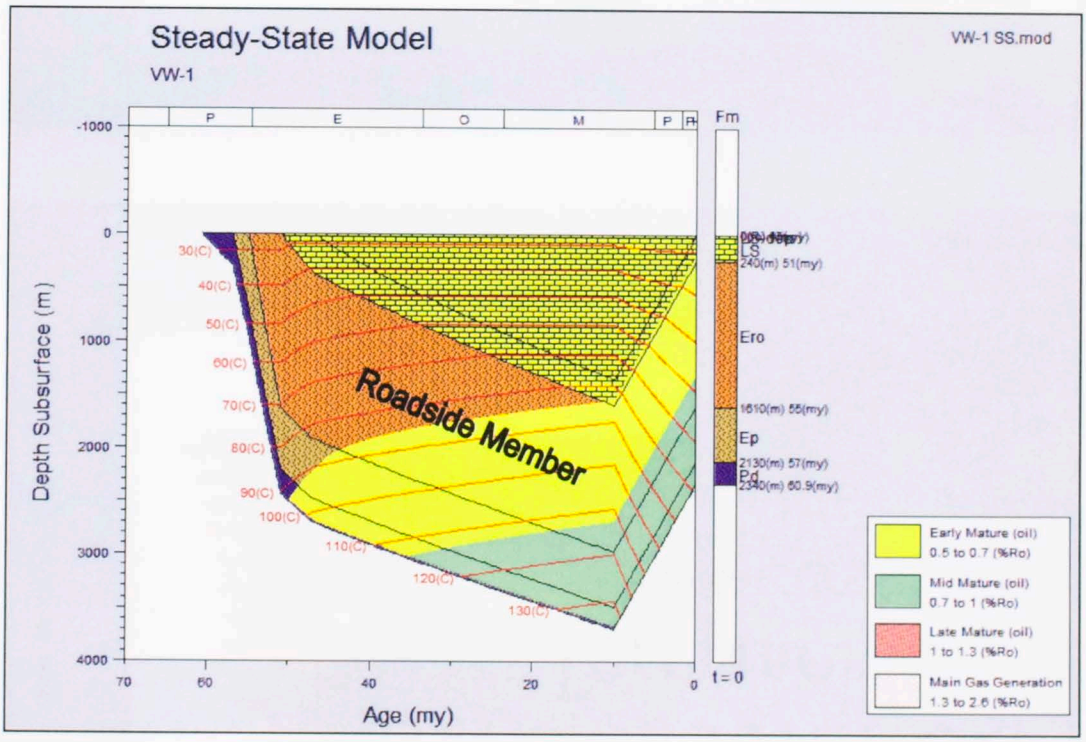

Figure 7.5.1: Burial History of VW-1 in steady-state heat flow conditions. Comparison of steady-state heat flow conditions to rifting heat flow 0.96 conditions in figure 7.5.2 shows that there is very little difference in the maturity of the rock units, and therefore, steady-state conditions will not continued to be displayed.

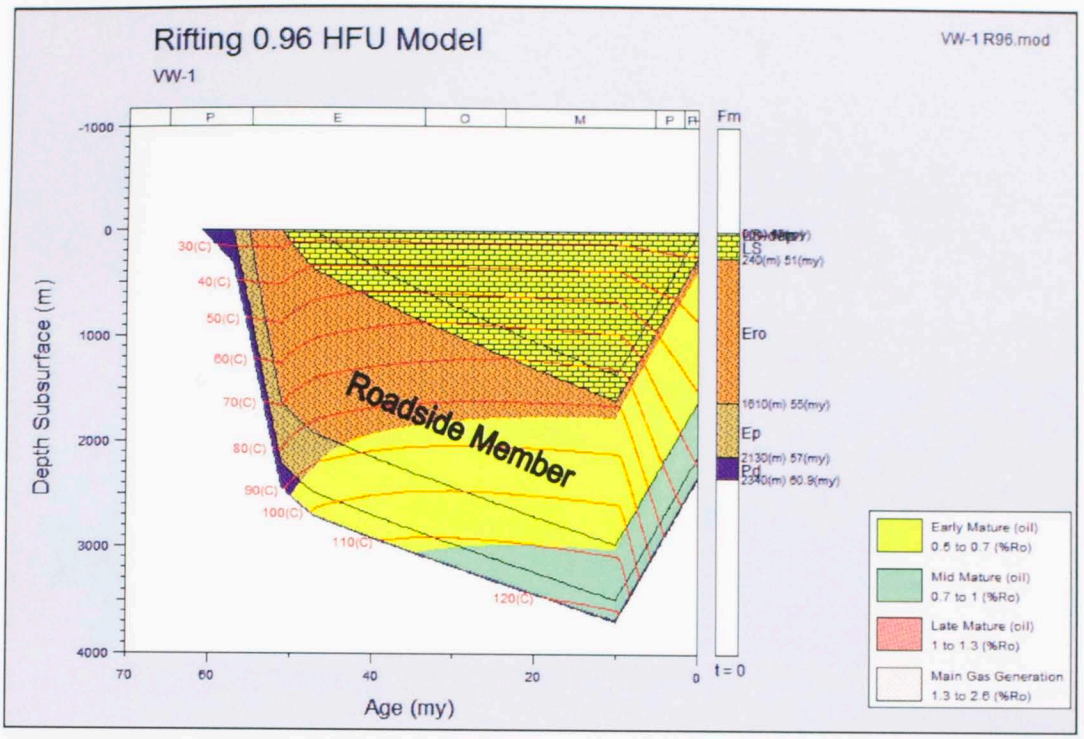

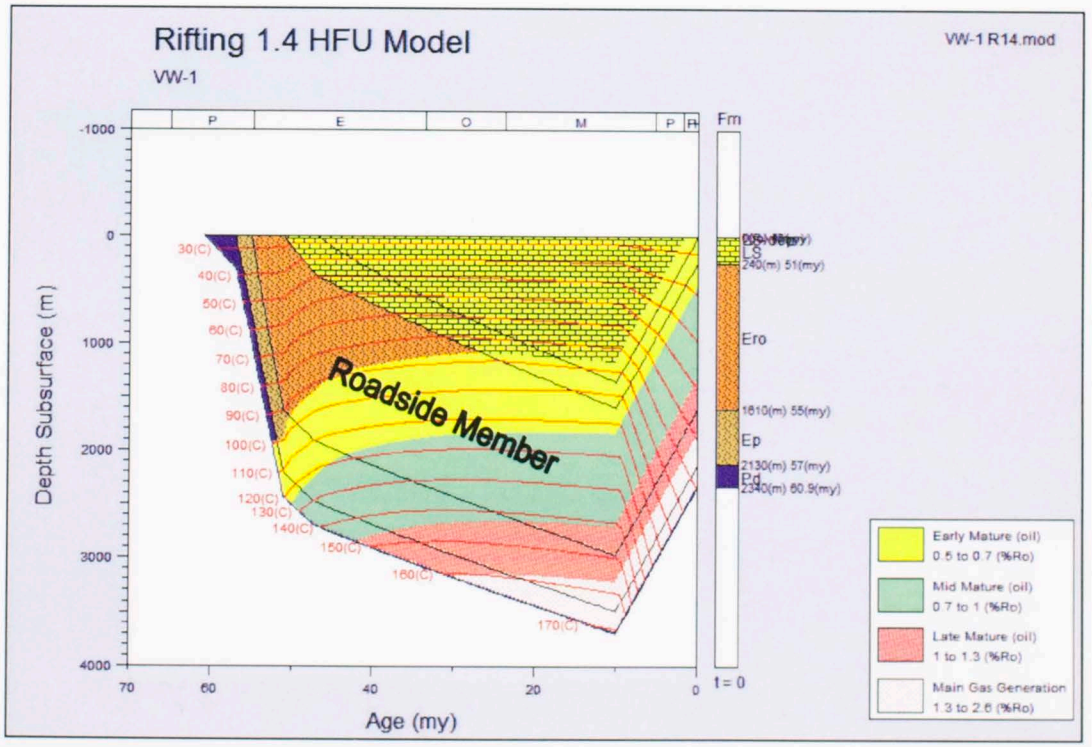

Figure 7.5.2: Burial History of VW-1 in rifting (0.96 H.F.U. and 1.4 H.F.U.) heat flow conditions.

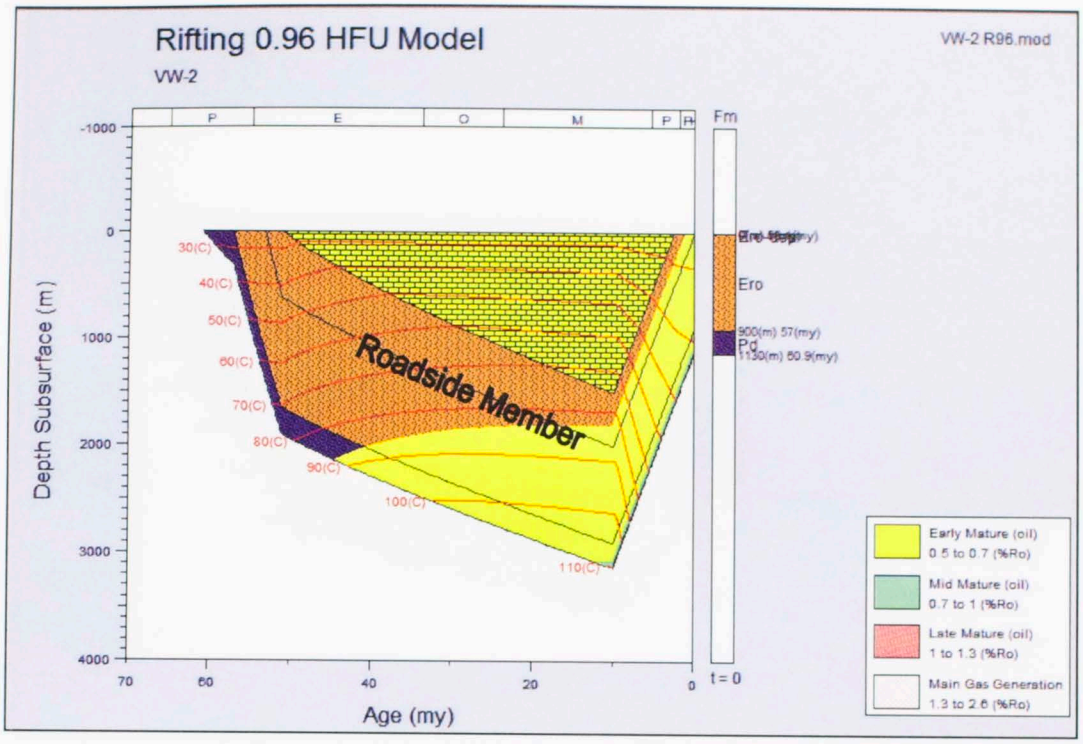

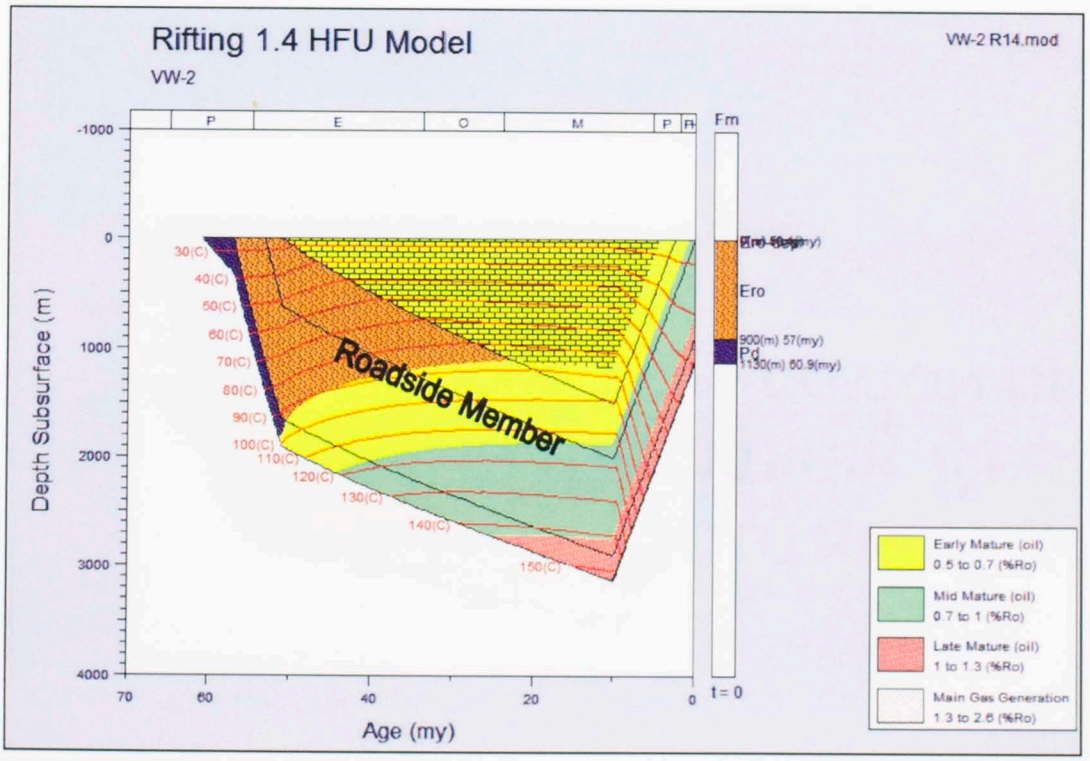

Figure 7.5.3: Burial History of VW-2 in rifting (0.96 H.F.U. and 1.4 H.F.U.) heat flow conditions.

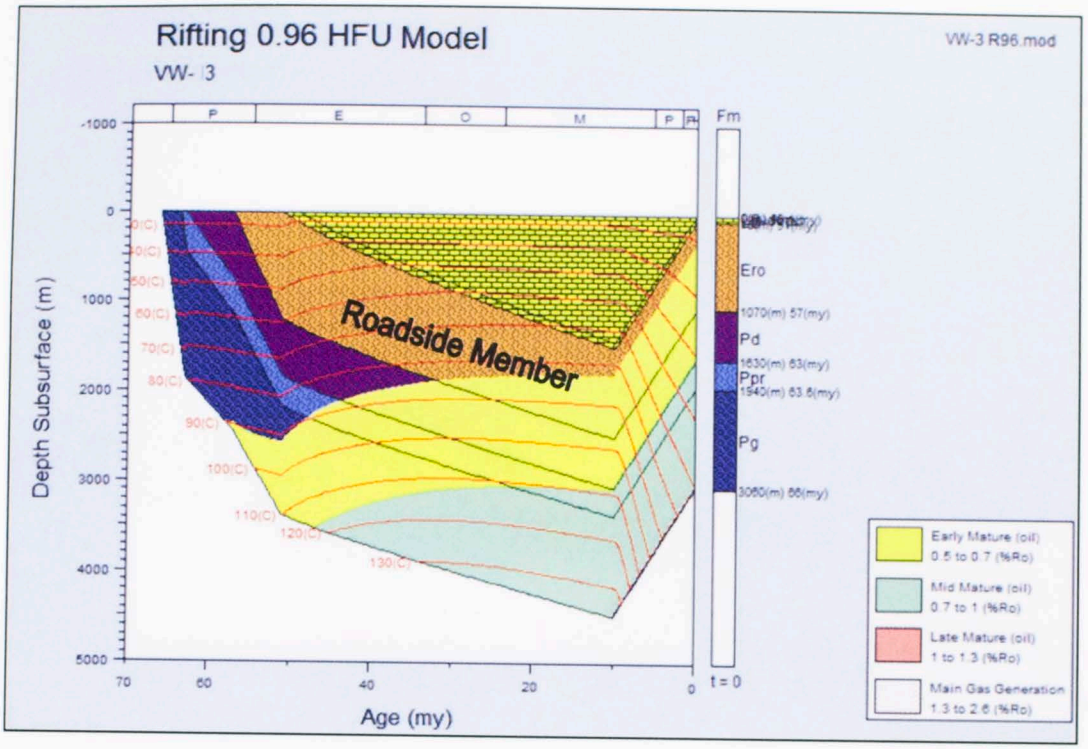

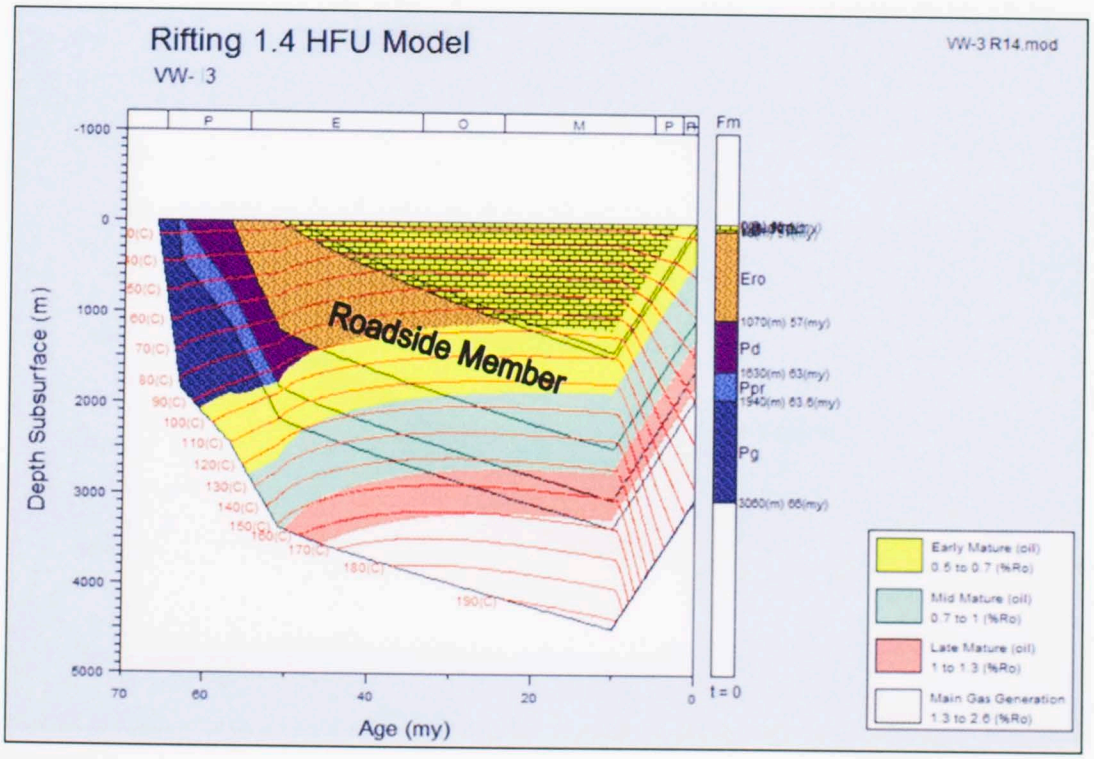

Figure 7.5.4: Burial History of VW-3 in rifting (0.96 H.F.U. and 1.4 H.F.U.) heat flow conditions.

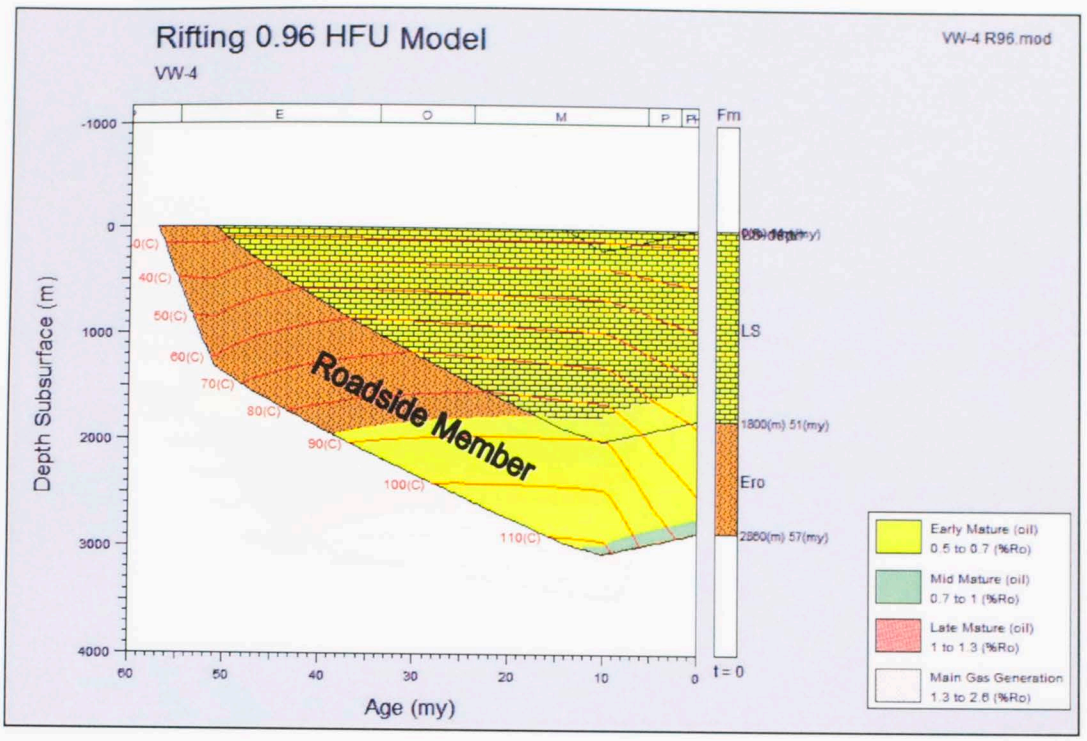

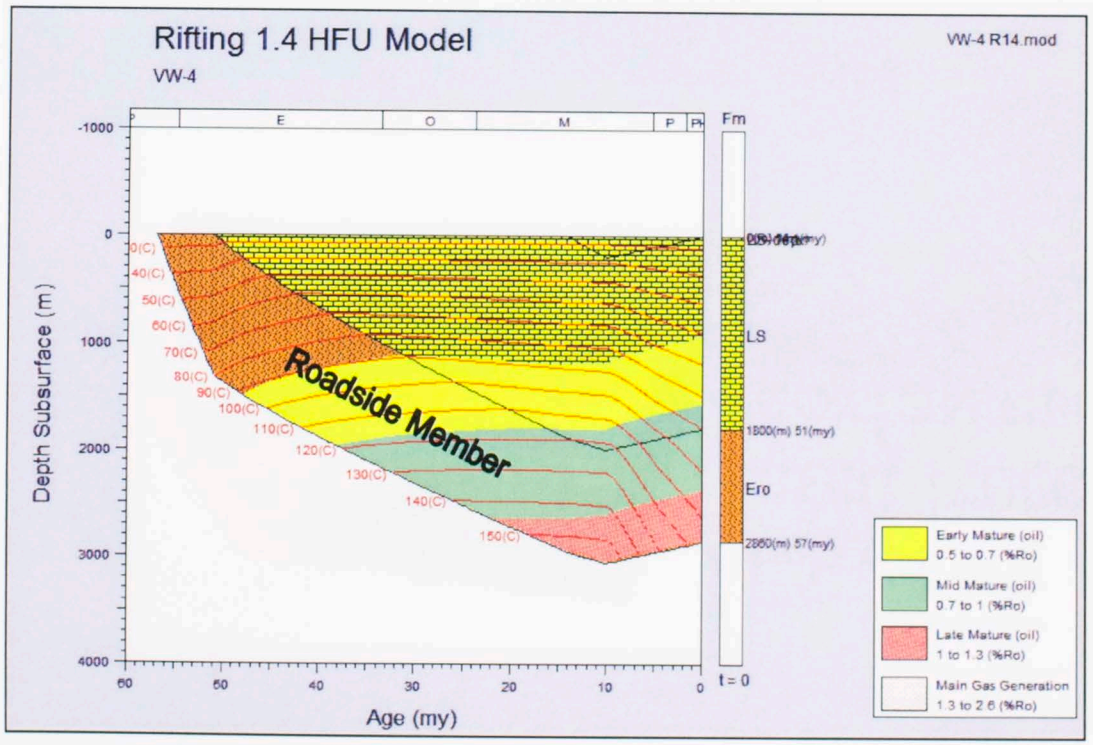

Figure 7.5.5: Burial History of VW-4 in rifting (0.96 H.F.U. and 1.4 H.F.U.) heat flow conditions.

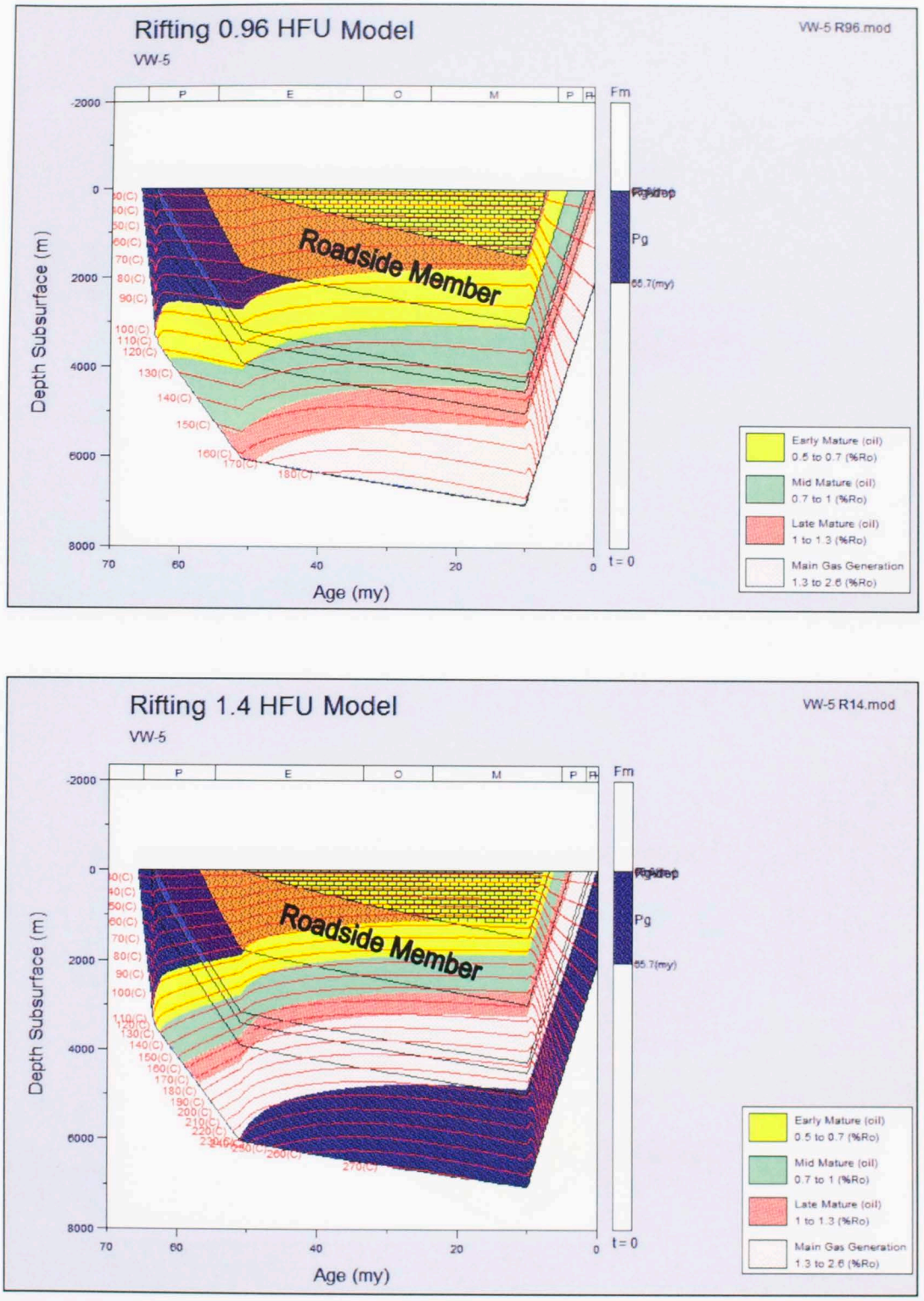

Figure 7.5.6: Burial History of VW-5 in rifting (0.96 H.F.U. and 1.4 H.F.U.) heat flow conditions.

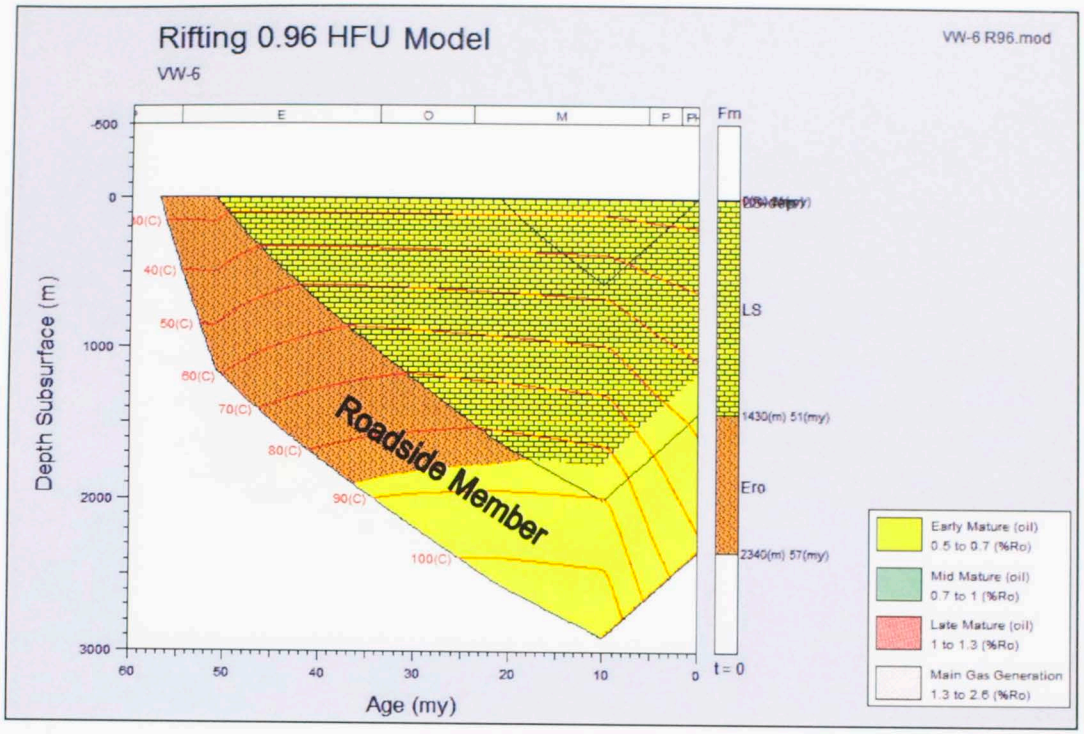

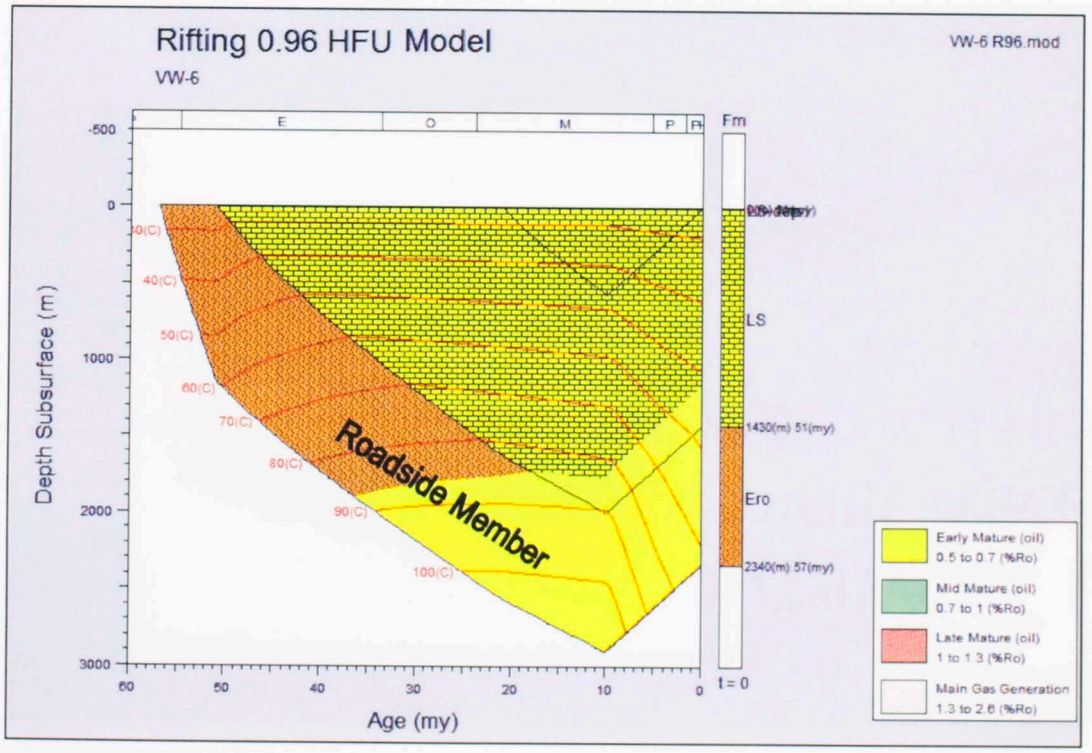

Figure 7.5.7: Burial History of VW-6 in rifting (0.96 H.F.U. and 1.4 H.F.U.) heat flow conditions.

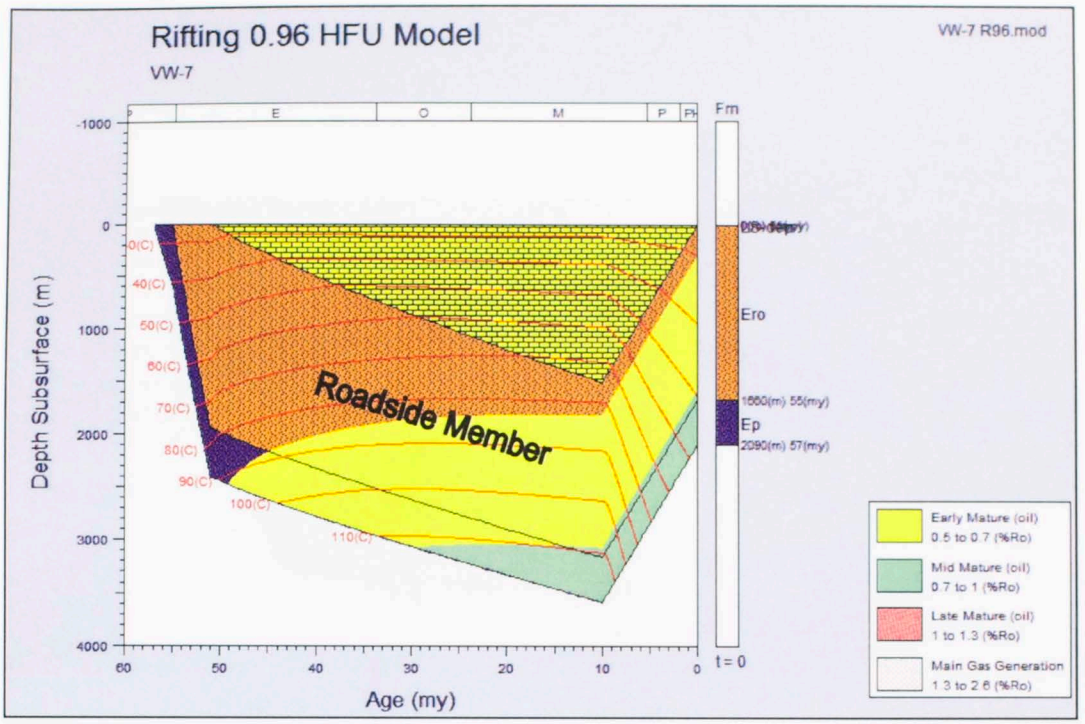

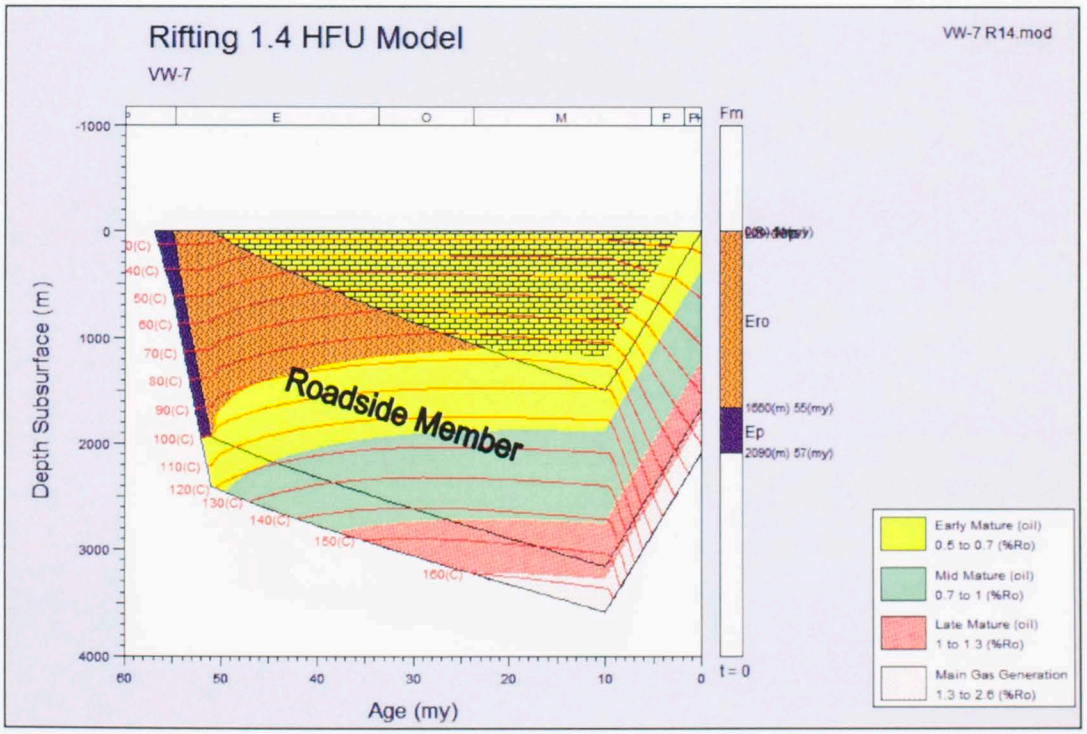

Figure 7.5.8: Burial History of VW-7 in rifting (0.96 H.F.U. and 1.4 H.F.U.) heat flow conditions.

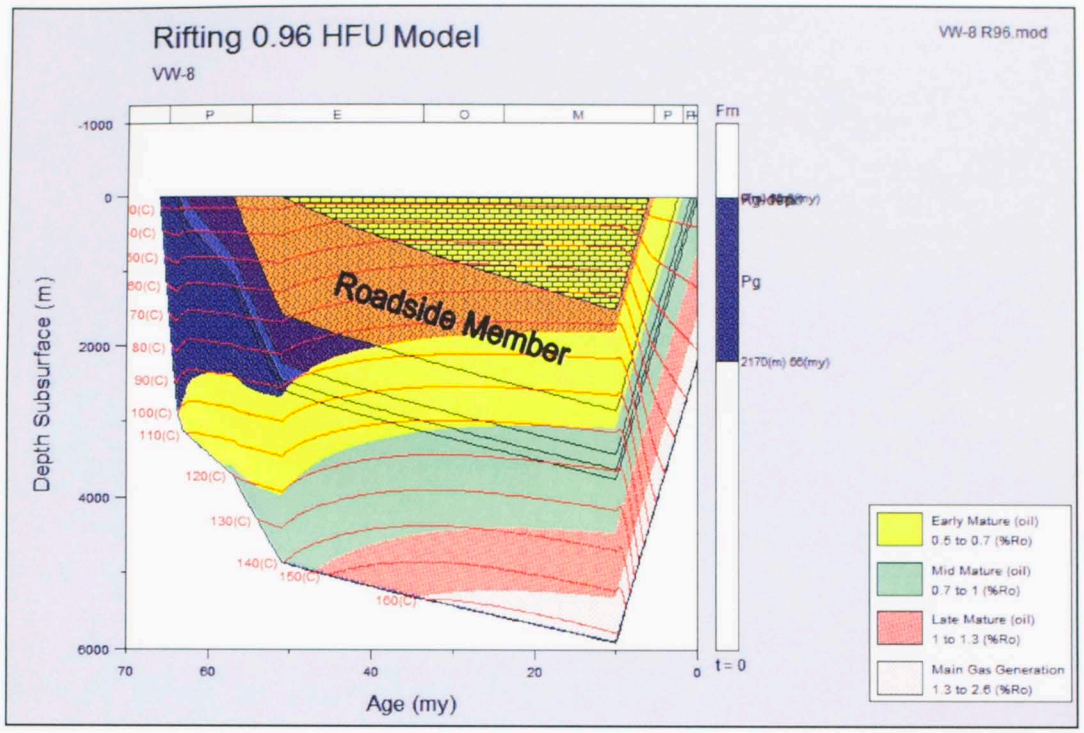

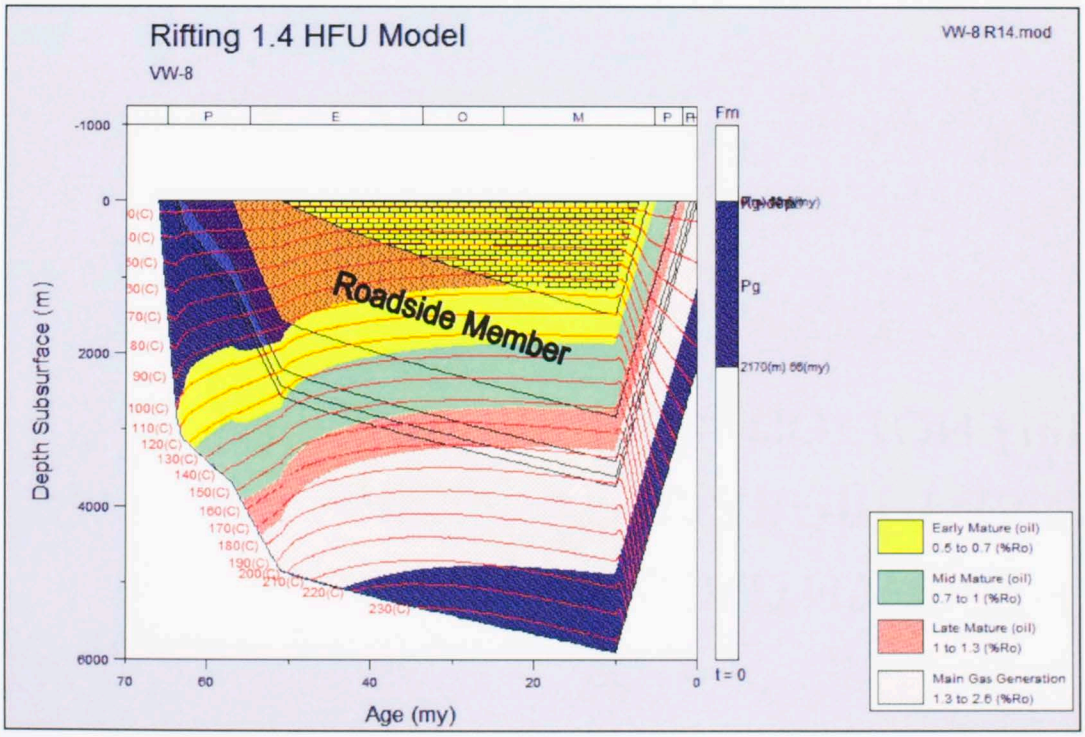

Figure 7.5.9: Burial History of VW-8 in rifting (0.96 H.F.U. and 1.4 H.F.U.) heat flow conditions.

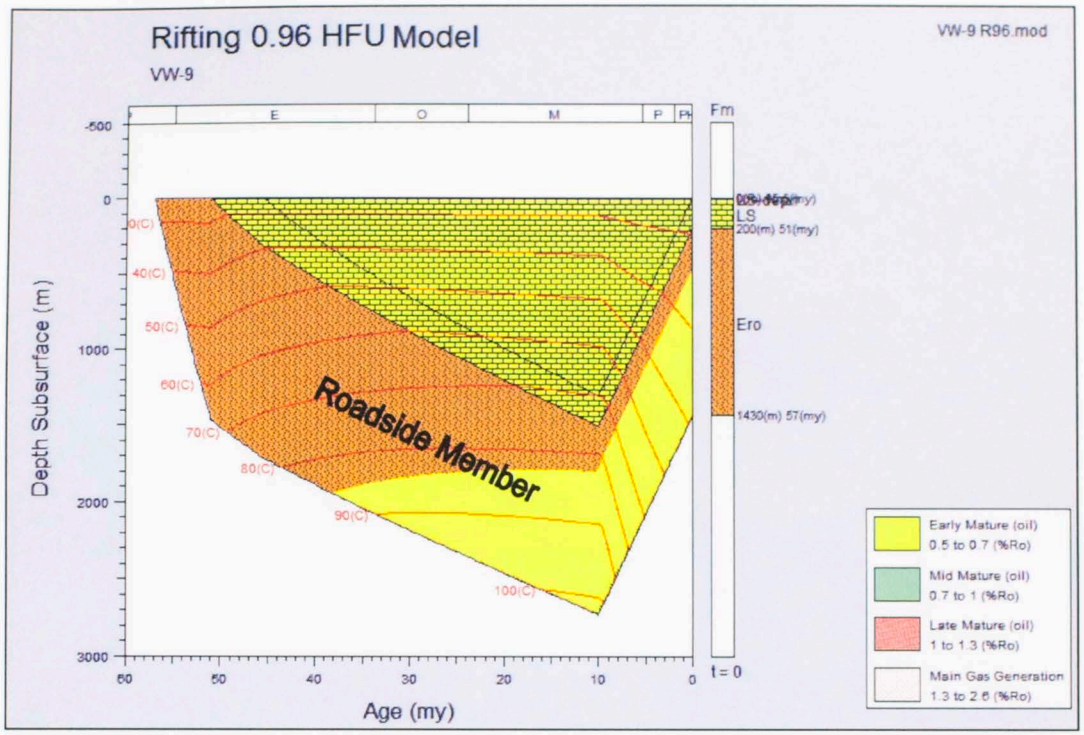

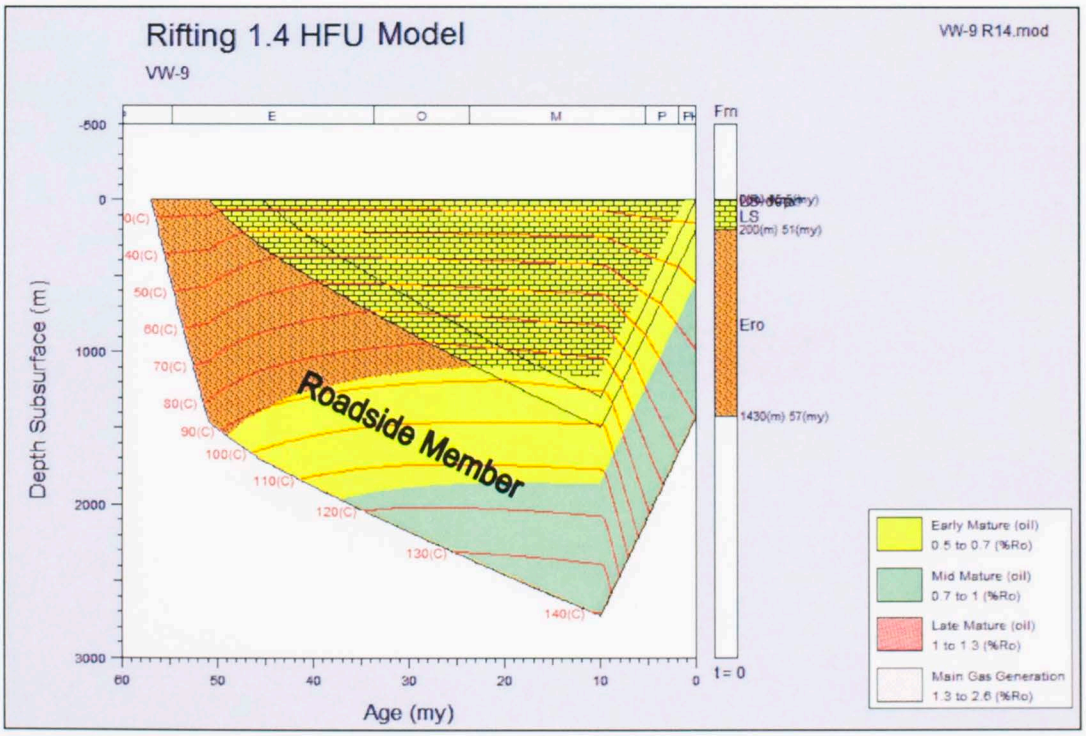

Figure 7.5.10: Burial History of VW-9 in rifting (0.96 H.F.U. and 1.4 H.F.U.) heat flow conditions.

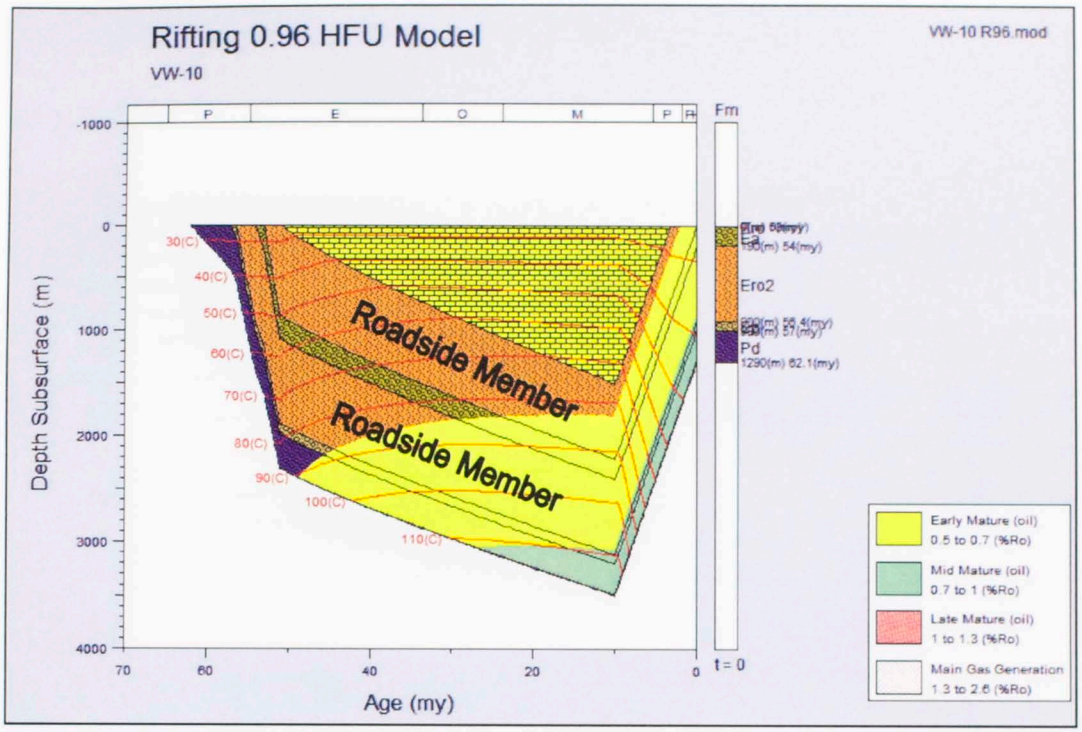

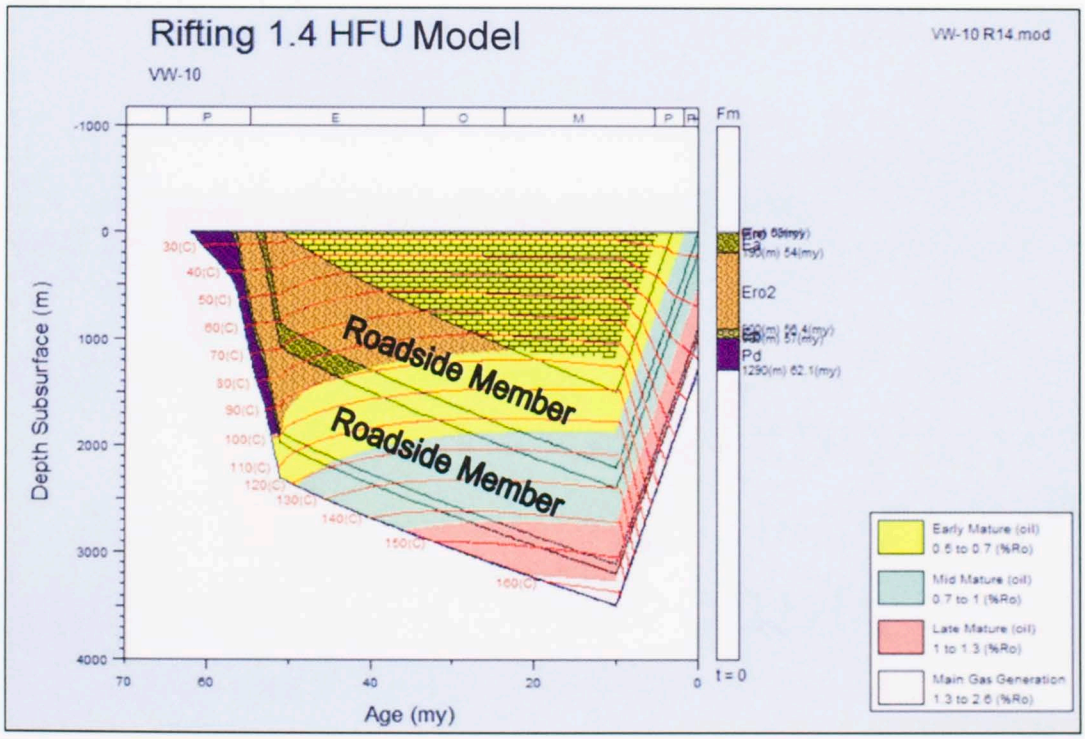

Figure 7.5.11: Burial History of VW-10 in rifting (0.96 H.F.U. and 1.4 H.F.U.) heat flow conditions.

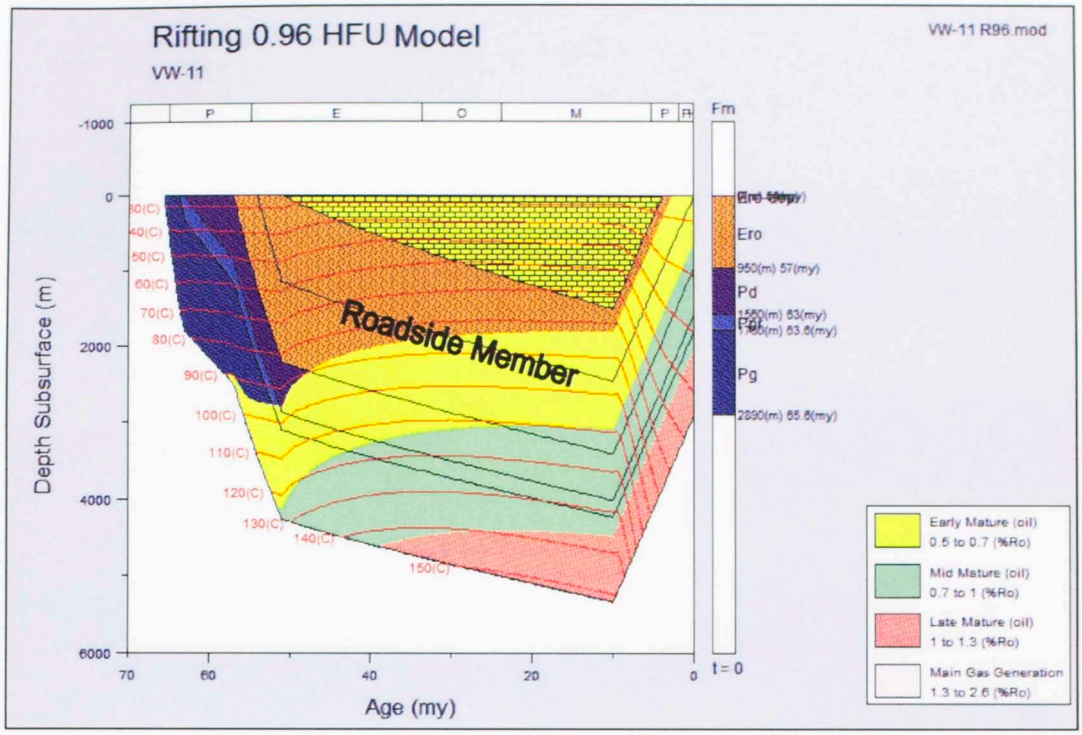

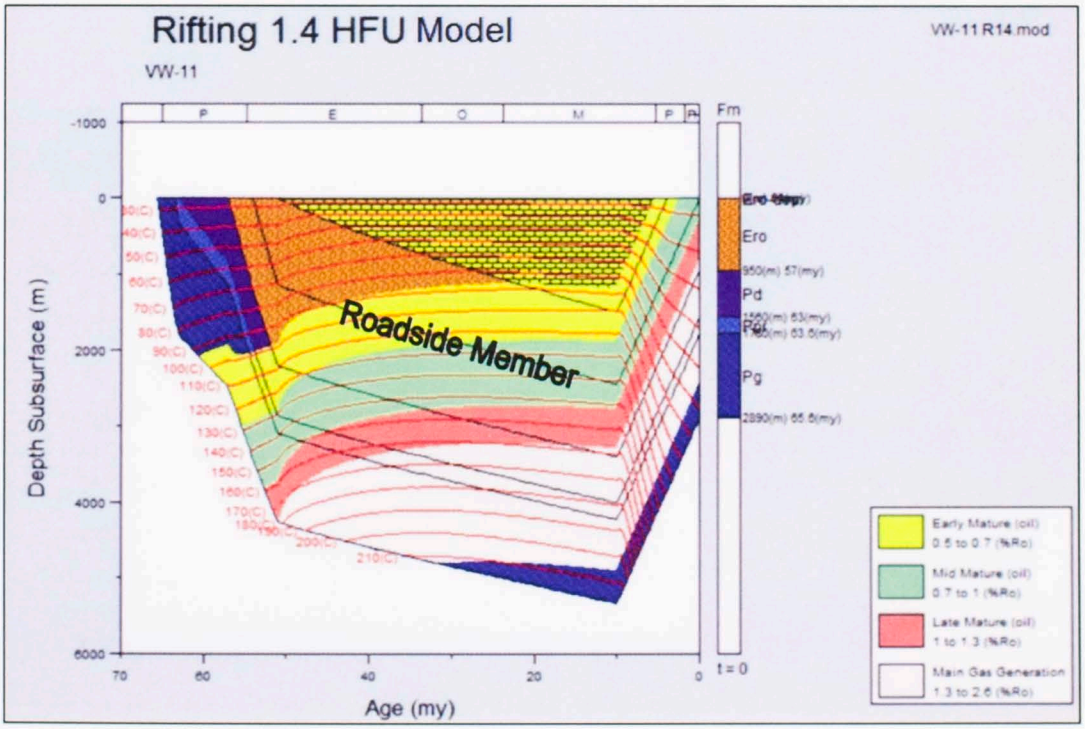

Figure 7.5.12: Burial History of VW-11 in rifting (0.96 H.F.U. and 1.4 H.F.U.) heat flow conditions.

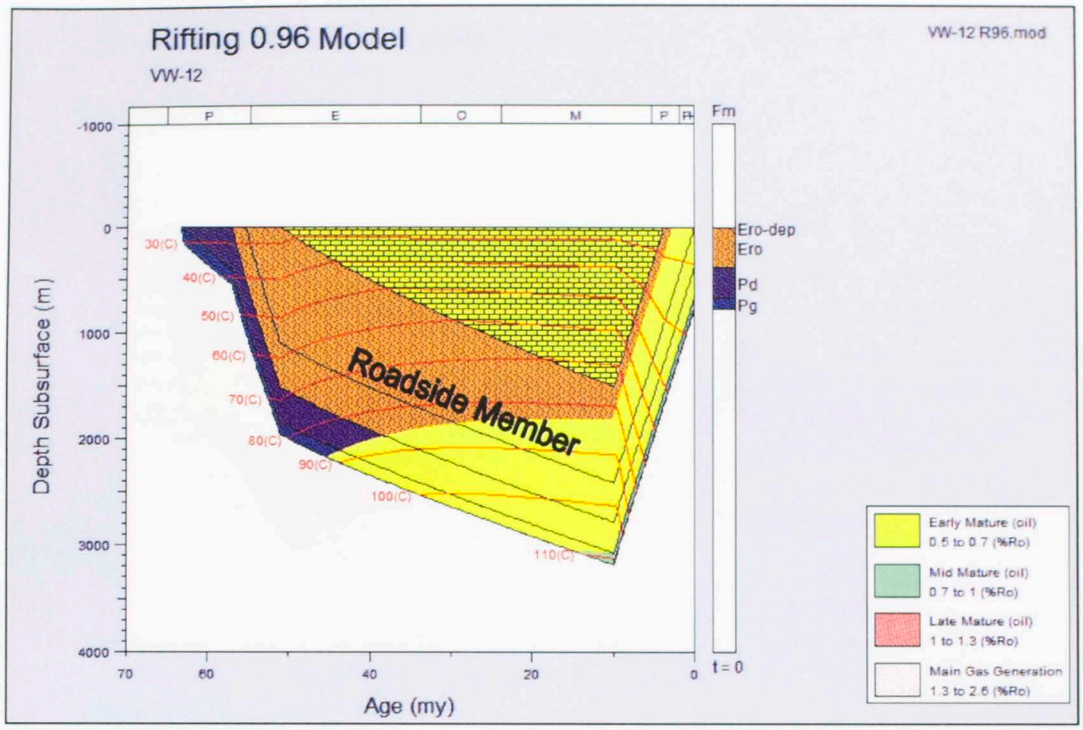

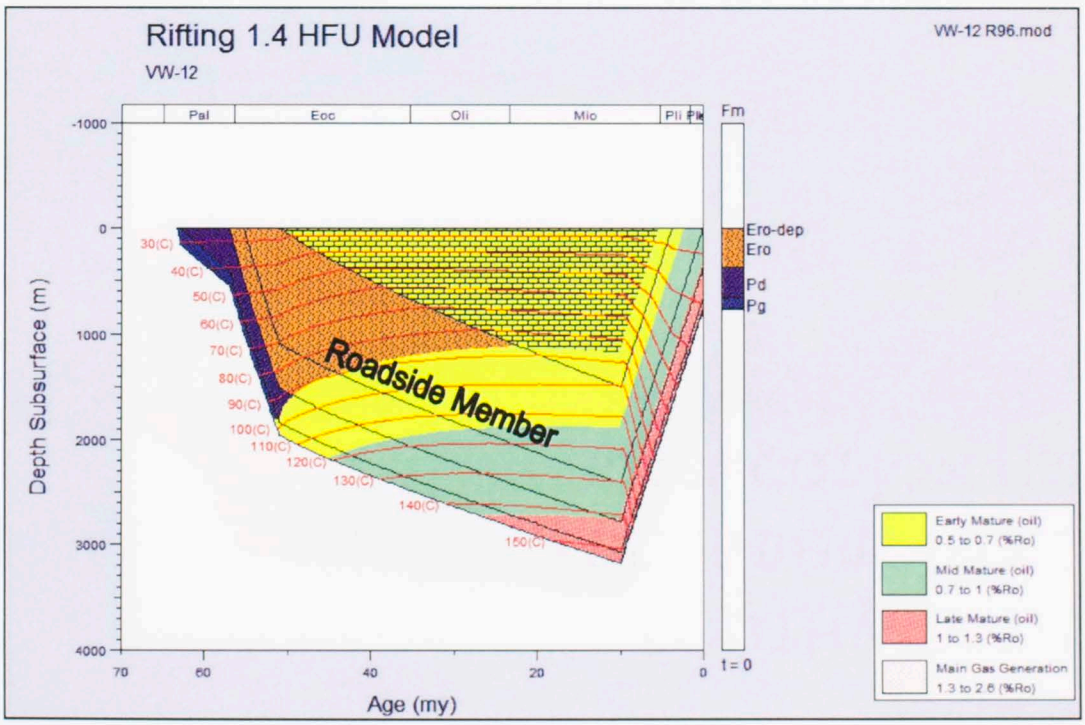

Figure 7.5.13: Burial History of VW-12 in rifting (0.96 H.F.U. and 1.4 H.F.U.) heat flow conditions.

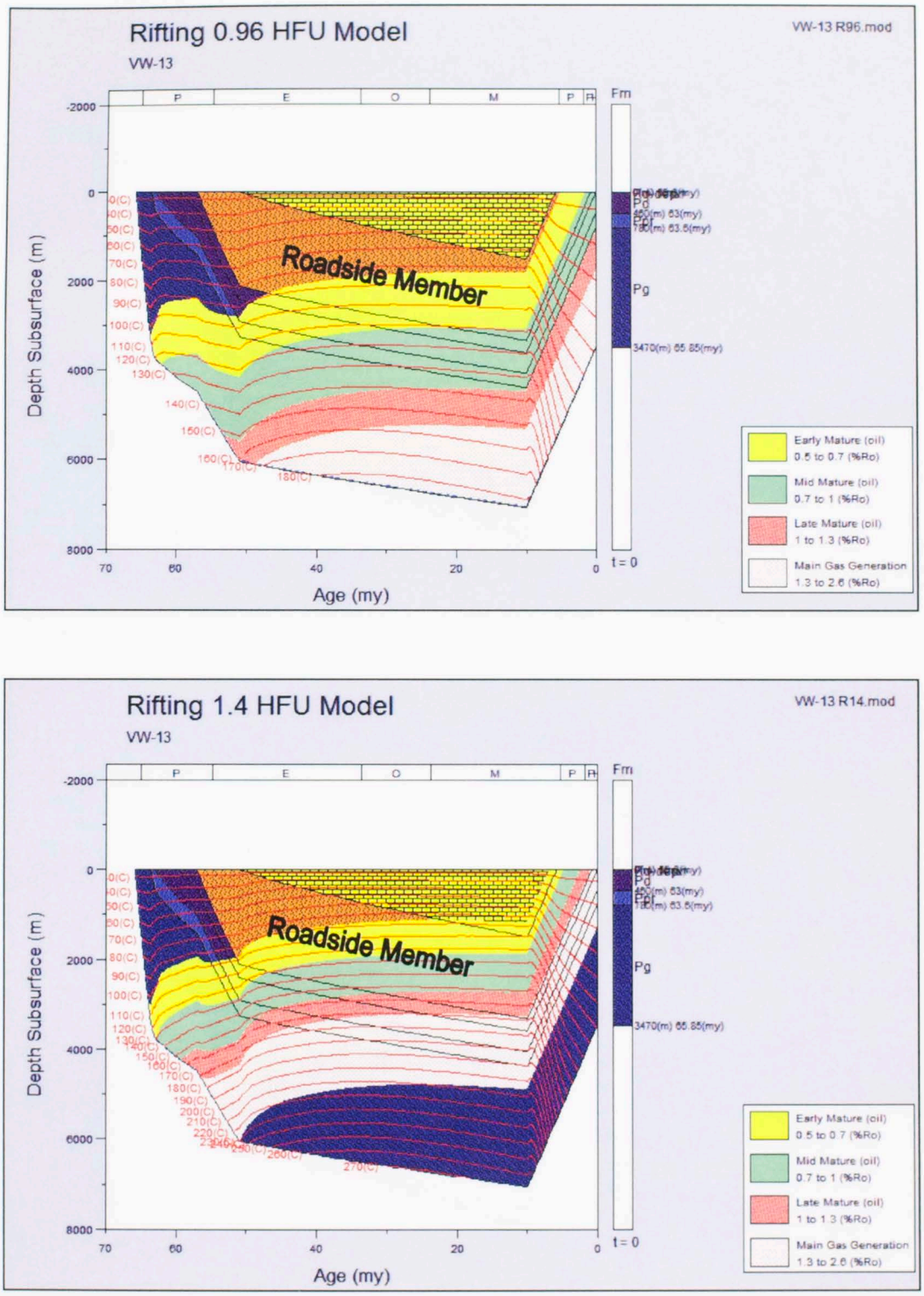

Figure 7.5.14: Burial History of VW-13 in rifting (0.96 H.F.U. and 1.4 H.F.U.) heat flow conditions.

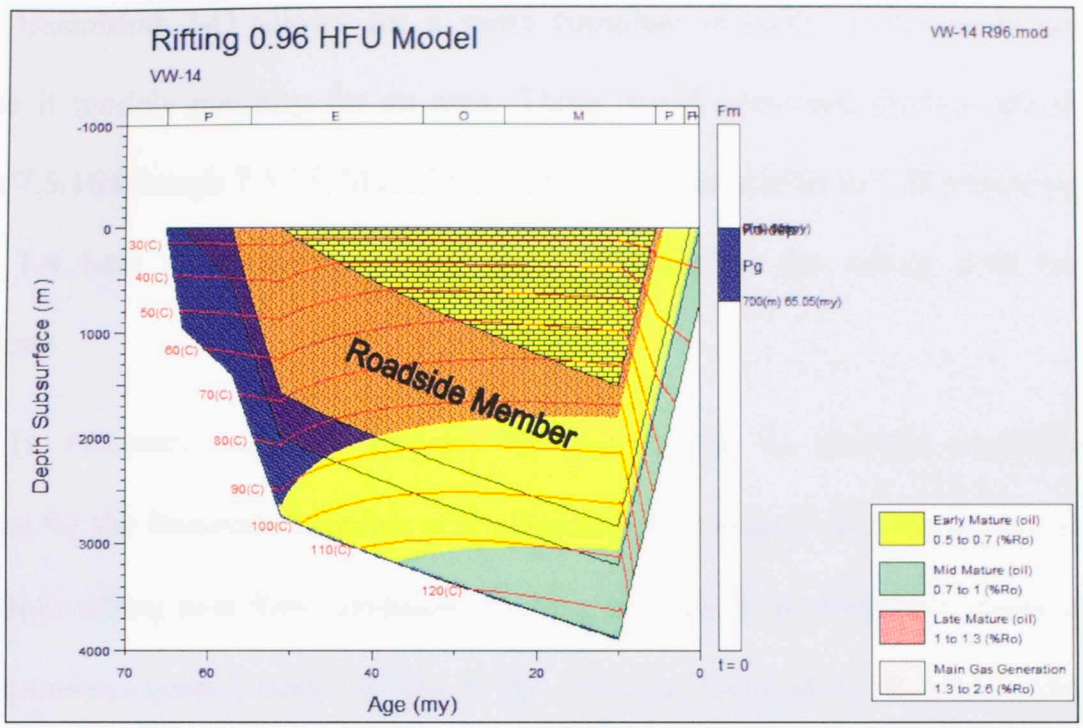

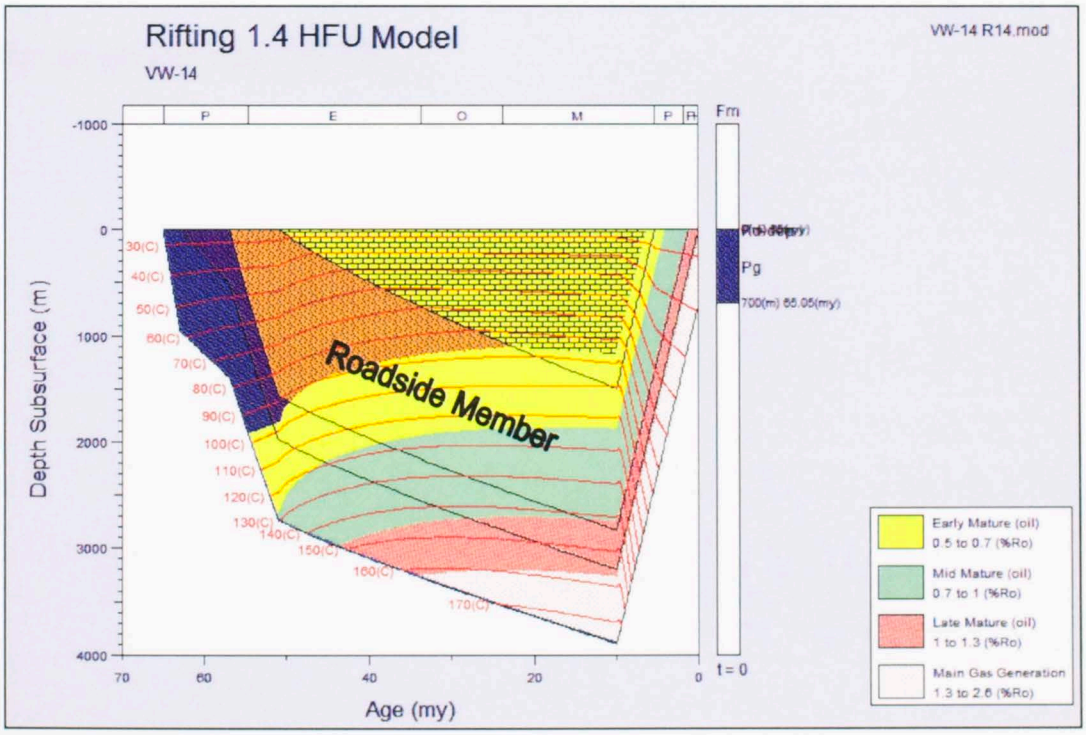

Figure 7.5.15: Burial History of VW-14 in rifting (0.96 H.F.U. and 1.4 H.F.U.) heat flow conditions.

BasinMod 2-D allows for a more complete maturity model to be generated because it models maturity for an area. These two-dimensional models are shown in figures 7.5.16 through 7.5.25. Maturity results in 2-D are similar to 1-D results in that the rifting 1.4 heat flow conditions are more mature than the rifting 0.96 heat flow conditions.

In summary, maturity analysis has shown that the thermal conditions were adequate for the Roadside Member of the Richmond Formation to have produced oil and gas in both rifting heat flow conditions. Rifting 1.4 heat flow conditions, however, have reach maturities greater than 2.6 $\%R_0$ in the deeper portions of the Roadside Member of the Richmond Formation; whereas, rifting 0.96 heat flow conditions have reached maturities no greater than 2.6 $\%R_0$.

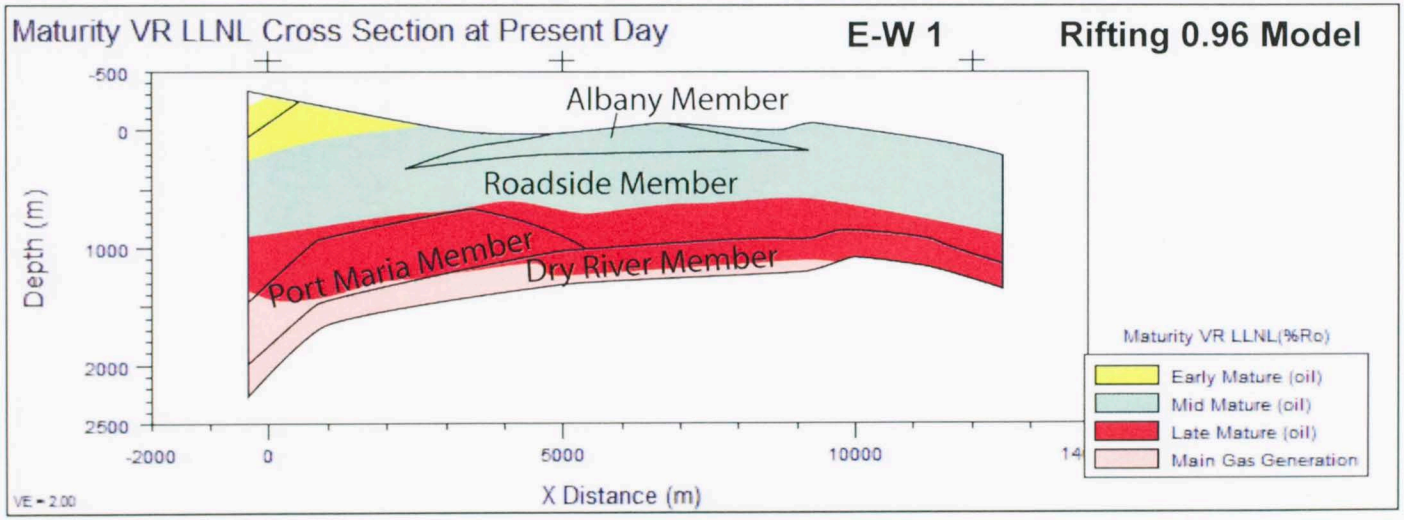

Figure 7.5.16: Maturity in cross-section E-W 1 for rifting 0.96 heat flow conditions. Windows are Early Mature 0.5 - 0.7 $\%R_0$ (yellow), Mid Mature 0.7 - 1.0 $\%R_0$ (green), Late Mature 1.0 - 1.3 $\%R_0$ (red), and Main Gas Generation 1.3 - 2.6 $\%R_0$ (light red).

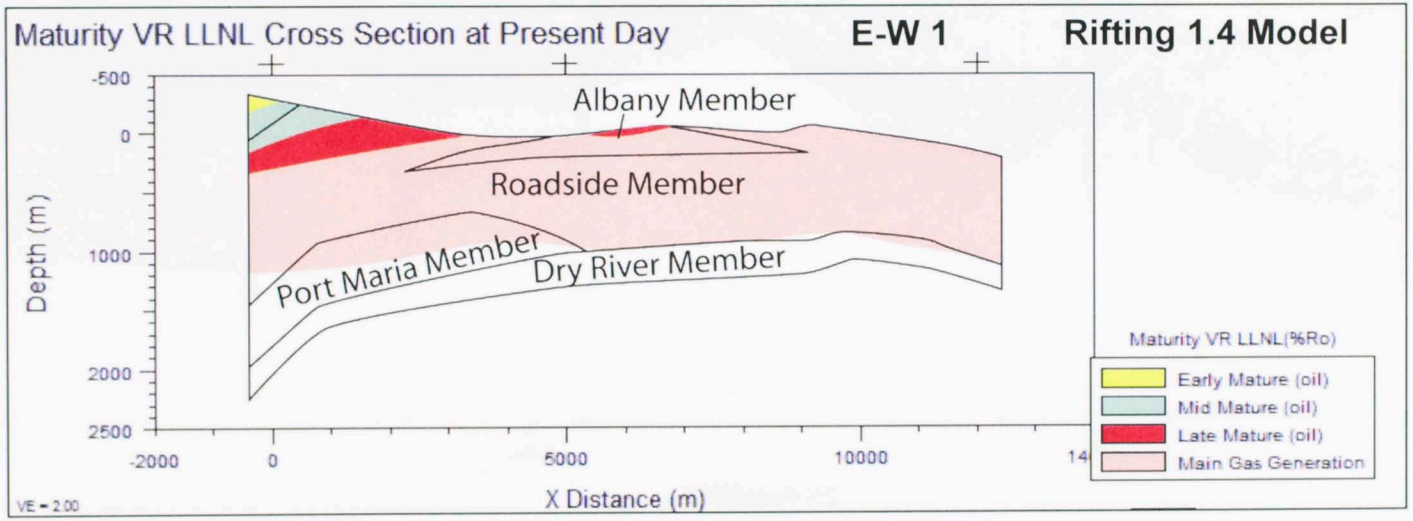

Figure 7.5.17: Maturity in cross-section E-W 2 for rifting 1.4 heat flow conditions. Windows are Early Mature 0.5 - 0.7 $\%R_0$ (yellow), Mid Mature 0.7 - 1.0 $\%R_0$ (green), Late Mature 1.0 - 1.3 $\%R_0$ (red), and Main Gas Generation 1.3 - 2.6 $\%R_0$ (light red).

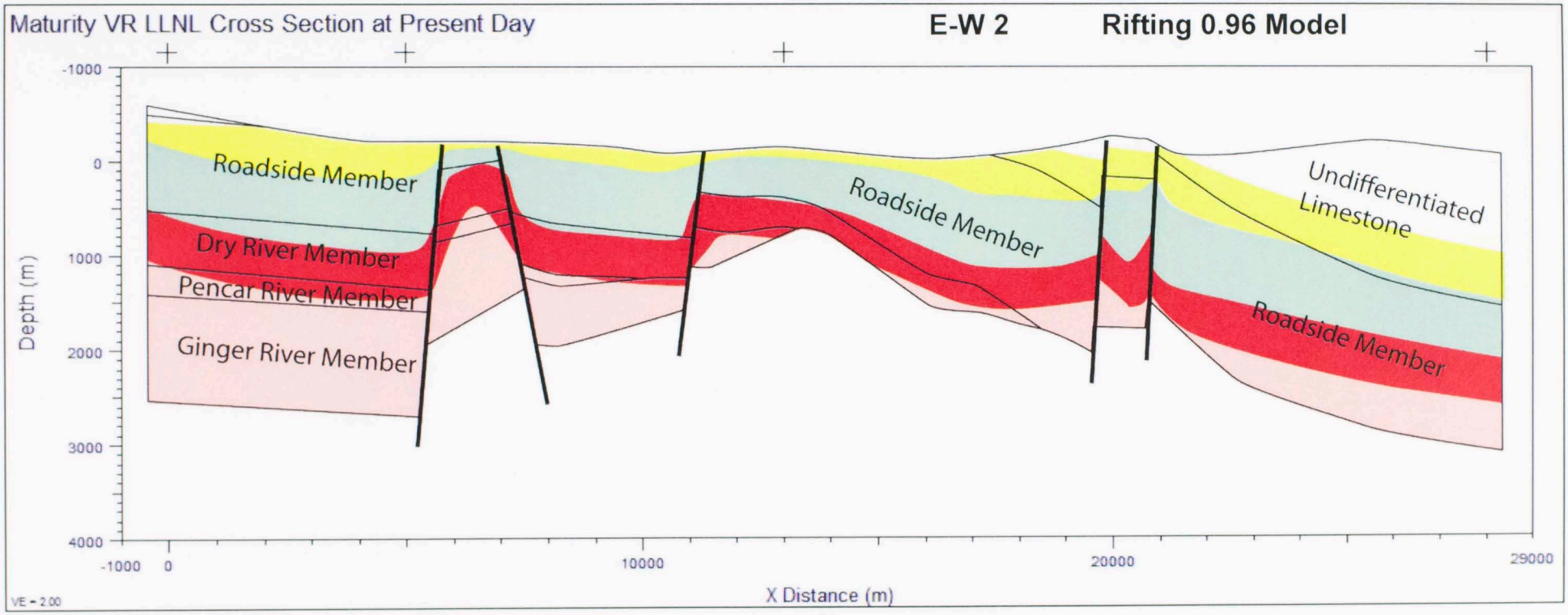

Figure 7.5.18: Maturity in cross-section E-W 2 for rifting 0.96 heat flow conditions. Windows are Early Mature 0.5 - 0.7 $\%R_0$ (yellow), Mid Mature 0.7 - 1.0 $\%R_0$ (green), Late Mature 1.0 - 1.3 $\%R_0$ (red), and Main Gas Generation 1.3 - 2.6 $\%R_0$ (light red).

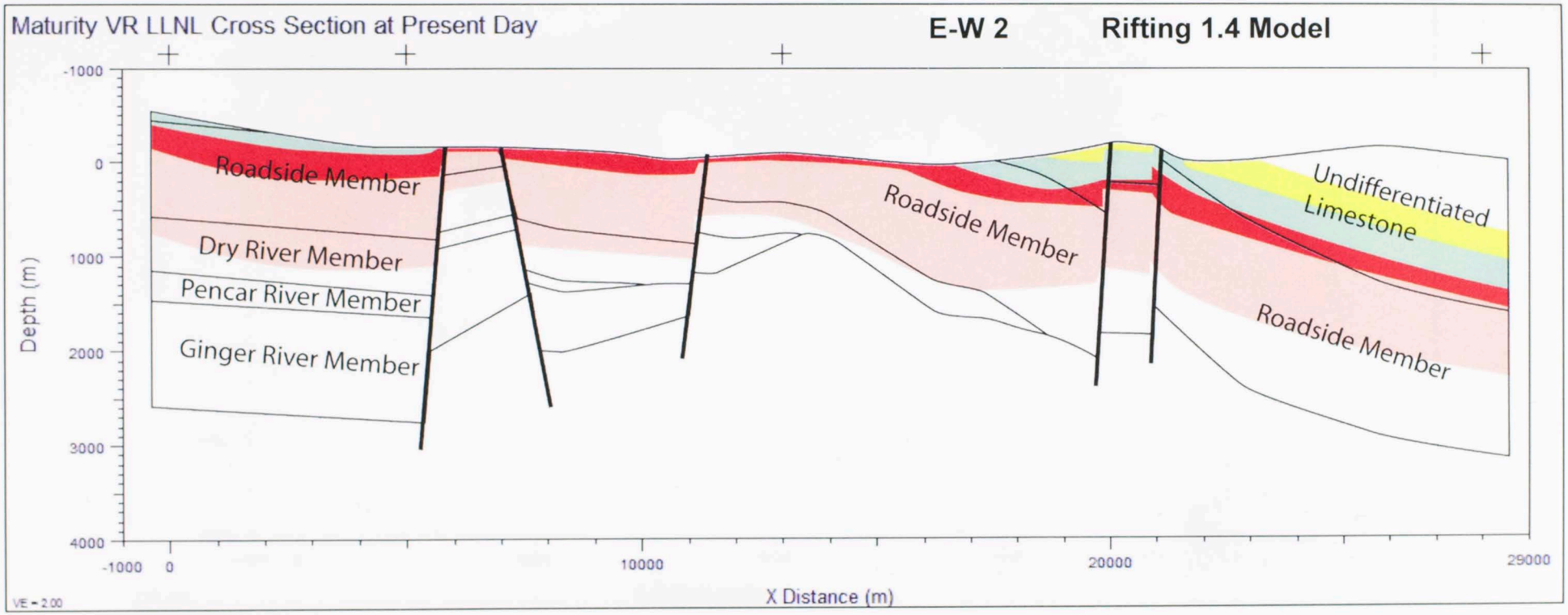

Figure 7.5.19: Maturity in cross-section E-W 2 for rifting 1.4 heat flow conditions. Windows are Early Mature 0.5 - 0.7 $\%R_0$ (yellow), Mid Mature 0.7 - 1.0 $\%R_0$ (green), Late Mature 1.0 - 1.3 $\%R_0$ (red), and Main Gas Generation 1.3 - 2.6 $\%R_0$ (light red).

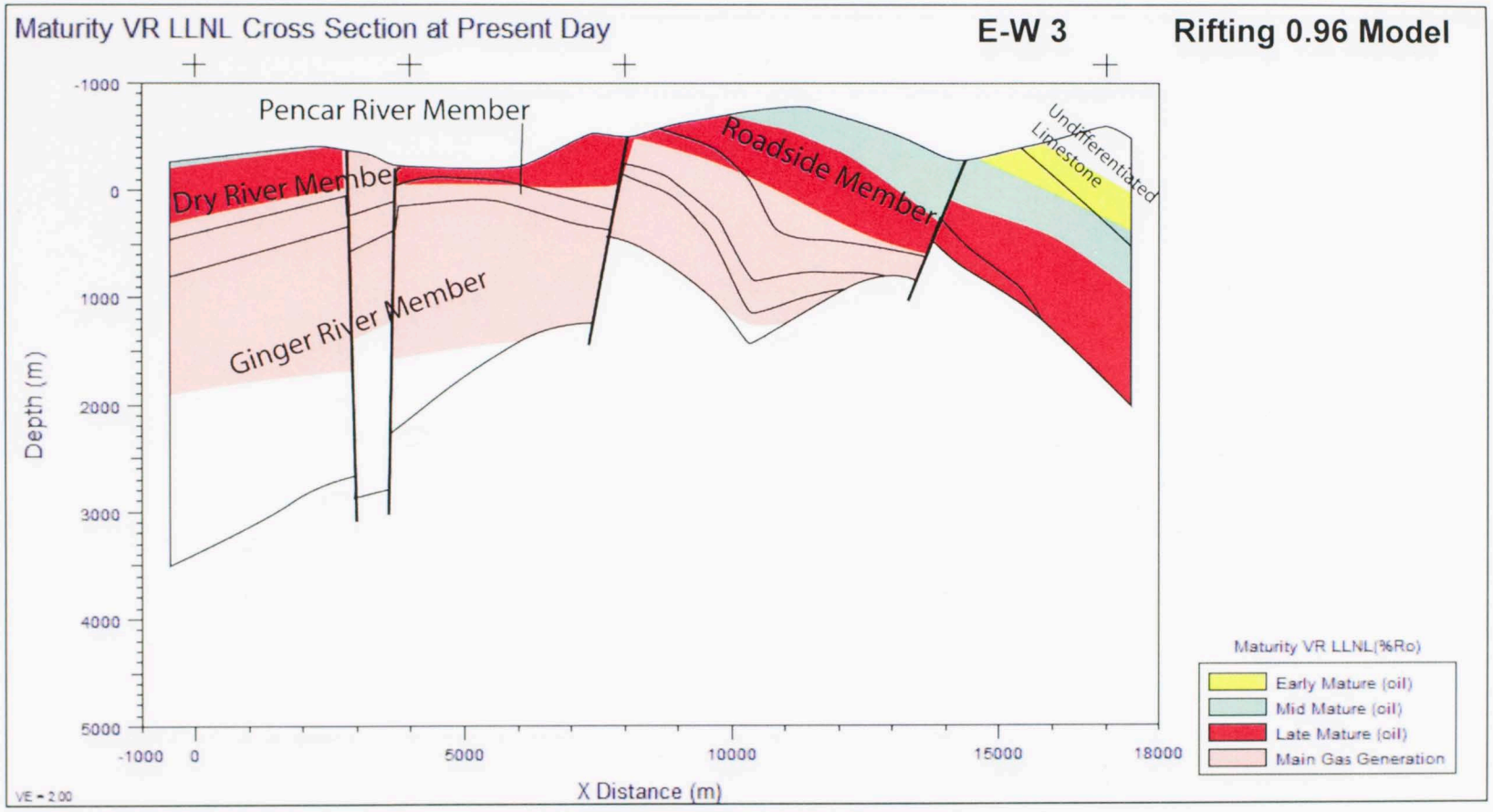

Figure 7.5.20: Maturity in cross-section E-W 3 for rifting 0.96 heat flow conditions. Windows are Early Mature 0.5 - 0.7 $\%R_0$ (yellow), Mid Mature 0.7 - 1.0 $\%R_0$ (green), Late Mature 1.0 - 1.3 $\%R_0$ (red), and Main Gas Generation 1.3 - 2.6 $\%R_0$ (light red).

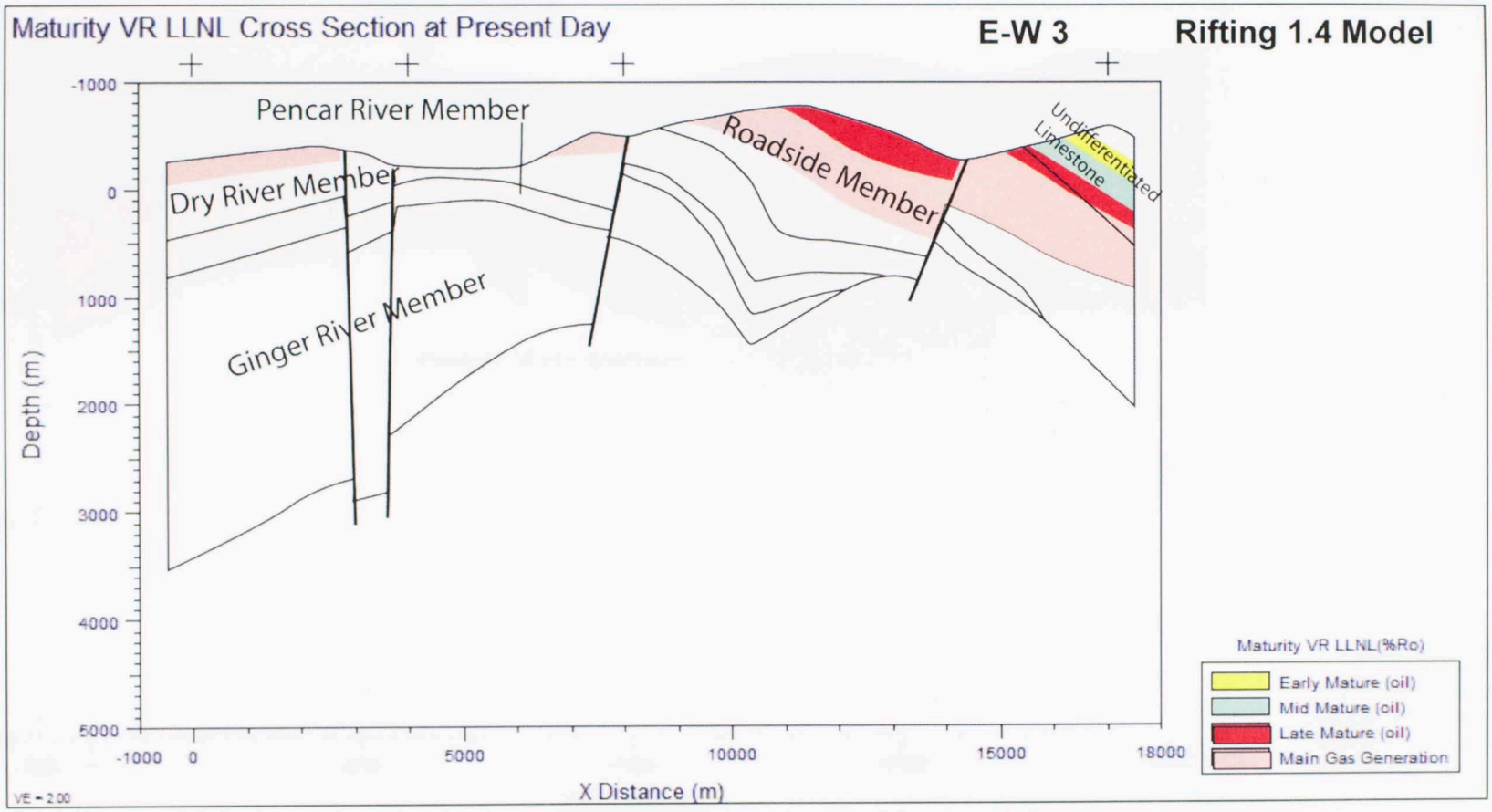

Figure 7.5.21: Maturity in cross-section E-W 3 for rifting 1.4 heat flow conditions. Windows are Early Mature 0.5 - 0.7 $\%R_0$ (yellow), Mid Mature 0.7 - 1.0 $\%R_0$ (green), Late Mature 1.0 - 1.3 $\%R_0$ (red), and Main Gas Generation 1.3 - 2.6 $\%R_0$ (light red).

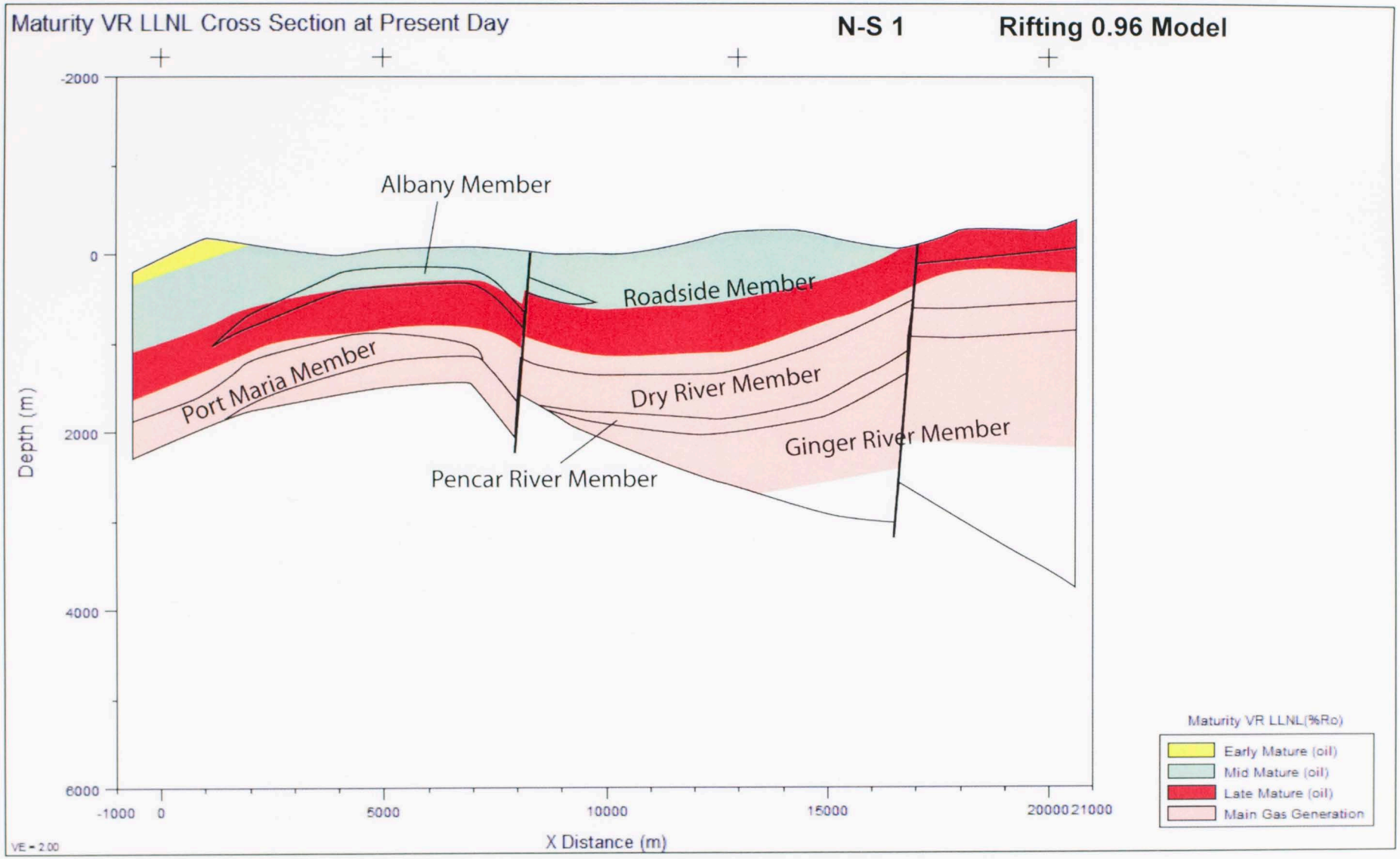

Figure 7.5.22: Maturity in cross-section N-S 1 for rifting 0.96 heat flow conditions. Windows are Early Mature 0.5 - 0.7 $\%R_0$ (yellow), Mid Mature 0.7 - 1.0 $\%R_0$ (green), Late Mature 1.0 - 1.3 $\%R_0$ (red), and Main Gas Generation 1.3 - 2.6 $\%R_0$ (light red).

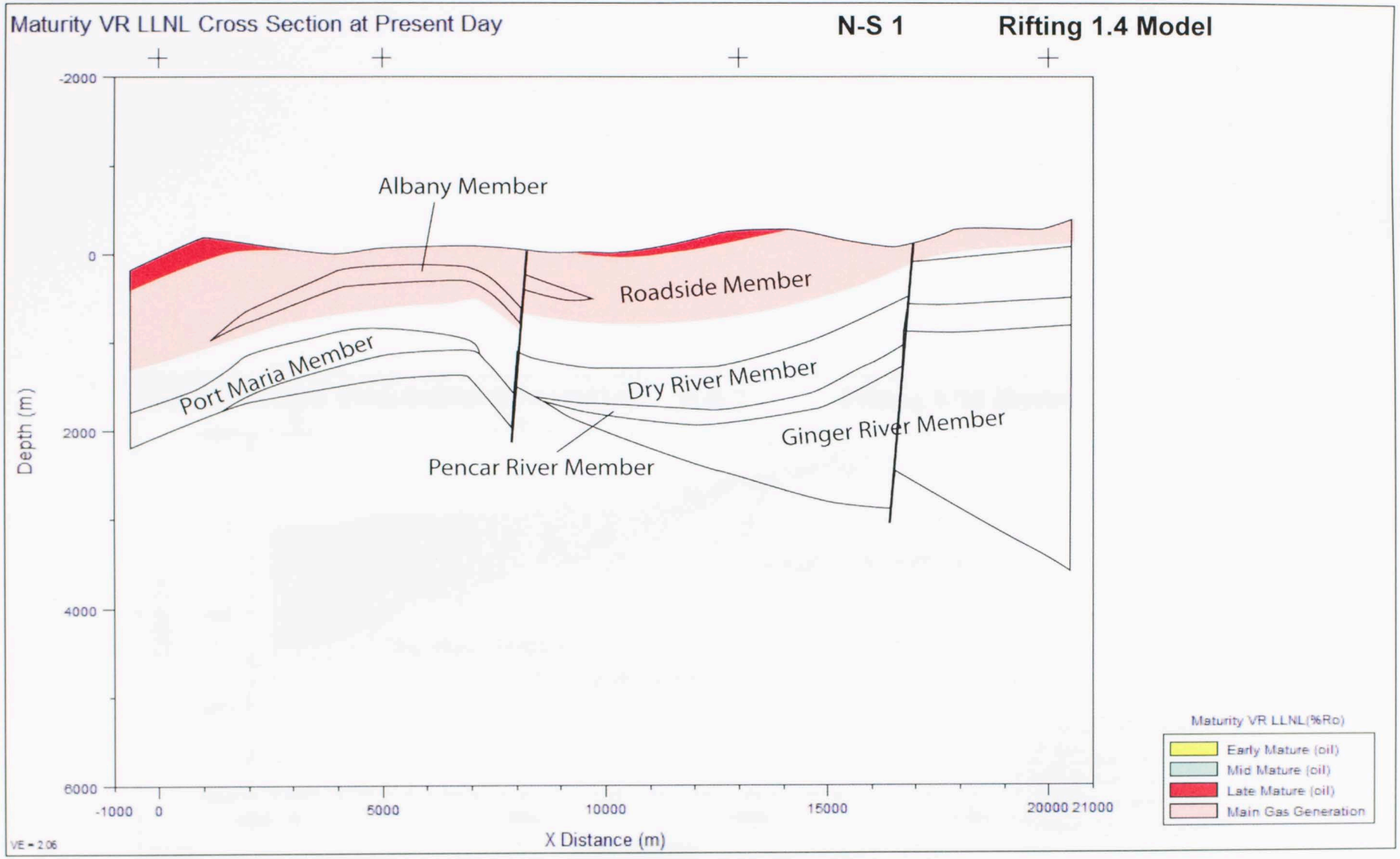

Figure 7.5.23: Maturity in cross-section N-S 1 for rifting 1.4 heat flow conditions. Windows are Early Mature 0.5 - 0.7 $\%R_0$ (yellow), Mid Mature 0.7 - 1.0 $\%R_0$ (green), Late Mature 1.0 - 1.3 $\%R_0$ (red), and Main Gas Generation 1.3 - 2.6 $\%R_0$ (light red).

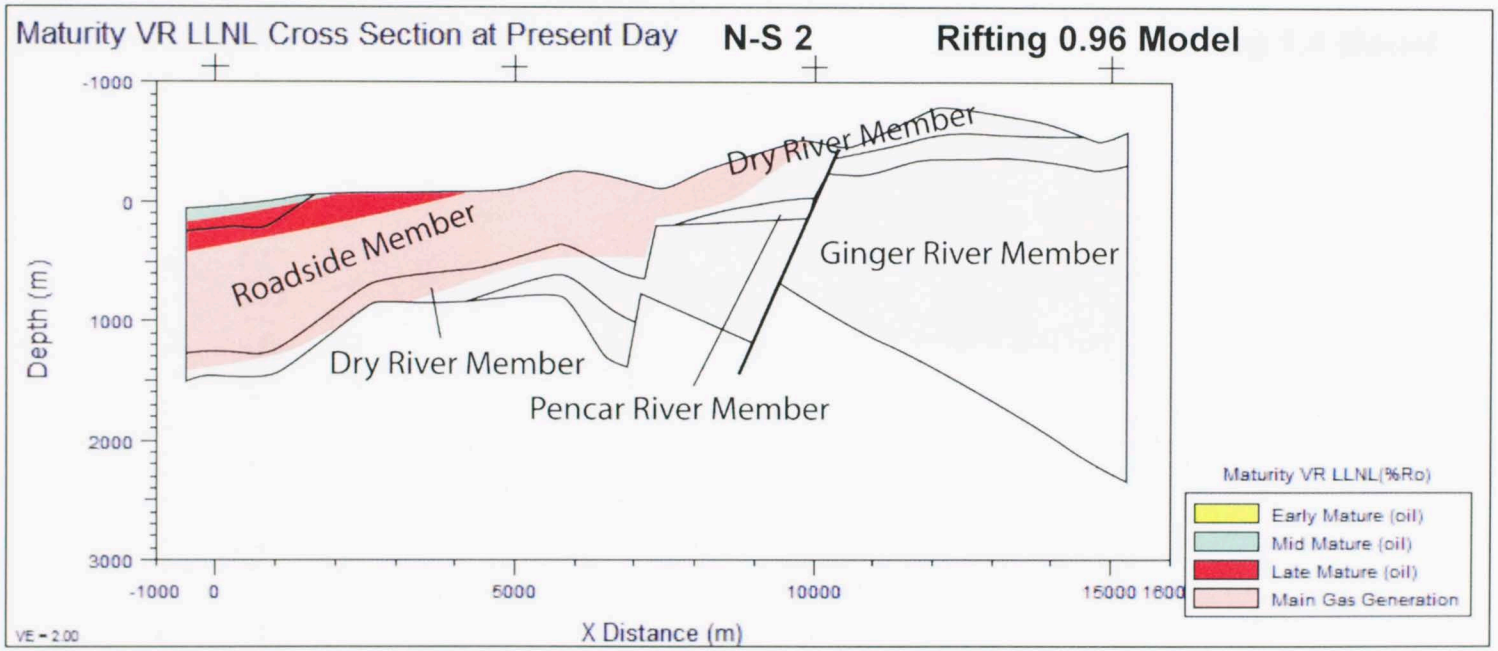

Figure 7.5.24: Maturity in cross-section N-S 2 for rifting 0.96 heat flow conditions. Windows are Early Mature 0.5 - 0.7 $\%R_0$ (yellow), Mid Mature 0.7 - 1.0 $\%R_0$ (green), Late Mature 1.0 - 1.3 $\%R_0$ (red), and Main Gas Generation 1.3 - 2.6 $\%R_0$ (light red).

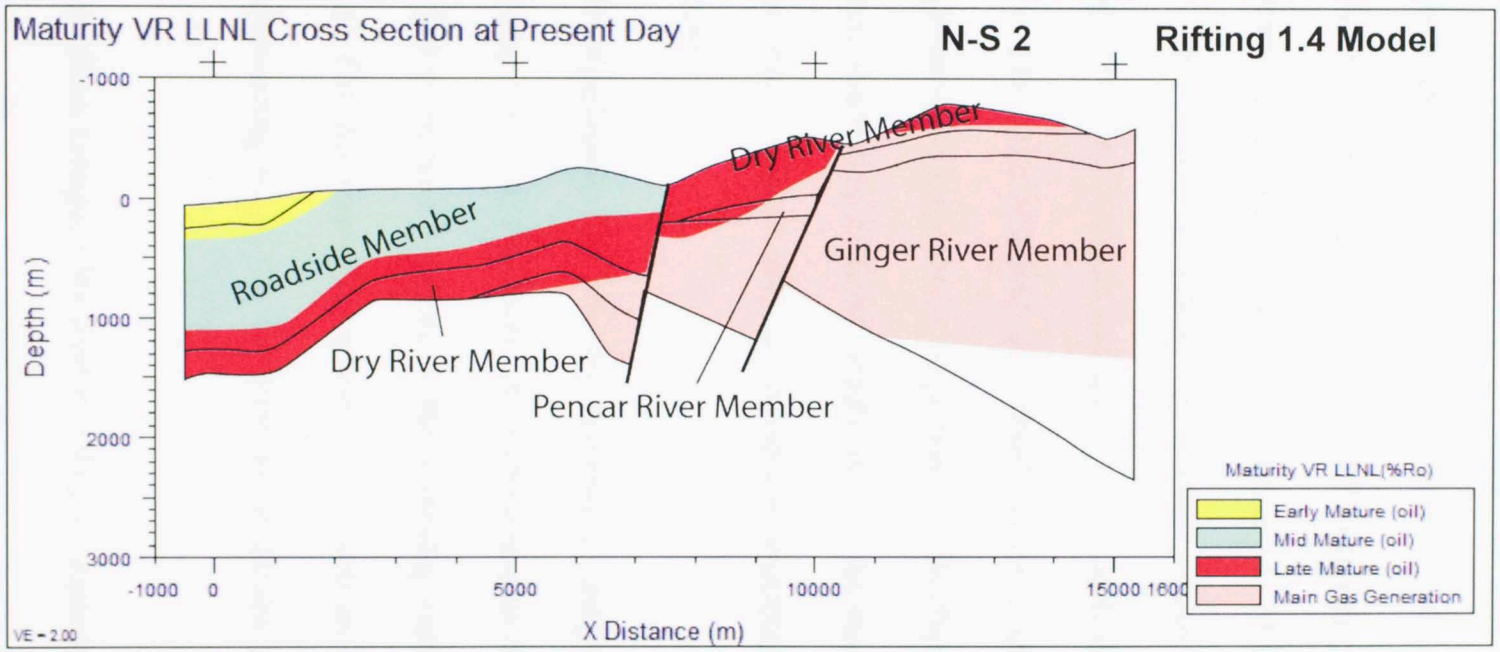

Figure 7.5.25: Maturity in cross-section N-S 2 for rifting 1.4 heat flow conditions. Windows are Early Mature 0.5 - 0.7 $\%R_0$ (yellow), Mid Mature 0.7 - 1.0 $\%R_0$ (green), Late Mature 1.0 - 1.3 $\%R_0$ (red), and Main Gas Generation 1.3 - 2.6 $\%R_0$ (light red).

7.6 Migration, Accumulation, and Traps

Though there has been no petroleum exploration in the Wagwater Trough, it is possible to calculate its hypothetical exploration potential using the data available. Hydrocarbon migration occurs given the availability of one or more of the following driving forces (Metwalli and Pigott, 2005): buoyancy or the upward force that pore water exerts on the less dense hydrocarbons (oil and gas); compaction or the loss of pore fluids as a result of the reduction in pore space as grains are packed closer together; hydrodynamic (water drive) or the flow of pore fluids through a carrier bed; diffusive or particles of hydrocarbon (liquid or gas) intermingling as a result of their spontaneous movement caused by thermal agitation. Hydrocarbon migration is divided into two phases: (1) primary migration, often referred to as fluid expulsion (i.e. the movement of generated hydrocarbons out of the source rocks), and (2) secondary migration (i.e. the movement of fluids into the reservoirs).

Primary Migration (fluid expulsion). For primary migration, compaction and buoyancy are likely the major driving forces in the study. As sedimentation progresses, grains in underlying layers are packed more closely owing to the overlying load, resulting in the loss of fluid in the pore space. For this reason, hydrocarbons, which are less dense than the subsurface water and surrounding rock, are the first to be driven out of the source rocks.

For hydrocarbons originating from kerogens BasinMod 1-D uses three methods of expulsion: (1) correlation of expulsion efficiency for oil and gas with calculated vitrinite reflectance, (2) correlation of expulsion efficiency with transformation ratio, and (3) porosity saturation.

The simplest method, the expulsion efficiency, is a calculation of the amount of generated hydrocarbons that are expelled from the source rock according to percentages assigned to different maturity values ($\%R_0$) for oil and gas. At a given vitrinite value, the expulsion efficiency is multiplied by the amount of hydrocarbon generated to get the amount expelled. The porosity saturation approach estimates how much of the porosity will be saturated with oil before expulsion begins. A porosity threshold is assigned for each source rock formation. Once the porosity has been saturated to this threshold, hydrocarbons generated beyond this threshold are expelled. For this study, saturation threshold is assigned a default BasinMod 1-D value of 0.2.

Figures 7.6.1 to 7.6.15 show the hypothetical timing and quantity of in situ production and expulsion of hydrocarbons for the fourteen virtual wells in this study. The earliest in situ oil in the Richmond formation in the rifting 1.4 H.F.U. conditions commenced at 52 Ma, while that in the rifting 0.96 H.F.U. conditions commenced at 49 Ma. First expulsion time was 50 Ma for rifting 1.4 H.F.U. conditions and 41 Ma for the rifting 0.96 H.F.U. conditions. The timing of hydrocarbon production is directly related to heat flow because rifting heat flow 1.4 conditions demonstrate higher heat flow than rifting heat flow 0.96 conditions.

The porosity reduction peaks for figures 7.6.1 to 7.6.15 imply potential advection rates and times of extruded waters from compacting sediments. These waters may or may not have the potential to carry or push hydrocarbons through migration pathways. Therefore, the early high peak (57 – 53 Ma) and the secondary peak (53 – 50 Ma) would have little effect, but the final flat peak (50 – 10 Ma) would have the greatest potential impact.

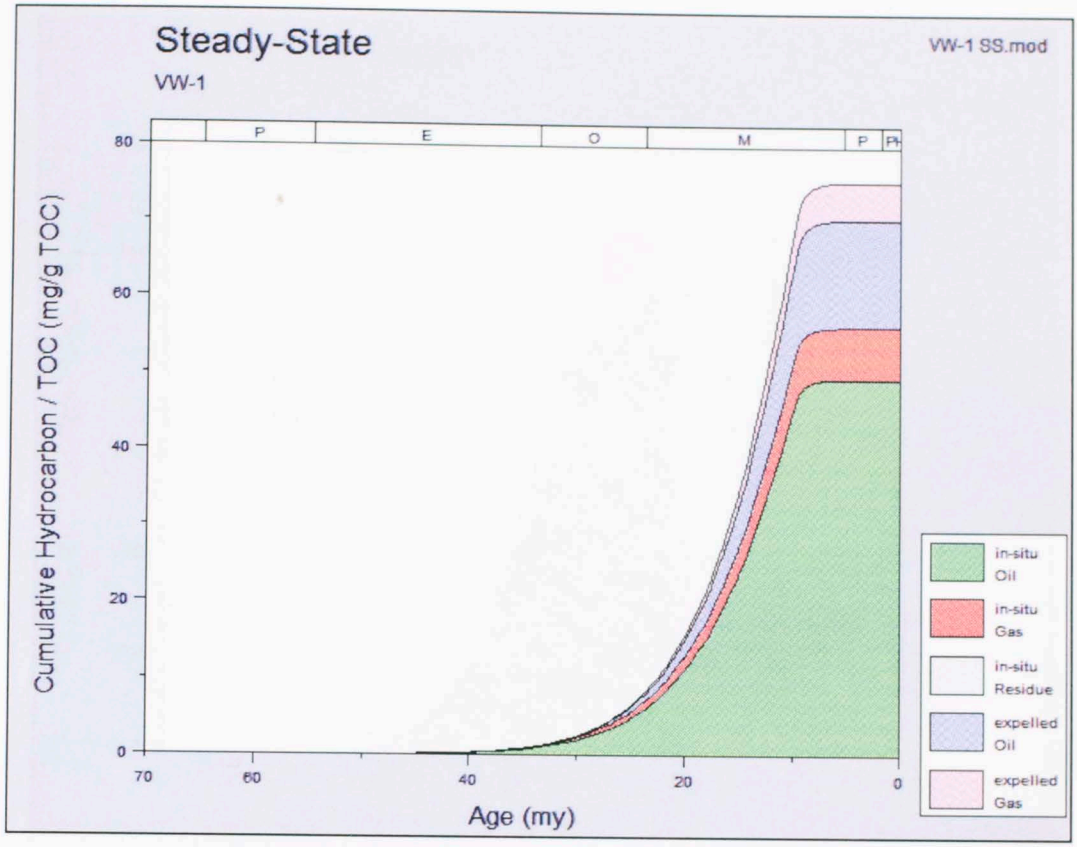

Figure 7.6.1: Hypothetical total hydrocarbon versus time graph in VW-1 for steady-state heat flow conditions.

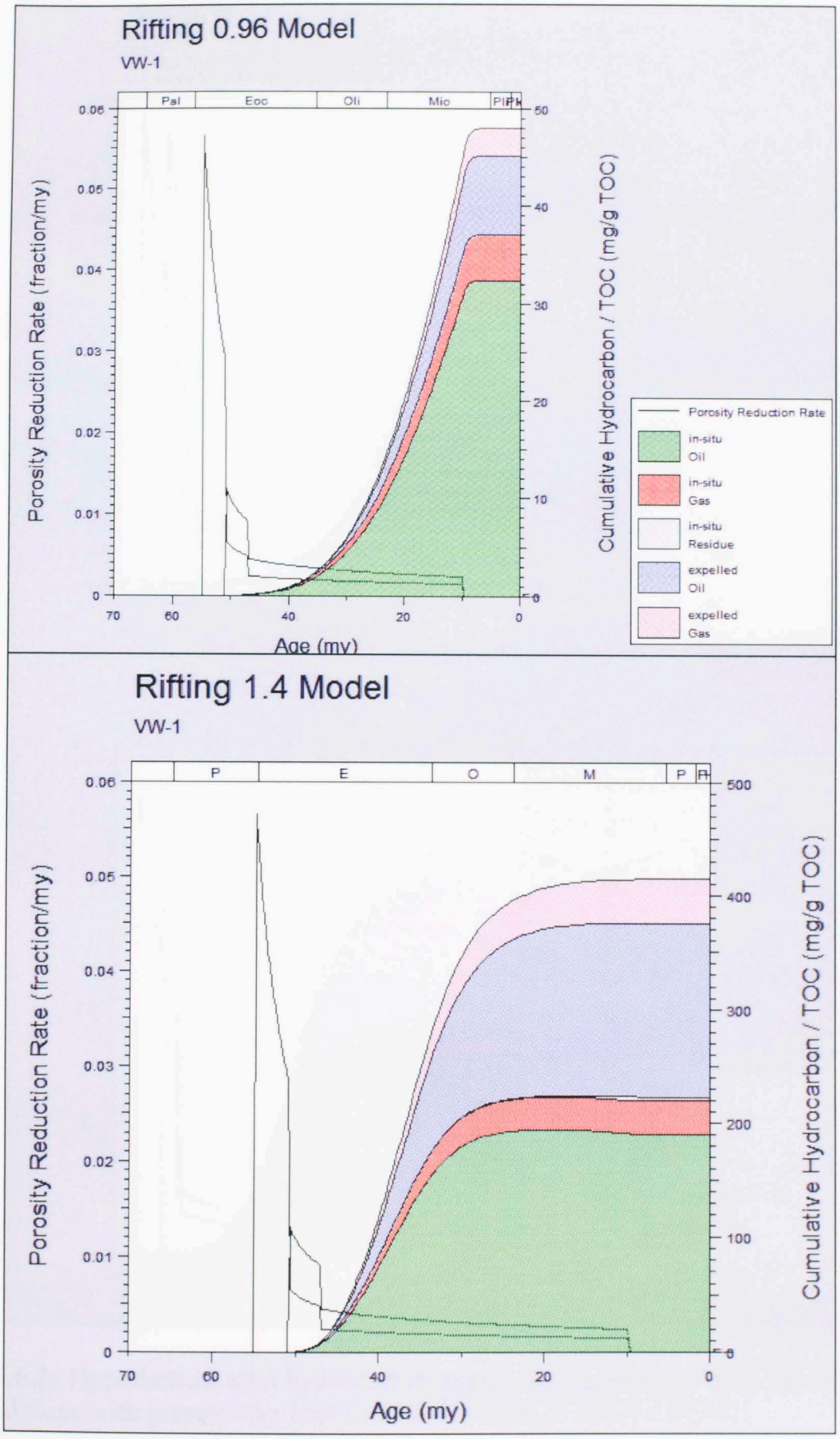

Figure 7.6.2: Hypothetical total hydrocarbon versus time graph in VW-1 for rifting heat flow conditions with present-day heat flow at 0.96 H.F.U. and 1.4 H.F.U.

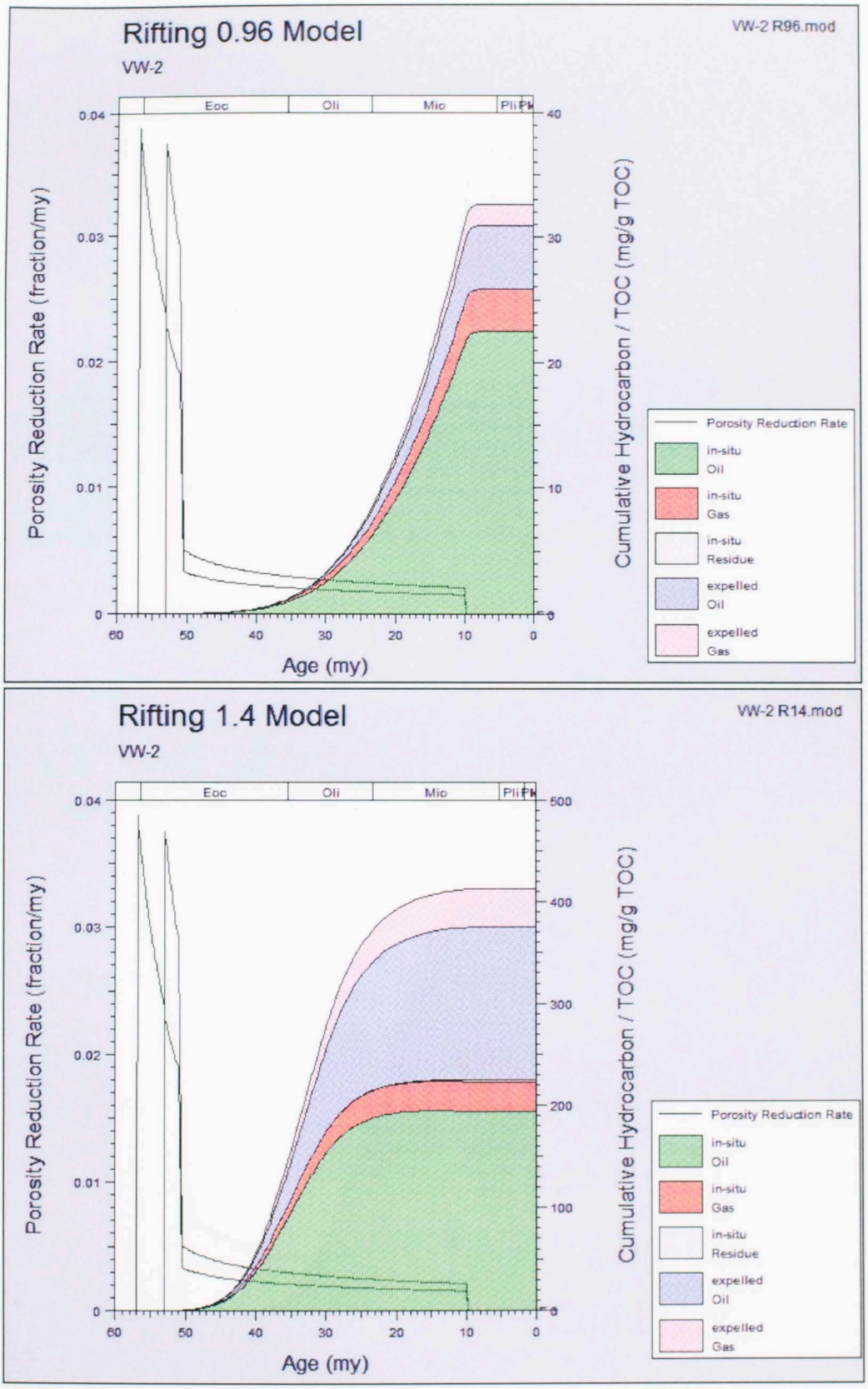

Figure 7.6.3: Hypothetical total hydrocarbon versus time graph in VW-2 for rifting heat flow conditions with present-day heat flow at 0.96 H.F.U. and 1.4 H.F.U.

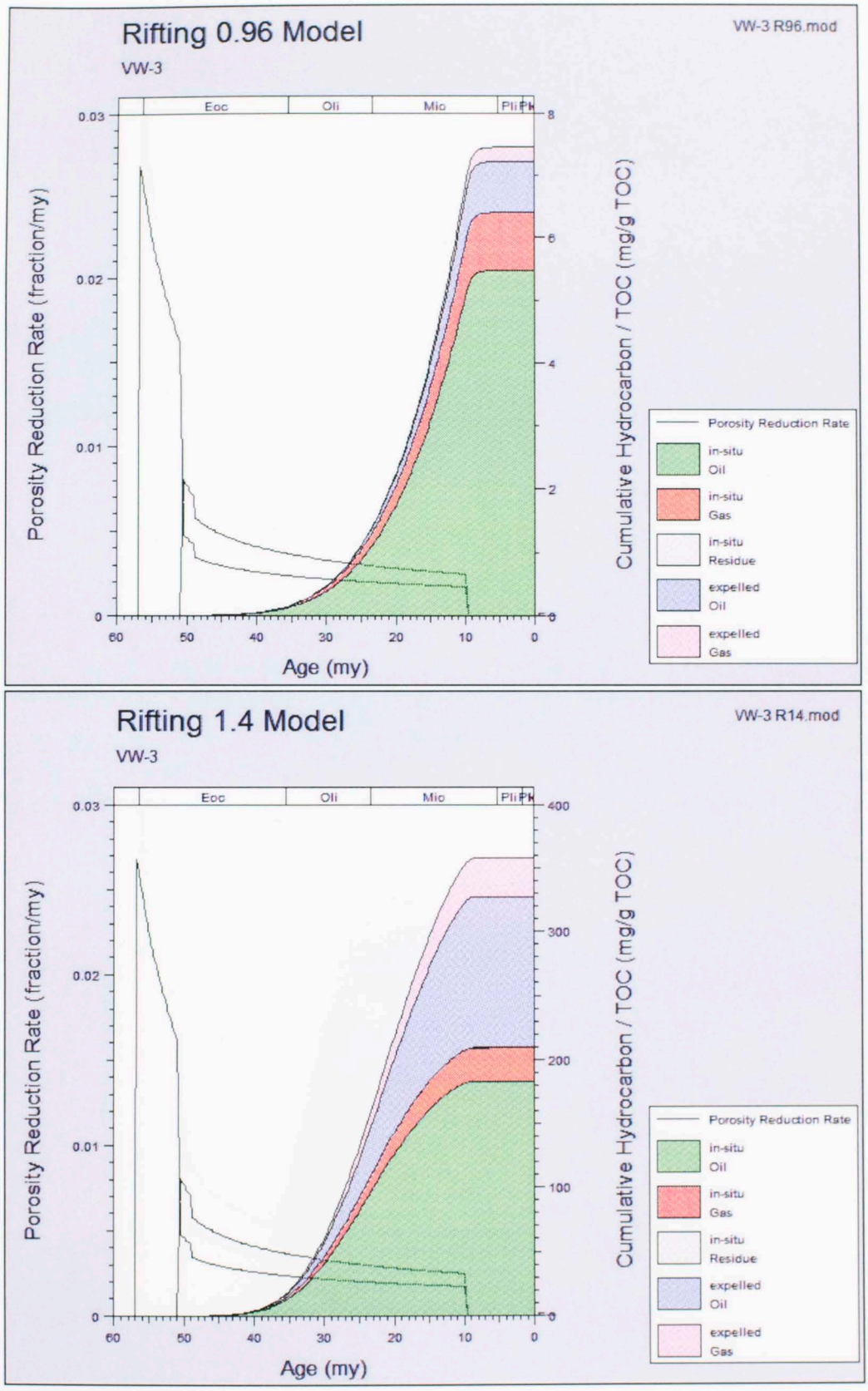

Figure 7.6.4: Hypothetical total hydrocarbon versus time graph in VW-3 for rifting heat flow conditions with present-day heat flow at 0.96 H.F.U. and 1.4 H.F.U.

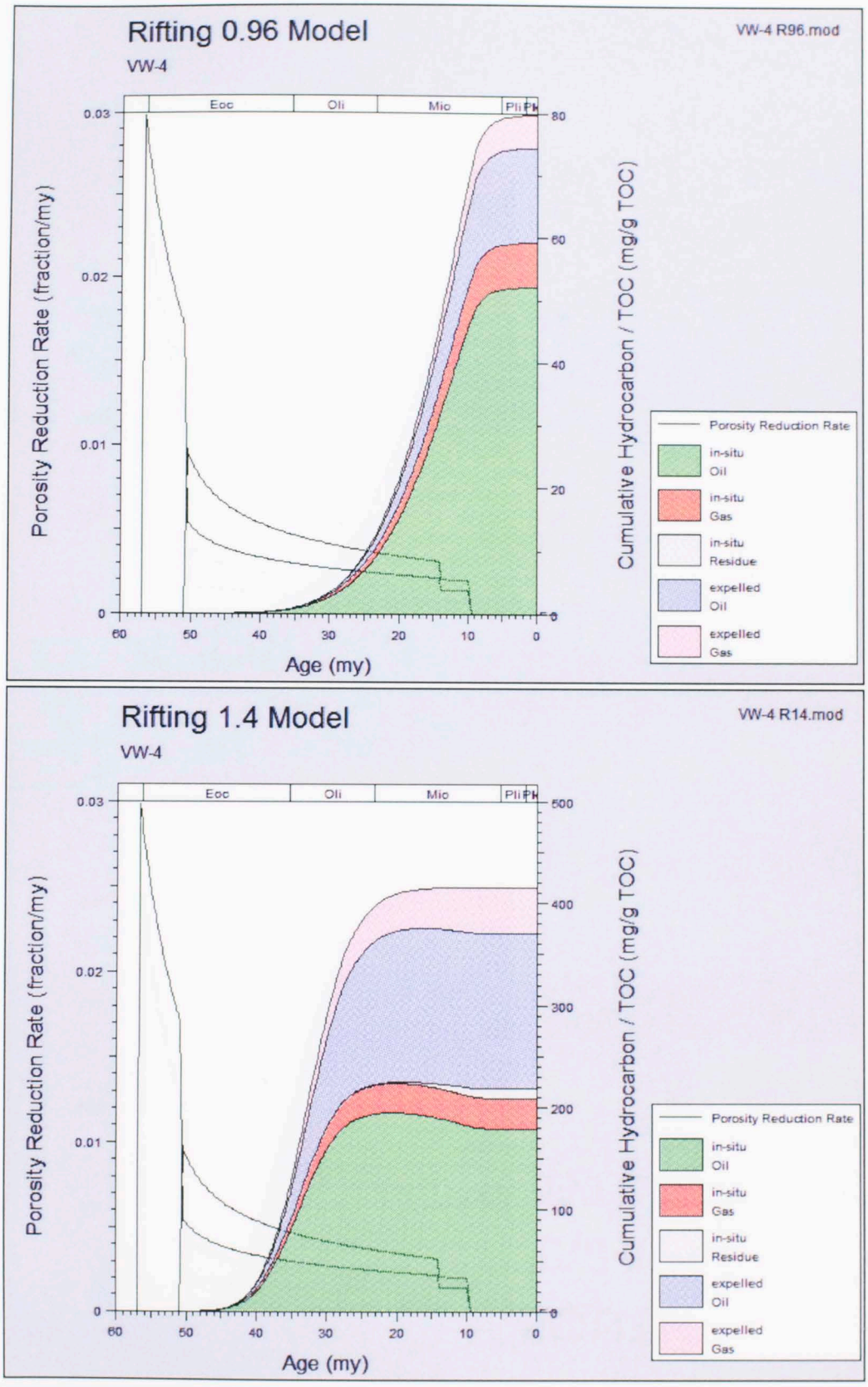

Figure 7.6.5: Hypothetical total hydrocarbon versus time graph in VW-4 for rifting heat flow conditions with present-day heat flow at 0.96 H.F.U. and 1.4 H.F.U.

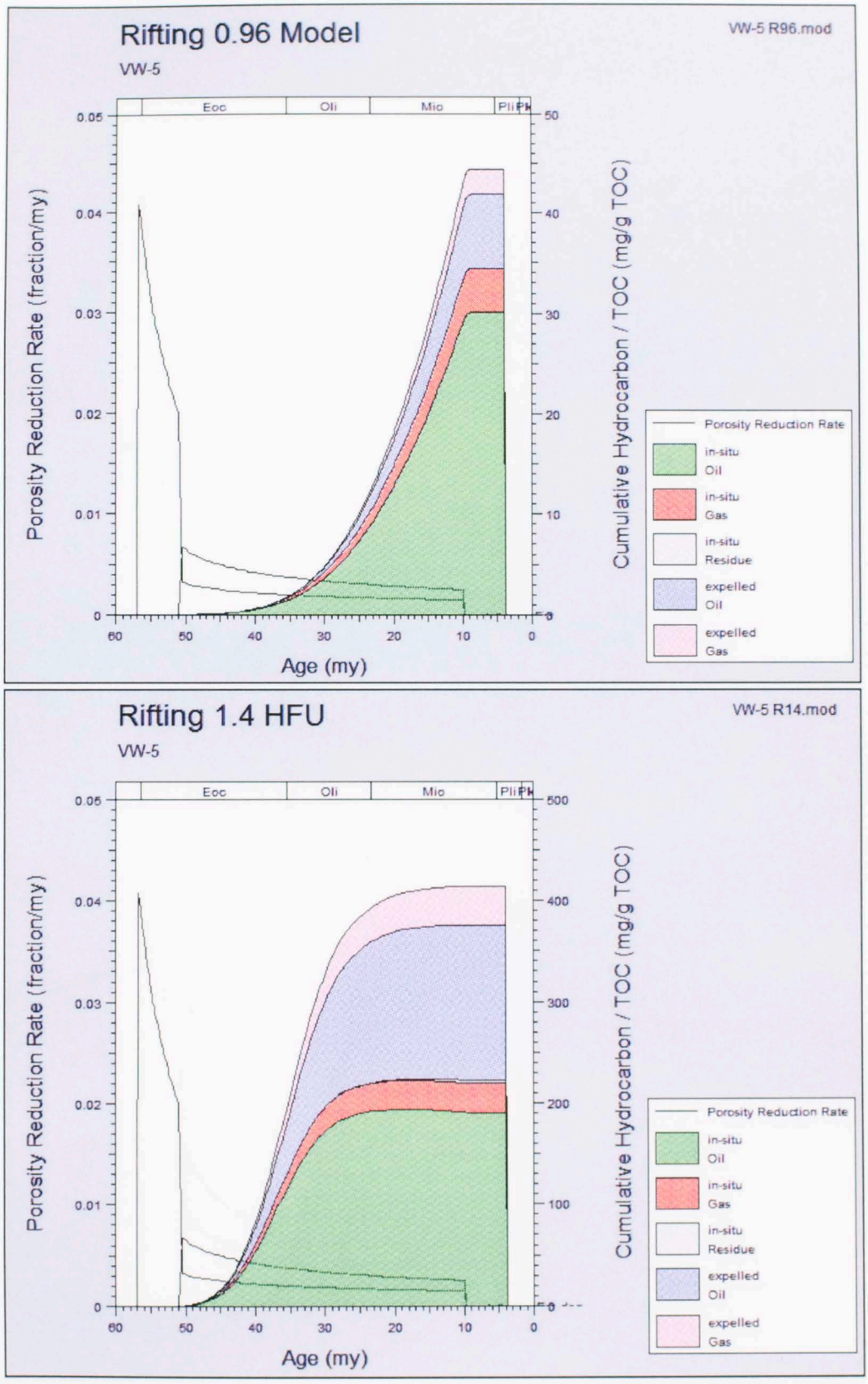

Figure 7.6.6: Hypothetical total hydrocarbon versus time graph in VW-5 for rifting heat flow conditions with present-day heat flow at 0.96 H.F.U. and 1.4 H.F.U.

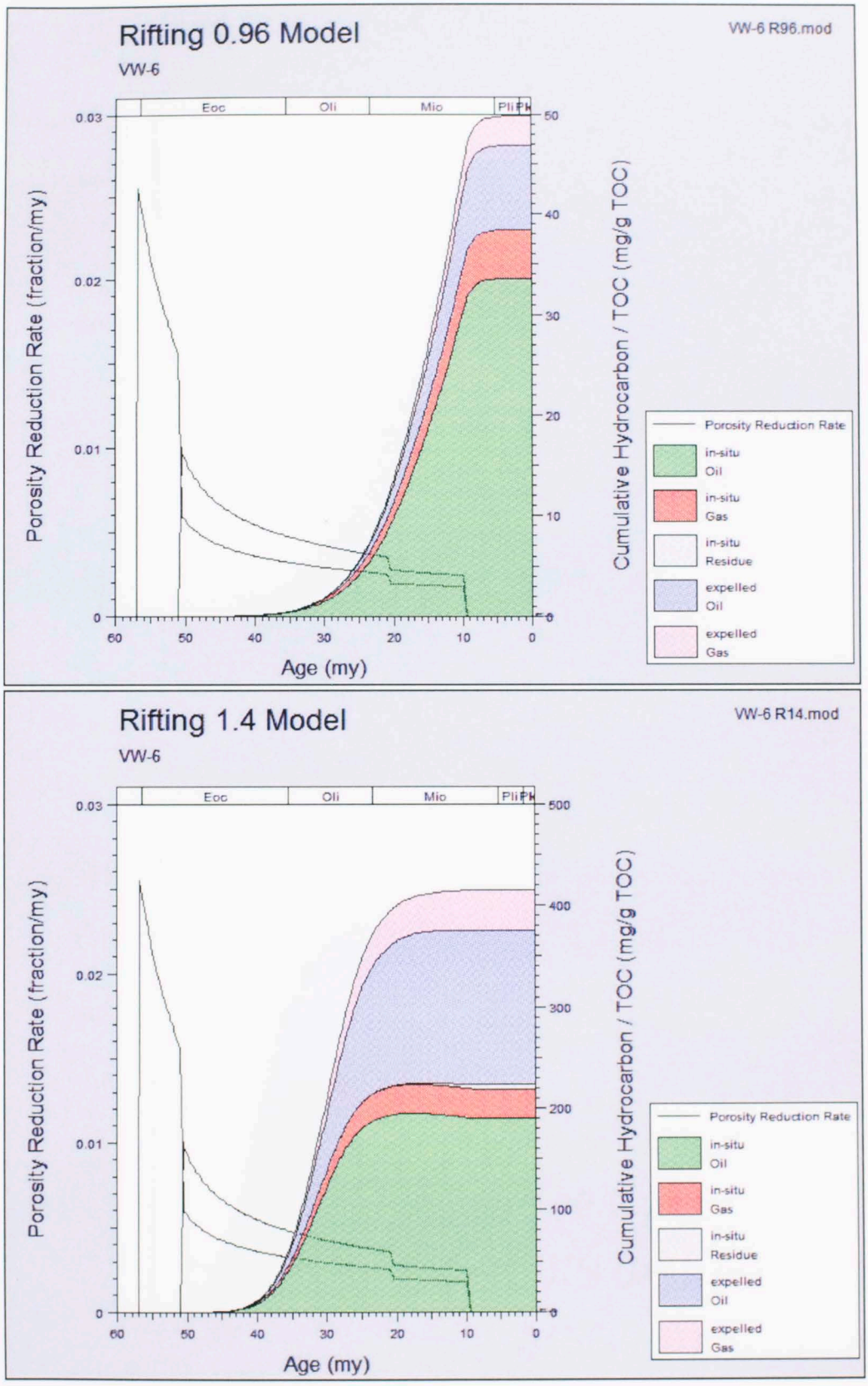

Figure 7.6.7: Hypothetical total hydrocarbon versus time graph in VW-6 for rifting heat flow conditions with present-day heat flow at 0.96 H.F.U. and 1.4 H.F.U.

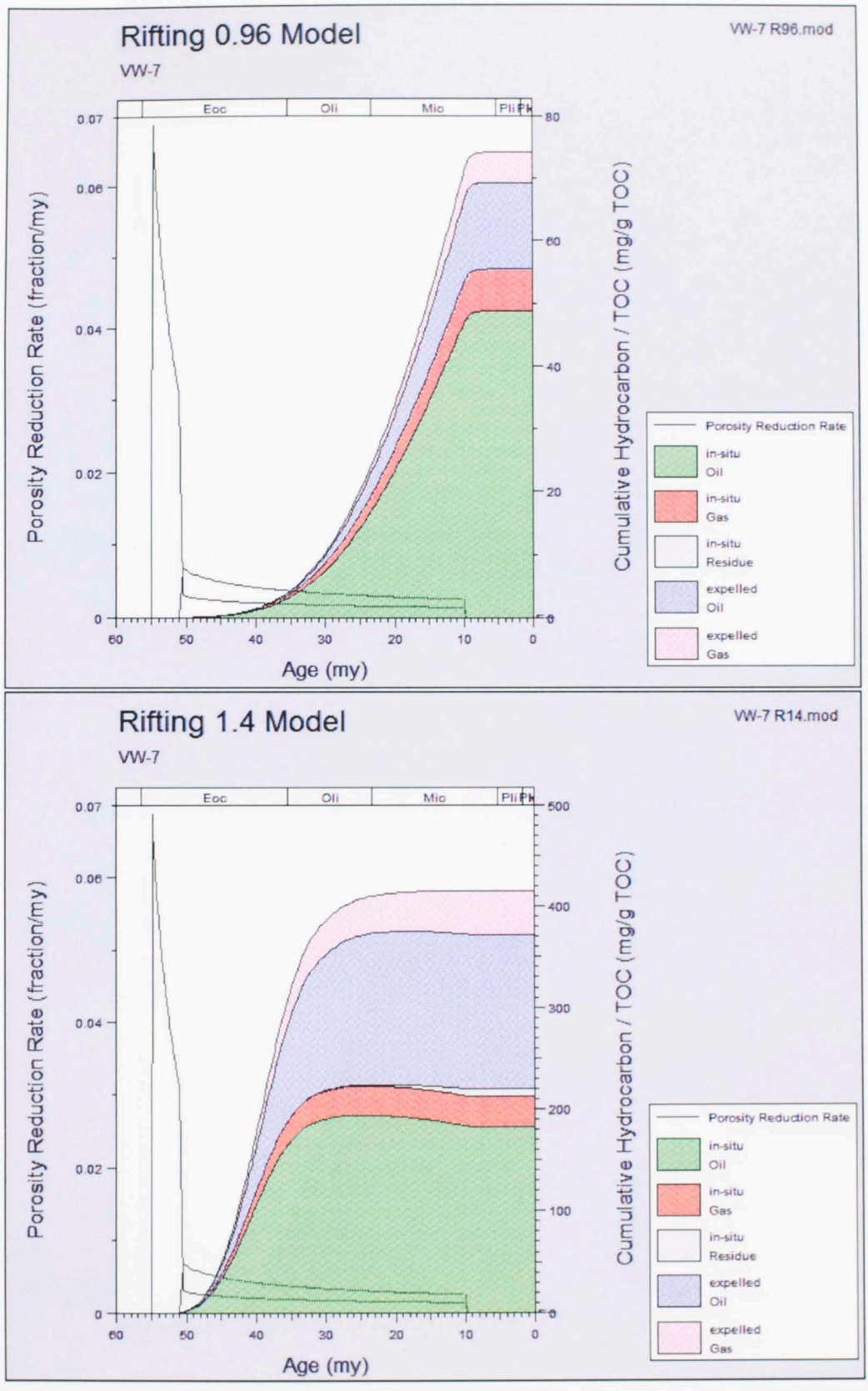

Figure 7.6.8: Hypothetical total hydrocarbon versus time graph in VW-7 for rifting heat flow conditions with present-day heat flow at 0.96 H.F.U. and 1.4 H.F.U.

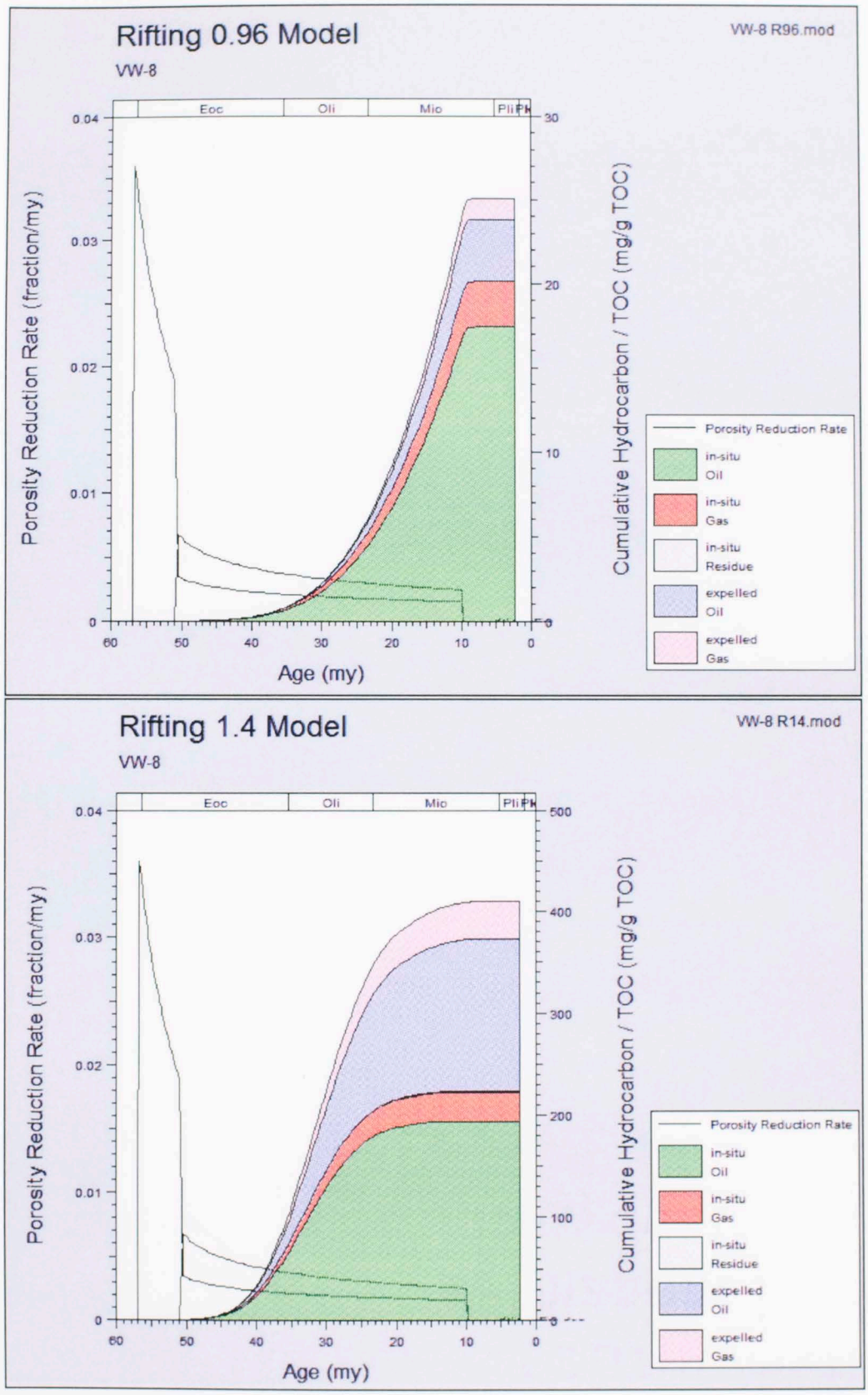

Figure 7.6.9: Hypothetical total hydrocarbon versus time graph in VW-8 for rifting heat flow conditions with present-day heat flow at 0.96 H.F.U. and 1.4 H.F.U.

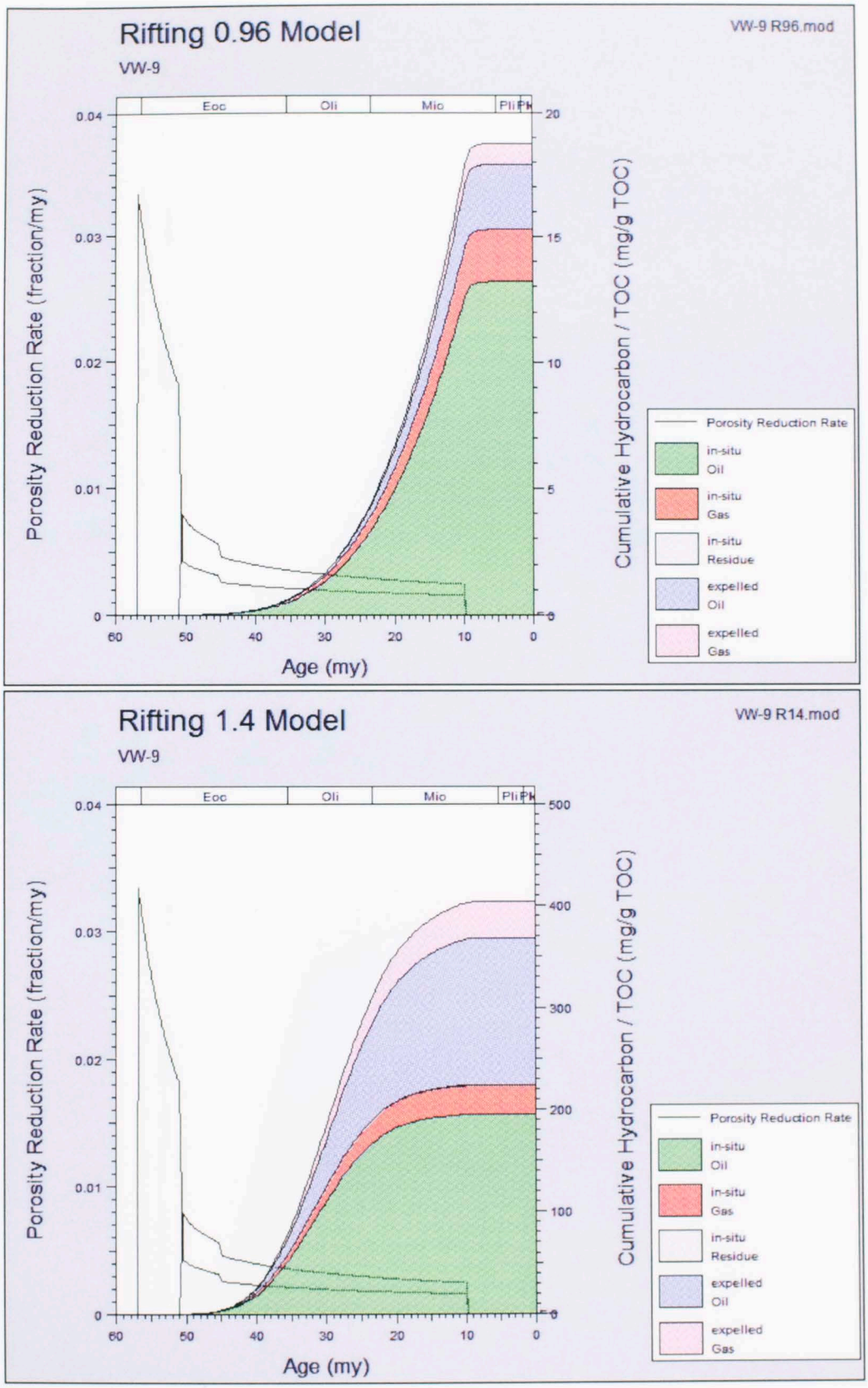

Figure 7.6.10: Hypothetical total hydrocarbon versus time graph in VW-9 for rifting heat flow conditions with present-day heat flow at 0.96 H.F.U. and 1.4 H.F.U.

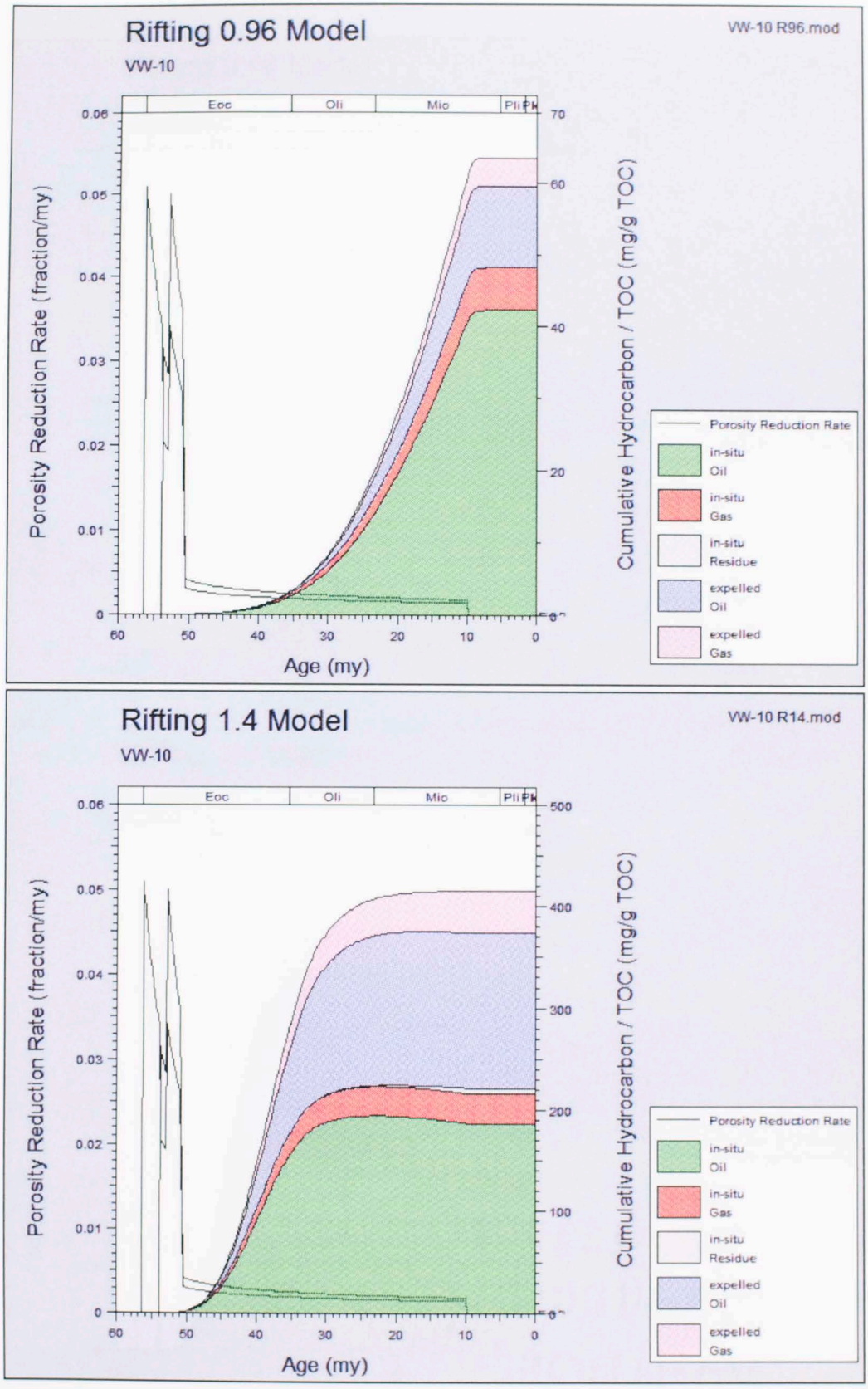

Figure 7.6.11: Hypothetical total hydrocarbon versus time graph in VW-10 for rifting heat flow conditions with present-day heat flow at 0.96 H.F.U. and 1.4 H.F.U.

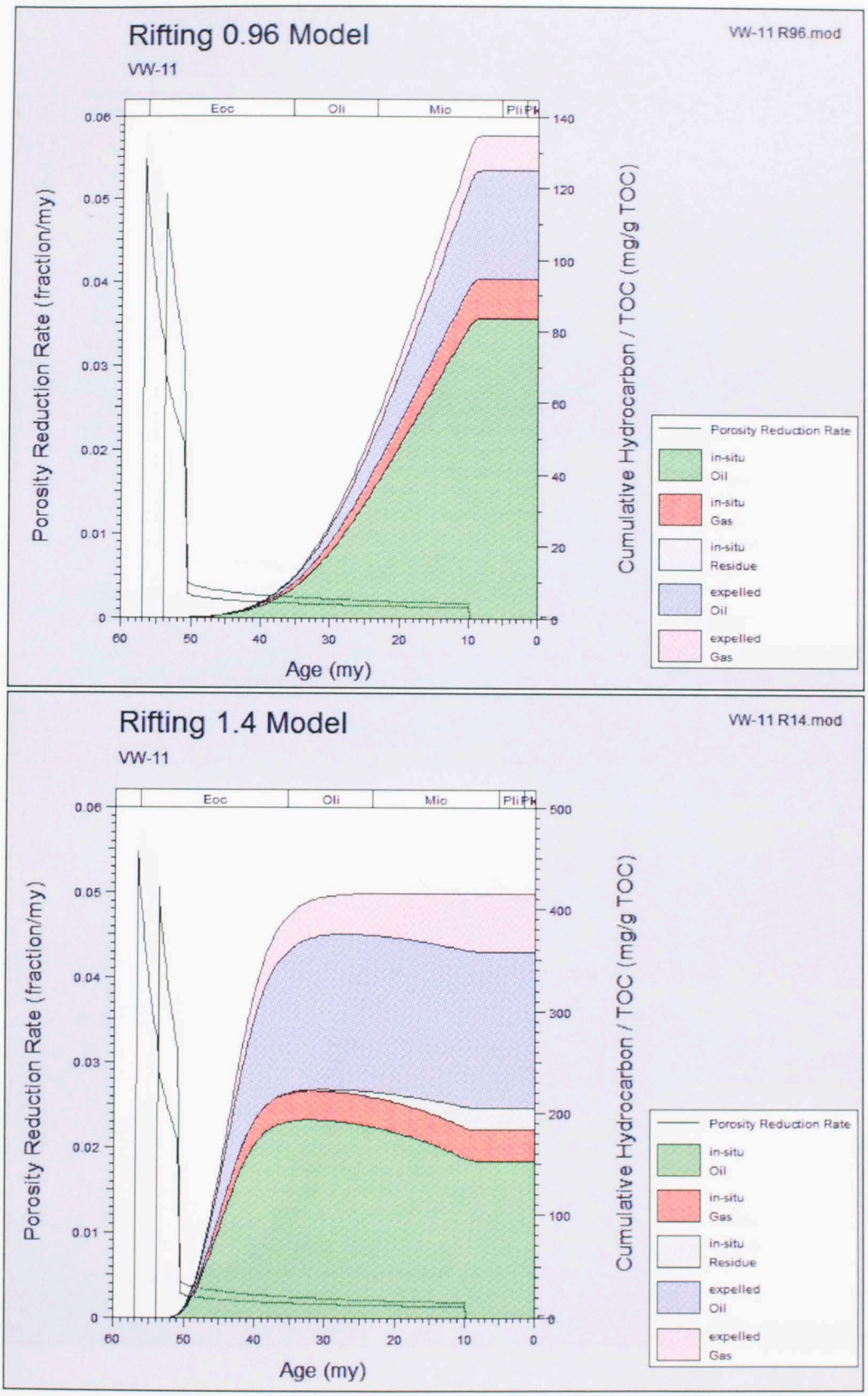

Figure 7.6.12: Hypothetical total hydrocarbon versus time graph in VW-11 for rifting heat flow conditions with present-day heat flow at 0.96 H.F.U. and 1.4 H.F.U.

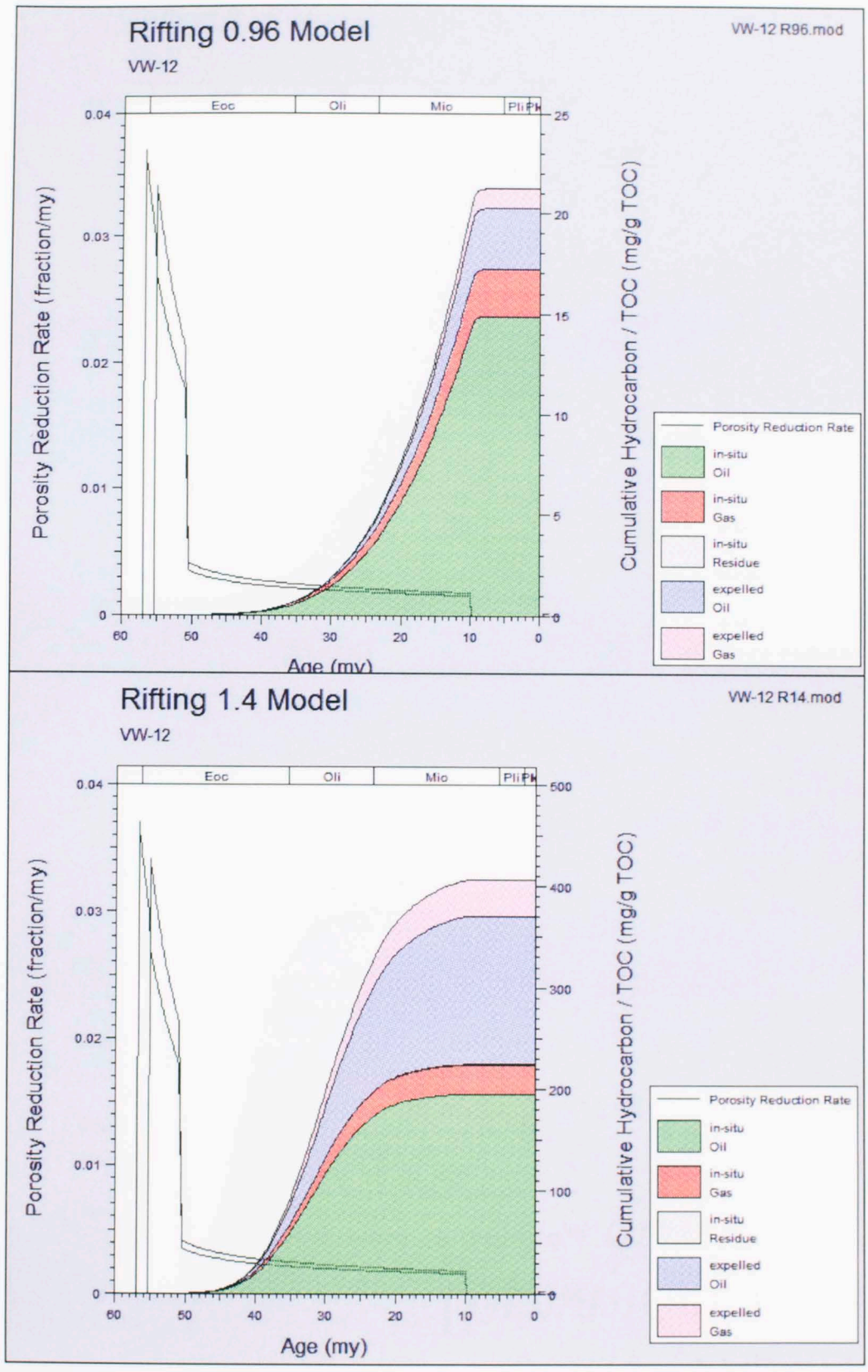

Figure 7.6.13: Hypothetical total hydrocarbon versus time graph in VW-12 for rifting heat flow conditions with present-day heat flow at 0.96 H.F.U. and 1.4 H.F.U.

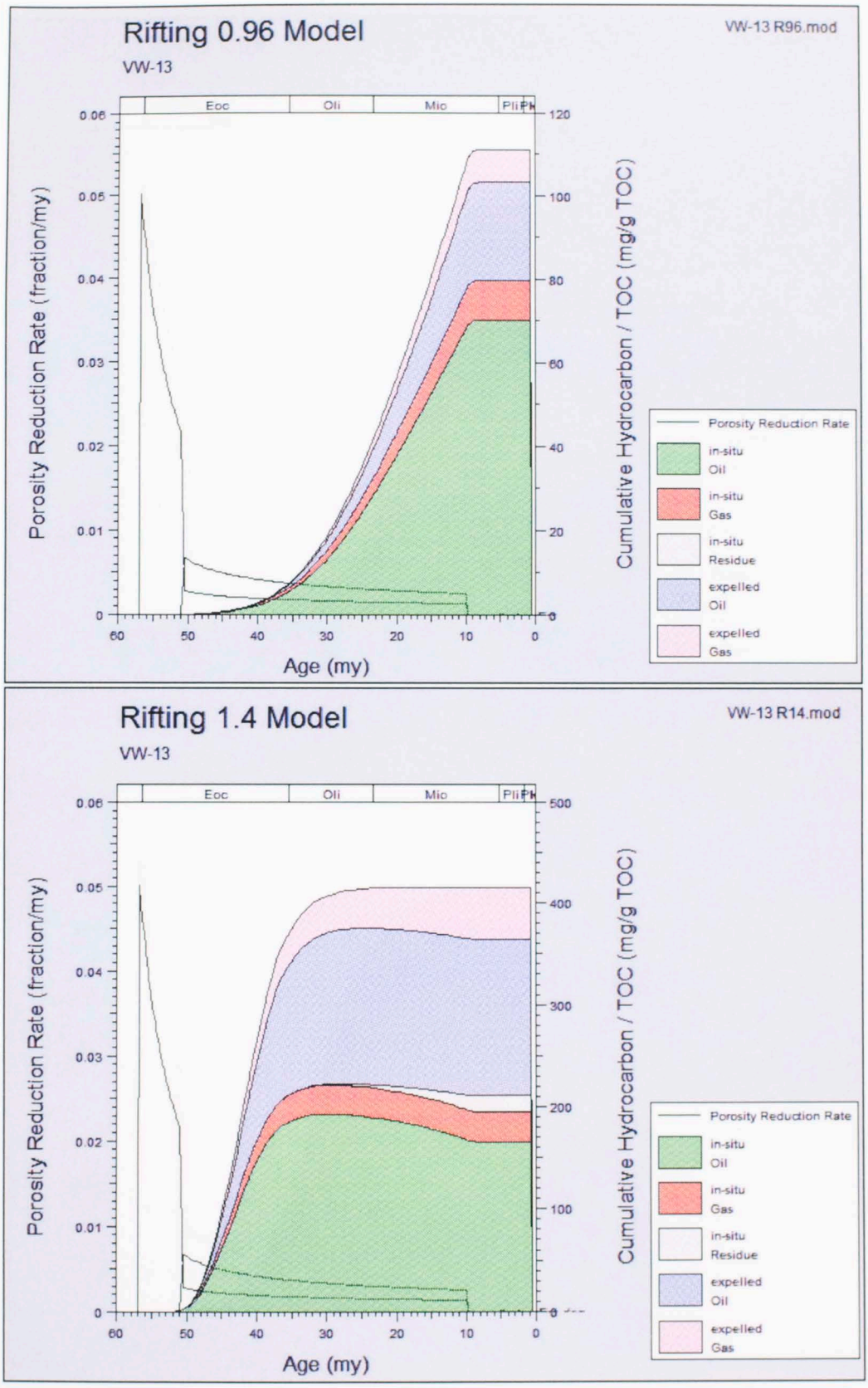

Figure 7.6.14: Hypothetical total hydrocarbon versus time graph in VW-13 for rifting heat flow conditions with present-day heat flow at 0.96 H.F.U. and 1.4 H.F.U.

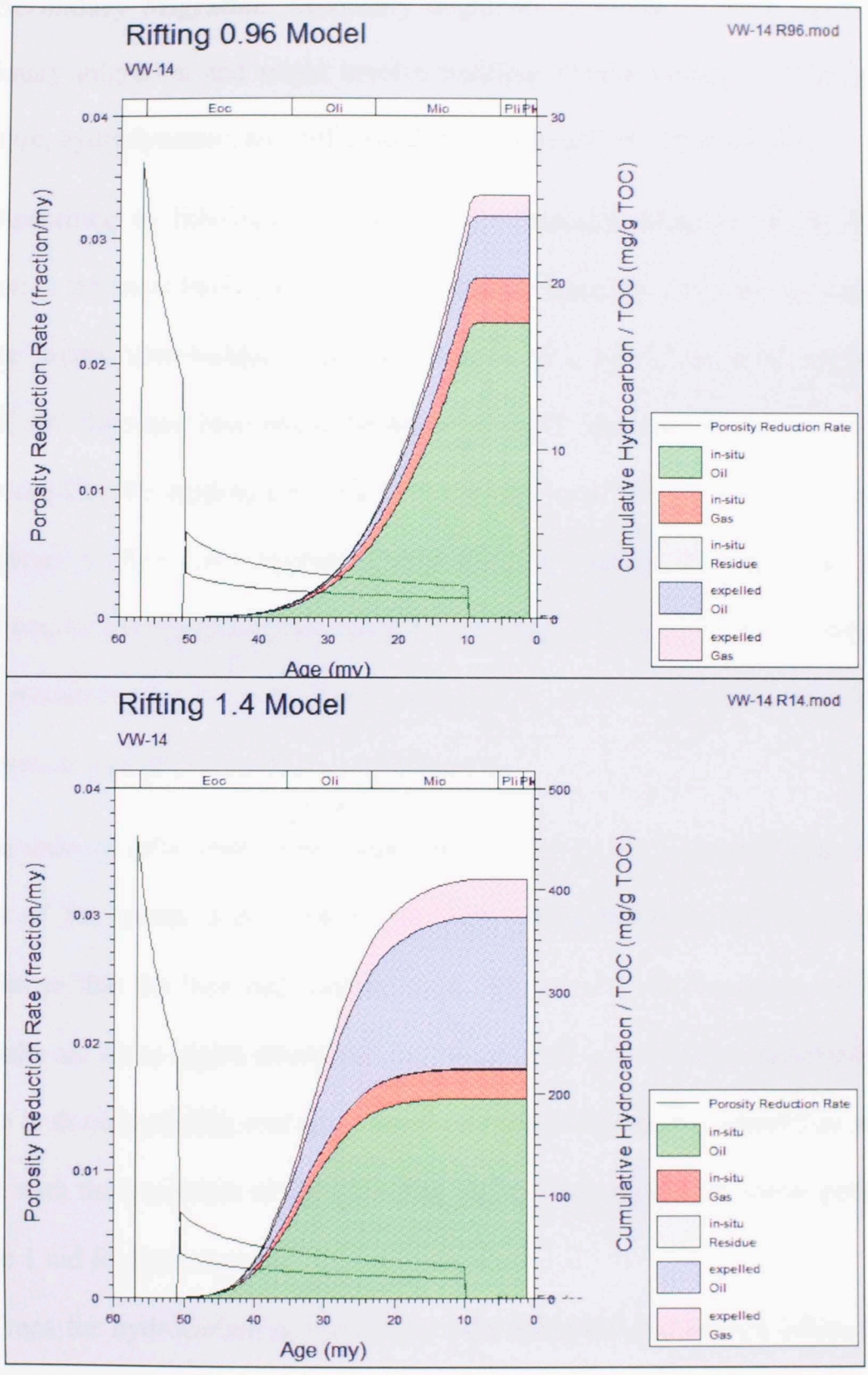

Figure 7.6.15: Hypothetical total hydrocarbon versus time graph in VW-14 for rifting heat flow conditions with present-day heat flow at 0.96 H.F.U. and 1.4 H.F.U.

Secondary Migration. Secondary migration, however, is much more complex than primary migration and might involve multiple driving forces, such as buoyancy, compaction, hydrodynamic, and diffusive drives (Metwalli and Pigott, 2005).

According to lithological properties, the Roadside Member of the Richmond Formation is the most likely candidate for a source, reservoir, and seal. It contains long sandstone lenses inter-bedded with shale layers. The sandstone beds would be the reservoir, and the shale beds would be the source rock and seal. Some assumptions are made to simplify the modeling process: (1) the sandstone beds are continuous allowing hydrocarbons to flow until trapped structurally, (2) because the sandstone beds are assumed continuous, hydrocarbons can only be trapped structurally and no stratigraphic traps are modeled, and (3) the horizontal permeability of the Roadside Member is 100 md and is constant throughout the basin and formation.

In order to effectively model hydrocarbon flow in the Wagwater trough, two end members of the model were created: (1) flow where faults are set as impermeable boundaries so that the flow only occurs within the pores of the formation and (2) flow where faults are set as highly permeable and do not inhibit the flow of hydrocarbons. For case I the fault permeability was set to 1 md, and case II the fault permeability was set to 1000 md with the exception of the bounding faults to the southwest where permeability was set to 1 md for both cases.

Traps for hydrocarbon accumulation were modeled and located where there are closures on structural highs. In the figures, traps are show in gray for non-hydrocarbon filled traps and green or red for oil and gas filled traps respectively. In case I traps along

fault boundaries are the most common trapping mechanism; however, case II uses permeable faults and all the traps are four-way closures on structural highs or anticlines.

Case I: Impermeable Faults

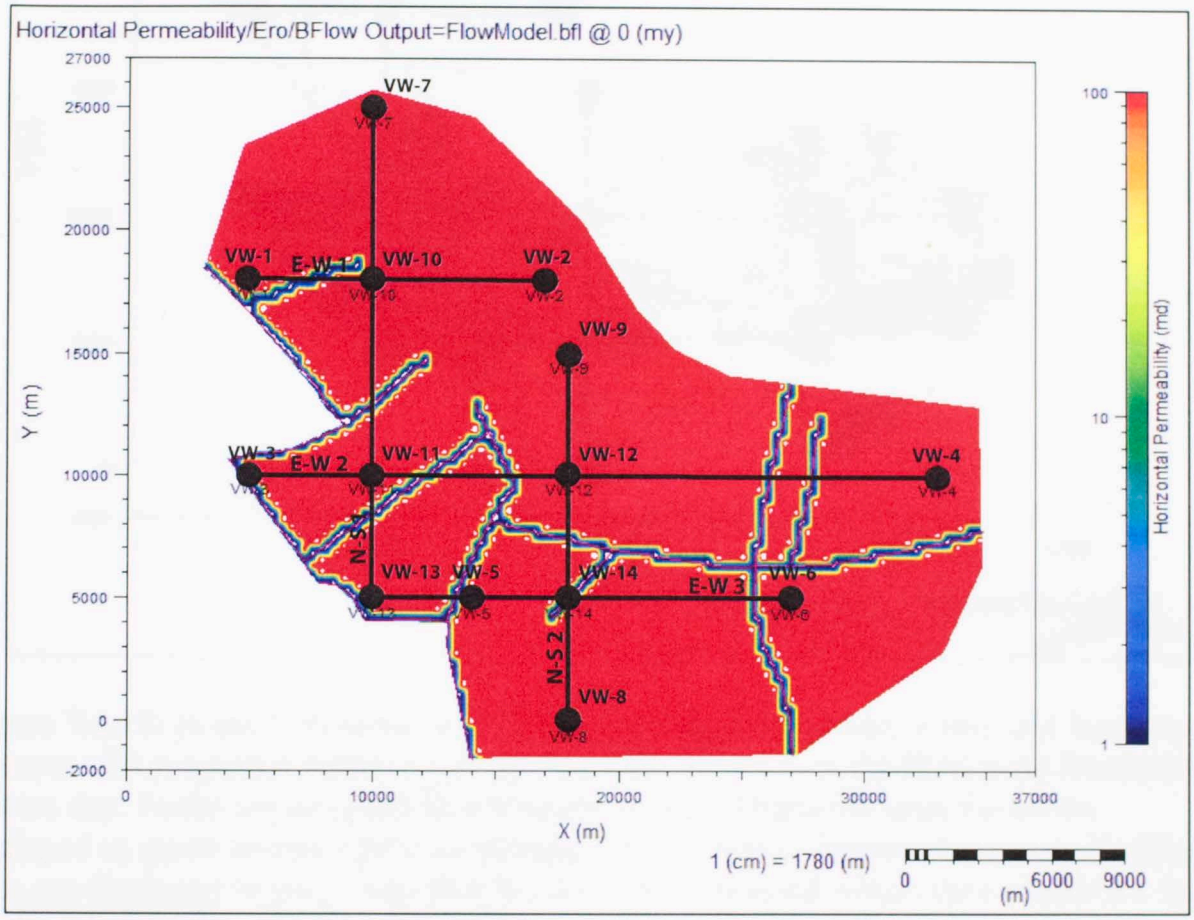

Figure 7.6.16: (Case I) For modeling purposes horizontal permeability of the Roadside Member of the Richmond Formation is assumed to be 100 md and constant throughout the basin except for the faults. In this case the faults are modeled at 1 md. This will create a modeled case where faults barriers for oil and gas flow and constrain flow within the individual fault blocks.

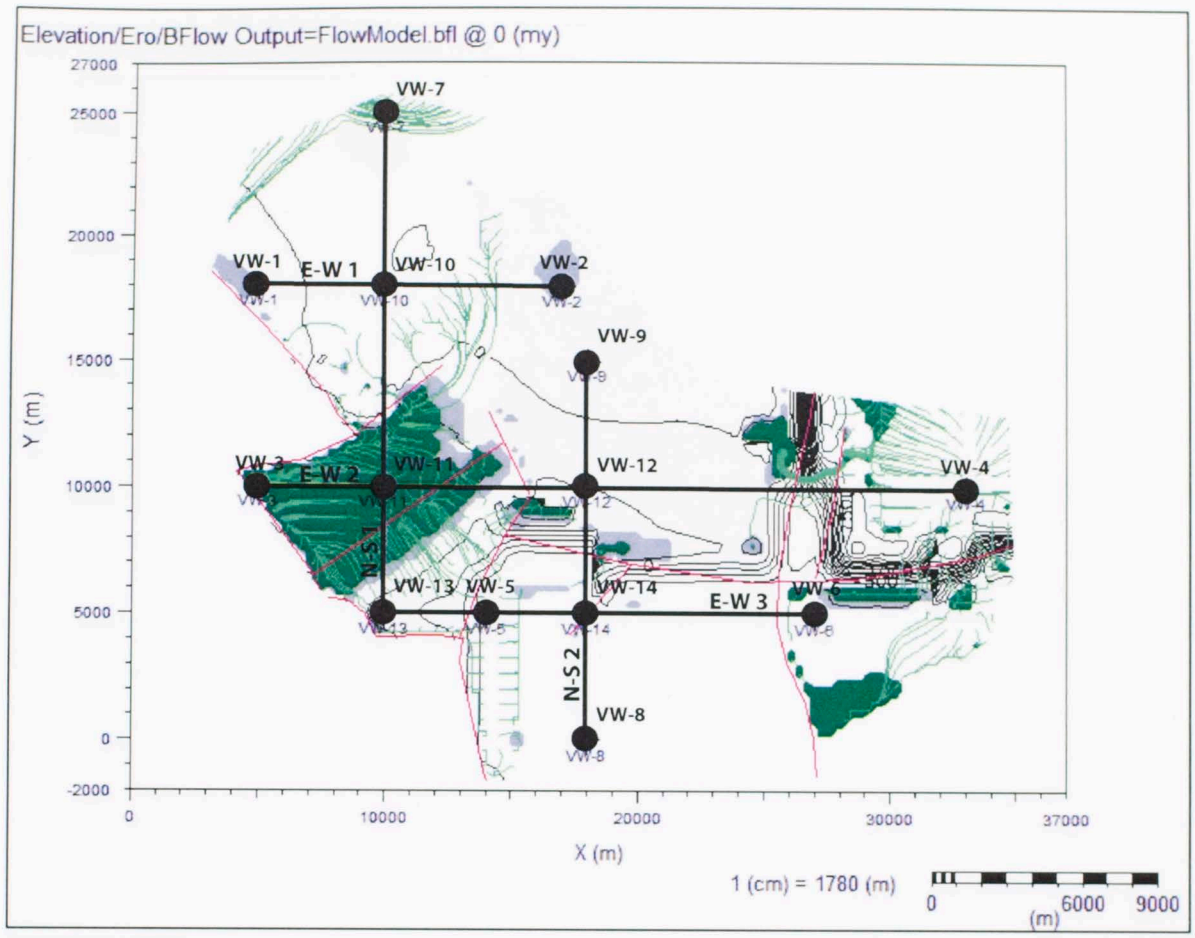

Figure 7.6.17: (Case I) Possible oil traps along impermeable fault zones and four-way closures with migration pathways in the Roadside Member of the Richmond Formation at present day. Faults are assumed impermeable (1 md). Migration lines for oil are displayed as green arrows while accumulated oil in traps is displayed in green. Unfilled traps are displayed in grey. Note that the flows are restricted within their respective fault blocks. Most of the oil generation and accumulation occurs in the western part of the study area near the Wagwater Fault. Not enough burial occurred in the eastern half to generate a significant amount of oil.

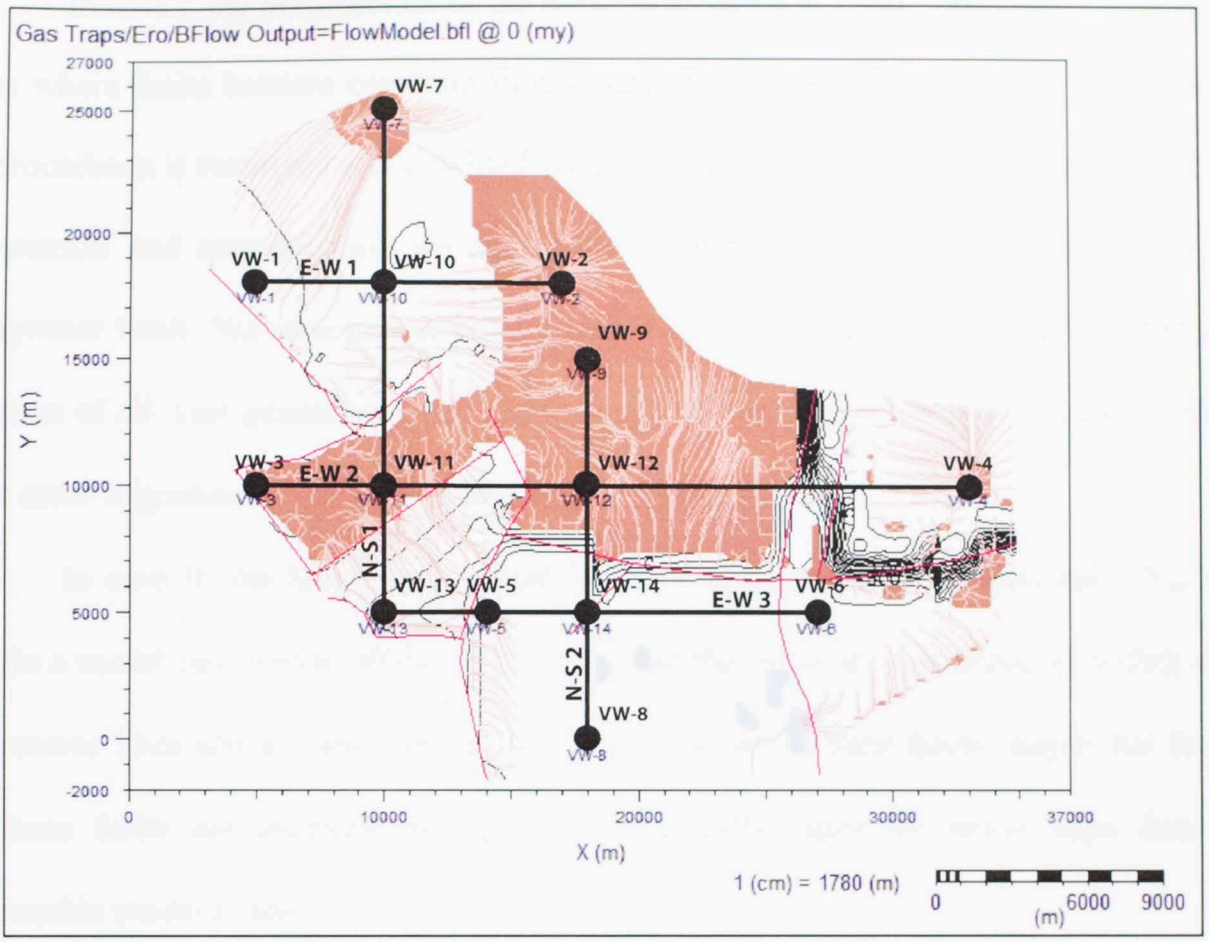

Figure 7.6.18: (Case I) Possible gas traps along impermeable fault zones and four-way closures with migration pathways in the Roadside Member of the Richmond Formation at present day. Faults are assumed impermeable (1 md). Migration lines for gas are displayed as red arrows while accumulated gas in traps is displayed in red. Unfilled traps are displayed shown in grey. Note that the flows are restricted within their respective fault blocks. Gas generation and migration trends are similar to the oil from figure 7.6.17. However there was more migration of gas in into the eastern region than oil.

In case I, the permeability of the faults is modeled at 1 md. This creates a modeled case where faults barriers constrain flow within the individual fault blocks. The flow of hydrocarbons is restricted and confined within the individual fault blocks. Most of the oil generation and accumulation occurs in the western part of the study area near the Wagwater Fault. Not enough burial occurred in the eastern half to generate a significant amount of oil. Gas generation and migration trends are similar to the oil. However there was more migration of gas in into the eastern region than oil.

In case II, the faults are assumed to have a permeability of 1000 md. This will create a model case where all the flow is free, and the flows are not restricted within their respective fault blocks, and hydrocarbons are allowed to flow freely across the faults. Because faults are assumed permeable in this model, there are fewer traps than the permeable model (Case I).

Case II: Permeable Faults

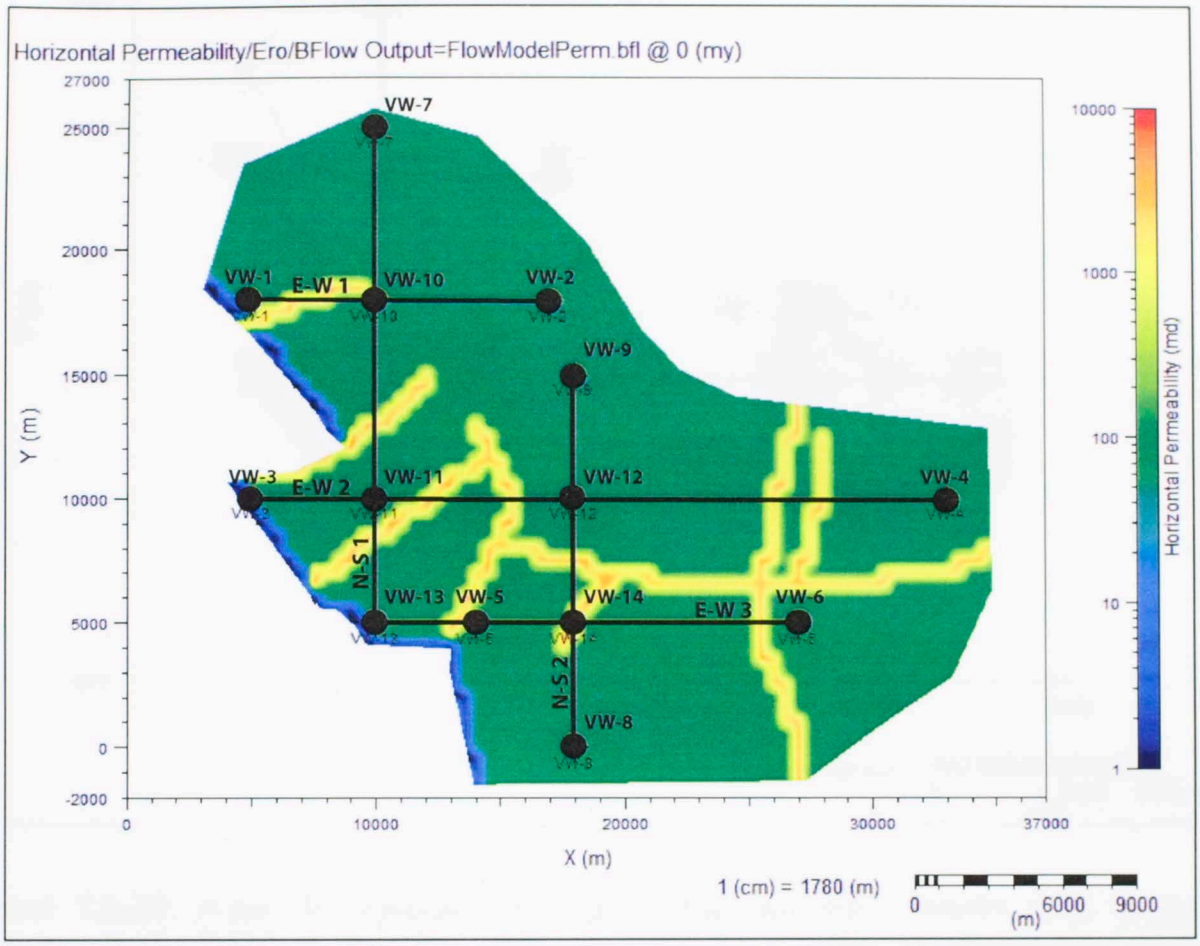

Figure 7.6.19: (Case II) For modeling purposes horizontal permeability of the Roadside Member of the Richmond Formation is assumed to be 100 md and constant throughout the basin except for the faults. In this case the faults are assumed to have a permeability of 1000 md. This will create a model case where all the flow is free as the model does not identify faults as a hindrance to flow.

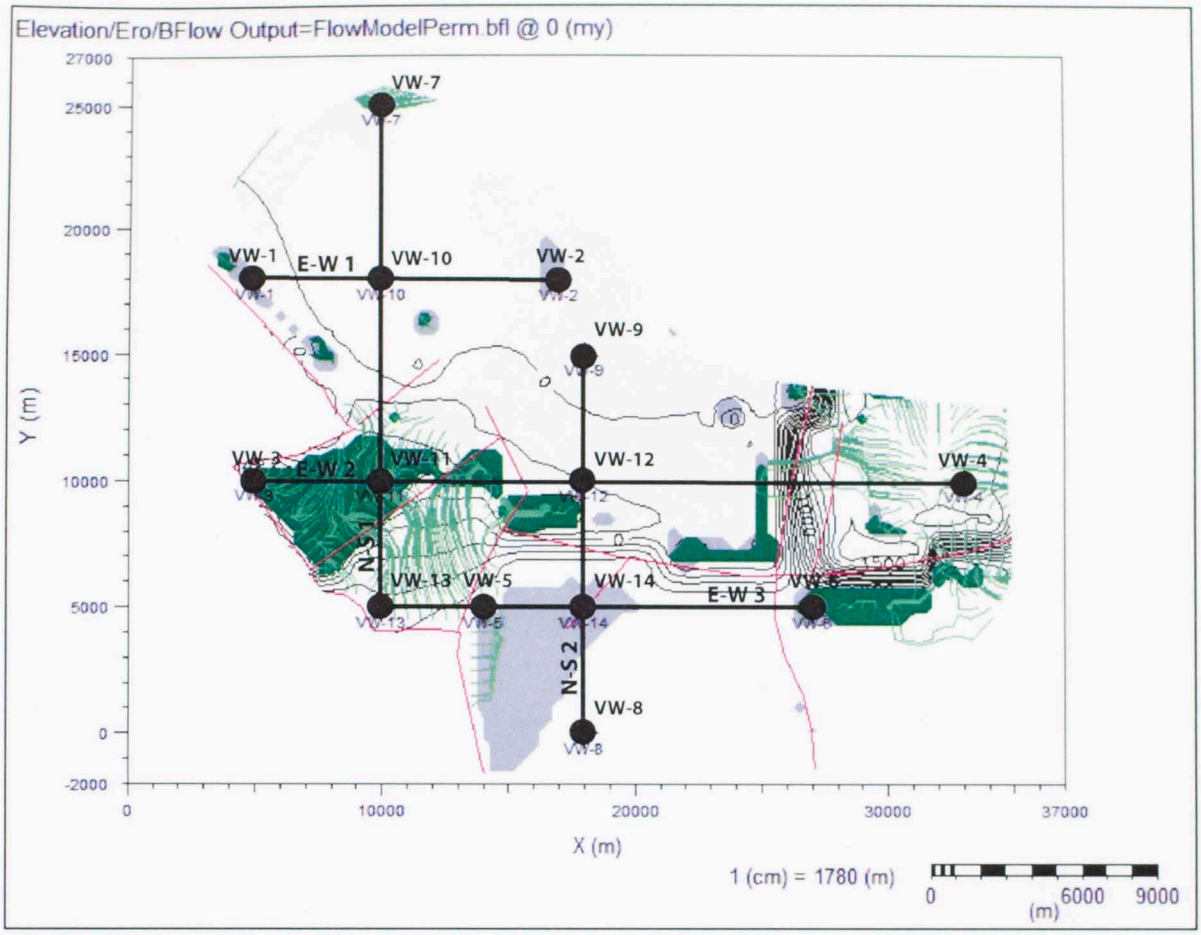

Figure 7.6.20: (Case II) Possible oil traps along four-way closures with migration pathways in the Roadside Member of the Richmond Formation at present day. With the exception of the basin bounding faults in the west, faults are assumed permeable (1000 md). Migration lines for oil are displayed as green arrows while accumulated oil in traps is displayed in green. Unfilled traps are displayed in grey. Note that the flows are not restricted within their respective fault blocks, and hydrocarbons are allowed to flow freely across the faults. Because faults are assumed permeable in this model, there are fewer traps than the permeable model (case 1).

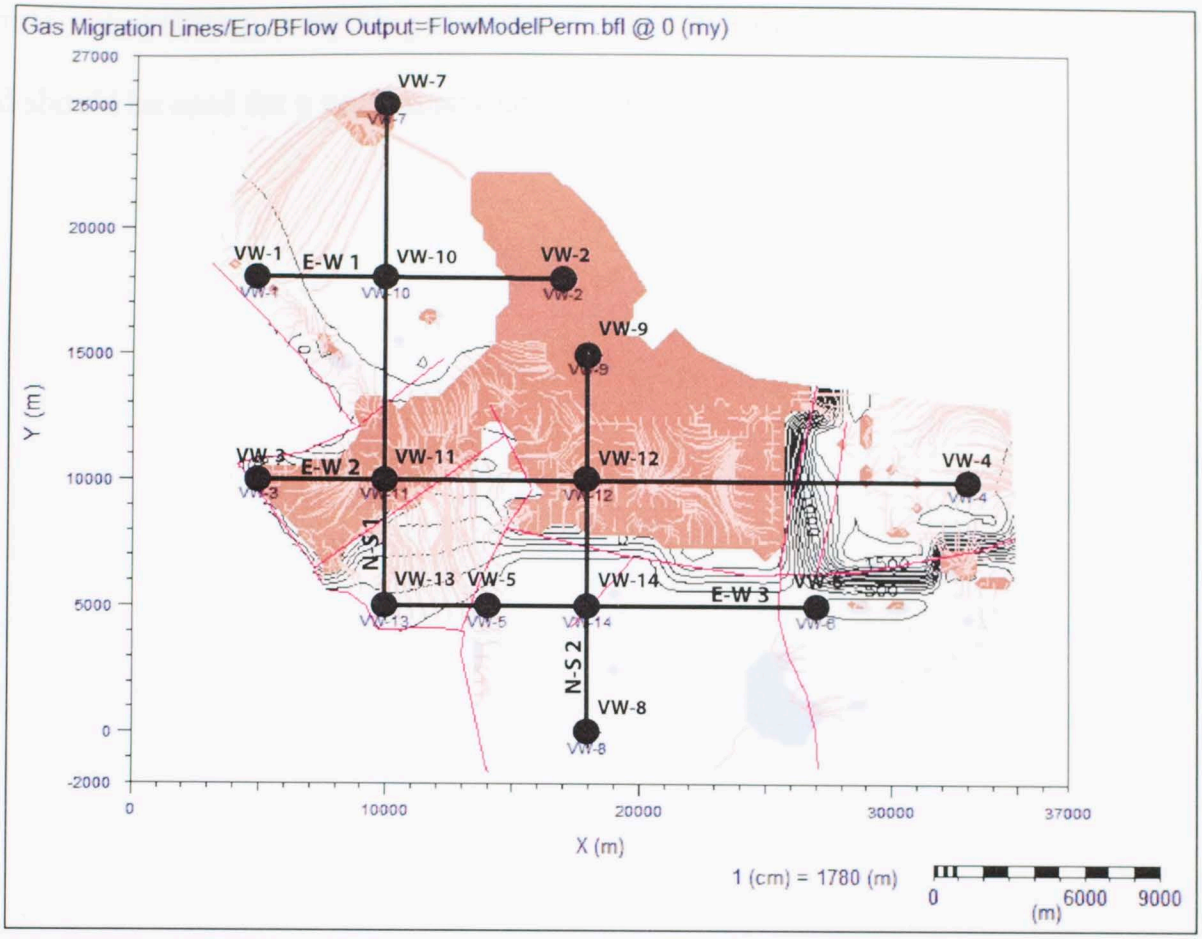

Figure 7.6.21: (Case II) Possible gas traps along four-way closures with migration pathways in the Eocene Roadside Member of the Richmond Formation at present day. Faults are assumed permeable (1000 md). Migration lines for gas are displayed as red arrows while accumulated gas in traps is displayed in red. Unfilled traps are displayed in grey. Note that the flows are not restricted within their respective fault blocks. There are fewer traps than the permeable model (case 1), because the faults are assumed to be permeable.

After all is said and done, there is a significant problem in the model. Although two end-member, all permeable versus all impermeable faults, are used, there is always the possibility of some faults being permeable and others being impermeable, and faults changing their permeability with time. Also BasinView usually uses seismic data to determine the depth of the unit surfaces between wells. Without seismic, which is the case in this study, structure and flow calculations are made only using the wells as data

points, extrapolating everything in between. Therefore these models are likely inaccurate and should be used for a preliminary studies only.

8. QUALITATIVE RISK ASSESSMENT OF THE WAGWATER TROUGH

Risk analysis uses a qualitative input to produce an arithmetic output. Petroleum system criticals are assessed on a scale of one to ten. Ten represents an excellent or favorable critical while one represents a poor or unfavorable critical. After performing a modeled basin analysis, a risk analysis for prospects in the basin can be performed.

Metwalli and Pigott (2005) divided a petroleum system into ten system criticals to effectively perform a risk analysis of the petroleum system. They are source rock quantity, source rock quality, source rock maturity, migration pathway connectivity, migration pathway permeability, migration pathway charge due to hydrocarbon buoyancy and hydrodynamic drive, reservoir volume, reservoir quality due to porosity and permeability conditions, seal potential including strength and closure, and timing. Table 7.3 lists each of these criticals with an assigned value between 1 and 10. These values are decided upon using data from the basin analysis model.

	Petroleum System Criticals	**Risk Value**
Source Rock Criticals	Quantity	4
	Quality	4
	Maturity	9
Migration Criticals	Pathway Connectivity	3
	Permeability	3
	Charge	5
Reservoir Seal Criticals	Volume	5
	Quality (Porosity and Permeability)	4
	Seal (Integrity and Closure)	4
Window	Timing	3
Arithmetic Total		**44**

Table 8.2: A qualitative assessment of the favorability of the Wagwater petroleum system. The ten petroleum system criticals are assigned a value that rates their effectiveness. A value of ten means they are extremely effective while a value of one means they are not effective at all.

Summing the risk values for the ten petroleum system criticals gives a score of 44 out of a possible 100. Using the ranges in table 8.3, the petroleum system in the Wagwater Trough is determined to have high risk for economical exploration.

Arithmetic Total	**Interpretation**
10 – 29	Very High Risk (Very Unfavorable)
30 – 49	**High Risk (Unfavorable)**
50 – 69	Moderate Risk (Neutral)
70 – 89	Some Risk (Favorable)
90 – 100	Very Low Risk (Very Favorable)

Table 8.3: Interpretation of the arithmetic total determined from table 7.2. The petroleum system of the Wagwater Trough has an arithmetic total of 44. This categorizes the system as high risk and unfavorable.

9. SUMMARY OF PETROLEUM SYSTEM ANALYSIS

The tectonic subsidence analyses of 14 virtual wells onshore, Jamaica reveal one fault mechanical episode and one uplift or shortening episode: 66-51 Ma / 1.66 β and 10-0 Ma / 0.81 β (Figure 9.1). The clastic sediments of the Wagwater and Richmond Formations were deposited from 66-51 Ma during a period of fault mechanical tectonic subsidence. The carbonate formations of the Yellow and White Limestone Groups were deposited from 51-10 Ma during a period of thermal tectonic subsidence. Much of the sediments of the Wagwater Trough have been eroded during a period of uplift from 10 Ma to present.

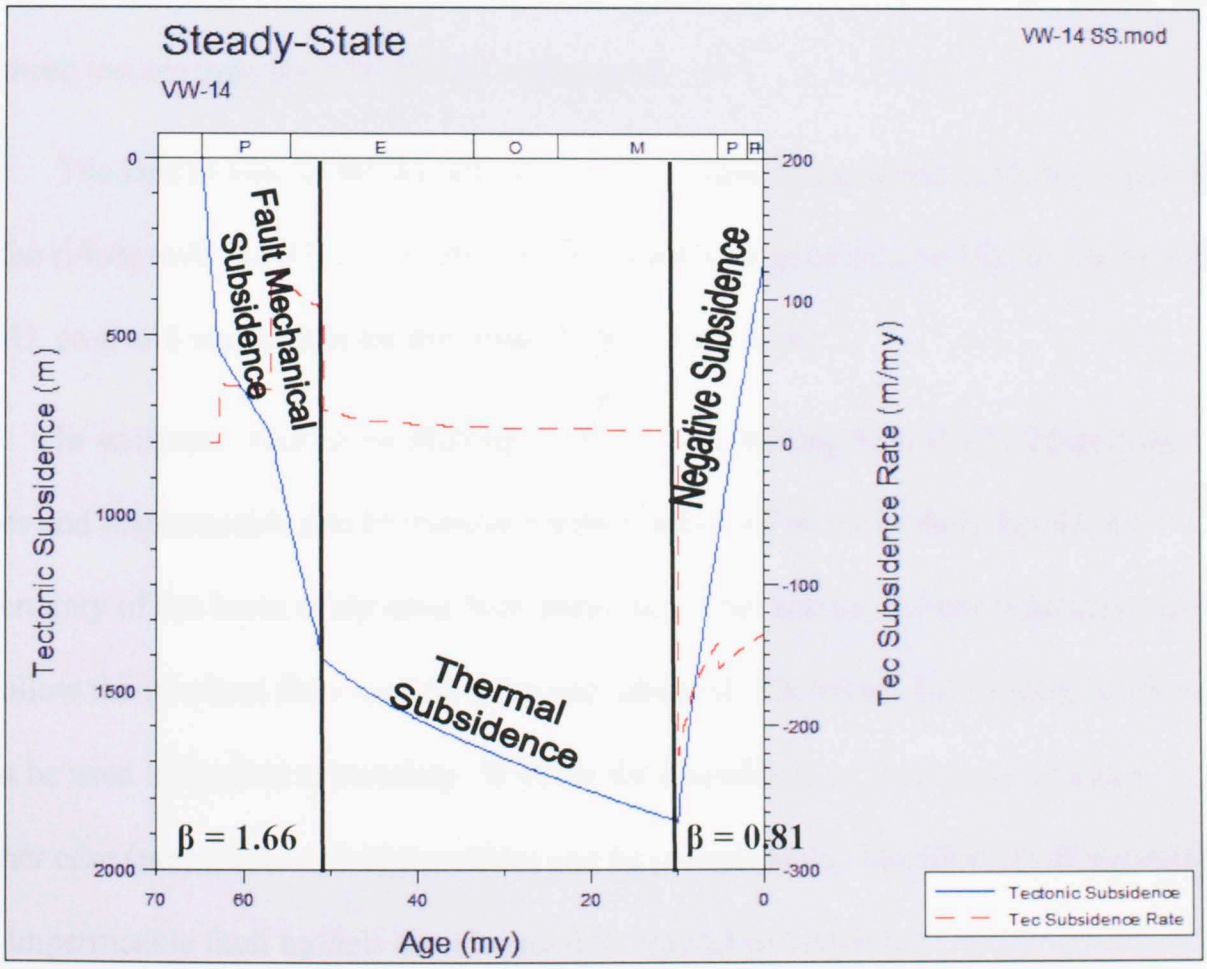

Figure 9.1: Tectonic subsidence and tectonic subsidence rate from VW-14, showing the tectonic episodes and betas through time.

In this study, the shale layers of the Eocene Roadside Member of the Richmond Formation has been identified as potential primary source rocks. Source rock volume and quality (e.g. TOC and kerogen type) of the formation were analyzed using both 1-D and 2-D basin modeling software. In each well, maturity analysis was conducted separately for three cases: steady-state heat flow, rifting heat flow with present-day heat flow of 0.96, and rifting heat flow with present-day heat flow of 1.4. The two rifting cases were created as end members for the actual basin heat flow, with the steady-state heat flow case being very similar to the rifting heat flow with present-day heat flow of 0.96 case. Due to the higher present-day heat flow, the rifting case of 1.4 H.F.U. has source rocks are more mature than the 0.96 H.F.U. rifting case.

The first in situ oil for the rifting 1.4 H.F.U. case commenced at 52 Ma, while that for the rifting 0.96 H.F.U. case is 49 Ma. First expulsion time was 50 Ma for rifting 1.4 H.F.U. case and was 41 Ma for the rifting 0.96 H.F.U. case.

In summary, four cases (Rifting 1.4 H.F.U. vs. Rifting 0.96 H.F.U. Heat Flow Cases and Impermeable and Permeable Faults Cases) which most likely bound the uncertainty of the basin study have been presented. The lack of vitrinite reflectance do not allow the two heat flow models to be geovalidated. Therefore, both rifting conditions must be used to bracket uncertainty. Without the knowledge of fault permeabilities, neither case (permeable or impermeable) can be geovalidated. Therefore, both permeable and impermeable fault models must be used to bracket uncertainty.

10. CONCLUSIONS

1. With respect to tectonic subsidence, the Wagwater Trough has one fault mechanical tectonic subsidence period (66-51 Ma / 1.66 β) and one uplift or shortening period (10-0 Ma / 0.81 β).
2. Average betas calculated using the three methods (1-D, 2-D, and 3-D) are similar. The 2-D method calculated betas that were slightly lower than the 1-D and 3-D methods because the cross-sections are at oblique angles to the axis of maximum extension and maximum shortening.
3. Rifting initiated as a result of dextral shear during the Early Paleocene (Wagwater time) on the southwest side of the northern Wagwater Trough as the hanging wall of the Wagwater Fault went down toward the northeast. Movement on the fault continued through the Early Eocene (Richmond time). The Yallahs-Silver Hill Fault activated on the east side of the Wagwater Trough during the Eocene as its hanging wall went down to the west.
4. Tectonic shortening, due to a reversal in the strike-slip tectonics from dextral to sinistral shear, has caused negative subsidence along a restraining bend. This has exposed the basin rocks to erosion. Most of Northern Wagwater Trough has exposures of the Richmond Formation at the surface.
5. Maturity of the potential source rocks was modeled for steady-state and two rifting heat flow cases: present-day heat flow at 0.96 H.F.U. and present-day heat flow at 1.4 H.F.U. The two rifting heat flow cases bracket the true heat flow models in the basin, with the steady-state heat flow case to create models very similar to the rifting heat flow case with present-day heat flow at 0.96 H.F.U.

6. The Richmond Formation is in both the oil and gas windows for both rifting heat flow cases, and it has likely produced both oil and gas.
7. The Richmond Formation has the best reservoir properties in the Wagwater Trough due to its sandstone lithology and good sorting; however, cementation has significantly reduced the porosity (less that 5% effective porosity).
8. The migration and accumulation of hydrocarbons is directly related to the permeability of faults. The impermeable fault model confines hydrocarbon migration within the individual fault blocks into many mostly three-way and two-way fault bounded closures. The permeable fault model allows the hydrocarbons to migrate through faults and into a few four-way structural closures.
9. The first in situ oil in the Richmond formation in the rifting 1.4 H.F.U. case commenced at 52 Ma, while that in the rifting 0.96 H.F.U. case is 49 Ma. First expulsion time was 50 Ma for rifting 1.4 H.F.U. case and was 41 Ma for the rifting 0.96 H.F.U. case.
10. The risk involved in exploring the Wagwater Trough for hydrocarbons is very high, scoring 45 out of 100. It is likely that most of the hydrocarbons in the Richmond Formation have escaped to the surface, and exploration is limited to the deeper zones only.
11. This model of the 3-D evolution of the Cenozoic Wagwater Trough should serve only as a preliminary basin study. In order to more accurately model the 3-D heat flow, hydrocarbon migration, and hydrocarbon volume the following is warranted: borehole temperature, source rock geochemical, and fault permeability measurements, and for a perfect world 3-D seismic.

BIBLIOGRAPHY

Allen, P. and J. Allen, 2005, Basin analysis, principles and applications, second edition: Oxford, Blackwell Publishing, 549 p.

Andrew, E.M., Paterson Grant and Watson Ltd, G. Wadge, S. Brookes, M. Royall, G. Draper, and E. Robinson, 1992, Bouguer Gravity: Kingston, Ministry of Production, Mining and Commerce, Jamaica Geological Survey Division, map number: 92-106, scale 1:250000, 1 sheet.

Arden, D., 1969, Geologic history of the Nicaraguan Rise: Transactions-Gulf Coast Association of Geological Societies, v. 19, p. 295-308.

Arden, D., 1975, Geology of Jamaica and the Nicaragua Rise: Nairn, A. E. M., and Stehli, F. H., eds., The Ocean Basins and Margins: New York, Plenum, v. 3, p. 617-661.

BasinFlow Manual, 2005, Platte River Associates Inc., Boulder, Colorado, 78 p.

BasinMod 1-D Manual, 2005, Platte River Associates Inc., Boulder, Colorado, 546 p.

BasinMod 2-D Manual, 2005, Platte River Associates Inc., Boulder Colorado, 603 p.

Burke, K., J. Grippi, and A. Sengor, 1980, Neogene structures in Jamaica and the tectonic style of the northern Caribbean Plate boundary zone: Journal of Geology, v. 88, p. 375-386.

Cambray, F.W., and P. Jung, 1970, Provenance of the Richmond Formation from sole markes: The Journal of the Geological Society of Jamaica, v. 11, p. 13-18.

Dahlberg, E.C., 1995, Applied Hydrodynamics in Petroleum Exploration, second edition: New York, Springer-Verlag, 295 p.

Draper, G., 1979, Tectonics of the regionally metamorphosed rocks of eastern Jamaica, Ph.D. thesis, University of the West Indies, Kington, Jamaica, 277 p.

Ekdale A.A., 1984, Ichnology : the use of trace fossils in sedimentology and stratigraphy, Society of Economic Paleontologists and Mineralogists, Tulsa, Oklahoma, 317 p.

Encyclopædia Britannica Online, 2009, Thermodynamics, http://www.britannica.com/EBchecked/topic/591572/thermodynamics (accessed March 18, 2009).

Eva, A.N., 1980, Petroleum potential of Jamaica; a case study of part of an ancient island arc: Technical Bulletin, United Nations, Economic and Social Commission for Asia and the Pacific, Committee for Co-ordination of Joint Prospecting for Mineral Resources in Asian Offshore Areas, n. 3, p 143-151.

Fowler, C.M.R., 1990, The solid earth, an introduction to global geophysics, an introduction to global geophysics: Cambridge, University Press, 472 p.

Green, G.W., 1977, Structure and stratigraphy of the Wagwater Belt, Kingston, Jamaica: Overseas Geology and Mineral Resources, v. 48, p. 21.

Grippi, J. and K. Burke, 1980, Submarine-canyon complex among Cretaceous island-arc sediments, western Jamaica: GSA Bulletin, v. 91, p. 179-184.

Holcombe, T.L., P.R. Vogt, J.E. Matthews, and R.R. Murchison, 1973, Evidence for seafloor spreading in the Cayman Trough: Earth and Planetary Science Letters, v. 20, p 357-371.

Hubbert, M.K., 1953, Entrapment of petroleum under hydrodynamic conditions: AAPG Bulletin, v. 37, p. 1954-2026.

Horsfield, W.T. and M.J. Roobol, 1974, A tectonic model for the evolution of Jamaica: Journal of the Geological Society of Jamaica, v. 14, p 31-38.

Johnson Ibach, L.E., 1982, Relationship between sedimentation rate and total organic carbon content in ancient marine sediments, AAPG Bulletin, v. 66, No. 2, p. 170-188.

Lowrie, W., 2007, Fundamentals of geophysics, second edition: Cambridge, University Press, 381 p.

Macdonald, K.C. and T.L. Holcombe, 1978, Inversion of magnetic anomalies and seafloor spreading in the Cayman Trough: Earth and Planetary Science Letters, v. 40, p. 407-414.

Mann, P., 1983, Cenozoic tectonics of the Caribbean; structural and stratigraphic studies in Jamaica and Hispaniola (Parts 1 and 2), unpublished Ph.D. thesis, Albany State University, Albany, NY, United States (USA), 688 p.

Mann, P., G. Draper, and K. Burke, 1985, Neotectonics of a strike-slip restraining bend system, Jamaica: Strike-slip Deformation, Basin Formation and Sedimentation: SEPM Spec Pub, p. 211-226.

Mann, P., and K. Burke, 1990, Transverse intra-arc rifting; Palaeogene Wagwater Belt, Jamaica: Marine and Petroleum Geology, v. 7, p. 410-427.

Martini, E., 1971, Standard Tertiary and Quaternary calcareous nannoplankton zonation: 2nd Planktonic Conference Proceedings, v. 2, p. 739-771.

Metwalli, F., and J. Pigott, 2005, Analysis of petroleum system criticals of the Matruh-Shushan Basin, Western Desert, Egypt: Petroleum Geoscience, v. 11, p. 157-178.

Mines and Geology Division, 1978, Port Maria Geological Sheet: Ministry of Mining and Natural Resources, Jamaica, map number: 2, scale: 1:50000, 30 sheets.

Mines and Geology Division, 1978, Port Maria Geological Sheet: Ministry of Mining and Natural Resources, Jamaica, map number: 22, scale: 1:50000, 30 sheets.

Mines and Geology Division, 1978, Port Maria Geological Sheet: Ministry of Mining and Natural Resources, Jamaica, map number: 24, scale: 1:50000, 30 sheets.

Mines and Geology Division, 1978, Port Maria Geological Sheet: Ministry of Mining and Natural Resources, Jamaica, map number: 25, scale: 1:50000, 30 sheets.

Ming-Jung, J. and Robinson, E., 1987, Calcareous Nannofossils and Larger Foraminifera in Jamaican Rocks of Cretaceous to Early Eocene age: Journal of the Geological Society of Jamaica, Special Issue, n. 10, p. 24-51.

O'Neal, M.V., 1984, A petrographic investigation of the Windsor Formation, St. Ann's Basin, implications concerning the Cretaceous tectonic history of northern Jamaica, M.S. thesis, University of Oklahoma, Norman, OK, United States (USA), 170 p.

Perry, C., 1984, The Wagwater Belt, Jamaica; the tectonic-geologic development of an aulacogen, M.S. thesis, University of Oklahoma, Norman, OK, United States (USA), 152 p.

Perry, C.L., and Pigott, J.D., 1983, Wagwater Trough, Jamaica; model for aulacogen transgressive sedimentation; AAPG annual convention with divisions SEPM/EMD/DPA: AAPG Bulletin, v. 67, p. 532.

Pigott, J.P., 2007, Written Communication.

Pigott, P., and N. Sattayarak, 1993, Aspects of sedimentary basin evolution assessed through tectonic subsidence analysis. Example: Northern Gulf of Thailand: Journal of Southeast Asia Earth Sciences, v. 8, p. 407-420.

Pindell, J., 1993, Regional synopsis of Gulf of Mexico and Caribbean evolution: Program and Abstracts - Society of Economic Paleontologists, Gulf Coast Section, Research Conference, v. 13, p. 251-274.

Pindell, J., 1994, Evolution of the Gulf of Mexico and the Caribbean: Donovan, S.K. and T.A. Jackson, Caribbean Geology: an Introduction, Kingston, Jamaica, University of the West Indies Publishers' Association, p. 13-40.

Robinson, E., 1967, Submarine slides in the White Limestone Group, Jamaica: American Association of Petroleum Geologists Bulleting, v. 51, p. 569-578.

Robinson, E., 1974, Field Guide to selected Jamaica geological localities: Wright, R.M., Kingston, Jamaica, Mines and Geology, Special Publication no. 1, p. 1-57.

Robinson, E., 1976, Lignite in Jamaica, with additional remarks on peat: Report to the Ministry of Mountain National Resources Jamaica, 63 p.

Rodrigues, K., 1983, Petroleum Source Rock Potential on Jamaica: Oil and Gas Journal, p. 115-119

Rodrigues, K, 1991, Organic Geochemistry and Petroleum Potential of Jamaica, Journal of Petroleum Geology, v. 14, p. 309-322.

Roobol, M.J., 1972, The volcanic geology of Jamaica: Transactions of the 6th Caribbean Geological Conference, Maragarita, Venezuela, p. 100-107.

Sclater, J.G. and P.A.F. Christie, 1980, Continental stretching, an explanation of the post-mid-Cretaceous subsidence of the central North Sea Basin: Journal of Geophysical Research, v. 85, p. 3711-3739.

Sykes, L.R., W.R. McCann, and A.L. Kafka, 1982, Motion of Caribbean plate during the last 7 million years and implications for earlier Cenozoic movements: Journal of Geophysic Research, v. 87, p. 10656-10676.

Trechmann, C.T., 1924, The Carbonaceous Shale or Richmond Formation of Jamaica: Geology Magazine, v. 61, p. 2-19.

Turcotte D.L. and G. Schubert, 2003, Geodynamics, second edition: Cambridge, United Kingdom, Cambridge University Press, 456 p.

Verweij, J.M., 1993, Hydrocarbon Migration Systems Analysis, Developments in Petroleum Science: Elsevier, v. 35, p. 276.

Wescott, W.A., and Ethridge, F.G., 1983, Eocene fan delta-submarine fan deposition in the Wagwater Trough, east-central Jamaica: Sedimentology, v. 30, p. 235-247.

Willis, R., 1981, Conjunctive management of groundwater hydraulics and water quality, Eos, Transactions, American Geophysical Union, v. 64, n. 45, p. 708-709.

Wright, R., 1996, Jamaica's energy, old prospects new resources, Petroleum Corporation of Jamaica, Kingston, Jamaica, 218 p.

APPENDICES

APPENDIX A

FIELD MAP

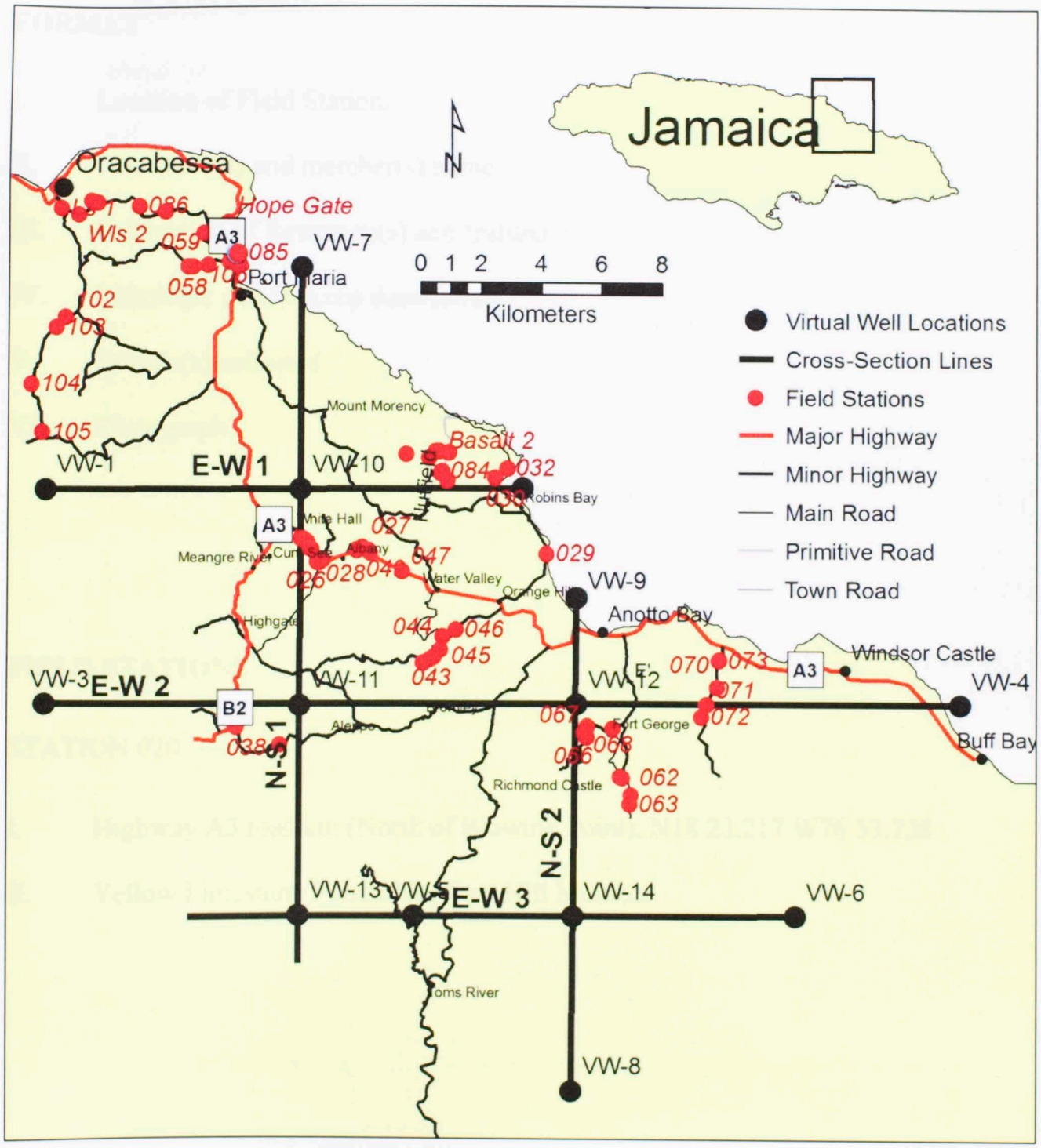

APPENDIX B

FIELD STATIONS

FORMAT

I. Location of Field Station.

II. Formation(s) and member(s) name.

III. Orientation of formation(s) and feature(s)

IV. Lithologic and Outcrop description

V. Sample(s) collected

VI. Photograph

FIELD STATIONS

STATION 020

I. Highway A3 road cut (North of Blowing Point), N18 23.217 W76 53.738

II. Yellow Limestone Formation, Font Hill Member

STATION 021

I. West across the bay from Blowing Point, N18 22.815 W76 53.668

II. Richmond Formation, Roadside Member

IV. About 50 meters of interbedded sand and shale. Sandstone layers are lensoidal and have thicknesses up to about 3 meters

VI.

STATION 022

I. Blowing Point (North of Port Maria), N18 22.780 W76 53.474

II. Richmond Formation, Port Maria Member

III. Northeast Dip less than 20 degrees

IV. Interbedded Sandstone with Conglomerate. Conglomerate up to 9 meters thick. Sandstone layers up to 1 meter thick.

STATION 023

I. Highway A3 east of White Hall, N18 17.870 W76 52.270

II. Richmond Formation

III. Bedding Strike: 312° Dip: 57° SW

IV. 15 meters of inter-bedded sands and shales. Sand channels do not appear laterally continuous if greater than 6 inches thick. Sand layers increase in numbers and thickness up-section.

V. Sample T-108 is part of a 2 ft thick Sandstone channel that is not laterally continuous. Sample T-2908 and T-3008 taken as well.

VI.

STATION 024

I. Highway A3 east of White Hall, N18 17.463 W76 51.877

II. Richmond Formation

IV. Conglomerate

STATION 025

I. Highway A3 east of White Hall, N18 17.499 W76 51.877

II. Richmond Formation

III. Bedding Strike: 296° Dip 7° S

IV. 16 meters of inter-bedded sandstone and shale layers.

V. Sample T-208 was taken from center of 14 inch sand with oil stains. Sample T-308 was taken from a layer of bioturbated sand and silt. Sample T-408 was taken from a sandstone layer right on top of T-308. Sample T-508 is taken from a layer less than one cm of nodular carbonate rock. Sample T-608 is taken from a siltstone layer.

VI.

STATION 026

I. Highway A3 east of White Hall (near station 025), N18 17.505 W76 51.855

II. Richmond Formation

STATION 027

I. Highway A3 east of Albany, N18 17.722 W76 51.120

II. Richmond Formation, Albany Member

III. Dips slightly to the northwest

IV. 7 meters of clast supported conglomerate. Cobble clasts vary in size up to 15 centimeters in diameter with the majority of clasts being 2 to 5 centimeters in diameter. The channels are an average of 1 to 2 meters in thickness which increases to the west.

VI. 

STATION 029

I. Beach south of Robins Bay, N18 17.684 W76 47.644

II. Coastal Limestone

IV. Beach of well-sorted and well-rounded pebbles with few cobbles. Also seen here is coastal limestone with many fossils including corals.

STATION 030

I. North of Robins Bay, N18 19.004 W76 48.631

II. Richmond Formation, Roadside Member

IV. Inter-bedded sandstone and shale with about 80% of the layers as sandstone.

STATION 031

I. North of Robins Bay, N18 19.165 W76 48.398

II. Likely Richmond Formation and Coastal Limestone contact

III. Strike: 346 Dip: 20 NE

IV. Non-layered Limestone uncomformibly overlays a layered clastic unit. Clastic unit contains carbonate sand. Non-layered limestone has fossils of corals and other reef organisms.

VI. 

STATION 038

I. Town of Richmond, N18 14.481 W76 53.434

II. Richmond formation

III. Strike: 144 Dip: 43 SW

IV. Layer of pebble sized conglomerate overlays sandstone.

V. Sample T-1008 taken of the sandstone.

VI. 

STATION 039

I. N18 14.171 W76 52.608

II. Richmond Formation, Roadside Member

III. Strike: 158 Dip: 12 SW

IV. Sandstone

STATION 040

I. Road between Highgate and Orange Hill, N18 15.674 W76 49.941

II. Richmond Formation, Roadside Member

III. Strike: 186 Dip: 15 W

IV. Sandstone beds vary 10 cm to 70 cm in thickness, and shale beds remain fairly constant with a thickness of 6 centimeters.

V. Samples T-1108 and T-1208 taken.

STATION 041

I. Road between Highgate and Orange Hill, N18 15.681 W76 49.925

II. Richmond Formation, Roadside Member

III. Strike: 182 Dip: 50 W

IV. Large sandstone beds about 36 centimeters thick.

STATION 042

I. Road between Highgate and Orange Hill, N18 15.748 W76 49.800

II. Richmond Formation, Roadside Member

IV. Large sandstone beds about 36 centimeters thick.

STATION 043

I. Road between Highgate and Orange Hill, N18 15.786 W76 49.739

II. Richmond Formation, Roadside Member

III. Strike: 213 Dip: 36 NW

IV. 10 meters of sandstone beds varying from 15 – 30 centimeters in thickness, inter-bedded with less than 3 centimeters thick shale beds.

V. Sample T-1308 taken of the sandstone.

VI.

STATION 044

I. Road between Highgate and Orange Hill, N18 15.917 W76 49.617

II. Richmond Formation, Roadside Member

III. Strike: 320 Dip: 38 N

IV. 60 meters of sandstone beds similar to station 043.

VI.

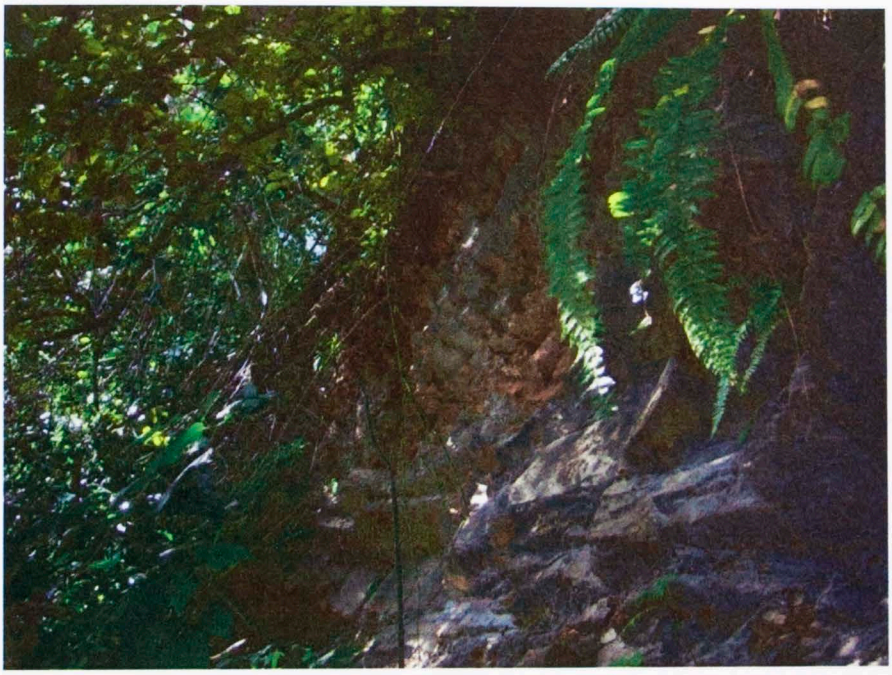

STATION 045

I. Road between Highgate and Orange Hill, N18 16.152 W76 49.578

II. Richmond Formation, Roadside Member

III. Strike: 100 Dip: 10 SW

IV. Inter-bedded sandstone and shale.

VI.

STATION 046

I. Road between Highgate and Orange Hill, N18 16.275 W76 49.331

II. Richmond Formation, Roadside Member

III. Strike: 094 Dip: 18 S

IV. 10 meters of inter-bedded sandstone and shale

VI.

STATION 047

I. Highway A3 west of Water Valley, N18 17.311 W76 50.358

II. Richmond Formation, Albany Member

IV. Albany Conglomerate Bed

STATION 048

I. Highway A3 east of Albany, N18 17.674 W76 51.000

II. Richmond Formation, Albany Member

IV. Albany Conglomerate Bed

STATION 049

I. Highway A3 east of Albany, N18 17.684 W76 51.213

II. Richmond Formation, Roadside Member

III. Strike 145 Dip 30 W

IV. 2-6 centimeter thick beds of equally thick sandstone and shale

V. T-3408, T-3508, T-3608, and T-3708

VI.

STATION 050

I. Fold east of White Hall on highway A3, N18 17.684 W76 52.066

II. Richmond Formation, Roadside Member

III. Regional Strike: 206 Dip: 02 NW

Forelimb Strike: 169 Dip: 64 W

Backlimb Strike: 215 Dip: 28 E

Toplimb Strike: 275 Dip: 04 SE

IV. This is a beautiful buckle fold in the formation that formed post basin development. It is probable that many of these folds exist throughout the formation and could make possible traps for hydrocarbons.

V. T-3108, T-3208, T-3308

STATION 057

I. Road west of Port Maria, N18 22.717 W76 54.435

II. Richmond Formation, Roadside Member

III. Strike: 095 Dip: 20 S

IV. 15 centimeters of sandstone exposed (highly weathered)

V. T-2008

VI.

STATION 058

I. Road west of Port Maria, N18 22.718 W76 54.357

II. Richmond Formation, Roadside Member

III. Strike: 143 Dip: 11 SW

IV. 15 centimeters of poorly exposed sandstone

V. T-2108

VI.

STATION 059

I. Road west of Port Maria, N18 22.750 W76 54.073

II. Richmond Formation, Port Maria Member

III. Strike: 267 Dip: 12 S

IV. 2 meters exposed of cobble to boulder sized conglomerate with 5-30 centimeters of sandstone in the middle. Carbonate cobbles and pebbles found in all layers, but most of the clasts are volcanic and metamorphic in origin.

V. Sample T-2208, Sample T-2308, Sample T-2408 (metamorphic and igneous conglomerate clasts), Sample T-2508(carbonate conglomerate Clast)

VI. 

STATION 060

I. Road south of Fort George, N18 13.652 W76 46.203

II. Richmond Formation, Port Maria Member

STATION 061

I. Road south of Fort George, N18 13.633 W76 46.160

II. Richmond Formation, Port Maria Member

STATION 062

I. Road south of Fort George, N18 13.320 W76 45.996

II. Richmond Formation, Port Maria Member

V. T-2608

STATION 063

I. Road south of Fort George, N18 13.155 W76 46.007

II. Richmond Formation, Roadside Member

III. Strike: 146 Dip: 42 W

V. T-2708

VI.

STATION 064

I. Road west of Fort George, N18 14.533 W76 46.345

II. Richmond Formation, Roadside Member

STATION 065

I. Road west of Fort George, N18 14.567 W76 46.825

II. Richmond Formation, Roadside Member

STATION 066

I. Road west of Fort George, N18 14.406 W76 46.850

II. Richmond Formation, Roadside Member

VI.

STATION 067

I. Road west of Fort George, N18 14.362 W76 46.838

II. Richmond Formation, Roadside Member

STATION 068

I. Road west of Fort George, N18 14.448 W76 46.880

II. Richmond Formation, Roadside Member

VI. 

STATION 069

I. Road south of Windsor Castle, N18 15.782 W76 44.363

II. White Limestone Formation

STATION 070

I. Road south of Windsor Castle, N18 15.294 W76 44.405

II. White Limestone Formation, Montpellier Member Equivalent

III. Strike: 240 Dip 12 E

IV. White chalk beds

V. T-2808

VI. 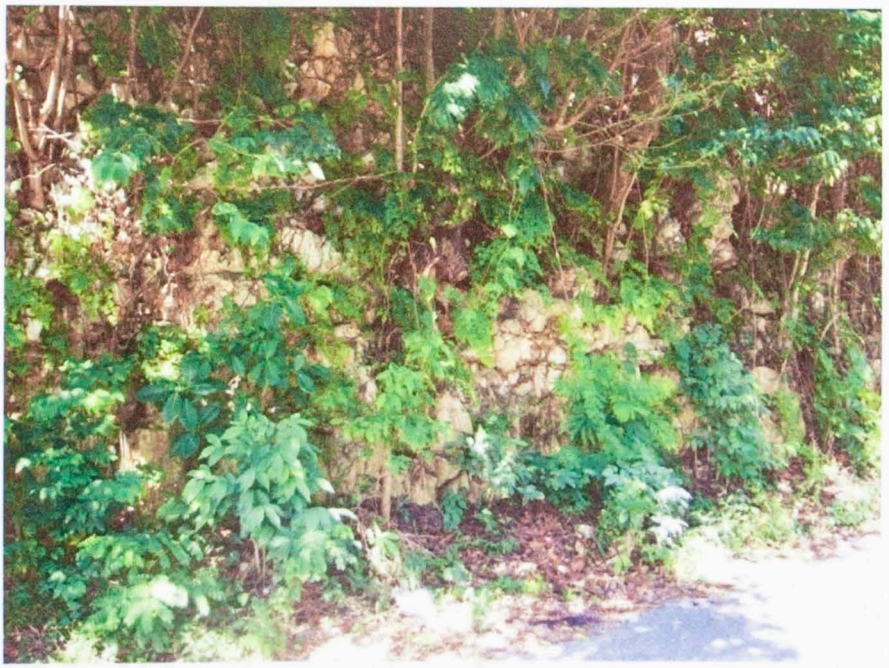

STATION 071

I. Road south of Windsor Castle, N18 14.982 W76 44.587

II. White Limestone Formation, Montpellier Member Equivalent

STATION 072

I. Road south of Windsor Castle, N18 14.749 W76 44.684

II. White Limestone Formation, Montpellier Member Equivalent

STATION 073

I. Road south of Windsor Castle, N18 15.773 W76 44.368

II. White Limestone Formation

IV. Similar to station 069

STATION 084

I. Nutfield Road (north of Nutfield), N18 19.106 W76 49.642

II. Nutfield Volcanics

IV. 5 meters of porphoritic vesicular basalt found in pillow-like structures

V. T-1408

VI. 

STATION 102

I. Road south of Orcabessa, N18 21.771 W76 56.721

II. Richmond Formation

STATION 103

I. Road south of Orcabessa, N18 21.582 W76 56.892

II. Richmond Formation

STATION 104

I. Road south of Orcabessa, N18 20.562 W76 57.342

II. Yellow Limestone Formation, Font Hill Member

STATION 105

I. Road south of Orcabessa, N18 19.700 W76 57.126

II. Yellow Limestone Formation, Font Hill Member

STATION 106

I. Blowing Point, N18 22.952 W76 53.546

II. Richmond Formation, Port Maria Member

III. Northeast Dip less than 20 degrees

APPENDIX C

VIRTUAL WELLS

Number	Latitude	Longitude	Northing Y (km)	Easting X (km)	Approx. Elevation (m above SL)
VR-1	18.312	-76.950	18	5	425
VR-2	18.312	-76.802	18	17	-25
VR-3	18.250	-76.950	10	5	500
VR-4	18.250	-76.664	10	33	-50
VR-5	18.185	-76.839	5	14	300
VR-6	18.185	-76.715	5	27	600
VR-7	18.378	-76.872	25	10	-50
VR-8	18.134	-76.784	0	18	500
VR-9	18.281	-76.784	15	18	-50
VR-10	18.312	-76.872	18	10	100
VR-11	18.225	-76.872	10	10	200
VR-12	18.250	-76.784	10	18	100
VR-13	18.185	-76.872	5	10	300
VR-14	18.185	-76.784	5	18	500

Virtual Well # 1

Formation or Event Name	Type	Begin Age (my)	Top Depth (m)	Present Thick (m)	Eroded Thick (m)	Lithology	Organofacies / Kerogen	Initial TOC (%)
Surface Erosion	E	10			-1360			
LS-dep	D	47			1360	Limestone	Type II (BMOD-1D LLNL)	3
LS	F	51	0	240		Limestone	Type II (BMOD-1D LLNL)	3
Ero	F	55	240	1370		Sandstone	Type II (BMOD-1D LLNL)	6
Ep	F	57	1610	520		Sandstone	Type III (BMOD-1D LLNL)	6
Pd	F	60.9	2130	210		Sandstone	Type III (BMOD-1D LLNL)	7

Virtual Well # 2

Formation or Event Name	Type	Begin Age (my)	Top Depth (m)	Present Thick (m)	Eroded Thick (m)	Lithology	Organofacies / Kerogen	Initial TOC (%)
Surface Erosion	E	10			-2000			
LS-dep	D	51			1500	Limestone	Type II (BMOD-1D LLNL)	3
Ero-dep	D	53.1			500	Sandstone	Type II (BMOD-1D LLNL)	6
Ero	F	57	0	900		Sandstone	Type II (BMOD-1D LLNL)	6
Pd	F	60.9	900	230		Sandstone	Type III (BMOD-1D LLNL)	5

Virtual Well # 3

Formation or Event Name	Type	Begin Age (my)	Top Depth (m)	Present Thick (m)	Eroded Thick (m)	Lithology	Organofacies / Kerogen	Initial TOC (%)
Surface Erosion	E	10			-1430			
LS-dep	D	49.1			1430	Limestone	Type II (BMOD-1D LLNL)	3
LS	F	51	0	70		Limestone	Type II (BMOD-1D LLNL)	3
Ero	F	57	70	1000		Sandstone	Type II (BMOD-1D LLNL)	6
Pd	F	63	1070	560		Sandstone	Type III (BMOD-1D LLNL)	5
Ppr	F	63.6	1630	310		Sandstone	Type II (BMOD-1D LLNL)	7
Pg	F	66	1940	1120		Sandstone	Type III (BMOD-1D LLNL)	10

Virtual Well # 4

Formation or Event Name	Type	Begin Age (my)	Top Depth (m)	Present Thick (m)	Eroded Thick (m)	Lithology	Organofacies / Kerogen	Initial TOC (%)
LS	F	51	0	1510		Limestone	Type II (BMOD-1D LLNL)	3
Ero	F	57	1510	1560		Sandstone	Type II (BMOD-1D LLNL)	6

Virtual Well # 5

Formation or Event Name	Type	Begin Age (my)	Top Depth (m)	Present Thick (m)	Eroded Thick (m)	Lithology	Organofacies / Kerogen	Initial TOC (%)
Surface Erosion	E	10			-5000			
LS-dep	D	51			1500	Limestone	Type II (BMOD-1D LLNL)	3
Ero-dep	D	57			1500	Sandstone	Type II (BMOD-1D LLNL)	6
Pd-dep	D	63			1290	Sandstone	Type III (BMOD-1D LLNL)	5
Ppr-dep	D	63.6			230	Sandstone	Type II (BMOD-1D LLNL)	7
Pg-dep	D	63.8			480	Sandstone	Type III (BMOD-1D LLNL)	10
Pg	F	65.7	0	2070		Sandstone	Type III (BMOD-1D LLNL)	10

Virtual Well # 6

Formation or Event Name	Type	Begin Age (my)	Top Depth (m)	Present Thick (m)	Eroded Thick (m)	Lithology	Organofacies / Kerogen	Initial TOC (%)
Surface Erosion	E	10			-570			
LS-dep	D	25.58			570	Limestone	Type II (BMOD-1D LLNL)	3
LS	F	51	0	930		Limestone	Type II (BMOD-1D LLNL)	3
Ero	F	57	930	1410		Sandstone	Type II (BMOD-1D LLNL)	6

Virtual Well # 7

Formation or Event Name	Type	Begin Age (my)	Top Depth (m)	Present Thick (m)	Eroded Thick (m)	Lithology	Organofacies / Kerogen	Initial TOC (%)
Surface Erosion	E	10			-1500			
LS-dep	D	51			1500	Limestone	Type II (BMOD-1D LLNL)	3
Ero	F	55	0	1660		Sandstone	Type II (BMOD-1D LLNL)	6
Ep	F	57	1660	430		Sandstone	Type III (BMOD-1D LLNL)	5

Virtual Well # 8

Formation or Event Name	Type	Begin Age (my)	Top Depth (m)	Present Thick (m)	Eroded Thick (m)	Lithology	Organofacies / Kerogen	Initial TOC (%)
Surface Erosion	E	10			-3740			
LS-dep	D	51			1500	Limestone	Type II (BMOD-1D LLNL)	3
Ero-dep	D	57			1330	Sandstone	Type II (BMOD-1D LLNL)	6
Pd-dep	D	63			580	Sandstone	Type III (BMOD-1D LLNL)	5
Ppr-dep	D	63.6			200	Sandstone	Type II (BMOD-1D LLNL)	7
Pg-dep	D	63.8			130	Sandstone	Type III (BMOD-1D LLNL)	10
Pg	F	66	0	2170		Sandstone	Type III (BMOD-1D LLNL)	10

Virtual Well # 9

Formation or Event Name	Type	Begin Age (my)	Top Depth (m)	Present Thick (m)	Eroded Thick (m)	Lithology	Organofacies / Kerogen	Initial TOC (%)
Surface Erosion	E	10			-1500			
LS-dep	D	51			1500	Limestone	Type II (BMOD-1D LLNL)	3
Ero	F	57	0	1230		Sandstone	Type II (BMOD-1D LLNL)	6

Virtual Well # 10

Formation or Event Name	Type	Begin Age (my)	Top Depth (m)	Present Thick (m)	Eroded Thick (m)	Lithology	Organofacies / Kerogen	Initial TOC (%)
Surface Erosion	E	10			-2210			
LS-dep	D	51			1500	Limestone	Type II (BMOD-1D LLNL)	3
Ero-dep	D	53			710	Sandstone	Type II (BMOD-1D LLNL)	6
Ea	F	54	0	190		Sandstone	Type III (BMOD-1D LLNL)	7
Ero	F	56.4	190	710		Sandstone	Type II (BMOD-1D LLNL)	6
Ep	F	57	900	90		Sandstone	Type III (BMOD-1D LLNL)	6
Pd	F	62.1	990	300		Sandstone	Type III (BMOD-1D LLNL)	5

Virtual Well # 11

Formation or Event Name	Type	Begin Age (my)	Top Depth (m)	Present Thick (m)	Eroded Thick (m)	Lithology	Organofacies / Kerogen	Initial TOC (%)
Surface Erosion	E	10			-2450			
LS-dep	D	51			1500	Limestone	Type II (BMOD-1D LLNL)	3
Ero-dep	D	54			950	Sandstone	Type II (BMOD-1D LLNL)	6
Ero	F	57	0	950		Sandstone	Type II (BMOD-1D LLNL)	6
Pd	F	63	950	610		Sandstone	Type III (BMOD-1D LLNL)	5
Ppr	F	63.6	1560	220		Sandstone	Type II (BMOD-1D LLNL)	7
Pg	F	65.6	1780	1110		Sandstone	Type III (BMOD-1D LLNL)	10

Virtual Well # 12

Formation or Event Name	Type	Begin Age (my)	Top Depth (m)	Present Thick (m)	Eroded Thick (m)	Lithology	Organofacies / Kerogen	Initial TOC (%)
Surface Erosion	E	10			-2410			
LS-dep	D	51			1500	Limestone	Type II (BMOD-1D LLNL)	3
Ero-dep	D	55.3			910	Sandstone	Type II (BMOD-1D LLNL)	6
Ero	F	57	0	370		Sandstone	Type II (BMOD-1D LLNL)	6
Pd	F	63	370	290		Sandstone	Type III (BMOD-1D LLNL)	5
Pg	F	63.3	660	110		Sandstone	Type III (BMOD-1D LLNL)	10

Virtual Well # 13

Formation or Event Name	Type	Begin Age (my)	Top Depth (m)	Present Thick (m)	Eroded Thick (m)	Lithology	Organofacies / Kerogen	Initial TOC (%)
Surface Erosion	E	10			-3270			
LS-dep	D	51			1500	Limestone	Type II (BMOD-1D LLNL)	3
Ero-dep	D	57			1410	Sandstone	Type II (BMOD-1D LLNL)	6
Pd-dep	D	59.6			360	Sandstone	Type III (BMOD-1D LLNL)	5
Pd	F	63	0	460		Sandstone	Type III (BMOD-1D LLNL)	5
Ppr	F	63.6	460	320		Sandstone	Type II (BMOD-1D LLNL)	7
Pg	F	65.85	780	2690		Sandstone	Type III (BMOD-1D LLNL)	10

Virtual Well # 14

Formation or Event Name	Type	Begin Age (my)	Top Depth (m)	Present Thick (m)	Eroded Thick (m)	Lithology	Organofacies / Kerogen	Initial TOC (%)
Surface Erosion	E	10			-3200			
LS-dep	D	51			1500	Limestone	Type II (BMOD-1D LLNL)	3
Ero-dep	D	57			1330	Sandstone	Type II (BMOD-1D LLNL)	6
Pd-dep	D	63			370	Sandstone	Type III (BMOD-1D LLNL)	5
Fault Hiatus	H	63.8						
Pg	F	65.05	0	700		Sandstone	Type III (BMOD-1D LLNL)	10

APPENDIX D

GEOLOGIC MAP OF THE NORTHERN WAGWATER TROUGH

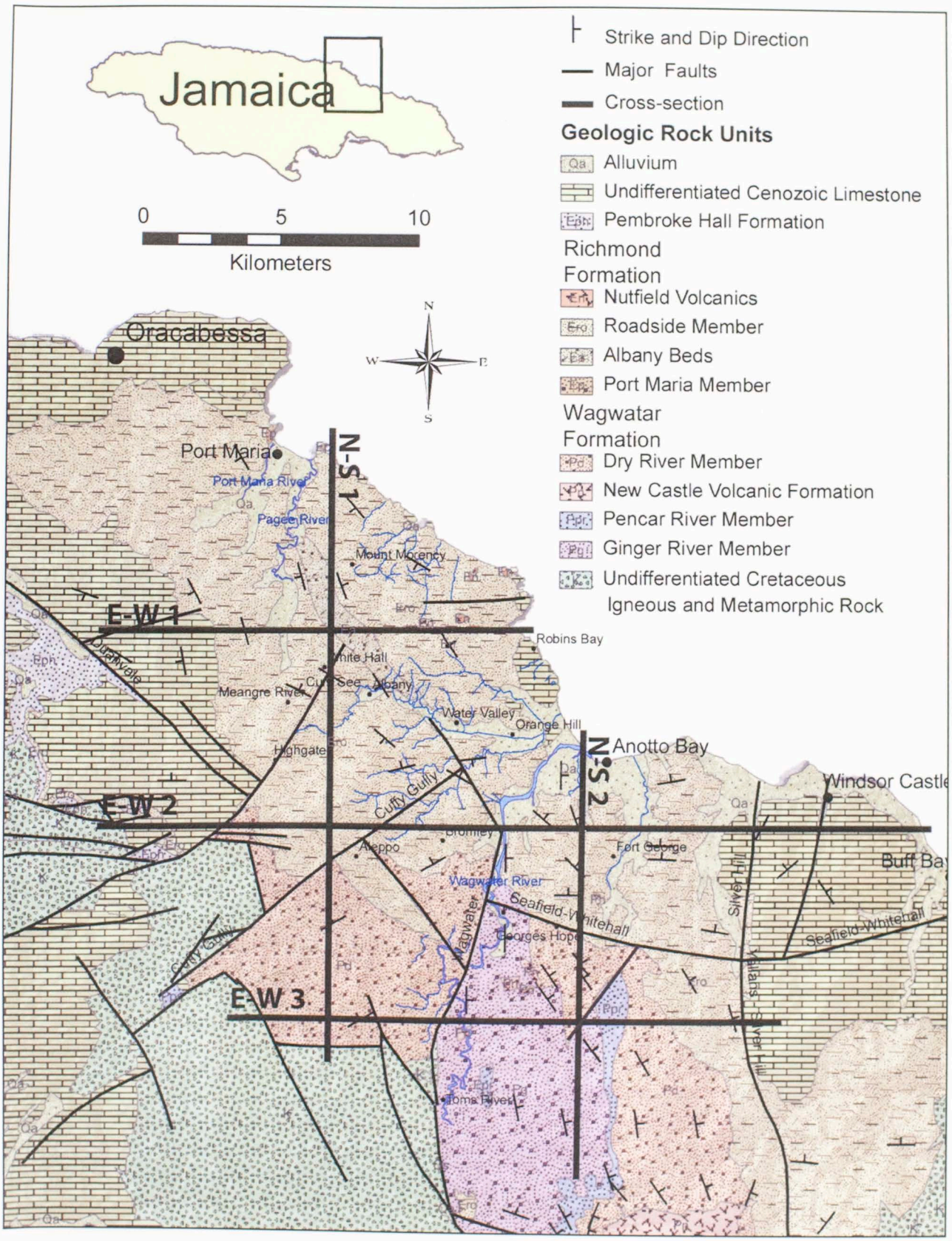

(after Mann and Burke, 1990; after Mines and Geology Division, 1978)